U.PORTO
FEUP FACULDADE DE ENGENHARIA
UNIVERSIDADE DO PORTO

Design of eco-efficient ultra-high performance fibre reinforced cement-based composite for rehabilitation/strengthening applications

Ana Mafalda Matos Teixeira Barbosa

Supervisors:
Doctor Sandra da Conceição Barbosa Nunes
Doctor José Luís Barroso de Aguiar

January 2020

Doctoral Program in Civil Engineering

Thesis submitted in partial fulfilment of the requirements for the degree in Doctor of Philosophy

To our little angels in the heaven. One day we will meet...
To our rainbow...

Acknowledgements

First of all, I would like to thank the financial support to FCT, namely though Research Grant PD/BD/113636/2015 within the Doctoral Program Eco-CoRe. I also thank Professor Jorge Brito and Professor João Ramoa Correia, which always provided the support needed. Collaboration and the supplying of raw materials by Refinery/Galp Energia, Secil, Omya Comital, Sika and EUROMODAL is also gratefully acknowledged.

I would like to sincerely thank my supervisor, Professor Sandra Nunes, for allowing me to work on this innovative subject, for her support, for her commitments and valuable comments during these four years. I also would like to thank the support of my co-supervisor Professor Barroso Aguiar, besides he has in-depth knowledge, he was always humble and kind. I am deeply indebted to Professor Carla Costa for sharing her profound knowledge in materials chemical field, which significantly contributed to the outcome of this work. I express my acknowledgement to Professor Paula Milheiro for her dedication to the statistical part of this work and her constant availability to help and contribute. I also thank Professor Mário Pimentel for his suggestions and always kept the door open to answer my questions and doubts.

I deeply indebted to Professor Joana Sousa Coutinho, my master, and also an inspiration of what i would like to be one day as a professional and as a Human being. It was a great honour work with Professor Joana Sousa Coutinho. I could learn what is truly work as a team, the perseverance and humility. Thanks for sharing her in-depth knowledge, namely, in the building materials field, always so humble and generous.

I would like to express a special thank to Professor Erik Schlangen and his team, which welcomed and supported me during my inter-ship in TU Delft. I would like to particularly thank Stefan and Maiko for incredible support and also for their friendship. I will never forget our (funny) moments in Microlab. I also would like to thank Professor Miguel Azenha and José Granja for their support during the implementation of a new experiment and for providing all facilities to perform that. Besides, I would like to thank my friend Francisco Araújo, who is always available to share his in-depth knowledge in the field of the building materials.

This work would not be possible without the unconditional support of Paula Silva and Claudio Ferraz. I would like to express my deep thank for their support, and namely their friendship. I will keep with me all the moments we had in the laboratory. A special thank to Paula, who was there when a storm came to my life.

I would like to express my acknowledgement to DEC, namely, Professor Humberto Varum, Dr.ª Julia Aroso, Marta Poinhas Costa, Paula Madeira, Anabela Cancela and Olivia Costa, for their availability to help me during all processes that a PhD involves.

To my offices mates, a big thanks, namely, Emanuel, José and Nuno, for theirs incredible support constant encouragement during last four years, and for the pleasant conversations and good moments we lived in that office. I will miss that, for sure.

I would like to especially thank my friend Tuba for giving me her unconditional friendship and share with me her (so different) culture. Thanks for being there in the darkest season of my life. No words would be enough to thank that. To my friend Filipa I would like to thank decades of friendship and for being there on all moments of my life. To Tânia and Sofia, i am deeply thankful for their friendship, besides distance, we are always together and nothing changes.

To my mummy and my grandpas, I feel really thankful I had a brave example, they taught me what the essential values of life are. Thanks for accept me and love me for what I am. Moreover, to my brother, Miguel, besides your differences, thanks for being there, always. To my family in low, I would like to express my acknowledgement for their support and for giving me a new family. A special thank for my nieces to provide me such happy moments and to make me improve my (weak) handmade skills in their plays.

Last but not least, the biggest thank, to my husband, Gilberto, my soulmate, my everything. Our story has been no perfect lately, but wake up with you every day and have you when i arrive home are the best moments of my day. Thanks for giving your unconditional love, for loving me for what I am and for making me want to be a better Ana Mafalda. I am proud of your family.

Abstract

The application of Ultra-high-performance fibre reinforced cement-based composites (UHPFRC) in structures is still in the beginning due to the high production cost lack of knowledge. Thus efforts are needed to make UHPFRC a more economical, eco-efficient and regular technology. An exciting field for a competitive application for UHPFRC is the rehabilitation and strengthening of reinforced or pre-stressed concrete structures, particularly when exposed to aggressive environments, in which a new layer of UHPFRC replaces the deteriorated concrete. The combination of existing concrete with the UHPFRC as a protective layer provides an efficient way of increasing the impermeability, the stiffness and structural resistance capacity while keeping compact cross-sections. As additional advantages are expected as reduction of maintenance routines and life-cycle cost, and longer service life.

The tensile performance is essential for coping with the typical high autogenous deformations of UHPFRC and for ensuring water-tightness even when subjected to critical tensile strains, namely in the rehabilitation or strengthening applications. Tensile performance mostly depends on the fibre-to-matrix bond mechanics and the fibre distribution/orientation. If the former can be tailored during mix design, the latter is influenced by the rheology, casting methods, geometry and dimensions of the structural element. Therefore, the "in-structure" tensile response can differ from that characterised in laboratory tests and cracking might occur in the UHPFRC layer. Cracking might alter the local transport properties of this protective layer, allowing rapid ingress of detrimental substances. Thus, further research is needed to study the influence of cracking on UHPFRC durability.

The present PhD research aimed to develop a new UHPFRC for rehabilitation or strengthening applications, employing locally available raw materials, namely in Portugal. Considering the target application, which requires on-site fabrication and standard technology, conventional curing methods were selected. Since typical high autogenous shrinkage can be a disadvantage of this composite, namely in these applications, the second core theme of this research was to achieve UHPFRC with

lower early-age shrinkage along with reducing its environmental and economic impact. Finally, characterise the influence of cracking (considering service conditions) on UHPFRC durability was also an objective to pursue.

Within the current PhD, for the first time, spent equilibrium catalyst (ECat), a waste generated in the oil refineries, was studied as an internal curing agent mitigating the UHPFRC autogenous shrinkage. The new UHPFRC mixture developed presented comparable performance with other UHPFRC, but incorporating lower contents of cement and silica fume, with advantages regarding the cost and the CO_2 emissions. Moreover, the replacement of natural sand with a waste (15% in volume) allows limiting the excessive exploitation of natural resources and waste recycling. Even though simple manufacture and curing procedures were employed, the new UHPFRC achieved a compressive strength of 147 and 156 MPa after 28 and 90 days, respectively; and exhibited a tensile strain-hardening behaviour with multiple microcracking formation, with uniaxial tensile peak stress and peak strain ranging from 11 to 15 MPa and 0.27–0.47%, respectively.

An evaluation of several standard durability indicators of new UHPC (without steel fibres) showed its very high durability compared to ordinary concrete and even high-performance concrete. Total porosity determined by MIP (lower than 5%) and sorptivity coefficient (0.014 mg/(mm$^2\sqrt{\text{min}}$)) showed the primary reason for UHPC enhanced durability is its highly dense matrix and very low capillary porosity.

The experimental characterisation of the capillary transport properties on cracked UHPFRC with different crack patterns and fibre dosages showed its excellent tightness to water. Sorptivity results of cracked UHPFRCs specimens remained in the range of 0.024 to 0.044 mg/(mm$^2\sqrt{\text{min}}$), which is relatively low when compared to that of a sound conventional concrete (0.09 mg/(mm$^2\sqrt{\text{min}}$)).

After 1-year chlorides exposure, UHPFRC specimens were in excellent condition with no significant losses in terms of flexural strength; however stiffness might be reduced. The chloride contents up to 20 mm depth were superior to chloride critical content suggested by European standard. This demonstrated that a cover depth of, at least, 20 mm of UHPFRC, would be recommended to protect a concrete substrate in hybrid structures.

Resumo

A aplicação do compósito cimentício de ultraelevado desempenho reforçado com fibras (UHPFRC) em estruturas encontra-se ainda no seu estado inicial devido, nomeadamente, ao elevado custo e falta de conhecimento, sendo necessários esforços para tornar o UHPFRC um material mais prático, económico, eco-eficiente e amplamente aceite. A utilização deste material pode ser competitiva em situações particulares, tais como, na reabilitação ou reforço de zonas especificas de infraestruturas de betão armado ou pré-esforçado. Aplicado em camadas finas, com ou sem armadura, substituindo camadas carbonatadas ou fissuradas, o UHPFRC permite uma franca melhoria das propriedades mecânicas e a drástica diminuição da permeabilidade de elementos estruturais expostos a ambientes agressivos. Prevê-se assim, um aumento da vida útil da estrutura bem como a redução de operações e custos de manutenção.

Porém, em estruturas híbridas de betão convencional e UHPFRC, um desafio importante é a restrição conferida pelo substrato à deformação livre da nova camada de UHPFRC, que gera tensões internas de tração. Deste modo, o desempenho em tração é essencial para suportar a elevada deformação autogénea característica dos UHPFRC, garantindo a sua baixa permeabilidade, mesmo quando submetido a tensões elevadas. O desempenho em tração depende principalmente da ligação fibra-matriz e da distribuição e orientação das fibras. A ligação fibra-matriz pode ser de certa forma otimizada. Por outro lado, a distribuição e orientação, é influenciada pela reologia, método de betonagem, geometria e dimensões do elemento estrutural. Portanto, a resposta à tração "in situ" pode diferir daquela caracterizada em testes de laboratório, e a fissuração da nova camada de UHPFRC pode ocorrer. Isto pode afetar as propriedades locais da camada protetora, permitindo a entrada de substâncias prejudiciais. Deste modo, é importante mais investigação sobre a durabilidade do UHPFRC num estado de serviço (fissurado).

O presente estudo teve como objetivo desenvolver e otimizar uma nova mistura de UHPFRC utilizando materiais locais (disponíveis em Portugal) e tendo em vista aplicações de reabilitação ou reforço com betonagem "in situ". Sendo a elevada deformação autogénea uma desvantagem deste compósito, principalmente para a aplicação

referida, o novo UHPFRC deveria apresentar uma menor retração, bem como menor impacte ambiental e custo. A implementação de uma metodologia para investigar a influência de microfissuras na durabilidade do UHPFRC também foi uma meta a alcançar.

Pela primeira vez, no presente estudo, o catalisador exausto de cracking catalítico (ECat), um resíduo gerado nas refinarias de petróleo, foi utilizado como agente de cura interna mitigando a retração autogénea do UHPFRC. A nova mistura de UHPFRC, apesar de incorporar menores dosagens de cimento e silica de funo, apresentou um desempenho mecânico e de durabilidade equivalente a misturas da mesma família, com vantagens face ao custo e emissões de CO_2. Adicionalmente, a incorporação de ECat pode minimizar a quantidade de resíduo enviada para aterro, transformando-o num subproduto com valor acrescentado bem como reduzir a exploração de recursos naturais. O novo UHPFRC alcançou uma resistência à compressão de 147 e 156 MPa após 28 e 90 dias de cura em água, respectivamente; e tração e extensão de pico entre 11 a 15 MPa e 0.27-0.47 %, respectivamente.

A avaliação de vários indicadores de durabilidade do novo UHPC (sem fibras) demonstrou excelentes propriedades no que se refere resistência à penetração de vários agentes agressivos, apesar da mistura concebida apresentar dosagens inferiores de cimento e sílica de fumo. Os resultados de porosidade avaliados com recurso a MIP (MIP $<$ 5%) e o coeficiente de absorção de água por capilaridade (0.014 mg/(mm$^2\sqrt{\text{min}}$)) foram a principal razão para a promissora durabilidade do novo UHPC, que se deve à sua matriz altamente densa e porosidade capilar muito baixa.

A caracterização experimental das propriedades de transporte por sucção capilar num estado fissurado, com diferentes padrões de fissuração e dosagens de fibras, mostrou que o novo UHPFRC pode ser uma excelente barreira face a substâncias aquosas, mesmo num estado fissurado. Os coeficientes de absorção de água por capilaridade dos UHPFRCs fissurados permaneceram entre 0.024 a 0.044 mg/(mm$^2\sqrt{\text{min}}$), o que é relativamente baixo quando comparado ao mesmo coeficiente de um betao convencional não fissurado (0.09 mg/(mm$^2\sqrt{\text{min}}$)).

Após 1 ano de exposição a ciclos de molhagem-secagem numa solução de cloretos (simulando água do mar), os provetes de UHPFRC não apresentaram perda significativa em termos de resistência à flexão; no entanto, a rigidez pode ser comprometida. O teor de cloretos até uma profundidade de 20 mm foi superior ao teor crítico de cloretos sugerido pela norma europeia. Isto indicou que uma camada de recobrimento de, pelo menos, 20 mm de UHPFRC seria recomendável para proteger um substrato de betão antigo em estruturas híbridas.

Contents

List of Figures

List of Tables

List of Abbreviations

Capital roman letters

AC	Alternating current
Adj-R^2	Adjusted R-Squared
ANOVA	Analysis of variance
ASR	Alkalis-silica reaction
BET	Brunauer-Emmett-Teller theory for measurement of specific surface area of materials
BFS	Blast Furnace Slag
C_2S	Dicalcium silicate (Belite)
C_3A	Tricalcium aluminate
C_3S	Tricalcium silicate (Alite)
C_4AF	Tetracalcium aluminoferrite
$Ca(OH)_2$ or CH	Calcium hydroxide
$CaCO_3$	Calcium carbonate
C_0	Initial chloride content [%]
Ccrit	Critical chloride content [%]
CCD	Central composite design
C-LDH	Calcined Layered Double Hydroxide
CO_2	Carbon dioxide
COD	Crack open displacement [µm]
COD_{fcf}	Crack open displacement at maximum stress [µm]
COD_{Fmax}	Crack open displacement at maximum load [µm]

COD_{load}	Crack open displacement under load (before unload) [µm]
COD_{res}	Crack open displacement residual (after unload) [µm]
CSH	Calcium silicates hydrate
D	Desirability function
DC	Direct current
Dflow	Spread flow diameter [mm]
D_{nssm}	Apparent chloride diffusion coefficient $[10^{-12}\ m^2\,s^{-1}]$
D_{crack}	Chloride penetration depth at maximum crack front [mm]
D_m	Average chloride penetration depth in non-cracked area [mm]
DOE	Design of experiments
ECat	Spent equilibrium catalyst
ECC	Engineered cementitious composites
F	Force [N/kN]
FA	Fly ash
FCC	Fluid Catalytic Cracking
Fe_2O_3	Iron oxide
F_{max}	Flexural maximum force [N/kN]
FRC	Fibre reinforced concrete
GGBFS	Ground granulated blast-furnace slag
GWP	Global Warming Potential
HPC	High-performance concretes
ITZ	Interfacial transition zone
LF	Limestone filler
LOI	Loss on ignition [%]
LVDT	Linear variable differential transformer

LWS	Lightweight sand
$MgSO_4$	Magnesium sulfate
MIP	Mercury intrusion porosimetry
MTCK	Metakaolin
Na_2Oeq	Equivalent alkali content [%]
NaCl	Sodium Chloride
NaOH	Sodium hydroxide
NS	Nano-silica
OC	Ordinary concrete
PC	Portland cement
PCE	Polycarboxylate-based
POR	Water permeable porosity [%]
PSD	Pore size distribution
QF	Quartz flour
R^2	R-Squared
Rc,2d	Compressive strength at 2 age days [MPa]
Rc,7d	Compressive strength at 7 age days [MPa]
Rc,28d	Compressive strength at 28 age days [MPa]
RCM	Rapid migration test
RCPT	Rapid Chloride Permeability Test
RH	Relative humidity [%]
RHA	Rice husk ash
RPC	Reactive powder concrete
RSM	Response surface methodology
S	Sorptivity $[mg/(mm^2\sqrt{min})]$
SAP	Super-absorbent polymers
SCHPC	Self-compacting high performance concrete
SCM	Supplementary cementitious materials

SEM	Scanning electron microscopy
SF	Silica fume
SiO_2	Silicon dioxide
Sp	Superplasticizer
Sp/p	Superplasticizer to powder weight ratio [%]
Std. Dev.	Standard Desviation
TBA	Treated Bagasse Ash
TiO_2	Titanium dioxide
UHPC	Cementitious matrix of an UHPFRC
UHPFRC	Ultra-high performance fibre reinforced cementitious composites
UHPFRC-1.5%	UHPFRC, including cement, limestone filler and silica fume as binder and 1.5% steel fibres (in volume)
UHPFRC-3.0%	UHPFRC, including cement, limestone filler and silica fume as binder and 3.0% steel fibres (in volume)
UTT	Uniaxial tensile test
VECat/Vsand	ECat to sand volume ratio [$m^3\,m^{-3}$]
Vf	Volume of fibres (%)
Vw/Vp	Water to powder volume ratio [$m^3\,m^{-3}$]

Small roman letters

d_{10}	Point in the size distribution, up to and including which, 10% of the total volume of material in the sample is contained [µm]
d_{50}	Point in the size distribution, up to and including which, 50% of the total volume of material in the sample is contained [µm]

d_{90}	Point in the size distribution, up to and including which, 90% of the total volume of material in the sample is contained [µm]
df	Diameter of fibres [mm]
f_{cf}	Flexure strenght [MPa]
f_{cr}	First-cracking stress [MPa]
lf	Length of fibres [mm]
lf/df	Aspect ratio of fibres
mtck/c	Metakaolin to cement weight ratio
sf/c	Silica fume to cement weight ratio
t	Time [days] or [hours]
tf	Final setting time [h]
w/b	Water to binder weight ratio
w/c	Water to cement weight ratio

Greek letters

ρ	Electrical resistivity [Ω m]
χ	Fibre factor

1 Introduction

1.1 Scope of the research

Nowadays, a highly developed infrastructures network is vital for prosperous economic growth. As a consequence industrialised countries have invested substantially in infrastructure, most of which made of reinforced or prestressed concrete [1]. However, many of these structures have suffered severe degradation since their construction due to combined effects of aggressive environments and significantly increased live loads [1]. The decline of highway pavements, airport runways, bridge decks, marine structures and other concrete structures poses severe concerns and requires billions of euros for renovation [2]. Accordingly, more than 50% of Europe's annual construction budget is spent on rehabilitating and refurbishing of existing deteriorated concrete structures [3]. Indeed, the cost of maintenance of bridges in Europe exceeds 1 billion euros per year [2]. Today, repair, retrofitting and rehabilitation of existing reinforced concrete structures (RCS) have become a large part of the construction activity in Europe, as well as, in many other developed countries worldwide. As a consequence, novel concepts for the rehabilitation of RCS are needed, as implementing and developing of new and cost-effective repair methods to extend their service life [1].

Over the last decades, considerable efforts to improve the behaviour of cementitious materials by incorporating fibres have led to the emergence of Ultra-High Performance Fibre Reinforced Cement-based Composites (UHPFRC). The difference between the cementitious fraction of UHPFRC (so-called UHPC) from ordinary concrete (OC) compositions lies mainly in the amount of cement and supplementary cementitious materials (SCM). The dosage of superplasticizer, the size of the aggregate and the lower water content ($w/b < 0.20$) also differ. Typical mix proportions of OC, self-compacting concrete (SCC) and UHPC are presented in Figure 1.1. Regarding the fibres, usually short high-strength steel fibres are employed, which allow incorporating a significant volume (fibre contents ranging, usually, from 2 to 4% in volume). This novel building material provides an unique combination of two essential properties for the structural engineer: extremely low permeability, which prevents the ingress of

detrimental substances and very high strength, namely, compressive strength higher than 150 MPa, tensile strength over 7 MPa with possible tensile strain-hardening (peak strains ranging from 3-10‰) and softening behaviour.

Considering these foremost properties, UHPFRC can be particularly interesting for rehabilitation or strengthening projects [4–11]. It can be applied as a protective watertight layer on areas exposed to severe environmental conditions (de-icing salts, marine environment, chemical attack) or as a strengthening layer, reinforced or not, on high mechanical loaded areas (concentrated forces, wear, fatigue, impact), as schematically shown in Figure 1.2. This novel material leads to increases in structural capacity (stiffness, ultimate strength) and expected durability is significantly improved, while keeping compact cross-sectional dimensions. This concept can be applicable both to rehabilitate and strengthen existing concrete structures and also for new building [1], [5], [6], [12], [13]. Additionally advantages are reduced overall construction time and risk, reduced work-force and smaller machinery required. Less environmental impact on the construction site due to shorter-duration temporary work, is also expected [8], [11], [14], [15]. Besides, UHPFRC elements require less maintenance due to improved durability, thus reducing life-cycle cost while yielding much longer service life [16–18]. Likewise, neighbouring communities would not be disturbed by the routines of maintenance or/and replacement of the facility, leading to a positive social effect [19]. Indeed, over the last years, under the impulse of MCS-EPFL [20], among others esearch groups [21], the application of thin UHPFRC layers, cast in place on existing structures (bridges and buildings), has demonstrated many advantages in terms of durability, sustainability, cost-efficiency and reduction of intervention time, highly appreciated by the commuters.

The high cost of UHPFRC is naturally a limitation on the practical application in real construction projects. Currently, UHPFRC blended mixtures commercially available in Europe are patented products with limited price competitiveness, as well as, limited suppliers and lack of information about the raw materials. Employing locally available materials and novel testing procedures to better understand its behaviour is of critical importance to make UHPFRC a more practical, cost-effective, eco-efficient and widely accepted material.

On the other hand, there are still some issues to address. Typically, UHPFRC presents significant autogenous shrinkage deformations. Although autogenous shrinkage takes place in any concrete, in OC this deformation is negligible since the menisci are developed in large capillaries generating weak tensile stresses. Instead, in the case of UHPFRC, these menisci are formed in very fine capillaries, so that the tensile stresses generated in the new rehabilitation layer of UHPFRC are significantly

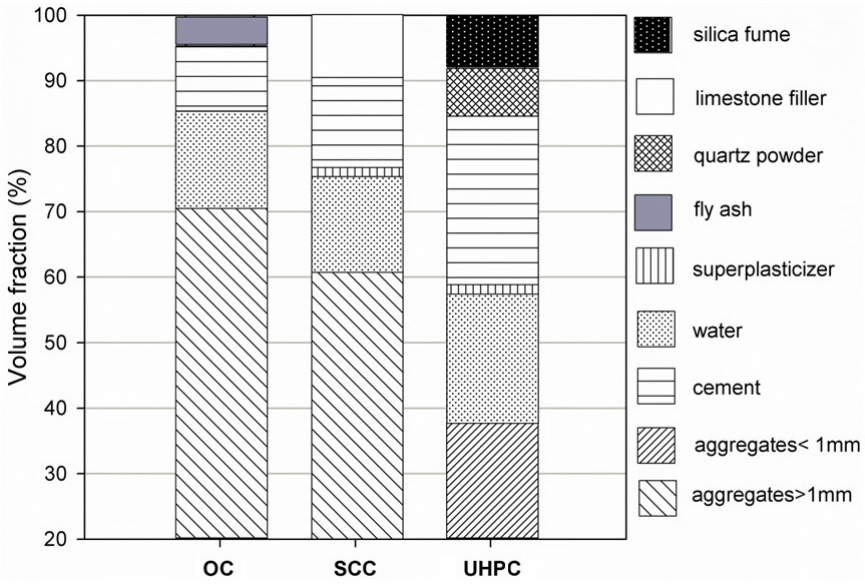

FIGURE 1.1: OC, SCC and UHPC typical mixtures.

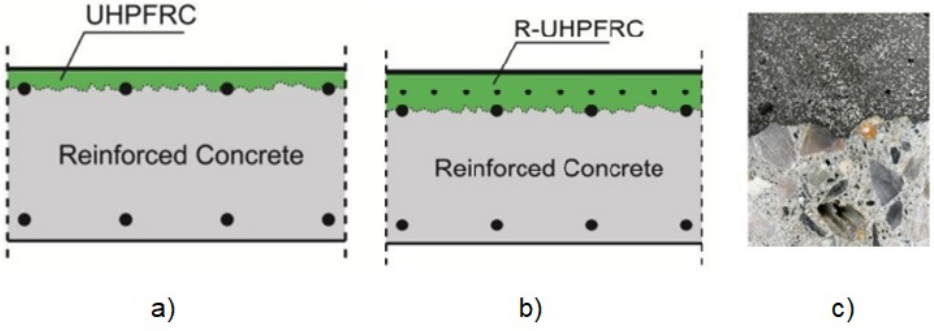

FIGURE 1.2: Basic configuration of composite structural elements combining UHPFRC and conventional RC: a) UHPFRC layer (thickness 25-40 mm) has a protective function only; b) R-UHPFRC layer (thickness 40-80 mm or more) has both structural resistance and protective functions; c) UHPFRC - concrete core showing the perfect bond between the two materials [22].

superior [13], [23], [24]. Various studies on autogenous shrinkage found in literature appoint its considerable magnitude as a consequence of the particular UHPFRC mixture composition (see Figure 1.1). A significant part of this shrinkage occurs at a very early age, namely, up to 1 days of age [13], [25], [26]. Indeed, according to the results of full-scale restrained shrinkage tests for thin UHPFRC slabs [27], shrinkage cracks occurred at a very early age (approximately 20h) from casting). Nevertheless, the magnitude of the internal stresses is influenced not only by the shrinkage rate and magnitude but also by the development of material properties during the first ages, namely, tensile creep and the evolution of the young modulus and strength. Indeed, the tensile performance is essential for coping with the typical high autogenous deformations of UHPFRC and for ensuring water-tightness even when subjected to critical tensile strains. Tensile performance mostly depends on the fibre-to-matrix bond mechanics and the fibre distribution/orientation. If the former can be tailored during mix design, the latter is influenced by the rheology, casting methods, geometry and dimensions of the structural element. Therefore, the "in-structure" tensile response can differ from that characterised in laboratory tests and cracking might occur in the UHPFRC layer. In some applications, micro-cracked UHPFRC could be subjected to aggressive environments. The unforeseen cracks would allow the ingress of aggressive agents leading to a more rapid deterioration of UHPFRC than it would be expected considering the durability based on the uncracked material [28–34]. Thus, further research on the durability of cracked UHPFRC is essential, particularly for particularly site structural applications [35].

1.2 Research objectives

The research effort focused on demonstrating the improved durability of UHPFRC for rehabilitation/strengthening of existing infrastructures. Considering the concept of hybrid structures where thin layers of UHPFRC apply in the critical locations of the existing structures controlling the cracking risk of UHPFRC at early ages is essential for ensuring enhanced long-term performance and longer service life. Thus a research programme was conducted to:

- Developing a new UHPC mixture for rehabilitation/strengthening applications employing local available raw materials and simple manufacturing and curing methods.
- Contributing to a step forward towards optimisation of this type of materials in terms of cost and sustainability.

- Monitoring relevant properties of the optimal mixture in the hardening phase.
- Studying the behaviour of the mixture under various corrosive environments.
- Studying the influence of loading (cracking in service conditions) in key durability parameters.
- Making UHPFRC a more practical, cost-effective, eco-efficient and widely accepted material.
- Promoting further use of UHPFRC.

1.3 Research strategy

The steps described below were followed as a research strategy:

1. Literature review and definition of performance requirements for new UHPFRC
    - Literature review focusing on the synergy of cement and supplementary materials (like limestone filler, silica fume, spent equilibrium catalyst from oil refinery or others) on UHPC properties in the fresh, hardening and hardened states.
    - Definition of performance criteria in fresh, hardening and hardened state, considering the rehabilitation/strengthening application with casting on site.
    - Systematisation of current approaches for experimental characterisation of early age behaviour of the material, namely, hydration kinetics, amount and rate of shrinkage and elasticity modulus development.
    - Literature review concerning the best test methods to characterise the resistance to ingress of aggressive agents of sound specimens, cracked and/or loaded specimens.
2. Formulation, characterisation and optimisation of mixtures in the fresh and hardened states
    - Selection and characterisation of constituent raw materials
    - Planning of experiments and mixtures optimisation
        - Selection of the design approach for achieving the required performance of new UHPC. Based on prior work (preliminary studies carried out during the first year of PhD programme [36], [37]) knowledge

on both the materials to be used and UHPFRC mix-proportions, the region to be investigated would be relatively close to the optimum.

  - Establishing of mix proportions based on the key factors (design variables or mixture parameters) affecting the performance requirements of UHPC.
  - Selection of response variables, i.e., tests to perform on fresh, hardening and hardened phases.
  - Performing experiments and adjusting regression models for the selected output variables.
  - Optimisation of new UHPC considering the performance criteria previously defined.

- Influence addition of fibres in the fresh state
  - Studying the effect of the composition of UHPFRC on workability (self-compacting characteristics), namely, the fibres dosage.
- Evaluation of mechanical behaviour
  - Characterisation of mechanical behaviour of new UHPFRC, with particular emphasis on the behaviour in tension.
- Durability testing (sound specimens)
  - Performing common accelerated laboratory testing including porosimetry, water capillary absorption, resistance to chloride ingress, resistance to carbonation, alkali-silica reaction susceptibility and resistance to external sulphates, to confirm the improved transport properties of this new composite material.
  - Comparison of the durability indicators obtained with same indicators reported in the literature for other property and non-property UHPCs.

3. Characterisation of mixtures in the hardening phase
   - Autogenous shrinkage
     - Measurement of autogenous shrinkage in sealed UHPC/UHPFRC specimens under (nearly) isothermal conditions following standard procedure in ASTM C1698.
4. Characterisation of UHPFRC durability under service conditions
   - Influence of micro-cracking on capillary water absorption of UHPFRC

  - Investigation on the influence of cracking on water transport by capillary suction in UHPFRC with different fibre dosages and different crack patterns.

- Chlorides ingress testing on sound, cracked and loaded and cracked UHPFRC specimens
  - Providing additional insight on long term durability of new UHPFRC by exposing specimens to a coupled degradation mechanism: cracking and chloride ingress.
  - Studying the self-healing effect on damaged (micro-cracked) specimens.

5. Writing the thesis and scientific papers.

1.4 Outline of the thesis

The structure of the current thesis is schematically shown in Figure 1.3 and it includes 7 Chapters, as described below:

Chapter 2 presents the preliminary studies carried out during the first year of the PhD, including numerical studies using DOE approach to design and optimise cement based composites for a specific application. These preliminary studies allowed establishing the methodology to be followed throughout the PhD work.

Chapter 3 describes experimental and numerical studies for the design and optimisation of new UHPC mixture (without fibres). To achieve this goal a DOE approach was utilised to determine the optimum combination of powder materials (cement, silica fume and limestone filler), aggregates (fine sand and ECat) and superplasticizer in UHPC production. UHPC mixtures were assessed regarding their deformability, setting time, autogenous shrinkage, resistivity and compressive strength. Regression models were derived and validated, which allow predicting selected properties of UHPC, along with the identification of the most significant effects of mixture parameters on each property of UHPC. After optimising the matrix, short steel fibres (3.0% by volume) were incorporated in UHPC and the performance of the resulting UHPFRC was further investigated by analysing its flowability, autogenous shrinkage evolution, mechanical performance, cost and environmental efficiency.

Chapter 4 focuses on the durability performance of new UHPC. As such, a series of durability tests, namely, porosity, electrical resistivity, water absorption by capillarity, penetration of chlorides and expansive reaction susceptibility, were performed. Results obtained were compared with results reported in literature for both other non-proprietary and commercially available UHPC materials.

Chapter 5 investigates the influence of cracking on water transport by capillary suction of new UHPFRC with different fibres dosages incorporation. After different damage levels were introduced on prismatic specimens, by means of four-point bending test, the crack pattern observed on the tensile face of the specimen was characterised; and then the sorptivity tests were carried out to develop an understanding of how micro- and macro-cracking formation in UHPFRC degrade its resistance to water penetration.

Chapter 6 addresses whether the new UHPFRC retains its long term durability after partial damage, by evaluating the chlorides ingress in both non-cracked, cracked-unloaded and cracked-loaded UHPFRC specimens, with a typical fibre content of 3.0%. After different damage levels were introduced on prismatic specimens, by means of four-point bending test, the crack pattern observed on the tensile face of the unloaded specimens was characterised. Then the specimens were subjected to wetting–drying cycles, using a concentrated chloride solution (3.5% NaCl), during 1 year. With this, it was possible to understand of how coupling micro- and macro-cracks and the chloride ions penetration affects the durability and the flexural performance of new UHPFRC.

Chapter 7 presents the global conclusions and recommendations for future research related to the developed UHPFRC.

As previously stated in section 1.3, a literature review was carried out and it is distributed throughout the chapters in each Introduction section (see Figure 1.3).

1.5 List of Publications

The following original research papers prepared by the author of the thesis corresponds to each chapter of this thesis, as follows:

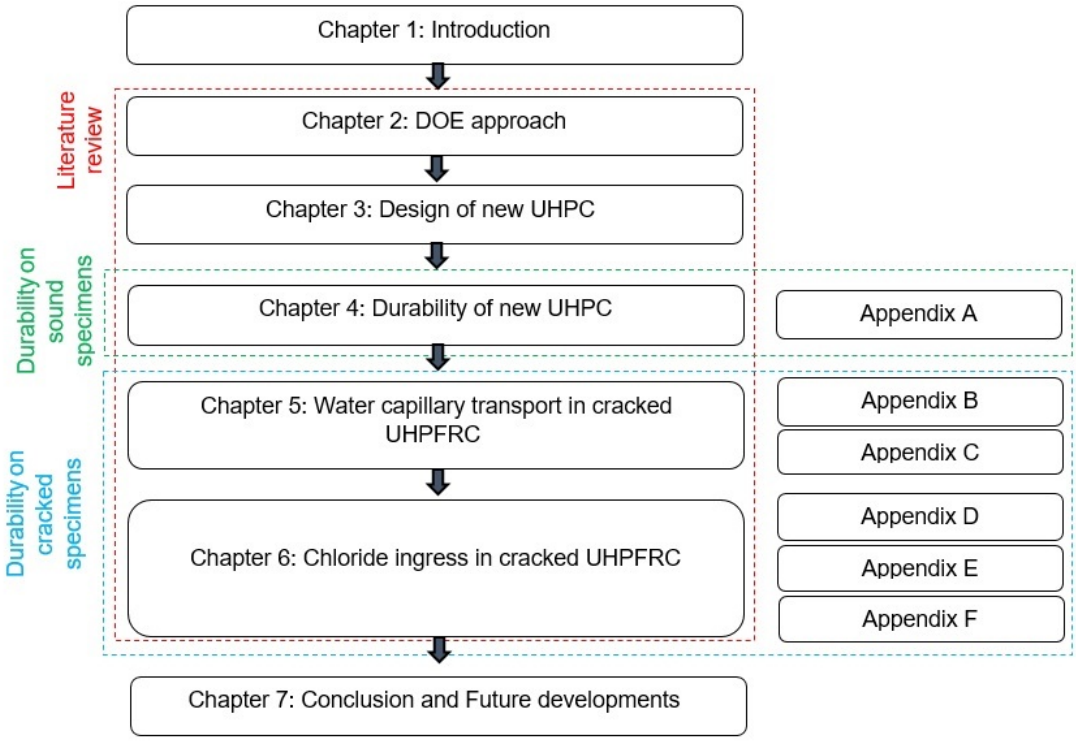

FIGURE 1.3: Outline of the thesis.

- Chapter 2: Matos, A.M., Maia, L., Nunes, S., Milheiro-Oliveira, P., "Design of self-compacting high-performance concrete: Study of mortar phase", Construction and Building Materials, Volume 167, 10 April 2018, Pages 617-630.
- Chapter 3: Matos, A.M., Nunes, S., Costa, C., Barroso-Aguiar, J.L., "Spent equilibrium catalyst as internal curing agent in UHPFRC", Cement and Concrete Composites, Volume 104, November 2019, Article number 103362.
- Chapter 4: Matos, A.M., Nunes, S., Costa, C., Barroso-Aguiar, J.L., "Durability of an UHPC containing spent equilibrium catalyst". **(submitted)**
- Chapter 5: Matos, A.M., Nunes, S., Barroso Aguiar, J.L., "Capillary transport of water in cracked and non-cracked UHPFRC specimens", Journal of Advanced Concrete Technology, Volume 17, Issue 5, May 2019, Pages 244-259.

  (This paper has been selected one of the three excellent papers of the year. The selection was a result of votes by the members of ACT advisory board and the Editorial Board. This selection result leads to a recommendation to the JCI Award 2019 by the Editor-in-Chief of ACT.)
- Chapter 6: Matos, A.M., Chaves-Figueiredo, S., Nunes, S., Barroso Aguiar, J.L., Schlangen, E., "Chloride ingress in cracked UHPFRC". **(submitted)**

Additionally, other papers in international and national conferences were published within the scope of this thesis:

- Ana Mafalda Matos, Stefan Chaves Figueiredo, Sandra Nunes, José L. Barroso-Aguiar, Erik Schlangen, "Chloride ion penetration into cracked UHPFRC during wetting–drying cycles", 3rd RILEM Spring Convention 2020 (RSCC2020), 10-14 March 2020, Guimarães, Portugal.
- Ana Mafalda Matos, Sandra Nunes, Carla Costa, José L. Barroso-Aguiar, "Characterization of non-proprietary UHPC for use in rehabilitation/strengthening applications", RheoCon2 RILEM Conference and SCC9 RILEM Symposium, 8-11 September 2019, Dresden, Germany. Part of the RILEM Bookseries book series (RILEM, Volume 23), Springer International Publishing, 2020.
- Ana Mafalda Matos, Sandra Nunes, José L. Barroso-Aguiar, "Non-proprietary UHPFRC for use in rehabilitation/strengthening applications", 3rd Doctoral Congress Engineering (DCE19), 27-28 June 2019, Porto, Portugal.
- Ana Mafalda Matos, Sandra Nunes, Carla Costa, J. Barroso-Aguiar, "Durabilidade de um material cimentício de ultraelevado desempenho reforçado com fibras metálicas", Betão Estrutural 2018, 7-9 November 2018, LNEC, Lisbon, Portugal [In Portuguese].
- Ana Mafalda Matos, Sandra Nunes, José L. Barroso Aguiar, "Influence of microcracking on capillary water absorption of an UHPFRC", SynerCrete'18 International Conference on Interdisciplinary Approaches for Cement-based Materials and Structural Concrete, 24-26 October 2018, Funchal, Madeira Island, Portugal.

  (This contribution was selected as outstanding. The authors were invited to submit a paper based on this contribution in a special issue of the Journal of Advanced Concrete Technology, published by the Japan Concrete Institute.)
- Ana Mafalda Matos, Stefan Chaves Figueiredo, Sandra Nunes, Erik Schlangen, "Durability of fibre reinforced cementitious composites: coupling mechanical and chloride environment loads", RILEM Week 2018, 26-29 August 2018, Delft, The Netherlands.
- Ana Mafalda Matos, José Granja, Sandra Nunes, José L. B. Aguiar, Miguel Azenha, "NDT of stiffness evolution of UHPFRC since casting", 2nd International RILEM/COST Conference on Early Age Cracking and Serviceability in Cement-based Materials and Structures (EAC2), 12-14 September 2017, ULB-VUB, Brussels, Belgium.

- Ana Mafalda Matos, Sandra Nunes, Carla Costa, J. Barroso-Aguiar, "Retração autogénea em betão de ultra-elevado desempenho reforçado com fibras", Betão Estrutural 2016, 2-4 November 2016, FCTUC, Coimbra, Portugal [In Portuguese].
- Ana Mafalda Matos, Sandra Nunes, Carla Costa, "Mitigation of early age shrinkage of UHPFRC by using spent equilibrium catalyst", International RILEM Conference on Materials, Systems and Structures in Civil Engineering Conference segment on Service Life of Cement-Based Materials and Structures, Volume 1, pages 395-403, 22-24 August 2016, Technical University of Denmark, Lyngby, Denmark.

References

[1] Bassam A Tayeh, B H Abu Bakar, M A Megat Johari, and Yen Lei Voo. Utilization of Ultra-High Performance Fibre Concrete (UHPFC) for Rehabilitation - a Review. In *The 2nd International Conference on Rehabilitation and Maintenance in Civil Engineering Utilization*, volume 54, pages 525–538. Elsevier B.V., 2013.

[2] Europe could save billions on concrete repairs - News - University of Bradford.

[3] Graham Tilly and Gifford. Performances of concrete repairs in practice.

[4] Eugen Brühwiler and Emmanuel Denarié. Rehabilitation of Concrete Structures Using Ultra- High Performance Fibre Reinforced Concrete. In *Second International Symposium on Ultra High Performance Concrete*, number 1, pages 895–902, Kassel, Germany, 2008.

[5] Eugen Bruhwiler and Emmanuel Denarie. Rehabilitation and Strengthening of Concrete Structures Using Ultra-High Performance Fibre Reinforced Concrete. *Structural Engineering International*, 23(4):450–457, 11 2013.

[6] Eugen Brühwiler and Emmanuel Denarié. Rehabilitation of concrete structures using Ultra-High Performance Fibre Reinforced Concrete. In *UHPC-2008: The Second International Symposium on Ultra High Performance Concrete*, number 1, pages 1–8, Kassel, Germany, 2008.

[7] Eugen Brühwiler and Emmanuel Denarié. Structural Rehabilitations with Ultra-High Performance Fibre Reinforced Concretes (UHPFRC) / Strukturelle Instandsetzung von Betonbrücken mit Ultra-hochleistungsfähigem Faserfeinkornbeton (UHFB). *Restoration of Buildings and Monuments*, 12(5-6):93–108, 1 2006.

[8] Sina Nabaei and Sébastien Nendaz. Rehabilitation of transportation infrastructures: the potential of new materials. In *IABSE Conference – Structural Engineering: Providing Solutions to Global Challenges*, Geneva, Switzerland, 2015.

[9] R. P. H. Vergoossen. Tailor made bridge design with Ultra-High-Performance Concretes, 2008.

[10] M. Bastien-Masse and E. Brühwiler. Ultra high performance fiber reinforced concrete for strengthening and protecting bridge deck slabs. In *7th International Conference on Bridge Maintenance, Safety and Management (IABMAS)'*, pages 2176–2182. Bridge Maintenance, Safety, Management And Life Extension, 2014.

[11] Kevin Zmetra, Arash E. Zaghi, and Kay Wille. Rehabilitation of Steel Bridge Girders with Corroded Ends Using Ultra-High Performance Concrete. In *Structures Congress 2015*, pages 1411–1422, Reston, VA, 4 2015. American Society of Civil Engineers.

[12] E Brühwiler. Rehabilitation and strengthening of concrete structures using Ultra-High Performance Fibre Reinforced Concrete. In Alexander et al., editor, *Concrete Repair, Rehabilitation and Retrofi tting III*, pages 72–79. Taylor & Francis Group, 2012.

[13] Katrin Habel. *Structural behaviour of elements combining Ultra-High Performance Fibre Reinforced Concretes (UHPFRC) and Reinforced Concrete*. PhD thesis, École Polytechnique Fédérale de Lausanne, 2004.

[14] Eugen Brühwiler and Emmanuel Denarié. Rehabilitation and Strengthening of Concrete Structures Using Ultra-High Performance Fibre Reinforced Concrete. *Structural Engineering International*, 4:450–457, 2013.

[15] G. Habert, E. Denarié, A. Šajna, and P. Rossi. Lowering the global warming impact of bridge rehabilitations by using Ultra High Performance Fibre Reinforced Concretes. *Cement and Concrete Composites*, 38:1–11, 4 2013.

[16] Peter Racky. Cost-effectiveness and sustainability of UHPC. In *International Symposium on Ultra High Performance Concrete*, page 797–805, Kassel, Germany, 2004.

[17] N. Randl, T. Steiner, S. Ofner, E. Baumgartner, and T. Mészöly. Development of UHPC mixtures from an ecological point of view. *Construction and Building Materials*, 67:373–378, 2014.

[18] AFGC. Documents scientifiques et techniques Bétons fibrés à ultra-hautes performances - recommandations, 2013.

[19] S. Abbas, M. L. Nehdi, and M. A. Saleem. Ultra-High Performance Concrete: Mechanical Performance, Durability, Sustainability and Implementation Challenges. *International Journal of Concrete Structures and Materials*, 10(3):271–295, 9 2016.

[20] Emmanuel Denarié. UHPFRC for the cast-in place reinforcement of offshore maritime signalization structures. In *HAC2018 | V Congreso Iberoamericano de Hormigón Autocompactante y Hormigones Especiales*, Valencia, 2018. Universitat Politècnica de València.

[21] N.M. Azmee and N. Shafiq. Ultra-high performance concrete: From fundamental to applications. *Case Studies in Construction Materials*, 9:e00197, 12 2018.

[22] Kerstin Wassmann, Eugen Brühwiler, and Peter Lunk. Strengthening of RC Slabs using UHPFRC – Concepts and Applications. In *4th International Symposium on Ultra-High Performance Concrete and High Performance Materials*, Kassel, Germany, 2016.

[23] K. Habel, J.-P. Charron, E. Denarié, and E. Brühwiler. Autogenous deformations and viscoelasticity of UHPFRC in structures. Part I: experimental results. *Magazine of Concrete Research*, 58(3):135–145, 4 2006.

[24] Agnieszka Switek-Rey, Emmanuel Denarié, and Eugen Brühwiler. Early age creep and relaxation of UHPFRC under low to high tensile stresses. *Cement and Concrete Research*, 83:57–69, 2016.

[25] Ingo Schachinger, Karl Schmidt, Detlef Heinz, and Peter Schießl. Early-Age Cracking Risk and Relaxation by Restrained Autogenous Deformation of Ultra High Performance Concrete. In *6th Internacional Symposio of high strength/high performance concrete*, pages 1341–1354, Leipzig, 2002.

[26] Mohammadhadi Kazemi Kamyab. *Autogenous Shrinkage and Hydration Kinetics of SH-UHPFRC under Moderate to Low Temperature Curing Conditions*. PhD thesis, Ecole Polytechnique Fédérale de Lausanne, Switzerland, 2013.

[27] Doo-Yeol Yoo, Kyung-Hwan Min, Joo-Ha Lee, and Young-Soo Yoon. Shrinkage and cracking of restrained ultra-high-performance fiber-reinforced concrete slabs at early age. *Construction and Building Materials*, 73:357–365, 12 2014.

[28] Shamsad Ahmad, Ibrahim Hakeem, and Mohammed Maslehuddin. Development of UHPC mixtures utilizing natural and industrial waste materials as partial replacements of silica fume and sand. *The Scientific World Journal*, 2014.

[29] Mo Alkaysi, Sherif El-Tawil, Zhichao Liu, and Will Hansen. Effects of silica powder and cement type on durability of ultra high performance concrete (UHPC). *Cement and Concrete Composites*, 66:47–56, 2 2016.

[30] Ahmed Tafraoui, Gilles Escadeillas, and Thierry Vidal. Durability of the Ultra High Performances Concrete containing metakaolin. *Construction and Building Materials*, 112:980–987, 2016.

[31] Nguyen Van Tuan, Guang Ye, Klaas van Breugel, Alex L. A. Fraaij, and Danh Dai Bui. The study of using rice husk ash to produce ultra high performance concrete. *Construction and Building Materials*, 25(4):2030–2035, 2011.

[32] Mo Alkaysi and Sherif El-Tawil. Effects of variations in the mix constituents of ultra high performance concrete (UHPC) on cost and performance. *Materials and Structures*, 49(10):4185–4200, 10 2016.

[33] Benjamin Graybeal and Jussara Tanesi. Durability of an Ultrahigh-Performance Concrete. *Journal of Materials in Civil Engineering - ASCE*, 19(10):848–854, 2007.

[34] Safeer Abbas, Ahmed M. Soliman, and Moncef L. Nehdi. Exploring mechanical and durability properties of ultra-high performance concrete incorporating various steel fiber lengths and dosages. *Construction and Building Materials*, 75:429–441, 2015.

[35] Agnieszka Switek-Rey, Emmanuel Denarié, and Eugen Brühwiler. Early age creep and relaxation of UHPFRC under low to high tensile stresses. *Cement and Concrete Research*, 83:57–69, 5 2016.

[36] Ana Mafalda Matos, Sandra Nunes, and Carla Costa. Mitigation of early age shrinkage of UHPFRC by using spent equilibrium catalyst. In *International RILEM Conference Materials, Systems and Structures in Civil Engineering 2016 Segment on Service Life of Cement-Based Materials and Structures*, Lyngby, Denmark, 2016.

[37] Ana Mafalda, Sandra Nunes, Carla Costa, and J. L. Barroso Aguiar. Retração autogénea em betão de ultra-elevado desempenho. In *Encontro Nacional BETÃO ESTRUTURAL - BE2016*, Coimbra, Portugal, 2016.

2 DOE approach to mixture design

Chapter 2 presents a preliminary study carried out during the first year of the PhD within the scope of "Statistical Methods" Course Unit of PRODEC. It shows the methodology used for the design of mortar mixtures which are adequate for SCC and with required performance in terms of early age properties. This methodology was developed in two phases: first, the statistical analysis and model fitting of data collected, second, the numerical optimisation of mixture parameters using the models derived in the previous stage. Contour plots and interaction diagrams representing the range of mixture parameters where SCC could be found are presented. Based on these results, SCC mortars were optimised in terms of specified early age properties. This part of the work was a preliminary step concerning the use DOE for mix design.

This Chapter corresponds to the published journal paper: Matos, A.M., Maia, L., Nunes, S., Milheiro-Oliveira, P., Design of self-compacting high-performance concrete: Study of mortar phase, Construction and Building Materials, Volume 167, 10 April 2018, Pages 617-630

2.1 Introduction

The concepts of self-compacting concrete (SCC) [1] and high-performance concrete (HPC) [2] can be combined to design a concrete able to simultaneously meet the performance requirements of self-compactability [3], high compressive strength and good durability. To realise these goals, the so-called self-compacting high-performance concrete (SCHPC) generally requires higher content of cementitious materials, lower water to binder mass ratio (w/b) and smaller maximum size of aggregates [4]. Supplementary cimentitious materials as ground granulated blast furnace slag (GGBS) [5], fly ash (FA) [6] and limestone filler (LF) [7] are often used in SCC to reduce cement content, improve workability and enhance mechanical and/or durability properties; therefore allowing to develop more eco-efficient and eco-friendly mixtures [8]. The performance of SCHPC is highly improved by incorporating very reactive materials such as silica fume (SF) [9], rice husk ash (RHA) [10] and metakaolin (MTCK) [11], [5]. Le et al. showed the advantages of using several additions in ternary binders,

combining cement with LF or FA and more reactive additions (RHA or SF), to produce SCHPC [4]. Compressive strengths of SCHPC in the range of 90-120 MPa were achieved at 28 days, while still exhibiting good self-compactability [4]. Gesoglu et al. [12] also found improved durability properties in SCC mixtures incorporating ternary mixtures of cement+GGBS+SF as compared to binary or quaternary mixtures of binders (cement; GGBS; FA; SF) [12]. Due to a constant demand for silica fume in the construction industry and limited availability, this industrial by-product becomes rather expensive. Rice husk ash can replace silica fume [10], but its availability is limited in some countries, like in Portugal. Metakaolin is an alternative very reactive addition [13] with a growing implementation in the concrete industry, which is more economical than silica fume, requires lower manufacturing temperatures compared to cement and its colour might be an advantage for architectural coloured concretes.

A comprehensive review of metakaolin effects on concrete properties can be found in [14]. A short summary of findings in studies on SCC incorporating metakaolin follows here: SCC with MTCK can be produced at different w/b, with adequate deformability, proper stability and passing ability [15]. Nevertheless, the replacement of cement by MTCK decreases the slump flow retention of the SCC mixtures [15]. The inclusion of MTCK increases the heat evolved during hydration, which is a function of the material fineness [16], thus increasing the cracking risk at early ages due to thermal stresses [17]. The dormant period is reduced according to the activity of the metakaolin [17]. It has been reported that the use of MTCK in SCC can have a positive effect on both short [15] and long term strength of concrete [18]. Compressive strength of SCC mixtures can surpass 100 MPa at 28 days and 120 MPa at 90 days [18]. The chlorides ion permeability decreases considerably with increased content of MTCK [19], [16]. Metakaolin refines the pore structure of the cement matrix and significantly improves the resistance to the transportation of water and the diffusion of chloride ions [20]. SCC incorporating MTCK generally exhibits lower gas permeability compared to the reference concrete mixtures [21]. Besides, the addition of MTCK was found effective in reducing concrete expansion by sulphate attack [20] and to reduce the harmful expansion due to alkali-silica reaction in concrete [22]. Both autogenous shrinkage [23] and drying shrinkage [24] were reduced by incorporating MTCK in SCC.

Much of the research work to date on SCC/SCHPC has focused on grey Portland cement, but white cement formulations might be necessary due to colour requirements for architectural applications [25], [26]. Each type of cement has unique characteristics (physical and chemical) and interacts with other constituents, especially

additions and admixtures, which reflect changes in performance properties for both fresh and hardened states [27], [28]. In terms of chemical components, white Portland cement is characterized by lower Fe_2O_3 and alkalis contents and higher free lime content compared to grey cements [29]. Because of the brightness of the white colour, white cement presents a higher fineness than grey Portland cement. This contributes to achieving more rapid setting and higher early compressive strength, meeting the requirements of EN 197-1. These common differences in white Portland cement compared with ordinary cement should not adversely affect the final concrete performance, thus requiring for a proper selection and combination of constituent materials at mix-design stage [30]. Partial replacement of white Portland cement by a pozzolanic material, with white/near-white colour such as metakaolin, can be beneficial considering economic, technical and environmental aspects [31].

Statistical factorial design approach has been used to design SCC/SCHPC mixtures incorporating metakaolin [19], [16], [32], [33]. This approach presents advantages over fully experimental and empirical methods. Instead of selecting one starting mixture and proceeding by trial and error for achieving a potential optimum solution, a set of trial mixtures covering a chosen range of proportions for each mixture constituent materials is defined according to a statistical experimental plan. After testing the trial mixtures and collecting data, experimental results are analysed, and statistical models are fitted to the data for each response variable (selected relevant concrete property considering the performance requirements). When each response is characterised by an equation (fitted model), several analyses are possible, including the simultaneous optimisation to meet several constraints. In this way, the statistical factorial design approach is very effective to simplify the test protocol required to optimise a given SCC mixture by reducing the number of trial batches to achieve a good balance among mixture parameters [34].

A three-level, three-factors plan (factors are water-binder ratio, binder content and metakaolin content), similar to a D-optimal plan, was developed by Dvorkin et al. to obtain the required concrete strength of SCHPC at minimum cost [33]. Concrete cost is lower when polycarboxylate type superplasticizer is used instead naphthalene formaldehyde type [33].

A central composite design (CCD) was used by Abouhussien and Hassan to study the effect of total binder content, percentage of cement replacement by MTCK and w/b on fresh state properties, compressive strength [32], chloride permeability and the expected service life of SCC mixtures [16]. This study yielded an optimum SCC mixture with a total binder of 490 $\mathrm{kg\,m^{-3}}$, a $w/b = 0.39$ and incorporating 19.9% MTCK in replacement of cement. This mixture achieved high flowability, low segregation

factor, good passing ability and high compressive strength at 28 days (82.1 MPa, in water-cured specimens) [32]. Besides, this mixture exhibited the lowest chloride permeability compared to counterpart SCC mixtures containing fly ash, slag, and silica fume [16].

Al-alaily and Hassan argued the prediction models and design charts developed based on a CCD are useful tools to design an optimum SCHPC incorporating MTCK with target chloride permeability and strength [19]. The mixture obtained from the numerical optimisation contained a total binder of 548 $\mathrm{kg\,m^{-3}}$, $w/b = 0.32$ and MTCK replacement of 24.4%, exhibiting a 28 days compressive strength and an apparent chlorides diffusion coefficient of 99 MPa and 0.36×10^{-12} $\mathrm{m^2\,s^{-1}}$, respectively [19].

2.2 Research scope and objectives

A new cruise terminal building was built in Porto to serve the north region of Portugal (see Figure 2.1). At the design stage, the use of an architectural white SCHPC was considered for the external spiral laminar element, which envelops the entire building structure. A self-compacting mixture was needed due to the complex geometry of this laminar element, high density of reinforcement (both prestressing and ordinary reinforcing steel) and good quality of surface finishing requirement (white architectural concrete). Since the building is located in a very aggressive environment and subjected to a high percentage of chlorides, special design considerations had to be taken to extend its service life. Based on findings of several studies reported in the previous section, a ternary mixture of white Portland cement+LF+MTCK was selected to produce a white SCHPC. A white Portland cement was chosen because of the colour requirements. LF is a commonly used supplementary material (type I addition) in SCC [7], and widely available in Portugal. Besides improving workability, LF can contribute to controlling temperature rise and thermal shrinkage cracking of SCC [35]. A very reactive MTCK was included to help to enhance the mechanical and durability properties of concrete. MTCK type was selected based on its colour (white) and a previous comparative study reported in [36].

For the successful design of a white SCHPC for this particular application, it was essential to understand the influence of material properties and mix-design parameters on workability, visco-elastic, mechanical and durability properties. For example, SCHPC may potentially be more susceptible to cracking during the first days after casting (when the concrete residual stress exceeds the concrete tensile strength), which can compromise durability. On the one hand, the incorporation of metakaolin

increases the heat evolved during hydration, which may lead to thermal stress cracking. Besides, due to the larger amount of paste and lower coarse aggregate content, SCC is more prone to a more significant creep and shrinkage than conventional concrete with normal consistency [35]. The use of different types of cement (as is the case of white cement) [36], additions [37] and low w/b can also modify the evolution of shrinkage deformations [35].

The aim of the present study, which is part of a wider research project on white SCHPC, is to investigate the effect of various constituents in mortar and to select the best combination of powder materials, w/b and superplasticizer dosage, in order to minimise shrinkage deformations and temperature rise due to heat of hydration, without compromising the self-compactability.

FIGURE 2.1: South Cruise Terminal of the Port of Leixões, in Porto, Portugal [38].

2.3 Research significance

From the foregoing literature survey, only a few studies were undertaken that use statistical factorial design approach to study SCHPC incorporating metakaolin [19], [16], [33]. Some durability related properties like the chloride permeability and chloride diffusion [19], [16] were modelled, but modelling of properties related to cracking risk of SCHPC incorporating metakaolin is missing from the literature. It should be noted that cracking during the first days after casting can compromise durability because it would enlarge permeability. In this paper a statistical factorial design approach was used to conduct a proper experimental investigation to develop mathematical data driven models and to optimise the paste phase of a white SCHPC. The developed models account for the effect of water to powder volume ratio, water to

cement weight ratio, superplasticizer to powder weight ratio, sand to mortar volume and metakaolin to cement weight ratio on the fresh state properties (deformability and viscosity), temperature rise due to heat of hydration, setting time, shrinkage and compressive strength. Although simple technological tests were used, this paper provides insight regarding material factors influence on several SCHPC-mortar properties. It proposes models which allow to reduce the risk of cracking during the first days of SCHPC made from white Portland cement and metakaolin, and thus contributing to improve durability of the structure.

2.4 Materials and methods

2.4.1 Raw Materials

The mortars were ternary mixtures of cement CEM II/A-L 52.5N (white), limestone filler and metakaolin. Table 2.1 summarises the relevant chemical and physical properties of these materials. Reference CEN sand conforming to EN 196-1 was employed in this study, which is a siliceous round grain natural sand (0.08-2 mm) with a specific gravity of 2570 $\mathrm{kg\,m^{-3}}$ and an absorption value of 0.68% by mass. A polycarboxylate type superplasticizer was used having a specific gravity of 1070 $\mathrm{kg\,m^{-3}}$ and 26.5% solid content. Tap water was used for all mortar mixes.

2.4.2 Test programme and mix proportioning

An experimental plan was designed in view of finding a statistically significant model explaining the relevant mortar properties as a function of the mortar mixture parameters.

A 2^{5-1} fractional factorial design consisting of 16 treatment combinations augmented by 10 axial runs plus 6 central runs was used, resulting in a central composite design with a total of 32 mortar trial mixtures. Mix proportions were established based on the following five key factors (design variables): water to powder volume ratio (Vw/Vp); water to cement weight ratio (w/c); superplasticizer to powder weight ratio (Sp/p); sand to mortar volume (Vs/Vm) and metakaolin to cement weight ratio (mtck/c). The effect of each key factor was evaluated at five levels $-\alpha$, -1, 0, $+1$, $+\alpha$, as shown in Table 2.2. The value of α was taken equal to $n_F{}^{1/4}$, where n_F is the number of points in the factorial part of the design [39], which makes the design rotatable. In the current study, this corresponds to taking α equal to 2.0. Table 2.3

TABLE 2.1: Chemical and physical properties of cement (CEM II/A-L 52.5 N-white), limestone filler and metakaolin.

	CEM II/A-L 52.5 N (white)	Limestone Filler	Metakaolin
Chemical composition (% by mass)			
SiO_2 (%)	20.36		51.70
Al_2O_3 (%)	5.10		43.20
Fe_2O_3 (%)	3.12		0.46
CaO (%)	62.72		
MgO (%)	1.81		
SO_3 (%)	3.44		
Na_2O (%)			
K_2O (%)			
Cl (%)	0.012		
Free CaO (%)	1.62		
Loss on ignition (%)	2.61		0.75
Insoluble residue (%)	1.33		
$CaCO_3$ (%)		> 98	
Physical properties			
Specific density ($kg\,m^{-3}$)	3160	2390	2200
Size distribution			
d_{10} (µm)	0.69	1.12	2.02
d_{50} (µm)	8.09	4.55	7.12
d_{90} (µm)	30.81	15.36	21.13
Initial set (min)	150		
Final set (min)	205		
Mechanical properties			
Rc,7 days (MPa)	40		
Rc,28 days (MPa)	52		

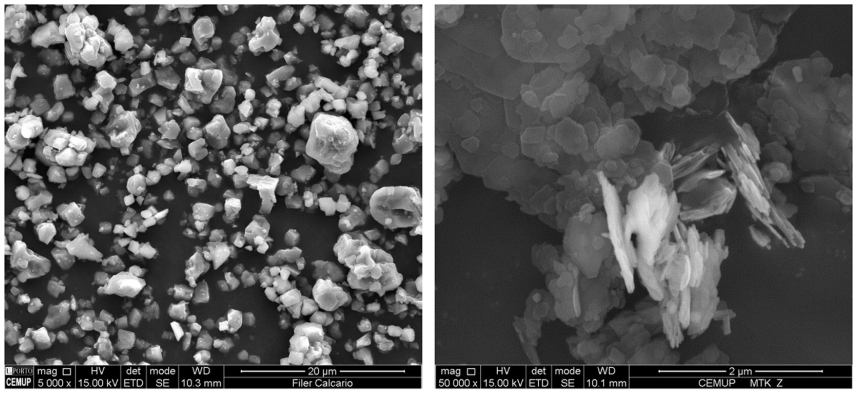

(a) (b)

FIGURE 2.2: Particle morphology of: a) limestone filler (×5000) and b) metakaolin (×50000)

presents the combinations of the levels of the five factors for all 32 trial mixtures. The interval range of the design variables (see Table 2.2) was established based on preliminary tests that confirmed minimum workability and the stability of the least and the most fluid mortar mixtures, respectively. For example, the relatively small Sp/p interval range is explained by the particular interaction between white cements and the polycarboxylate type superplasticizer used, corroborating with [27]. The proportioning of all 32 trial mixtures was carried out in terms of absolute volume using the values of Vw/Vp, w/c, Sp/p, Vs/Vm and mtck/c for each constituent in Table 2.3, with subsequent conversion to proportions by weight using the specific gravities of the mortar ingredients. For more details concerning mixture formulation, see [40].

TABLE 2.2: Correspondence between coded values and actual values of design variables.

Design variables	-2	-1	0	+1	+2
Vw/Vp	0.800	0.850	0.900	0.950	1.000
w/c	0.360	0.385	0.410	0.435	0.460
Sp/p	0.680%	0.690%	0.700%	0.710%	0.720%
Vs/Vm	0.400	0.425	0.450	0.475	0.500
mtck/c	0.030	0.060	0.090	0.120	0.150

TABLE 2.3: Level combinations considered in the experimental plan (coded values of design variables).

	Ci	F1	F2	F3	F4	F5	F6	F7	F8	F9	F10	F11	F12	F13	F14	F15	F16	CC1	CC2	CC3	CC4	CC5	CC6	CC7	CC8	CC9	C10
Vw/Vp	0	-1	+1	-1	+1	-1	+1	-1	+1	-1	+1	-1	+1	-1	+1	-1	+1	-2	+2	0	0	0	0	0	0	0	0
w/c	0	-1	-1	+1	+1	-1	-1	+1	+1	-1	-1	+1	+1	-1	-1	+1	+1	0	0	-2	+2	0	0	0	0	0	0
Sp/p	0	-1	-1	-1	-1	+1	+1	+1	+1	-1	-1	-1	-1	+1	+1	+1	+1	0	0	0	0	-2	+2	0	0	0	0
Vs/Vm	0	-1	-1	-1	-1	-1	-1	-1	-1	+1	+1	+1	+1	+1	+1	+1	+1	0	0	0	0	0	0	-2	+2	0	0
mtck/c	0	+1	-1	-1	+1	-1	+1	+1	-1	-1	+1	+1	-1	+1	-1	-1	+1	0	0	0	0	0	0	0	0	-2	+2

Table 2.4: Mortars mixing sequence.

Task	Duration
add cement + limestone filler + fine aggregate + 0.81 of total water and mix	1.0min+*+1.0min
add rest of water + superplasticizer and mix	1.0min+*+1.0min
resting	1.0min
mix	0.5min

(*) stoppage to scrape material adhering to the mixing bowl; mixing at low speed (140 ± 5 rotations $\cdot$ min^{-1})

2.4.3 Preparation and testing of specimens

Mixtures were tested in a random order to reduce the effects of external variables not explicitly included in the experimental plan. The mixtures were prepared in batches of 2.42 l using a two-speed mixer according to the standard EN 196-1. Table 2.4 presents the mixing procedure followed for mortars preparation. After mixing, mortars fresh state properties were assessed using the mini slump flow and the mini V-funnel tests [1]. Then, three prismatic specimens ($40 \times 40 \times 160$ mm^3), three cylinders (27 mm diameter and 250 mm length) and four cylindrical containers (46 mm diameter and 55 mm high) were moulded for determining compressive strength, shrinkage deformation and temperature evolution generated by heat of hydration, respectively.

The mini slump flow test was used to assess deformability by measuring the final average flow diameter of the spread area [1]. The mini V-funnel test was used to evaluate the viscosity and passing ability of the mortar by recording mortar flow time [1]. Each experiment was carried out two times; thus, the average of the two results was taken as the flow diameter (Dflow) and flow time (Tfunnel).

A semi-adiabatic test was conducted to measure temperature development of all 32 mixtures in the experimental plan, using the experimental set-up shown in Figure 2.3. Approximately 35 min after the beginning of mixing, the cylindrical containers with fresh mortar samples were fitted in the centre of an insulated box (made of extruded polystyrene to reduce heat losses), the box was closed, and the temperature readings started. The temperature of each mortar sample was continuously monitored, during 24 h, through the installation of temperature sensors (PT100), outside the bottom part of each container, connected to an automatic acquisition system. All tests were carried out in a room with controlled environmental conditions ($T = 20 \pm 2$ °C and $HR = 50 \pm 5\%$). Four curves of temperature evolution with time were obtained for

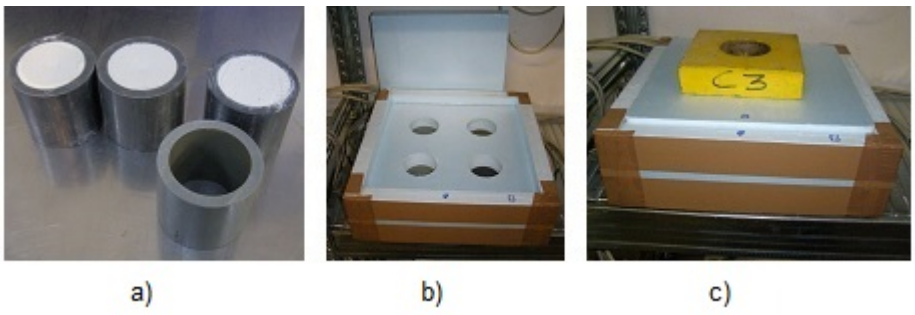

FIGURE 2.3: Experimental set-up to measure temperature evolution of mortar under semi-adiabatic conditions: a) PVC cylindrical containers and mortar samples; b) insulated box with four cavities to insert the containers; c) insulated box in closed position while running the test.

each mortar mixture, and the temperature increase relative to the room temperature was computed for all mixtures (see Figure 2.4-a). Figure 2.4-b exhibits the average of the four curves. From this average curve, three relevant points were selected; namely, the point corresponding to the peak temperature (tmax; ΔTmax) and the points corresponding to the initial set (ti, ΔTi) and final set (tf, ΔTf), as shown in Figure 2.4-b. The initial and final setting times were determined using the derivatives method [23], such that initial set occurs when the second derivative of temperature attains its maximum and final set occurs when the first derivative attains its maximum, as shown in Figure 2.5-a and -b, respectively. For the numerical differentiation of experimental data curves, the Savitzky–Golay smoothing filter was used by fitting successive subsets of adjacent data points, corresponding to a time interval of 61 minutes, with a five-degree polynomial by the least-squares method.

The procedure used to evaluate the different mortars shrinkage followed a procedure similar to the American standard ASTM C 596 [41]. One has used cylindrical mortar bars (27 mm diameter and 250 mm length) with inserted steel studs partially embedded at each end. The first measurement was at the age of 24 ± 0.25 h, after demoulding. Then, the specimens were stored in a climatic room at 20 ± 2 °C and $HR = 50 \pm 5\%$. Measurements were repeated over time, more specifically at 7, 14, 28 and 56 days of age. After each length measurement, the specimens were weighted on a high precision balance. For each mixture in the experimental plan, shrinkage deformation and mass loss against time are reported, as an average of results on three identical mortar bars at each age.

Prismatic specimens, $40 \times 40 \times 160$ mm^3, were demoulded one day after casting and kept for 28 days in a water tank (20 ± 2 °C), and then compressive strength was performed following EN 196-1. The average of six cubic specimens, resulting from

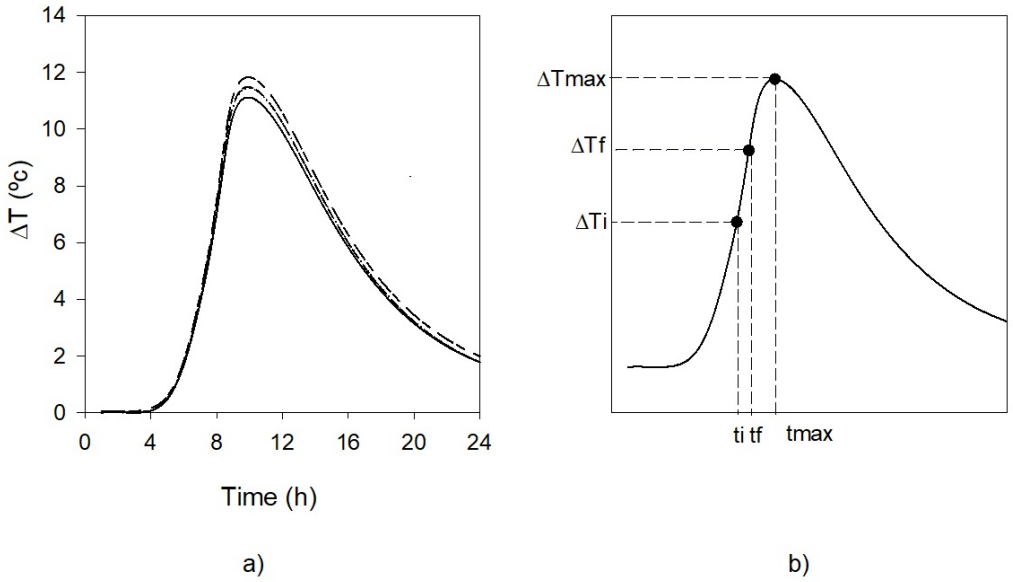

FIGURE 2.4: Relative increase of temperature with time: a) Example of four curves obtained for one of the mixes (F4) and b) corresponding average curve.

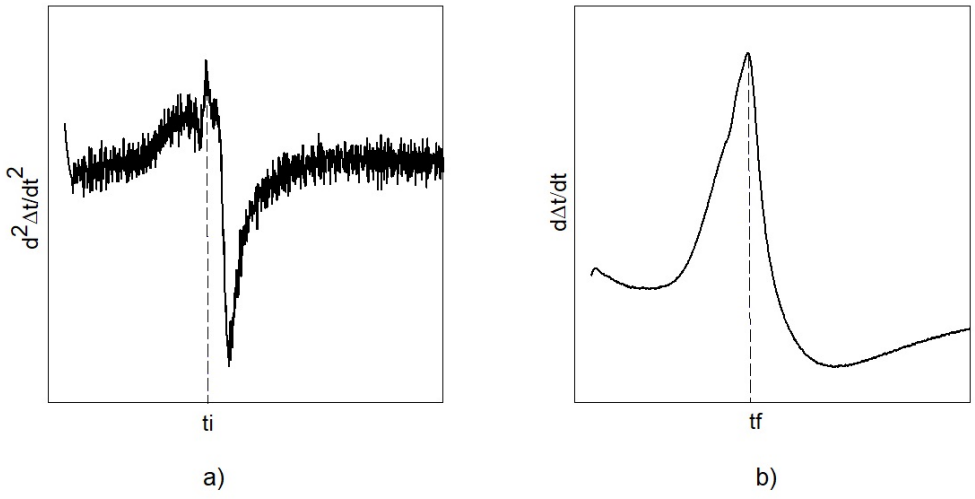

FIGURE 2.5: Plot of the a) second derivative of the temperature with respect to time and b) first derivative of the temperature, as a function of time.

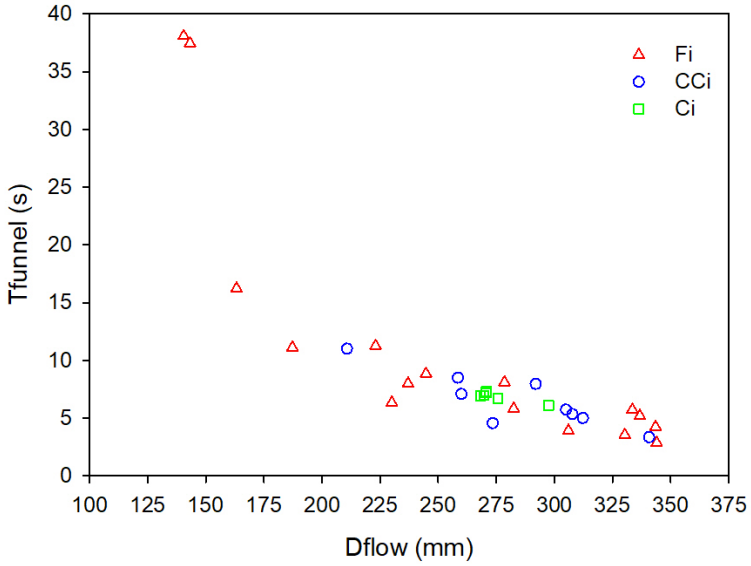

FIGURE 2.6: Fresh state test results of all 32 mixtures in the experimental plan.

the three prismatic specimens, was taken as the compressive strength at 28 days (fc_28d) of each trial mixture.

2.5 Test results and discussion

Figure 2.6 presents the V-funnel flow time (Tfunnel) versus slump flow diameter (Dflow) obtained for the tested mortar mixtures. These results show a typical trend of increase of slump-flow diameter with a reduction in flow time. The implemented experimental plan covers a wide range of mortars with Dflow ranging from 102 to 344 mm and Tfunnel ranging from 2.9 to 38.1 s. Observed spectra of Dflow and Tfunnel seem to be adequate, because these intervals include target values of Dflow and Tfunnel (250 mm and 10 s, respectively), according to Okamura et al. [1]. All Dflow and Tfunnel results are also listed in the 2nd and 3rd columns of Table 2.5. In the case of axial point CC10 mixture, it was not possible to measure the flow time due to occurrence of blocking in the V-funnel.

Figure 2.7 presents the average temperature evolution curves obtained in the current study. From these curves, data on relevant points was obtained, namely, (tmax; ΔTmax), (ti, ΔTi) and (tf, ΔTf). Scatter plots are depicted in two groups in Figure 2.8: the first group relating variables expressing temperature variations (ΔTmax, ΔTi, ΔTf) (Figure 2.8-a); and the second group relating variables which express the relevant times mentioned above, tmax, ti and tf (Figure 2.8-b). Pearson's correlation

TABLE 2.5: Experimental test results used in the modelling.

	Dflow (mm)	Tfunnel (s)	Δtmax (°C)	ti (h)	tf (h)	Sh_7d (10^{-6})	Sh_14d (10^{-6})	Sh_28d (10^{-6})	fc_28d (MPa)
C1	276.0	6.68	12.10	6.73	7.43	622	722	754	79.50
C2	268.0	6.95	11.90	6.49	7.20	662	780	801	86.47
C3	270.0	6.97	11.90	6.53	7.24	650	761	783	86.22
C4	271.0	7.31	11.99	6.58	7.26	643	757	736	90.18
C5	271.0	7.19	12.52	7.41	8.08	659	764	733	86.63
C6	297.5	6.10	12.23	7.11	7.79	614	718	698	89.56
F1	143.0	37.45	12.99	5.68	6.28	618	714	686	91.31
F2	306.0	3.91	14.13	7.03	7.58	713	852	847	89.63
F3	343.5	4.24	12.49	7.22	7.22	584	728	708	82.24
F4	230.0	6.34	11.35	6.29	6.96	750	866	888	83.92
F5	337.0	5.19	13.49	7.08	7.70	679	790	821	89.89
F6	187.0	11.11	13.83	6.13	6.67	715	831	797	87.79
F7	245.0	8.84	11.17	6.34	7.05	726	837	855	85.01
F8	344.0	2.87	13.51	7.03	7.75	708	831	813	83.86
F9	278.5	8.10	12.18	6.79	7.41	595	701	672	90.55
F10	163.0	16.23	12.71	6.28	6.94	629	705	702	88.45
F11	223.0	11.25	9.44	6.08	6.87	569	637	634	85.66
F12	330.0	3.55	11.08	7.12	7.98	663	760	788	79.40
F13	140.5	38.08	11.44	5.84	6.52	558	629	609	89.86
F14	282.5	5.82	12.53	6.77	7.47	661	797	764	85.75
F15	333.5	5.74	11.47	7.60	8.33	550	646	614	81.69
F16	237.0	7.99	10.26	6.37	7.16	654	738	763	79.65
CC1	292.0	7.95	10.55	6.53	7.18	573	645	655	90.37
CC2	273.5	4.56	13.80	7.00	7.75	705	818	797	83.15
CC3	211.0	11.00	14.01	6.56	7.18	666	762	739	93.41
CC4	312.0	5.00	10.76	6.95	7.75	647	722	681	80.64
CC5	260.0	7.08	12.25	6.93	7.61	660	762	733	84.30
CC6	305.0	5.73	11.63	6.98	7.65	639	729	753	84.52
CC7	308.0	5.34	13.63	6.77	7.35	709	852	823	83.97
CC8	258.5	8.50	9.93	6.69	7.40	558	613	599	80.83
CC9	341.0	3.35	12.62	7.38	8.09	653	762	736	80.04
CC10	102.0	*	10.96	5.12	5.78	648	705	694	87.68

Notes: (*) impossible to measure

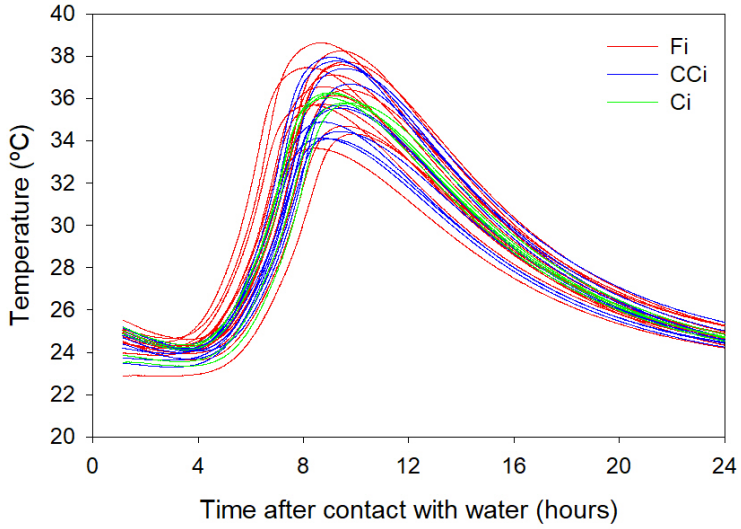

FIGURE 2.7: Temperature evolution with time of all 32 mixtures in the experimental plan.

coefficient is presented for each pair. Figure 2.8 shows a strong correlation (≥ 0.93) between the three temperature variations, as well as, between the three relevant times. Given these strong correlations, only ΔTmax, ti and tf were modelled in the current study. The corresponding values are presented in Table 2.5 (columns 4 to 6).

The shrinkage of free specimens can be the sum of all the types of shrinkage that occurred (drying shrinkage plus autogenous shrinkage). Figure 2.9 presents the evolution of total shrinkage deformation and mass loss for all mixtures included in the experimental plan, up to 56 days. From Figure 2.9-a, one can see that all the mortar specimens suffered the most of shrinkage on the first ages. Since measurements started at the age of 24 hour, a significant part of autogenous shrinkage had already occurred; thus the deformation measurements reported in the current paper are mainly due to drying shrinkage, which is intimately related to water loss to the surrounding external environment. Results of shrinkage deformation at 7, 14 and 28 days (Sh_7d, Sh_14d, Sh_28d) used in modelling are presented in columns 7 to 9 of Table 2.5, as well as, the average 28 days compressive strength results (fc_28d) in the last column. Table 2.6 presents a statistical summary of the 32 experimental results and the 6 central points. The mathematical models provided good fits for all response variables Dflow, Tfunnel, ΔTmax, ti, tf, Sh_7d, Sh_14d and Sh_28d, except for the case of fc_28d, given that, for this variable, the coefficient of variation evaluated on the central points is close to the coefficient of variation assessed on the 32 points of the factorial design.

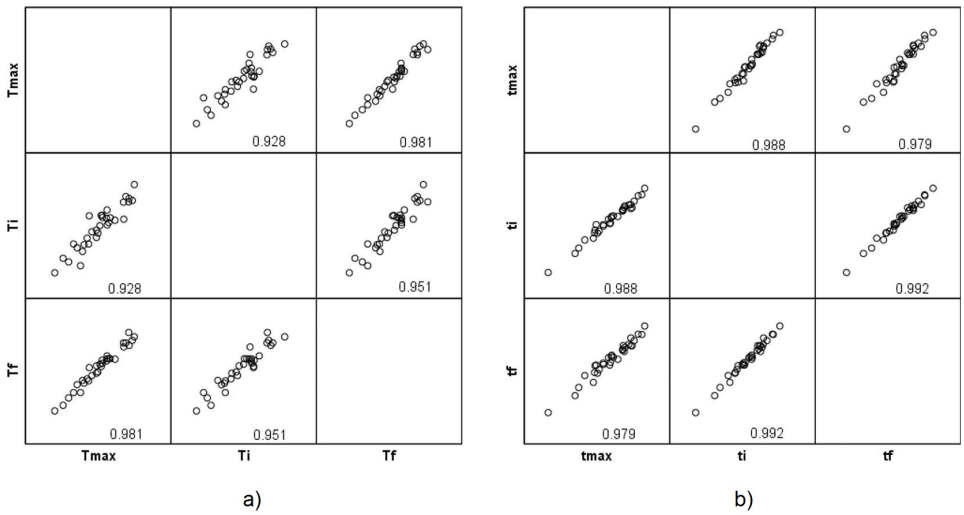

FIGURE 2.8: Scatter plots: a) variables describing temperature variations and b) variables describing relevant times. The corresponding Pearson's correlation coefficient is indicated in the scatter plots.

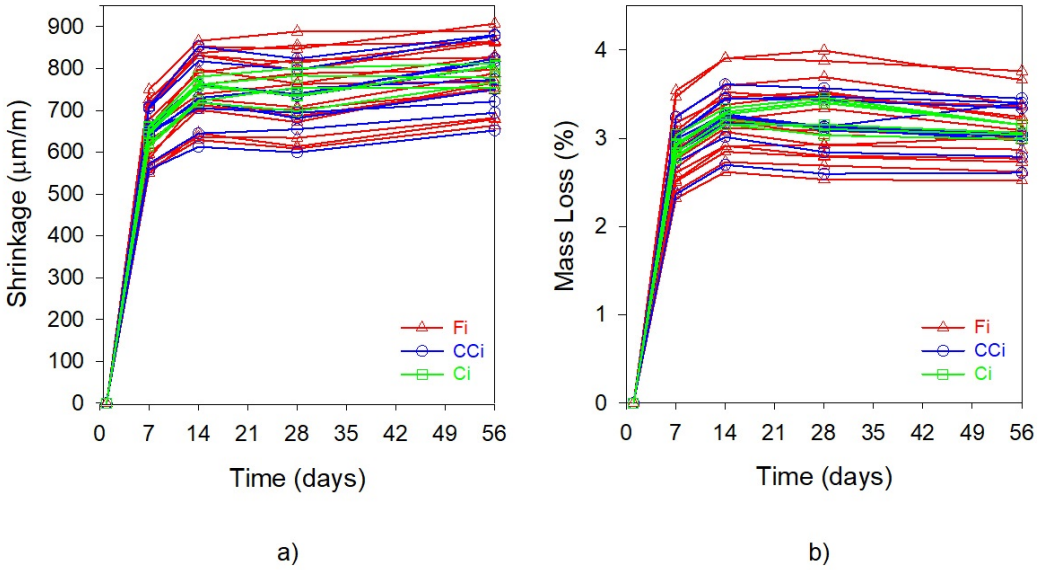

FIGURE 2.9: Temperature evolution with time of all 32 mixtures in the experimental plan.

TABLE 2.6: Descriptive statistics of the results for all 32 mixtures and for 6 central mixtures.

	Dflow (mm)	Tfunnel (s)	Δtmax (°C)	ti (h)	tf (h)	Sh_7d ($\times 10^{-6}$)	Sh_14d ($\times 10^{-6}$)	Sh_28d ($\times 10^{-6}$)	fc_28d (MPa)
All 32 mixtures									
minimum	102.0	2.87	9.44	5.12	5.78	550	610	599	79.40
maximum	344.0	38.08	14.13	7.60	8.33	750	866	888	93.40
mean	263.7	8.92	12.09	6.67	7.35	646	748	740	85.69
Std. deviation	62.9	8.18	1.22	0.53	0.55	52.6	68.3	74.1	3.95
Coef. var. (%)	23.9	91.7	10.1	8.0	7.5	8.1	9.1	10.0	4.6
6 central mixtures									
minimum	268.0	6.10	11.9	6.49	7.2	614	718	698	79.50
maximum	297.5	7.31	12.52	7.41	8.08	662	780	801	90.20
mean	275.5	6.87	12.11	6.81	7.5	642	751	751	86.43
Std. deviation	11.09	0.43	0.24	0.37	0.36	19.50	24.65	36.96	3.79
Coef. var. (%)	4.0	6.3	2.0	5.4	4.8	3.0	3.3	4.9	4.4

2.6 Response Models

The experimental data presented in Table 2.5 were utilised to develop polynomial regression models for each response variable as a function of the five design variables considered in the present study. The statistical analysis for Dflow, Tfunnel and fc_28d responses has already been illustrated in previous work [42]; thus only the analysis and model fitting of shrinkage deformation at seven days (Sh_7d) is described in detail in the next section. The same statistical procedure was followed for the remaining variables, and the corresponding fitted models are presented in Section 2.6.2.

2.6.1 Statistical analysis of data and fitting of (Sh_7d) model

2.6.1.1 Model fitting

The central composite design adopted for the estimation of a full quadratic model as follows:

$$y = \beta_0 + \sum_{i=1}^{k} \beta_i x_i + \sum_{i=1}^{k} \beta_{ii} {x_i}^2 + \sum_{i<j} \sum \beta_{ij} x_i x_j + \varepsilon \tag{2.1}$$

where y represents the model response variable; x_i correspond to the design variables considered; the letter β's is used for model parameters (β_0 is the independent term, β_i represents the linear effect of x_i, β_{ii} represents the quadratic effect of x_i and β_{ij} represents the linear-by-linear interaction between x_i and x_j); and ε is the fitting error. The model parameters β_0, β_i, β_{ij} can be estimated by means of a multi-linear regression analysis. In the course of the analysis, it may happen that some of the terms in Equation 2.1 may not be significant. The significance of each factor on a given response can be evaluated using a Student's t-test. In the present work, a step-by-step backward elimination was used to eliminate non-significant terms in the regression model. The significance level used for the entry of a variable in the model was 5%.

Table 2.7 presents the results obtained from performing an ANOVA for Sh_7d response. The regression model is significant, since the associated value of the Fisher's statistics is 36.11, giving a p-value smaller than 10^{-4}. The lack of fit is not significant relative to pure error ($p - value = 0.84 > 0.05$). Table 2.7 also presents p-values for the marginal tests on each of the model parameters. Non-significant terms were

Table 2.7: ANOVA tests for Sh_7d response.

Tests for	Source	SS	DOF	MS	F-value	p-value
Significance of regression	Model	80236.53	9	8915.17	36.11	< 0.0001
	Residual	5431.99	22	246.91		
	Total	85668.53	31			
Lack of fit	Lack of fit	3530.81	17	207.69	0.55	0.8396
	Pure Error	1901.19	5	380.24		
Partial significance of each predictor variable	Vw/Vp	32250.37	1	32250.37	130.62	< 0.0001
	w/c	0	1	0	0	0.9986
	Sp/p	329.55	1	329.55	1.33	0.2604
	Vs/Vm	34835.25	1	34835.25	141.09	< 0.0001
	mtck/c	138.88	1	138.88	0.56	0.4612
	(Vw/Vp)×(Sp/p)	1692.87	1	1692.87	6.86	0.0157
	(w/c)×(mtck/c)	6469.52	1	6469.52	26.2	< 0.0001
	(Sp/p)×(Vs/Vm)	2417.36	1	2417.36	9.79	0.0049
	(Vs/Vm)×(mtck/c)	2102.73	1	2102.73	8.52	0.0080
	Residual	5431.99	22	246.91		

Notes: SS=sum of squares; DOF=degrees of freedom; MS=mean of squares

excluded from the model (p-value in the t-Student test above 0.05), in a first step, but then the Sp/p and mtck/c were included to keep the hierarchy of the model. Sum of squares values indicates that individual effects of Vw/Vp and Vs/Vm are the most significant to explain Sh_7d variation. Some interaction effects were also found to be significant, which reveals some curvature in the Sh_7d response. The model for Sh_7d, in terms of coded variables, including the residual standard deviation, along with the correlation coefficients, is presented in column 7 of Table 2.9. Squared terms for all independent variables are non-significant in the response, therefore, were excluded from the model. It is estimated that the regression model explains 91% of the variability of Sh_7d response. The replicate standard deviation value is 19.50 (see Table 2.6), which is very close to 15.71 (column 7 of Table 2.9), which indicates a potentially good fit of the regression model.

2.6.1.2 Model adequacy checking and diagnosis

The Durbin–Watson test was used to detect the presence of autocorrelation in the residuals from the regression analysis (see Table 2.8 for the value of the test statistic). When compared to the lower and upper limits, for this case $Q_{\mathrm{L}} = 0.836$ and $Q_{\mathrm{U}} = 2.205$ with a 5% significance level, one has that the value of the test statistic is

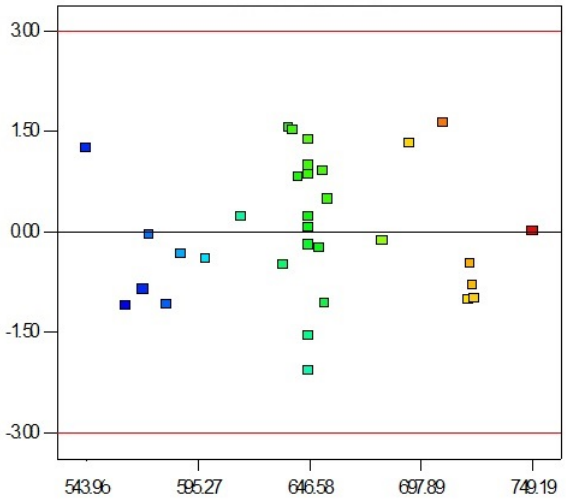

FIGURE 2.10: Plot of residuals versus Sh_7d fitted values.

higher than Q_U, which seems to indicate no evidence of positive auto-correlation but inconclusive regarding the presence of negative auto-correlation in the residuals.

The final selected model should be such that residuals are independent and normally distributed with zero mean and constant variance. They should not be correlated to any predictor. Several plots of residuals versus the predictor and the response variables were analysed looking for patterns or other evidence of bad behaviour of residuals (see Figure 2.10). There is no reason to suspect of any violation of the independence centrality or constant variance assumptions.

The normality assumption of the residuals was checked using the normal probability plot (see Figure 2.11). If the underlying error distribution were normal, this plot would be close to a straight line. Figure 2.11 shows no evidence of violation of this assumption. The results of Kolmogorov confirm this conclusion–Smirnov (Lilliefors version) and Shapiro–Wilk tests with $p - value > 0.05$ on both tests, see Table 2.8).

Identification of points that may considerably reduce the quality of the regression model (e.g. leverage points and regression outliers) for their eventual removal from the data-set was carried out by analysing the Cook's distance. If there are no outliers, these distances are of approximately equal amplitude and less than 1.0 [42]. For the current Sh_7d model, all Cook distance measures were smaller than 0.5, the studentised residuals remained in the interval [-2, 2], and no leverage points were detected. This analysis enables to conclude that the model established in the 7^{th} column of Table 2.9 is adequate to give the relationship between the response variable Sh_7d and the predictors.

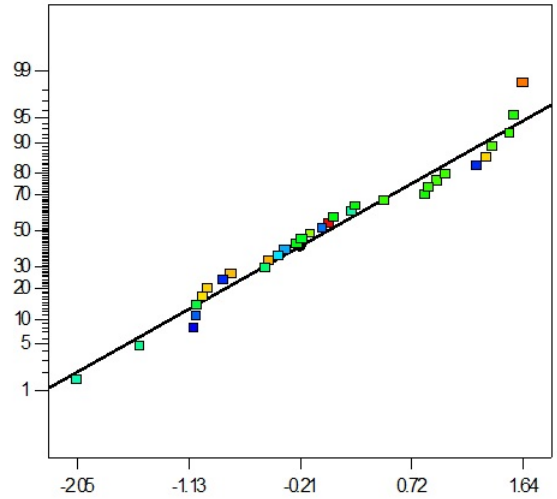

FIGURE 2.11: Normal probability plot of residuals for Sh_7d fitted model.

TABLE 2.8: Tests on residuals.

Test	Statistic	DOF	p-value
Kolmogorov–Smirnov Unstandardised residuals	0.096	32	0.200
Shapiro-Wilk Unstandardised residuals	0.967	32	0.418

2.6.2 Models for other responses

The procedure described in Section 2.6.1 was followed for all the remaining response variables, and the corresponding fitted models (in terms of coded variables). Table 2.9 present the models obtained along with the residual error standard deviations and the correlation coefficients. A variable transformation of the form was used in order to stabilise the Tfunnel response variance and improve the resulting model, which corroborates with previous studies [34], [42].

It important highlight that a large proportion of the variability of response variables is explained by the obtained regression models (Adj-R^2 values are considerably high ≥ 83.6 %), except in the case of fc_28d response ($Adj - R^2 = 57.8\%$). As remarked before, in the current experimental plan, a minimal variation was found for fc_28d results (4.6%) as compared to the experimental error (4.4%) (see Table 2.6). It was decide to abandon finding a good model for the fc_28d response.

TABLE 2.9: Fitted numerical models (design variables in coded values).

Model terms	Dflow (mm)	[Tfunnel (s)] $^{-0.5}$	ΔTmax (°C)	ti (h)	tf (h)	Sh_7d ($\times 10^{-6}$)	Sh_14d ($\times 10^{-6}$)	Sh_28d ($\times 10^{-6}$)	fc_28d (MPa)
Independent	278.410	0.380	12.089	6.780	7.464	646.178	747.960	739.890	85.690
Vw/Vp	-0.020	**0.038**	**0.468**	0.056	*NS*	**36.657**	**43.590**	**43.730**	**1.340**
w/c	**27.130**	**0.047**	**-0.794**	**0.140**	**0.190**	-0.006	-2.390	2.100	**3.220**
Sp/p	7.440	0.005	*NS*	*NS*	*NS*	3.706	*NS*	6.230	*NS*
Vs/Vm	-10.230	-0.026	**-0.803**	*NS*	*NS*	**-38.098**	**-54.740**	**-54.850**	*NS*
mtck/c	**-61.000**	**-0.090**	-0.459	**-0.510**	**-0.512**	2.406	-10.960	-7.350	*NS*
(Vw/Vp)×(Sp/p)	*NS*	*NS*	*NS*	*NS*	*NS*	-10.268	*NS*	-17.970	*NS*
(Vw/Vp)×(mtck/c)	5.907	*NS*	*NS*	0.120	*NS*	*NS*	*NS*	*NS*	*NS*
(w/c)×(mtck/c)	9.560	0.012	-0.310	*NS*	*NS*	**20.108**	**23.400**	**33.010**	*NS*
(Sp/p)×(Vs/Vm)	-5.720	-0.012	*NS*	*NS*	*NS*	-12.220	*NS*	*NS*	*NS*
(Vs/Vm)×(mtck/c)	*NS*	0.001	*NS*	*NS*	*NS*	-11.464	-15.100	*NS*	*NS*
$(w/c)^2$	-4.760	*NS*	*NS*	*NS*	*NS*	*NS*	*NS*	*NS*	*NS*
$(mtck/c)^2$	**-14.83**	*NS*	*NS*	**-0.150**	**-0.148**	NS	NS	NS	*NS*
Error term									
Mean	0	0	0	0	0	0	0	0	0
Std. Dev.	10.470	0.020	0.380	0.220	0.230	15.710	33.690	21.710	2.560
R^2	98.10%	97.10%	91.70%	86.20%	83.80%	93.70%	91.70%	84.00%	60.50%
Adj-R^2	97.20%	96.00%	90.10%	83.60%	82.10%	91.10%	89.90%	79.30%	57.80%

Notes: NS=non-significant term

2.6.3 Significant individual and interaction effects

The estimates of the model coefficients presented in Table 2.9, obtained for the coded variables, indicate the relative effect of the various mixture parameters on each response. Higher values indicate a stronger influence of the design variable in the response. For each model, the three most significant parameters are typed bold, and the most significant term is underlined as well. A positive coefficient means that the response (or transformed response) variable will increase if the given mixture parameter rises and vice-versa. As such, the results in Table 2.9 clearly show that mtkc/c exhibited the most substantial effect, a negative effect, on the fresh state properties and on both the initial and final setting times, followed by the w/c, representing a strong positive effect. This can be explained by the substantial reactivity of metakaolin [17]. A significant quadratic term on mtkc/c was also found for these mortar properties, except for Tfunnel. Concerning the maximum temperature rise of mortars, Vs/Vm and w/c were found to be the most significant terms. As expected, an increase of Vs/Vm or w/c was found to reduce the maximum rise in temperature of mortars, since both contribute to reduce the amount of cement per m^3. According to the formulation used in this study, the cement content, in terms of weight, can be computed as follows:

$$Wc = \frac{1}{\frac{w}{c}} \times \frac{Vw}{Vp} \times \left(\frac{1 - \frac{Vs}{Vm}}{1 + \frac{Vw}{Vp}} \right) \times \rho_w \tag{2.2}$$

where ρ_{w} represents the specific gravity of water. This relation is also represented graphically in Figure 2.12-a.

The mixture parameters Vs/Vm and Vw/Vp were found to be the most significant terms on all shrinkage responses. Shrinkage decreases with an increase of Vs/Vm because the paste content reduces. The water content, in terms of weight, can be computed as follows:

$$Ww = \frac{Vw}{Vp} \times \left(\frac{1 - \frac{Vs}{Vm}}{1 + \frac{Vw}{Vp}} \right) \times \rho_w \tag{2.3}$$

This relation is also represented graphically in Figure 2.12-b, to help the visualisation of the effect of Vw/Vp on water content. Since, for a given value of Vs/Vm, the water content increases with Vw/Vp, one could expect an increase of shrinkage. This explains the significant influence of Vw/Vp on shrinkage too.

Generally speaking, Sp/p exhibited the lowest influence on mortar properties, as compared to other mixture parameters. This can be explained by the short range

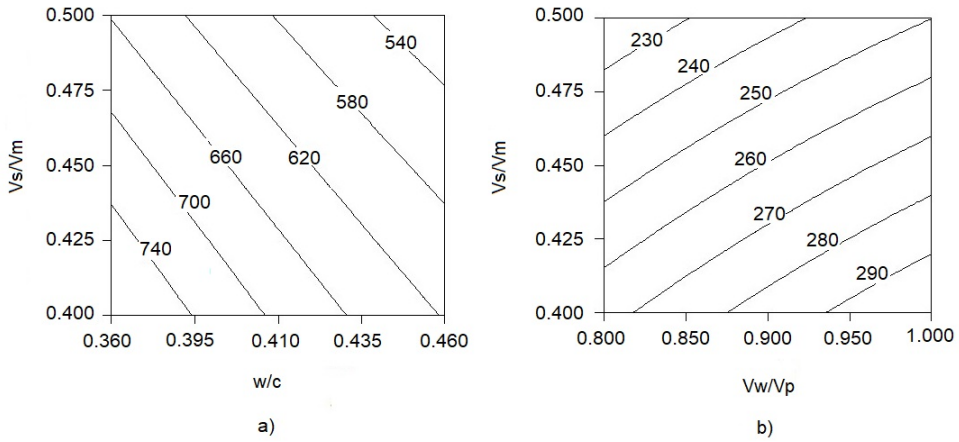

FIGURE 2.12: Contour plots of a) cement content ($\mathrm{kg\,m^{-3}}$) and b) water content ($\mathrm{kg\,m^{-3}}$).

of variation of Sp/p in the experimental plan (see Table 2.2), which was determined by the intense dispersion action of the superplasticizer used (Viscocrete 3008). A significant interaction effect between w/c and mtck/c was also found on all shrinkage responses as displayed in Figure 2.13. Although the fact that it was decided to abandon establishing a model for fc_28d, ANOVA revealed that w/c has the most substantial influence on fc_28d, as could be anticipated.

2.7 Mortar mixtures optimisation

The empirical models obtained for the relevant mortar properties can be used for the optimisation of mixture proportions using any suitable optimisation method or tool. In the current study, the optimisation module of commercial software Design-Expert [43] was used for the simultaneous optimisation of multiple responses obtained from the experimental plan. In the present study, the optimisation was developed in two stages, as explained in the following sections.

2.7.1 Self-compacting mortar mixtures

In a first stage, the developed empirical models were utilised to determine the range of mortar mixture parameters that satisfy the self-compactability requirements, i.e. to determine the mixtures which exhibit a mini-slump flow diameter of 260 mm and flow time of 10 s. The optimisation problem was defined as indicated in column A of Table 2.10, with importance weights for all goals set equal.

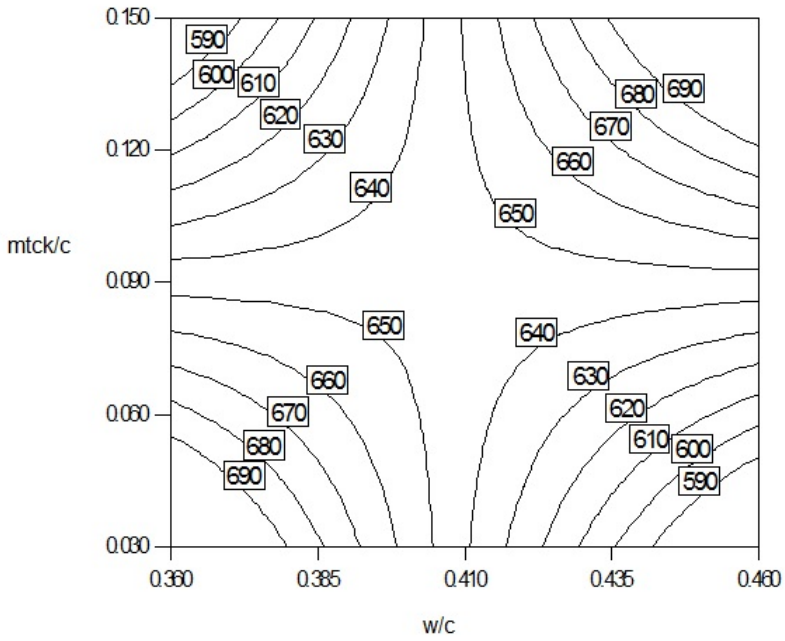

FIGURE 2.13: Contour plot of Sh_7d as a function of w/c and mtck/c ($Vw/Vp = 0.90$, $Sp/p = 0.70\%$ and $Vs/Vm = 0.45$).

The optimisation module in Design-Expert searches for a combination of factor levels that simultaneously satisfy the goals placed on each of the responses and factors. The procedure makes use of a desirability function (D). The general process consists on (i) compute the individual desirabilities ($0 \leq di \leq 1$, where $di = 1$ if the response is at its goal and $di = 0$ if the response is outside an acceptable region); (ii) combine them using the geometric mean, which gives an overall desirability function; (iii) finally, choose the factor levels that maximise the overall desirability (D). In the current study, only solutions with $D \geq 0.995$ were taken as optimal solutions. The optimal solutions found is shown in Figure 2.14. It was found that $Vs/Vm = 0.500$ had no solutions, relatively few solutions were found for $Vs/Vm = 0.400$, $Vs/Vm = 0.425$ and $Vs/Vm = 0.450$. On the other hand, $Vs/Vm = 0.475$ presented a wide range of solutions.

The adjusted values of mtck/c and Sp/p for each pair (w/c, Vw/Vp), with Vs/Vm equal to 0.475, were used to obtain the contour plots presented in Figure 2.15-a. The grey shading in this Figure represents the distance to the centre of the modelled region (d), which can be computed as follows:

$$d = \sqrt{\sum_{i=1}^{k} \left(\frac{x_i - x_{i,0}}{\Delta x_i} \right)^2} \tag{2.4}$$

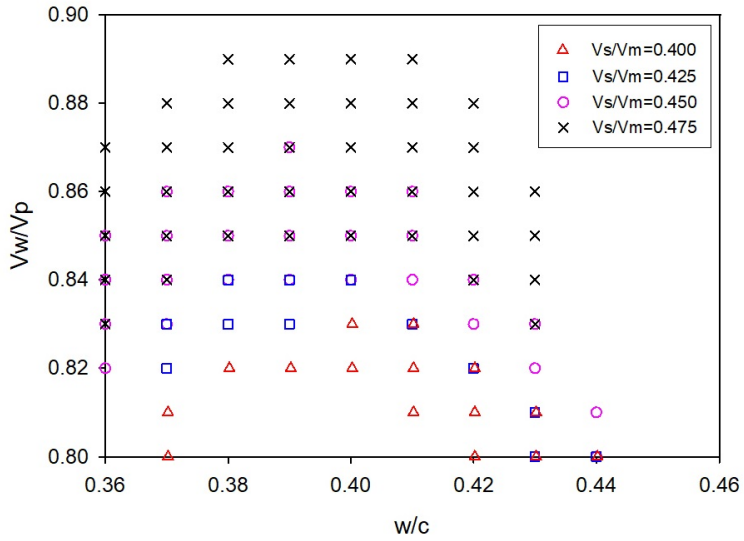

FIGURE 2.14: Region of optimised SCC mortars, as a function of Vs/Vm.

where x_i corresponds to the actual value of the i^{th} design variable, $x_{i,0}$ is the actual value of the i^{th} variable at the centre of the design and Δxi is the variable variation (in actual values) corresponding to a unit change in the coded variable. Estimated responses obtained from the optimisation were plotted in Figure 2.15-b to depict the variations of maximum temperature rise of mortar and shrinkage at 7 days. Similar contour plots were produced for the remaining analysed response variables, but are not included here due to limitations of space. This type of graphics is useful to visually analyse how certain mixture parameters influence the studied early–ages properties and serves as a basis for finding the optimal solution. Figure 2.15-b clearly shows that SCC mortars exhibiting, simultaneously, low Tmax and low Sh_7d can be found for higher w/c and lower Vw/Vp.

2.7.2 Optimal SCC mortar mixture to minimise cracking risk

In a second stage, the optimisation aimed to find the mortar mixture that leads to the best overall performance targeting eco-efficiency, economy and other engineering properties, namely, self-compactability and low cracking risk at early ages (to not impair the durability of the structure). Compressive strength results at 28 days of all mixtures were relatively high; thus, no additional requirement was necessary concerning this property. Because of these performance requirements, mortar mix proportions were optimised to satisfy the optimisation constraints indicated in column B of Table 2.10. The eco-efficiency and economy requirements are considered

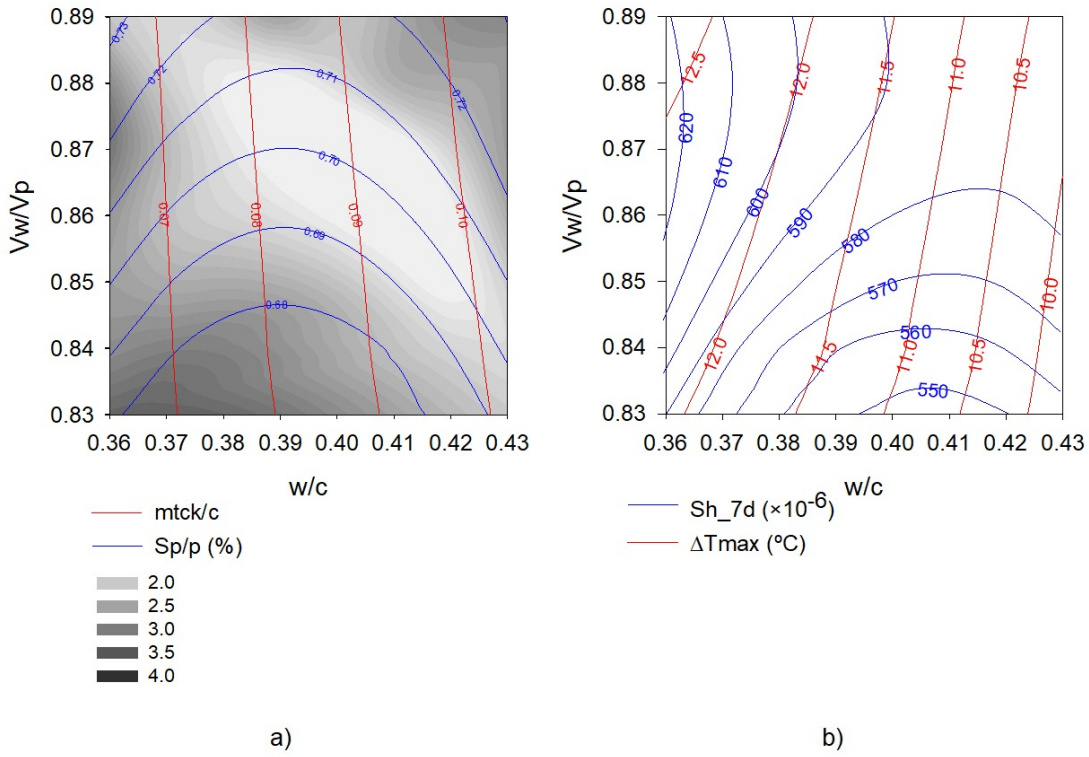

FIGURE 2.15: Range of design variables (absolute values) for optimised mortars with a) Vs/Vm=0.475 and b) estimated values of ΔTmax and Sh_7d.

TABLE 2.10: Optimisation criteria.

	A	B
Design Variables:		
Vw/Vp	Equal to c_1	In range
w/c	Equal to c_2	In range
Sp/p	In range	In range
Vs/Vm	Equal to c_3	Maximise
mtck/c	In range	In range
Response Variables:		
Dflow (mm)	Target is 260	In range [259,261]
Tfunnel (s)	Target is 10	In range [9.8,10.2]
ΔTmax (°C)	None	Minimise
ti (h)	None	None
tf (h)	None	None
Sh_7d ($\times 10^{-6}$)	None	Minimise
Sh_14d ($\times 10^{-6}$)	None	None
Sh_28d ($\times 10^{-6}$)	None	None
fc_28d (MPa)	None	None

Notes: c_1 varying from 0.800 to 1.000 by steps of 0.010;
c_2 varying from 0.360 to 0.460 by steps of 0.010;
c_3 varying from 0.400 to 0.500.by steps of 0.025;
range of design variables (coded values) was set at [-2.0; 2.0]

indirectly by maximising Vs/Vm. Both ΔTmax and Sh_7d were minimised to accomplish low cracking risk. An additional constraint should be implemented since the error function that is associated with each response model increases with the distance to the centre of the modelled region, d, computed according to Equation 2.4. Only solutions with $d \leq 2.5$ were accepted. The mixture parameters of best mortar found are: $Vw/Vp = 0.888$; $w/c = 0.428$; $Sp/p = 0.71\%$; $Vs/Vm = 0.500$; $mtkc/c = 0.096$. The corresponding estimated properties are presented in Table 2.11. It is interesting to notice that, by considering very narrow acceptance intervals for the fresh state properties (column B in Table 2.10) instead of target values (column A in Table 2.10), more solutions could be found including for higher Vs/Vm.

Compared to the central mixture of the experimental plan (see Table 2.5) the optimised mixture exhibits less risk of segregation in the fresh state (higher V-funnel time) and adequate flowability, along with lower ΔTmax and shrinkage deformations. For similar Dflow and fine aggregate content, the optimised mixture compared to mixture CC8 (see Table 2.5) exhibits slightly improved Tfunnel (from 8.5 to 9.8 s), lower ΔTmax (from 9.9 to 9.7 °C) and lower Sh_7d (from 558×10^{-6} to 540×10^{-6}). This shows that the numerical optimisation allowed further improvement of the mortar properties in the fresh state and in terms of cracking risk at early ages.

Table 2.11: Estimated mortar properties of optimised mixture to minimise cracking risk.

	Dflow (mm)	Tfunnel (s)	ΔTmax (ºC)	ti (h)	tf (h)	Sh_7d ($\times 10^{-6}$)	Sh_14d ($\times 10^{-6}$)	Sh_28d ($\times 10^{-6}$)	d
Predicted	258.9	9.8	9.7	6.8	7.5	540	621	636	2.44
95% PI low	231.0	7.3	8.8	6.3	7.0	499	572	557	
95% PI high	286.5	13.8	10.5	7.2	8.0	581	671	715	

(*) Lower and higher bounds of prediction interval with 95% confidence level

2.8 Conclusions

This study aimed to investigate the effect of SCHPC-mortar design variables and to select the best combination of powder materials (in a ternary mixture of white Portland cement+LF+MTCK), w/b and superplasticiser dosage, to minimise shrinkage deformations and maximum temperature rise due to heat of hydration, without compromising the self-compactability. The following conclusions can be drawn from this study:

- Quadratic models were found to be adequate to describe several mortar properties over the experimental region, namely, slump-flow diameter, V-funnel time, maximum temperature rise, initial and final setting times and shrinkage deformations.
- mtck/c exhibited the strongest effect on the slump-flow diameter, V-funnel time and on both the initial and final setting times. An increase of mtck/c reduces the slump-flow diameter, increases the flow time and reduces both the initial and final setting times.
- After mtck/c, w/c was found to be the most influencing variable on the slump-flow diameter, V-funnel time and setting time. w/c affects these mortar properties opposite to mtck/c.
- Vs/Vm and w/c were found to be the most significant design variables to the maximum temperature rise of mortars. As expected, an increase of Vs/Vm or w/c, meaning lower cement content, was found to reduce the maximum temperature increase of mortars.
- Shrinkage was most influenced by Vs/Vm and Vw/Vp. Shrinkage decreases with an increase of Vs/Vm because the paste content reduces. From mixture formulation, for a given value of Vs/Vm, the water content increases with Vw/Vp. This explains the great influence of Vw/Vp on shrinkage too.

- Due to the short range of variation of Sp/p used in the current experimental plan, Sp/p exhibited the lowest influence on mortar properties, as compared to other mixture parameters.
- Numerical optimisation allowed further improvement of the mortar properties in the fresh state and in terms of cracking risk during the first days.
- DOE approach can contribute to understand better, optimise and design the mortar phase (or paste phase in the sense that concrete can be obtained replacing the standard sand by the real aggregates) of SCHPC for applications with very demanding performance requirements.

References

[1] Hajime Okamura and Masahiro Ouchi. Self-Compacting Concrete. *Journal of Advanced Concrete Technology*, 1(1):5–15, 2003.

[2] P C Aïtcin. High Performance Concrete (HPC). *36th Conference on Our World in Concrete & Structures*, (August):14–16, 2011.

[3] EFNARC. The European Guidelines for Self-Compacting Concrete - Specification, Production and Use, 2005.

[4] Ha Thanh Le, Matthias Müller, Karsten Siewert, and Horst-Michael Ludwig. The mix design for self-compacting high performance concrete containing various mineral admixtures. *Materials & Design*, 72:51–62, 2015.

[5] P. Dinakar, Kali Prasanna Sethy, and Umesh C. Sahoo. Design of self-compacting concrete with ground granulated blast furnace slag. *Materials & Design*, 43:161–169, 1 2013.

[6] Miao Liu. Self-compacting concrete with different levels of pulverized fuel ash. *Construction and Building Materials*, 24(7):1245–1252, 7 2010.

[7] Geert De Schutter. Effect of limestone filler as mineral addition in self-compacting concrete. In S Teng MH Zhang CT Tam, KCG Ong, editor, *36th Conference on Our World in Concrete & Structures : 'Recent Advances in the Technology of Fesh Concrete*, pages 49–54, Ghent, Belgium: Ghent University, Department of Structural engineering, 2011.

[8] Guangcheng Long, Yu Gao, and Youjun Xie. Designing more sustainable and greener self-compacting concrete. *Construction and Building Materials*, 84:301–306, 6 2015.

[9] A KH Kwan. Use of condensed silica fume for making high-strength, self-consolidating concrete. *Canadian Journal of Civil Engineering*, 27(4):620–627, 8 2000.

[10] Nguyen Van Tuan, Guang Ye, Klaas van Breugel, Alex L. A. Fraaij, and Danh Dai Bui. The study of using rice husk ash to produce ultra high performance concrete. *Construction and Building Materials*, 25(4):2030–2035, 2011.

[11] H.S. Wong and H. Abdul Razak. Efficiency of calcined kaolin and silica fume as cement replacement material for strength performance. *Cement and Concrete Research*, 35(4):696–702, 4 2005.

[12] Mehmet Gesoğlu, Erhan Güneyisi, and Erdoğan Özbay. Properties of self-compacting concretes made with binary, ternary, and quaternary cementitious blends of fly ash, blast furnace slag, and silica fume. *Construction and Building Materials*, 23(5):1847–1854, 5 2009.

[13] C.-S Poon, L Lam, S.C Kou, Y.-L Wong, and Ron Wong. Rate of pozzolanic reaction of metakaolin in high-performance cement pastes. *Cement and Concrete Research*, 31(9):1301–1306, 9 2001.

[14] Rafat Siddique. *Waste Materials and By-Products in Concrete*. Springer Berlin Heidelberg, Berlin, Heidelberg, 2008.

[15] Rahmat Madandoust and S. Yasin Mousavi. Fresh and hardened properties of self-compacting concrete containing metakaolin. *Construction and Building Materials*, 35:752–760, 2012.

[16] Ahmed A. Abouhussien and Assem A.A. Hassan. Optimizing the durability and service life of self-consolidating concrete containing metakaolin using statistical analysis. *Construction and Building Materials*, 76:297–306, 2 2015.

[17] El-Hadj Kadri, Said Kenai, Karim Ezziane, Rafat Siddique, and Geert De Schutter. Influence of metakaolin and silica fume on the heat of hydration and compressive strength development of mortar. *Applied Clay Science*, 53(4):704–708, 10 2011.

[18] P. Dinakar and S.N. Manu. Concrete mix design for high strength self-compacting concrete using metakaolin. *Materials & Design*, 60:661–668, 2014.

[19] Hossam S.Al-alaily and Assem Hassan. Refined statistical modeling for chloride permeability and strength of concrete containing metakaolin. *Construction and Building Materials*, 114:564–579, 2016.

[20] O.R. Kavitha, V.M. Shanthi, G. Prince Arulraj, and V.R. Sivakumar. Microstructural studies on eco-friendly and durable Self-compacting concrete blended with metakaolin. *Applied Clay Science*, 124-125:143–149, 5 2016.

[21] Efstratios G. Badogiannis, Ioannis P. Sfikas, Dimitra V. Voukia, Konstantinos G. Trezos, and Sotirios G. Tsivilis. Durability of metakaolin Self-Compacting Concrete. *Construction and Building Materials*, 82:133–141, 5 2015.

[22] Terrence Ramlochan, Michael Thomas, and Karen A Gruber. The effect of metakaolin on alkali–silica reaction in concrete. *Cement and Concrete Research*, 30(3):339–344, 3 2000.

[23] S. N. Manu and P. Dinakar. Fresh and Mechanical Properties of High Strength Self Compacting Concrete Using Metakaolin. In K. Scrivener and A. Favier, editors, *1st International Conference on Calcined Clays for Sustainable Concrete*, pages 509–515, Dordrecht, Netherlands, 2015. Springer, Dordrecht.

[24] Erhan Güneyisi, Mehmet Gesoğlu, and Erdoğan Özbay. Strength and drying shrinkage properties of self-compacting concretes incorporating multi-system blended mineral admixtures. *Construction and Building Materials*, 24(10):1878–1887, 10 2010.

[25] Valeria Corinaldesi. Combined effect of expansive, shrinkage reducing and hydrophobic admixtures for durable self compacting concrete. *Construction and Building Materials*, 36:758–764, 11 2012.

[26] Gemma Rodríguez, Ana Blanco, Pablo Pujadas, and Antonio Aguado. Self-Compacting Concrete in the Temple of Sagrada Familia. *Journal of Architectural Engineering*, 23(3):04017005, 9 2017.

[27] Sandra Nunes, Paula Milheiro Oliveira, Joana Sousa Coutinho, and Joaquim Figueiras. Interaction diagrams to assess SCC mortars for different cement types. *Construction and Building Materials*, 23(3):1401–1412, 3 2009.

[28] Lino Maia, Miguel Azenha, Mette Geiker, and Joaquim Figueiras. E-modulus evolution and its relation to solids formation of pastes from commercial cements. *Cement and Concrete Research*, 42(7):928–936, 2012.

[29] Peter Hewlett. *Lea's Chemistry of Cement and Concrete*. Elsevier Science & Technology Books, Amsterdam, 4 edition, 2004.

[30] Samindi Samarakoon, Orjan Sletbakk Vie, and Remi Kleiven Fjelldal. Self-Compacting White Concrete Mix Design Using the Particle Matrix Model. *International Journal of Civil, Environmental, Structural, Construction and Architectural Engineering*, 9(7):802–806, 2015.

[31] L.M. Dellinghausen, A.L.G. Gastaldini, F.J. Vanzin, and K.K. Veiga. Total shrinkage, oxygen permeability, and chloride ion penetration in concrete made with white Portland cement and blast-furnace slag. *Construction and Building Materials*, 37:652–659, 12 2012.

[32] Ahmed Abouhussien and Assem Hassan. Application of Statistical Analysis for Mixture Design of High-Strength Self-Consolidating Concrete Containing Metakaolin. *J. Mater. Civ. Eng.*, 26(6), 2014.

[33] L. Dvorkin, A. Bezusyak, N. Lushnikova, and Y. Ribakov. Using mathematical modeling for design of self compacting high strength concrete with metakaolin admixture. *Construction and Building Materials*, 37:851–864, 2012.

[34] Sandra Nunes, Helena Figueiras, Paula Milheiro Oliveira, Joana Sousa-Coutinho, and Joaquim Figueiras. A methodology to assess robustness of SCC mixtures. *Cement and Concrete Research*, 36(12):2115–2122, 2006.

[35] Kamal Khayat, Geert De Schutter, RILEM Technical Committee 228-MPS on Mechanical Properties of Self-Compacting Concrete., and International Union of Testing and Research Laboratories for Materials and Structures. Mechanical properties of self-compacting concrete : state-of-the-art report of the RILEM technical committee 228-MPS on mechanical properties of self-compacting concrete. Technical report, 2014.

[36] Helena Figueiras, Sandra Nunes, Joana Sousa Coutinho, Joaquim Figueiras, H Figueiras, S Nunes, J Sousa Coutinho, and J Figueiras. Durability Performance of SCC Mortars Including Different Types of Metakaolin. In *12th Int. Conf. Durab. Build. Mater. Components*, Porto, Portugal, 2011.

[37] Gonzalo Barluenga, Irene Palomar, and Javier Puentes. Early age and hardened performance of cement pastes combining mineral additions. *Materials and Structures*, 46(6):921–941, 6 2013.

[38] Porto Cruise Terminal - APDL.

[39] Douglas C Montgomery. *Design and Analysis of Experiments*, volume 2. John Wiley & Sons, Inc., Hoboken, 8 edition, 2012.

[40] Helena Figueiras, Sandra Nunes, Joana Sousa-Coutinho, and Carmen Andrade. Linking fresh and durability properties of paste to SCC mortar. *Cement and Concrete Composites*, 45:209–226, 1 2014.

[41] ASTM. ASTM C 596 - Standard Test Method for Drying Shrinkage of Mortar Containing Hydraulic Cement, 2001.

[42] Sandra Nunes, Ana Mafalda Matos, Tiago Duarte, Helena Figueiras, and Joana Sousa-Coutinho. Mixture design of self-compacting glass mortar. *Cement and Concrete Composites*, 43:1–11, 10 2013.

[43] State-Ease Corporation. Design-expert software.

3 Design of new UHPC

The main goal of the current Chapter was to optimise UHPC mixtures incorporating the spent equilibrium catalyst (ECat) to mitigate autogenous shrinkage. DOE approach was used to optimise mixtures targeting different engineering properties, namely, self-compactibility, low early-age shrinkage and cracking risk, improved durability and high mechanical performance. The statistical models established indicated that ECat exhibits a strong positive effect on the autogenous shrinkage mitigation of UHPC attributed to the water absorbed in the porous of ECat particles. The proposed optimal UHPC represents the best compromise between low autogenous shrinkage and high resistivity without impairing self-compatibility and compressive strength. This optimal UHPC combined with 3% high-strength steel fibres (lf/df=65) proved to be comparable to other UHPFRCs, in terms of mechanical behaviour, and more eco-friendly and cost-efficient than UHPCs reported in the literature.

This Chapter corresponds to the published journal paper: Matos, A.M., Nunes, S., Costa, C., Barroso-Aguiar, J.L., Spent equilibrium catalyst as internal curing agent in UHPFRC, Cement and Concrete Composites, Volume 104, November 2019, Article number 103362.

3.1 Introduction

Ultra-high performance fibre reinforced cementitious composites (UHPFRC) has become one of the promising materials for the next generation of infrastructures – that need to be more resilient and sustainable - because of its outstanding mechanical properties, excellent durability characteristics, and good workability [1]. UHPFRC refers to the family of composite materials containing a large amount of short steel fibres evenly embedded in an ultra-compact cementitious matrix (hereafter, UHPC) with a high content of the binding phase including cement and supplementary cementitious materials (SCM), commonly silica fume (SF), and a very low water to binder ratio ($w/b < 0.2$) [2]. However, the typical high amount of cement (700–850 $\mathrm{kg\,m^{-3}}$) and SF ($> 20\%$ of cement content) present in the UHPFRC mixtures [3]

cause some drawbacks, in terms of the limited availability of SF, especially in developing countries, the high production cost, and in the early-ages properties namely due to adverse effects on the heat of hydration and dimensional stability.

The replacement of part of the cement clinker with additions such as SCM is an interesting solution to reduce the cement content, and it contributes to sustainable development [4]. This is particularly relevant in the case of UHPFRC considering the fact that a significant quantity of cement clinker remains unhydrated [5] (thus acting as a filler material), due to its very low water to binder ratio. Many SCM other than SF have been successfully incorporated in UHPFRC such as pulverized fly ash, ground granulated blast furnace slag, metakaolin, steel slag powder, rice husk ash, and nanoparticles (nano-SiO_2, nano-$CaCO_3$, nano-TiO_2, nano-Fe_2O_3, etc.), as well as limestone filler (LF), as reported in a review paper by Shi et al. [2]. The use of locally available additions is a key factor to save energy, reduce cost and decrease CO_2 emissions from the production of UHPFRC. From this perspective, the incorporation of LF in UHPFRC is expected to have few limitations to implement, because it is a global available raw material, it involves modest changes in existing production lines, and it requires no new quarries nor large investments [6]. A new concept of UHPFRC production using LF as a partial cement surrogate was first developed at MCS-EPFL within ARCHES project, aiming to make the application of UHPFRC technology feasible with a wide range of cements and superplasticisers [7]. Huang et al. reported that partial replacement of cement with limestone (d_{50}=8 µm), up to 54%, is beneficial for the workability and compressive strength of UHPC [8]. By incorporating LF in UHPC, the hydration degree increased from 39% to 66%, due to the facilitation of the nucleation and growth of outer calcium silicate hydrates [8].

SF is a principal constituent material in UHPC, which main beneficial effects include: (1) the filling effect, significantly improving the packing density of the system and the interfacial transition zone (ITZ) between the binding paste and aggregates; (2) the lubricating effect, resulting from the spherical shape of its particles leading to improved workability; and (3) the pozzolanic effect, contributing to produce additional hydration products and, thus, enhancing strength and durability [9]. However, since SF is an industrial by-product, its availability is limited, and due to increasing demand for good quality SF in the construction industry, it becomes rather expensive. These motivated some research studies on alternative very reactive SCM, such as rice husk ash (RHA) [6], metakaolin [10] and fine glass powder [11]. Tuan [9] reported that there is a synergistic effect between RHA and SF on the workability and the compressive strength of UHPFRC. The best combination regarding compressive strength and workability was obtained with 10% RHA and 10% SF [9]. Another

important positive effect of RHA addition is the mitigation of autogenous shrinkage, due to its water absorption capacity in the porous structure [9].

UHPFRC exhibits large shrinkage values, but, unlike conventional concrete, autogenous shrinkage represents the largest portion of the total shrinkage (from 75% up to 100% depending on the mixture) [3]. Moreover, this phenomenon occurs in the first one or two days after casting, being possible to show deformations of around 1000 $\mu m\,m^{-1}$ in 24 h [12]. This very high autogenous shrinkage of UHPC is due to its very low w/b ratio and very high content of SF which causes a significant drop in the internal relative humidity (RH) in the cement paste during the hardening process that leads to the occurrence of self-desiccation in the absence of an external source of water [13]. After mixing, when a layer of fresh UHPFRC is applied over an existing concrete, the restriction conferred by the substrate to the new layer deformation generates internal tensile stresses. The magnitude of these internal stresses depends on the development of material properties during early ages, namely, the magnitude and evolution of shrinkage, tensile creep and the evolution of the modulus of elasticity. When UHPFRC exhibits significant strain hardening behaviour in tension only very fine micro-cracks can occur [14]. Nevertheless, in zones with lower fibre content or unfavourable fibres orientation [14] larger cracks might occur in the UHPFRC layer, which might impair the long term performance of UHPFRC. For these reasons, several attempts have been made to mitigate the autogenous shrinkage of UHPFRC. To counteract the significant drop in the internal RH in the cement paste during the hardening and, thus, the self-desiccation, several strategies of internal curing have been proposed for UHPC, including the use of saturated lightweight sand [15], superabsorbent polymers (SAP) [16], [17], [18], recycled coral-based materials [19], [20], and rice husk [9].

Meng and Khayat [15] employed pre-saturated lightweight sand (LWS) (nominal size of 4.75 mm) as an internal curing agent to prepare UHPC. The optimum LWS to natural sand ratio was found to be 25%, resulting in a compressive strength of 158 MPa and autogenous shrinkage limited to 365 $\mu m\,m^{-1}$, at 28 days. Incorporation of pre-saturated LWS was also found to promote cement hydration and reduce total porosity [15].

Dudziak and Mechtcherine [17] showed that the use of SAP and additional water during mixing leads to a reduction in deformation due to autogenous shrinkage, with a consequent positive effect on the generated tensile stresses at very early ages. The addition of 0.3% SAP by mass of cement plus extra water resulted in a reduction of about 30% in autogenous shrinkage after one day of measurement. A further reduction in the magnitude of autogenous shrinkage deformations can be achieved

with increasing dosages of SAP and extra water [17]. However, SAP lead to the formation of voids, initially filled with water and subsequently dried out, which might negatively affect compressive strength [17].

In order to minimise the negative impact of the large pores on concrete strength, smaller size SAP (a solution-polymerized SAP with a particle size < 63 µm in the dry state) were employed by Justs et al. [18]. This allowed to reach compressive strengths of almost 150 MPa at 28 days as well as to extend cement hydration further beyond the stage when there is no free capillary pore space for precipitation of hydration products, thanks to the additional space introduced by the SAP.

Wang et al. [19] found that addition of recycled coral-based materials (micro-coral sand and/or coral sand) is effective in decreasing the autogenous shrinkage of UHPC, which can be attributed to the internal curing provided by the porous structure of the coral.

A different strategy for internal curing was followed by Tuan [9], by incorporating RHA (5–10 µm) in UHPC. Due to its porous structure, RHA particles may absorb a certain amount of free water during mixing (20% by mass of RHA content [9]), acting as "micro water reservoirs". The absorbed water in RHA particles can compensate the drop of relative humidity in cement paste during the hydration of cement, therefore, contributing to mitigating the high autogenous shrinkage of UHPC [21]. Besides, it improves the cement paste microstructure due to a long-lasting pozzolanic reaction of RHA [21]. However, the geographical availability of RHA is minimal in Portugal (almost null). Thus, the research team searched for alternative materials, especially industrial by-products locally available that might reveal similar behaviour. A potential candidate to internal curing agent is the spent equilibrium catalyst (ECat), a waste generated by the oil refinery industry since it exhibits high water absorption ability and is also a pozzolanic material.

The equilibrium catalyst is used in the Fluid Catalytic Cracking (FCC) process during the conversion of low-value heavy gas oils into more valuable lighter compounds, namely gasoline [22], [23]. During this process, the catalyst loses adequate levels of activity and selectivity and has to be removed from the process giving rise to a waste [24] which is mainly disposal of in landfills. Every year, the oil industry generates about 840000 tonnes ECat each year [25] of which 1700 tonnes of ECat/year in Portugal. The ECat is a white-grey fine powder (with a typical particle size of 75 µm) mainly comprising four components: an aluminosilicate faujasite-type zeolite; an essentially amorphous alumina matrix which is also catalytically active; a clay, usually kaoline; and a binder that provides physical integrity to the catalyst [23]. The exact composition of this catalyst depends on the manufacturer because it is

specially designed to meet the specific requirements of the FCC unit is going to be used and its typical oil feedstock. Due to its aluminosilicate chemical composition and a very high specific surface ($> 100\ m^2\,g^{-1}$) [23] (mainly provided by the zeolite and matrix constituents), ECat has a potential pozzolanic activity.

Previous studies revealed that ECat can be used as SCM partially replacing either cement (10–20%, by mass) [26], [27], [28], [29] or sand (ca. 10%, by mass) [30], [31] in both traditional and self-compacting mortars and concrete, contributing typically to an improvement of overall performance including durability [32], [33] although decreasing the flowability of the cement-based materials in the fresh state [26], [28], [31], [34]. Torregrosa [35] incorporated an ECat (d_{50}=10 µm, i.e smaller than typical) in UHPC/UHPFRC as a partial or total surrogate of silica fume. The results of this study showed that the ECat led to a decrease in the workability of UHPC mixtures in the fresh state but less marked than that promoted by similar content of SF. Moreover, although the difference between compressive strength of ECat and SF UHPC mixtures with 2 days was not noticeable, at 7 and 28 days, ECat mixtures revealed higher strength than that of SF mixtures. Since this difference was more remarkable in the mixtures with 7 days, the ECat pozzolanic reaction was faster than that of SF. Concerning the flexural strength, the differences between the use of ECat or condensed SF were not very significant [35]. However, the influence of ECat on autogenous shrinkage and durability of UHPFRC remains unreported.

In the current study, for the best of author knowledge, ECat is for the first time used as an internal curing agent to produce UHPFRC, aiming to reduce its autogenous shrinkage without impairing mechanical properties and durability. To achieve this goal a central composite design (CCD) was utilized to determine the optimum combination of powder materials (cement, silica fume and limestone filler), aggregates (fine sand and ECat) and superplasticizer in UHPC production. The water to cement weight ratio was constant of 0.25, and the partial replacement of the fine sand with ECat was kept within the range of 0–30%, by volume. UHPC mixtures were assessed regarding their deformability, setting time, autogenous shrinkage, resistivity and compressive strength. Regression models were derived and validated, which allow predicting selected properties of UHPC, along with the identification of the most significant effects of mixture parameters on each property of UHPC. After optimising the matrix, short steel fibres (3% by volume) were incorporated in UHPC and the performance of the resulting UHPFRC was further investigated by analysing its flowability, autogenous shrinkage evolution, mechanical performance, cost and environmental efficiency.

3.1.1 Research significance

Considering the concept of hybrid structures where thin layers of UHPFRC are applied in the critical locations in terms of environmental exposure and mechanical demand [36], applicable to the rehabilitation/strengthening of the existing infrastructures, controlling the cracking risk of UHPC at early ages is essential for ensuring an enhanced long-term performance and longer service life. Reducing the early-age shrinkage is one way to improve the resistance to microcracking of UHPFRC. Besides reducing autogenous shrinkage, the use of spent equilibrium catalyst (ECat) in UHPC, as an internal curing agent, has the potential to enhance hydration due to more availability of water in the system and the pozzolanic activity of ECat. This can allow achieving new UHPC mixtures with comparable performance but lower cement content, which brings advantages regarding cost and CO_2 emissions. Moreover, the possibility of replacing natural sand with a residue generated by the oil refinery industry allows both limiting the excessive exploitation of naturally occurring river sand and a waste recycling that is diverted away from landfills.

3.2 Materials and Methods

3.2.1 Raw materials

UHPC were produced using the following solid materials: Type I Portland cement (CEM I 42.5 R, complying with EN 197-1); limestone filler; silica fume; equilibrium catalyst (ECat) generated byn Sines Refinery, Portugal, and siliceous natural sand (water absorption and density of 0.5% and 2570 $\mathrm{kg\,m^{-3}}$, respectively). A polycarboxylate-based high-range water reducer (Sp) with a solid mass content of 40% and density of 1080 $\mathrm{kg\,m^{-3}}$ was used. Steel fibres with 0.2 mm in diameter and 13 mm in length ($lf/df = 65$) were incorporated to produce UHPFRC (see Figure 3.1). The tensile strength and modulus of elasticity of the fibres are 2750 MPa and 200 GPa, respectively. Tap water was used, in accordance with standard EN 1008.

Figure 3.2 shows the particle size distributions (PSD) of all solid materials. The PSD of the sand was obtained following the standard EN 933-1, the PSD of SF was determined by Transmission Electron Microscopy, and the PSD of the remaining solid materials were obtained by laser diffraction. ECat possesses a narrow particle size range, around 80 µm, in between cement and sand curves.

FIGURE 3.1: Steel fibres employed to produce UHPFRC.

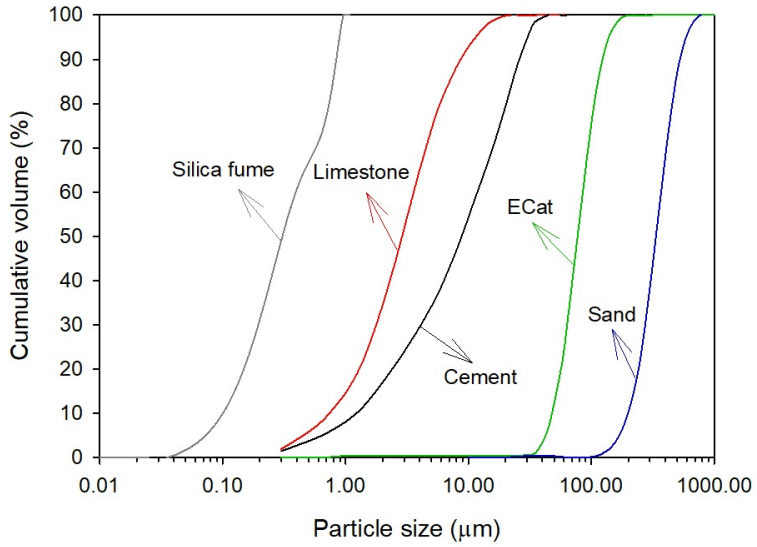

FIGURE 3.2: Particle size distribution of all solid materials.

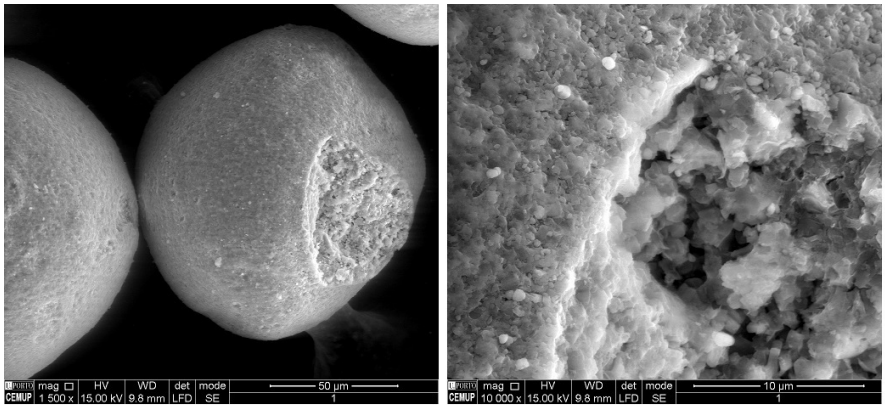

FIGURE 3.3: Secondary electron mode SEM image of ECat's particle morphology: a) entire particle view (×1500); b) external surface and internal porosity (×10000).

Table 3.1 summarises the relevant chemical and physical properties of cement, LF, ECat and SF. The bulk chemical compositions were obtained by X-ray fluorescence spectrometry (XRF), and the loss on ignition (LOI) was evaluated following EN 196-2. Density of cement and LF was obtained according to Portuguese LNEC specification E−64 [37]; the density of ECat was determined according to EN 1097-6. Although the Blaine method is often used to assess the cement specific surface area, the BET method is more appropriate to determine the specific surface area of ECat since, particularly due to its zeolite constituent, it is a highly micro-porous material (as shown in Figure 3.3) in which most of the surface area is internal and, therefore, only accessible using nitrogen adsorption-desorption. The high specific surface of the ECat (150 070 $m^2\,kg^{-1}$) with water affinity explains its significant water absorption. The 24 h water absorption of ECat is 30%, by mass, at saturated surface-dry basis, according to the standard EN 1097-6. A similar absorption capacity was found by Su et al. [31]. ECat's water absorption (30% by mass) was taken into account in the total water added to the UHPC mixtures. The pozzolanic reactivity of ECat and SF was assessed using the modified Chapelle test method (according to French standard NF P18-513). Results reveal that 1540 and 1577 mg of $Ca(OH)_2$ are consumed per g of ECat and per g of SF, respectively, during the pozzolanic reaction suggesting that both materials have high pozzolanic activity.

3.2.2 Design of experiments and mixtures proportions

UHPFRC mix design needs intensive laboratory testing to assess raw materials compatibility and to optimise mix-proportions while satisfying the several performance

TABLE 3.1: Chemical and physical properties of cement (CEM I 42.5R), limestone filler, ECat and silica fume.

	CEM I 42.5R	Filler	ECat	Silica fume
Chemical composition (% by mass)				
SiO_2 (%)	19.08		40.30	> 90
Al_2O_3 (%)	5.08		54.45	
Fe_2O_3 (%)	3.16		0.45	
CaO (%)	61.31		0.06	
MgO (%)	1.82		0.15	
SO_3 (%)	2.90		0.00	
Na_2O (%)	0.15		0.43	
K_2O (%)	0.58		0.02	
Cl (%)	0.07			
Free CaO (%)	1.17			
Loss on ignition (%)	2.54		1.05	
Insoluble residue (%)	0.94			< 3.00
$CaCO_3$ (%)		> 98		
Physical properties				
Specific density ($kg\,m^{-3}$)	3110	2680	2660	2200
Specific surface area ($m^2\,kg^{-1}$)	437.5 (Blaine)	500-600 (Blaine)	150070 (BET)	19632 (BET)
Initial setting time (min)	141			
Final setting time (min)	201			
Mechanical properties				
Rc,2 days (MPa)	32.2			
Rc,7 days (MPa)	47.4			
Rc,28 days (MPa)	60.8			

TABLE 3.2: Coded and actual values of independent variables.

Design variables	Code	-2	-1	0	+1	+2
Vw/Vp	*X1*	0.355	0.375	0.395	0.415	0.435
Sp/p	*X2*	2.00%	2.20%	2.40%	2.60%	2.80%
VECat/Vs	*X3*	0.000	0.075	0.150	0.225	0.300
sf/c	*X4*	0.005	0.025	0.045	0.065	0.085

requirements. This is particularly relevant both when a large number of constituent materials are used, as well as, when new and unconventional materials are incorporated, such as industrial by-products.

In the current study, experiments were conducted according to a Central Composite Design (CCD) [38], one of the most common experimental designs used for modelling and optimisation of self-compacting mortar/concrete [39], [40], conventional steel fibre reinforced concrete [41], and also UHPC mixtures [42], [43], [44]. The experimental factorial design approach is an efficient means to assess the influence of key mixture variables on UHPC/UHPFRC properties, being valid for a wide range of mixture proportions. It is useful to identify the main effects for the variables under study, as well as to unveil any existing interactions between those variables. Such understanding can facilitate the test protocol required to optimize UHPC, hence reduce the effort necessary to achieve the target engineering properties, namely, self-compactability, low risk of early age cracking, durability and high mechanical performance. The Design-Expert software [45] was used to assist in following stages of the study: experiments design, statistical analysis of data, fitting of empirical models using regression analysis (performing the analysis of variance (ANOVA) and the residuals analysis) and, finally, optimisation.

Four key design variables (*Xi*, i=1 to 4) were selected to derive the regression models: water to powder volume ratio (Vw/Vp); the superplasticizer to powder weight ratio (Sp/p); ECat to sand volume ratio (VECat/Vs) and SF to cement weight ratio (sf/c). Based on a preliminary study [12] the ranges of the selected design variables were established as indicated in Table 3.2. The correspondence between coded and actual values of the independent variables points is also indicated in Table 3.2. The water to cement weight ratio (w/c) and the fine aggregate (siliceous sand + ECat) content were set fixed and equal to 0.25 and 0.39 $m^3\,m^{-3}$, respectively.

In this study, 30 mixtures were investigated, consisting of 24 factorial points augmented with 8 axial points, plus 6 replications of the central point. The corresponding mixture proportions are presented in Table 3.3. Both the contents of cement

and SF in all mixtures are relatively low as compared to typical UHPFRC mixtures (see Section 3.1) [3]. In the current study one used far less SF than the amount theoretically required for total consumption of $Ca(OH)_2$ released from cement hydration (18% by weight of cement, according to [46]), thus providing an opportunity for both pozzolanic materials to react but not completely in most of the cases (excepted for CC5). Given the beneficial effects of limestone filler mentioned before and its abundant availability in Portugal, an extensive range of variation in limestone filler content was allowed, from almost 0 up to 543 $kg\,m^{-3}$. The mixing water ranged from 145 to 171 $kg\,m^{-3}$. It should be pointed that the mixing water indicated in Table 3.3 was corrected to take into account the water present in the superplasticizer and the water absorption of fine sand; nevertheless, more water was added initially to saturate ECat (30% of ECat weight), as high as 93.4 $kg\,m^{-3}$. A relatively high dosage of Sp (18-30 $kg\,m^{-3}$) was necessary to obtain mixtures with the improved workability (self-compacting ability). This also facilitated the casting of specimens, particularly the corrugated tubes used to measure autogenous shrinkage.

For each setting in Table 3.3, the final spread diameter (*Y1*), final setting time (*Y2*), autogenous shrinkage (*Y3*), resistivity (*Y4*) and the 28 days compressive strength (*Y5*) were evaluated. A CCD allows the identification of empirical models by fitting a second-order polynomial equation to the experimental data for each selected response variable *Yi*. The general form of the second-order model is:

$$y = \beta_0 + \sum_{i=1}^{k} \beta_i x_i + \sum_{i=1}^{k} \beta_{ii} {x_i}^2 + \sum_{i<j} \sum \beta_{ij} x_i x_j + \varepsilon \tag{3.1}$$

where y the predicted response; x_i correspond to the design variables; β_0, β_i, β_{ii} and β_{ij} are the model parameters and ε is the fitting error.

3.2.3 Mixing procedure and specimens preparation

UHPC mixtures (Table 3.3) were tested in a random order and prepared in batches of 1.40 L, using a mixer in accordance with EN 196-1. The mixing procedure had the following steps: (1) mixing ECat (dry state) with 80% mixing water plus the water needed for ECat absorption for 5 min; (2) adding sand and remaining powder materials and mixing for 2.5 min; (3) stopping to scrape material adhering to the mixing bowl and mixing for another 2.5 min; (4) introducing the rest of the water plus 75% of Sp and mixing for 2.5 min; (5) adding the rest of Sp and mixing for 3.5 min. The rotation speed of the mixer was always constant and set equal to 140 rpm. The total mixing time was longer than usual because of an additional of 5 min in

TABLE 3.3: Experimental plan and mixture proportions.

Ref.	Coded variables				Quantity ($kg\,m^{-3}$)						
	Vw/Vp	Sp/p	VECat/Vs	sf/c	Cement	LF	SF	ECat	Sand	Mixing water	Sp
Ci	0	0	0	0	690.90	273.54	31.09	155.61	851.96	158.39	23.89
F1	-1	-1	-1	-1	665.45	453.37	16.64	77.81	927.13	151.38	24.98
F2	1	-1	-1	-1	715.62	364.31	17.89	77.81	927.13	164.41	24.15
F3	-1	1	-1	-1	665.45	453.37	16.64	77.81	927.13	148.65	29.52
F4	1	1	-1	-1	715.62	364.31	17.89	77.81	927.13	161.78	28.54
F5	-1	-1	1	-1	665.45	453.37	16.64	233.42	776.78	151.38	24.98
F6	1	-1	1	-1	715.62	364.31	17.89	233.42	776.78	164.41	24.15
F7	-1	1	1	-1	665.45	453.37	16.64	233.42	776.78	148.65	29.52
F8	1	1	1	-1	715.62	364.31	17.89	233.42	776.78	161.78	28.54
F9	-1	-1	-1	1	665.45	193.96	43.25	77.81	927.13	154.45	19.86
F10	1	-1	-1	1	715.62	85.35	46.52	77.81	927.13	167.72	18.64
F11	-1	1	-1	1	665.45	193.96	43.25	77.81	927.13	152.28	23.47
F12	1	1	-1	1	715.62	85.35	46.52	77.81	927.13	165.68	22.03
F13	-1	-1	1	1	665.45	193.96	43.25	233.42	776.78	154.45	19.86
F14	1	-1	1	1	715.62	85.35	46.52	233.42	776.78	167.72	18.64
F15	-1	1	1	1	665.45	193.96	43.25	233.42	776.78	152.28	23.47
F16	1	1	1	1	715.62	85.35	46.52	233.42	776.78	165.68	22.03
CC1	-2	0	0	0	639.26	375.27	28.77	155.61	851.96	144.79	25.04
CC2	2	0	0	0	739.65	177.48	33.28	155.61	851.96	171.23	22.81
CC3	0	-2	0	0	690.90	273.54	31.09	155.61	851.96	160.78	19.91
CC4	0	2	0	0	690.90	273.54	31.09	155.61	851.96	156.00	27.87
CC5	0	0	-2	0	690.90	273.54	31.09	0.00	1002.30	158.39	23.89
CC6	0	0	2	0	690.90	273.54	31.09	311.22	701.61	158.39	23.89
CC7	0	0	0	-2	690.90	542.86	3.45	155.61	851.96	154.91	29.69
CC8	0	0	0	2	690.90	4.22	58.73	155.61	851.96	161.87	18.09
				Minimum	639.26	4.22	3.45	0.00	701.61	144.79	18.09
				Maximum	739.65	542.86	58.73	311.22	1002.30	171.23	29.87

step (1), to allow the ECat water absorption. After mixing, all specimens were cast in one lift without any mechanical vibration due to the self-compacting ability of the mixtures. The specimens were then covered with a plastic sheet and demoulded after 1 day. Thereafter, the samples were maintained in water, at 20 ± 2 °C, until the age of testing.

The aftermost UHPFRC mixtures preparation followed the same mixing procedure – except the fibres incorporation during two min before the end of the mixing process – and conditions of specimens preparation.

3.2.4 Test methods

3.2.4.1 Workability and setting time

Immediately after mixing, the slump-flow diameter was measured using a mini-cone according to EFNARC recommendations. Due to the high content of very fine materials and very low water/binder ratio, UHPC mixtures typically exhibit high viscosity, with low risk of segregation, for this reason, no additional test was carried out to characterize the fresh state. The final setting times were determined in accordance with standard EN 196-3.

3.2.4.2 Autogenous shrinkage

Two samples of each mixture were cast in corrugated plastic tubes and stored at a constant temperature, 20 ± 2 °C, and $RH = 50 \pm 2\%$, immediately after casting. Although the experimental plan was set to have all mixtures with the self-compacting ability in the fresh state, a slight vibration was applied during casting, to guarantee the complete filling of the corrugated tubes. Autogenous shrinkage was measured following the procedure described in the American standard ASTM C1698. Shrinkage measurements were continuously recorded (each minute) using linear variable differential transformers (LVDTs) and a data Taker DT500 acquisition system. The final setting time, previously determined, was considered as "time-zero" for the autogenous shrinkage evaluation [47]. In all mixtures, the autogenous deformation of two tested samples had a similar trend with a deviation of less than 58 $\mu m\,m^{-1}$. Since the variation in temperature of the thin samples during hydration is small and almost the same among the different mixtures, the effect of the thermal dilatation to the value of autogenous shrinkage was not considered. Smoeck et al. [48] carried out similar tests and monitored the internal temperature over time both on specimens placed in

a polyakylene-glycol termobath at 20 °C and on specimens placed in a chamber with controlled temperature (20±2 °C). The maximum temperature increase in specimens placed in the termobath was only 0.6 °C, while for specimens placed in the chamber a temperature peak of 3.5 °C was registered. Nevertheless, this additional peak of 3.5 °C had little influence on the overall results, corresponding to an error approximately 1%, lower than the measuring error of the test.

3.2.4.3 Resistivity and compressive strength

Cubic specimens (50 mm^3) were produced to assess the electrical resistivity and compressive strength. As mentioned before, specimens were kept under water in a chamber under controlled temperature (20±2 °C) and removed just for a few minutes to perform the resistivity test at predefined ages: 7, 14, 21 and 28 days.

The two-electrode method was used to determine the resistivity of the specimens under alternating current (AC). AC measurements are generally preferred since the use of direct current (DC) may induce polarisation of the electrodes [47]. Plain mortar with high moisture contents was found to be frequency-independent for the 1Hz–100 kHz frequency range [49]. The resistivity was measured with two stainless steel plates pressed to opposing (mould) surfaces via wetted cloth. A signal generator applied a sinusoidal current of 100 Hz frequency, and the resistivity (ρ) was computed as follows:

$$\rho = \frac{V.A}{L.I} \tag{3.2}$$

where V is the potential difference (V); I is the current intensity (A); L is the distance between electrodes (m); and A is the area of the electrode in contact with the mortar sample (m^2). At each age three specimens were tested and the corresponding average was taken as the test result.

At the age of 28 days, subsequently to the resistivity measurements, the compressive strength was evaluated according to ASTM C109/C109M. Three samples from each mixture were tested.

3.2.4.4 Uniaxial tensile test

The uniaxial tensile test (UTT) was only performed in UHPFRC mixtures using dog bone-shaped specimens with tested section length of 92 mm and cross section of 30×40 m^2, after 28 curing days in a controlled environment room (20±2 °C and $HR >$

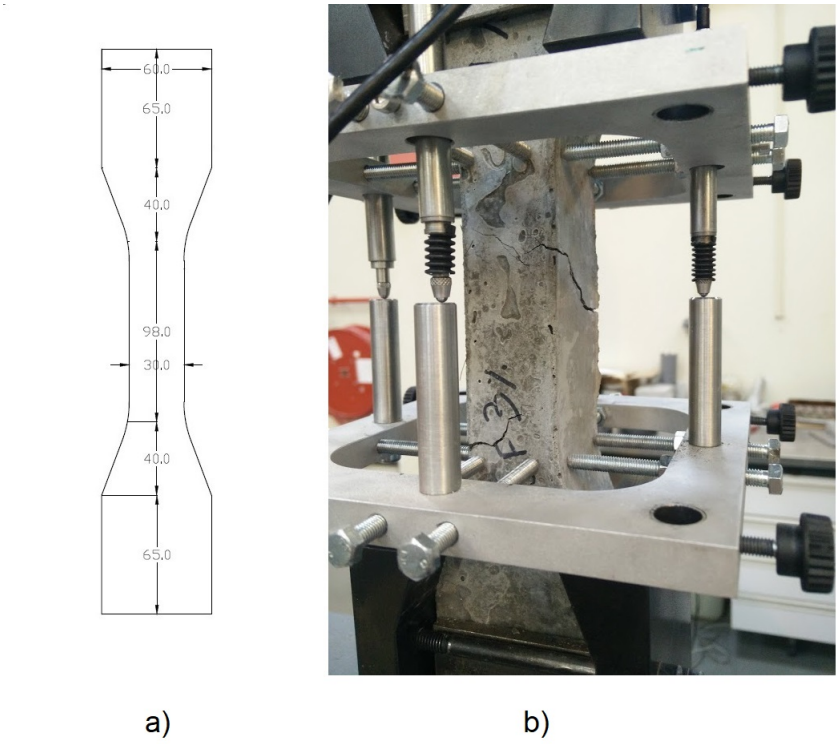

FIGURE 3.4: Uniaxial tensile test setup: a) Specimens geometry [unites mm] and b) LVDTs arrangement.

95%). Six specimens were tested at a displacement rate of 0.003 mm s^{-1} applied by an Instron testing machine with a 300 kN capacity load cell. The displacement rate was kept constant until the end of the test. The elongation of the specimens was measured using four LVDT's system coupled along the tested section length of the specimen (see Figure 3.4).

3.3 Results

3.3.1 Test results

3.3.1.1 Workability and setting time

Table 3.4 (second and third columns) presents the results of slump flow diameter (Dflow) and final setting time (tf) for all the mixtures included in the experimental plan. Regarding the fresh state behaviour, all mixtures exhibited self-compacting ability, with slump flow diameters ranging from 229 to 350 mm. The final setting times ranged from 1.42 to 3.75 h. An extensive range of setting time results for UHPC can be found in the literature [1], [50] since it varies significantly with the type

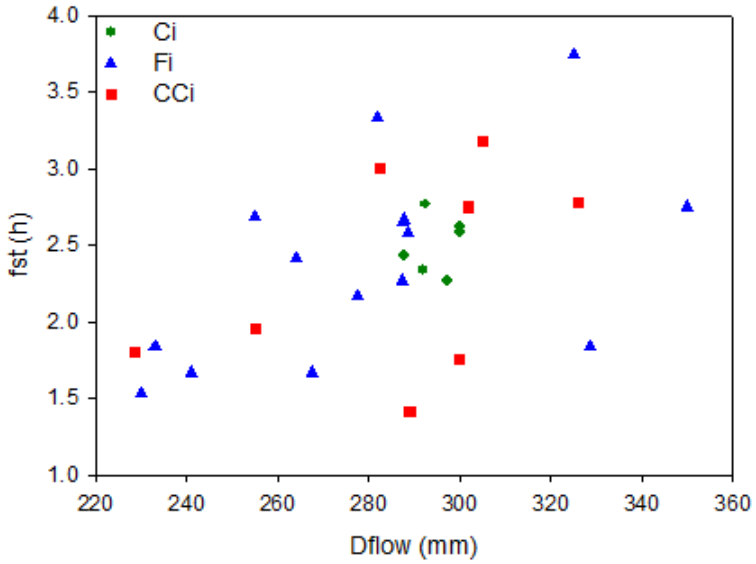

FIGURE 3.5: Slump flow diameter and final setting time results of mixtures included in 3.3.

and amount of superplasticizer and type of cementitious materials used. A general tendency of longer final setting times with increasing flowability was observed in the current study as depicted in Figure 3.5.

3.3.1.2 Autogenous shrinkage

Figure 3.6 shows the autogenous shrinkage evolution of all mixtures up to 20 h (after final setting time). Even though a wide range of deformations was found (494 to 1011 $\mu m\,m^{-1}$), the evolution over time presents a similar trend. During the first hours from the final setting, autogenous shrinkage exhibited a strong increase, after which a dramatic reduction in the slope of the curves was observed. Wang et al. [19] also reported the autogenous shrinkage of plain UHPC increases fast in the early stage, and almost keep stable after 24 h, reaching 1175 $\mu m\,m^{-1}$ at 7 days. Nevertheless, it is worth pointing that results of autogenous shrinkage depend on the method used to define "time–zero", as highlighted by Huang and Ye [50]. Results of autogenous shrinkage deformation at 20 h (a_shr_20h) after the final setting time were used in modelling and are presented in the fourth column of Table 3.4.

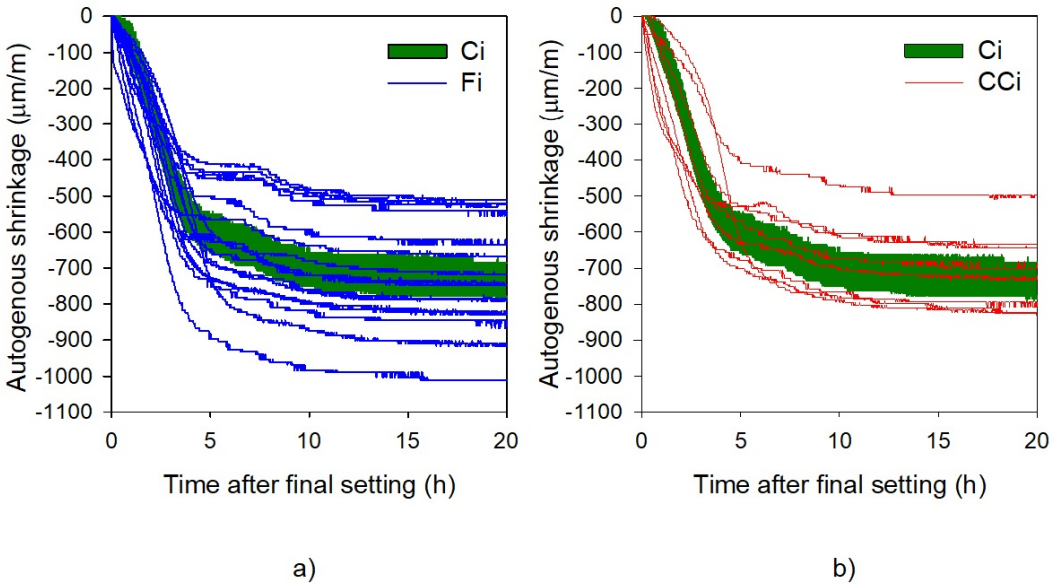

FIGURE 3.6: Autogenous shrinkage evolution of mixtures included in Table 3.3: a) mixtures Fi and b) mixtures CCi, and range of results obtained with Ci mixtures.

3.3.1.3 Electric resistivity

Figure 3.7 presents the electrical resistivity development up to 28 days. As expected, the electrical resistivity of tested mixtures increased with age due to continued hydration, leading to finer pore network with less connectivity. Resistivity results at 28 days ranged from 147 to 474 Ω m, which indicates a very compact matrix. As a reference, after 10 years a dense-aggregate concrete incorporating $> 5\%$ silica fume, submerged at 20 °C, is expected to exhibit a resistivity from 300 to 1000 Ω m [47]. Mix CC5 (without incorporation of ECat) exhibited the highest gain in resistivity achieving 121, 192 and 474 Ω m after 7, 14 and 28 days, respectively. Figure 3.7 also suggests that resistivity of all mixtures will continue to increase further beyond the 28 days. The 5th column in Table 3.4 includes the resistivity at 28 days data, which was used for modelling.

3.3.1.4 Compressive strength

The last column of Table 3.4 lists the 28 day compressive strength (Rc_28d) test results. The compressive strength of tested mixtures achieved a minimum of 103 MPa and a maximum of 143 MPa at 28 days, without any special curing treatment. Due to the absence of fibres a brittle failure was observed, which is responsible for a higher scatter in the compressive strength results of each mixture. Moreover, the

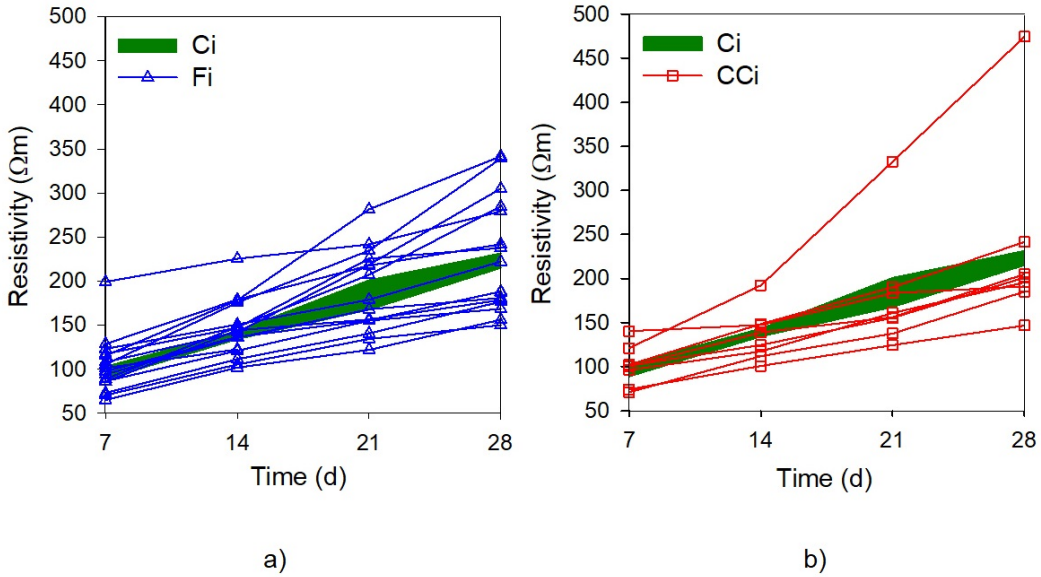

FIGURE 3.7: Electrical resistivity evolution over time for mixtures included in Table 3.3: a) mixtures Fi and b) mixtures CCi, and range of results obtained with Ci mixtures.

summary of descriptive statistics in Table 3.5 reveals that both the average and the coefficient of variation of compressive strength results found for central mixtures and for all the mixtures are very close, which can be a consequence of the constant w/c ratio and relatively small range of variation of reactive materials other than cement (SF and ECat). This indicates it will not be possible to find a good fit for the Rc_28d response model, as confirmed in the next section. Contrarily, for all the other response variables the coefficient of variation evaluated on the central points is significantly smaller than the coefficient of variation evaluated on the 30 mixtures, thus good fitting models could be expected.

3.3.2 Fitted models

The procedure to find an appropriate model establishing relationships between mix design variables and the responses involves two main steps:

- Fitting a second-order polynomial model using regression analysis and ANOVA, including the removal of non-significant terms in the model ($p - value > 0.05$).
- Model adequacy checking by examining the residuals, looking for trends and/or outliers.

A detailed description of this procedure can be found in a previous publication by the author [40] (Chapter 2) or in specialised bibliography [38].

TABLE 3.4: Test results for all mixtures included in the CCD experimental plan.

Ref.	Dflow (mm)	tf (h)	a_shr_20h ($\mu m\,m^{-1}$)	ρ_28 d ($\Omega\,m$)	Rc_28d (MPa)
C1	292.5	2.8	725.1	231.2	107.4
C2	288.0	2.4	777.2	247.2	127.5
C3	292.0	2.3	685.1	225.5	133.4
C4	297.5	2.3	708.9	206.2	118.3
C5	300.0	2.6	718.8	229.2	123.4
C6	300.0	2.6	674.1	215.1	125.2
F1	233.0	1.8	747.9	241.7	124.4
F2	288.5	2.6	791.3	221.9	116.1
F3	255.0	2.7	716.5	279.2	114.8
F4	282.0	3.3	709.1	237.5	114.0
F5	230.0	1.5	523.3	175.0	113.4
F6	287.5	2.3	555.5	168.5	116.1
F7	241.0	1.7	519.9	188.1	110.6
F8	264.0	2.4	512.1	178.6	115.1
F9	287.8	2.7	818.9	339.2	132.1
F10	350.0	2.8	1011.2	305.0	143.1
F11	287.5	2.7	829.2	341.8	135.0
F12	325.0	3.8	844.7	284.7	124.7
F13	267.5	1.7	667.2	176.5	118.0
F14	328.5	1.8	746.8	150.0	123.5
F15	277.5	2.2	609.0	187.4	107.9
F16	302.0	2.8	708.6	156.2	119.9
CC1	255.0	2.0	719.7	246.2	102.9
CC2	326.0	2.8	823.9	195.6	140.3
CC3	300.0	1.8	701.8	201.1	106.6
CC4	282.5	3.0	712.4	204.8	110.0
CC5	305.0	3.2	825.9	474.2	129.3
CC6	289.0	1.4	645.0	146.7	112.6
CC7	228.5	1.8	497.5	191.0	111.2
CC8	310.0	2.7	794.0	185.1	126.1

TABLE 3.5: Descriptive statistics of the results for all 30 mixtures as well as only for the 6 central mixtures.

	Dflow (mm)	tf (h)	a_shr_20h ($\mu m\,m^{-1}$)	ρ_28d ($\Omega\,m$)	Rc_28d (MPa)
All 30 mixtures					
Mean	285.8	2.4	710.7	227.7	120.1
Minimum	228.5	1.4	497.5	146.7	102.9
Maximum	350.0	3.8	1011.2	474.3	143.1
Std deviation	29.5	0.6	114.5	68.8	10.2
Coef. Var (%)	10.3	23.3	16.1	30.2	8.5
6 central mixtures					
Mean	295.0	2.5	714.9	225.7	122.5
Minimum	288.0	2.3	674.1	206.2	107.4
Maximum	300.0	2.8	777.2	247.2	133.4
Std deviation	4.9	0.2	36.3	1.1	8.9
Coef. Var (%)	1.7	7.6	5.1	6.3	7.3

Table 3.6 summarises the fitted models with the design variables expressed in coded values, along with the residual error standard deviation and the correlation coefficients. An inverse transformation was applied to ρ_28d response data in order to stabilise the response variance and improve the resulting model [38]. ANOVA showed that these models are significant when describing the effect of Vw/Vp, Sp/p, VECat/Vs and sf/c on the modelled responses. From the results of R^2/Adj-R^2 in Table 3.6, it can be concluded that the obtained regression models explain a large proportion of the variability of the analysed properties, except in the case of Rc_28d response ($Adj - R^2 = 47\%$), because of the reasons pointed before in section 3.3.1.4.

3.3.2.1 Main individual and interaction effects

The models presented in Table 3.6 reflect the relative significance of each term on the response variables.

The Dflow of UHPC was mainly influenced by the sf/c and Vw/Vp. The positive influence of sf/c on the flowability may be attributed to the increased packing density due to the inclusion of extremely small spherical silica fume particles [51]. For a given water content, when packing density increases more free water is available in the system which leads to improved flowability. An increase of Vw/Vp corresponds to an increase in the water content, thus a thicker water layer is formed around

TABLE 3.6: Empirical fitted models (design variables in coded values).

Model terms	Dflow (mm)	tf (h)	a_Shr_20h ($\mu m\,m^{-1}$)	$1/(\rho\_28d)$ ($\Omega\,m$)	Rc_28d (MPa)
Independent	291.24	2.407	726.78	4.45E-03	122.50
Vw/Vp	**20.42**	**0.27**	**27.33**	**2.75E-04**	**3.08**
Sp/p	-3.08	**0.283**	NS	-8.96E-05	-1.57
VECat/Vs	-5.95	**-0.395**	**-82.84**	**1.12E-03**	**-4.72**
sf/c	**21.16**	0.152	**73.04**	-8.07E-05	**4.56**
(Vw/Vp)×(Sp/p)	**-7.76**	NS	NS	NS	NS
(VECat/Vs) ×(sf/c)	NS	NS	NS	**3.29E-04**	NS
$(Sp/p)^2$	NS	NS	NS	1.04E-04	-3.04
$(sf/c)^2$	-6.86	NS	-20.12	2.02E-04	NS
Error term					
Mean	0.00	-0.01	0.00	0.01	0.00
Std. Dev.	1.04	1.02	1.04	1.03	1.00
R^2	96.0%	87.5%	84.8%	96.6%	56.1%
Adj-R^2	94.9%	85.5%	82.3%	95.5%	47.0%

the solid particles which explains the larger slump flow diameter [51]. The slightly negative effect of VECat/Vs on flowability might be attributed to the not fully water saturation of ECat particles reached during the initial time (5 min) of the UHPC mixture procedure.

The final setting time of UHPC was mainly influenced by VECat/Vs, Sp/p and Vw/Vp. As expected, an increase of water content or superplasticizer dosage, particularly for relatively high dosages, retards the final setting [28], [40]. Also, previous studies revealed that ECat incorporation in cement-based materials led to shorten the setting time due to its highly porous micro-structure that provides a large specific surface area (150 070 $m^2\,kg^{-1}$) for the ECat under study, with high water absorption ability (30%, section 3.2.1) [52], [34].

Autogenous shrinkage had a major influence of sf/c. As reported in previous studies [13], autogenous shrinkage increases with increasing SF content, which causes a significant drop in the internal RH in the cement paste during the hardening leading to the occurrence of self-desiccation in the absence of an external source of water. An opposing significant effect was found for VECat/Vs, which proves a remarkable beneficial effect to mitigate autogenous shrinkage of UHPC. This effect is attributed to the absorbed water in the porous ECat particles that can be released during the first day of hydration to compensate the drop of RH in UHPC. This result supports the

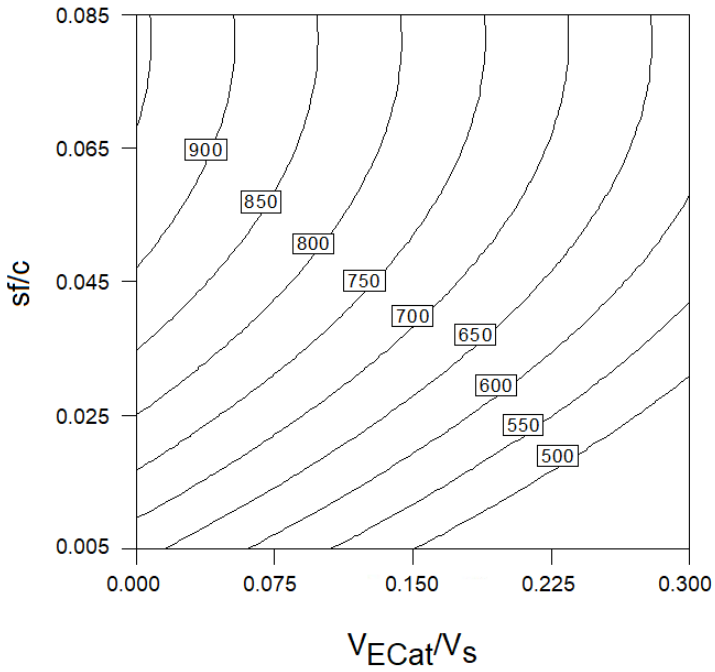

FIGURE 3.8: Contour plot of autogenous shrinkage $\mu m\, m^{-1}$ ($Sp/p = 2.40\%$ and $Vw/Vp = 0.395$).

idea that ECat can act as an internal curing agent to mitigate the high autogenous shrinkage of UHPC. The above mentioned opposite effects of sf/c and VECat/Vs on autogenous shrinkage can be observed in Figure 3.8 (Sp/p and Vw/Vp set fixed at 2.40% and 0.395, respectively).

Both, resistivity and compressive strength properties at 28 days are negatively affected by the ECat incorporation as sand partial surrogate, and positively affected by sf/c. This effect of ECat incorporation on these properties was the opposite of the anticipated given the high pozzolanic activity of ECat that promote the formation of additional hydration products and, thus, the refinement of capillary porosity and the decrease of the porous interconnectivity in the cement matrix. The increasing of resistivity and compressive strength with ECat incorporation was found in previous studies [26], [28], [29]. However, in the present study, UHPC mixtures incorporated two very highly reactive pozzolanic materials, SF and ECat, both simultaneously competing for the calcium hydroxide that presumably is not enough to complete both reactions. As such, a negative synergistic effect might had occurred that lead to the decrease on the resistivity and compressive strength, at 28 days, as the ECat content increased.

The interaction effect ($\frac{VECat}{Vsand} \times \frac{sf}{c}$) was also found to be significant to explain the resistivity at 28 days, which is graphically represented in Figure 3.9. This figure

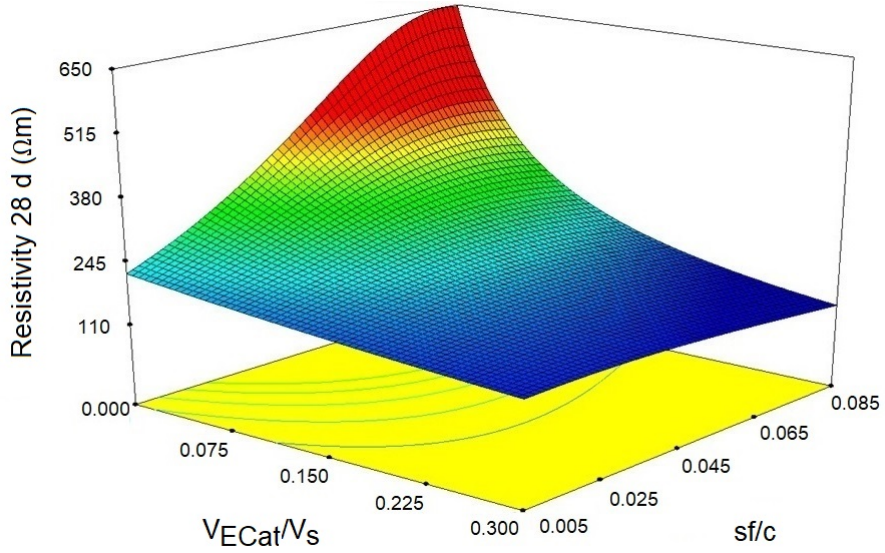

FIGURE 3.9: Interaction effect of VECat/Vs and sf/c on resistivity at 28 days (Sp/p=2.40% and Vw/Vp=0.395).

shows that the decrease in resistivity with an increase of VECat/Vs is stronger for higher values of sf/c. Table 3.6 also shows that the resistivity at 28 days decreases with an increase of Vw/Vp, since by increasing the water content the total porosity and pores connectivity increase, thus lowering the resistivity.

3.3.2.2 Mixtures optimisation

The optimisation of UHPC mixtures was performed using the response surface of the models presented in Table 3.6 as the basis for finding the best solution. Numerical optimisation was performed based on the desirability function approach available in the commercial software (Design-Expert) [45].

Table 3.7 shows the four different optimisation scenarios implemented and the corresponding UPHC mixtures composition. In brief, in scenarios A and B the main objective is to minimise autogenous shrinkage; in scenario C the main objective is to maximise resistivity as an indicator of material durability; and finally, scenario D aimed to obtain the best solution possible in order to simultaneously minimise shrinkage and maximise resistivity (both constraints having equal importance). After finding a candidate solution for the optimisation problem, attention must also be paid to the distance to the centre of the CCD plan (d), computed as indicated in the last line of Table 3.7. The distance to the centre of the CCD plan should not exceed 2 by far (region of the original data), because the fitted models may no longer predict in a reasonable way outside of the CCD region. In general, the design

variables (coded values) were always set to be in the range of [-2, +2], except when the final optimised solution was very far from the centre of the experimental plan, as was the case of Mixture A (optimal solution Scenario A) for which $d = 3.35$. To avoid this situation the range of design variables Vw/Vp, Sp/p and VECat/Vs was limited in some cases as shown in Table 3.7. Concerning the response variables, the reasoning behind the selected constraints (Table 3.7) was the following:

- For all scenarios, the target minimum slump flow diameter of UHPC was 300 mm, considering that after fibres incorporation (3% content) some deformability loss can be expected [53].
- In scenarios A, B and D autogenous shrinkage was minimised aiming to reduce the early-ages cracking risk.
- In scenarios C and D resistivity was maximised looking for to improve the resistance against the penetration of liquid or gas substances.

Since the observed variation in the compressive strength for all the tested mixtures was not very significant (8.5%), and close to the experimental error (7.3%), it was not possible to distinguish the mixtures regarding the compressive strength. Thus, no constraint was added related to this response variable.

Table 3.7 presents the optimum solutions (in terms of coded values). As could be expected from the discussion in the previous section, scenario A led to a mixture with the highest VECat/Vs the lowest sf/c. In contrast to scenario C led to VECat/Vs low and relatively high sf/c. In turn, the mixture resulting from scenario D represents the best compromise between low autogenous shrinkage, at early ages, and high resistivity at 28 days. Concerning the distances to the centre of the experimental plan of mixtures A to D, one can note that $d_A > d_B > d_C > d_D$ with d_A and d_B being higher than 2.5.

3.3.2.3 Optimised mixtures validation

In order to validate the numerical models obtained (Table 3.6), the optimised mixtures (A to D) and an additional central mixture (C7) were prepared in the laboratory and tested following the procedures described in sections 3.2.3 Mixing procedure and specimens preparation, 3.2.4 Test methods. Table 3.8 shows both the experimental (measured) and predicted results. Uncertainty in the fitted models is provided for a 95% confidence interval. The ratio between the predicted-to-measured values in general range from 0.8 to 1.11, which confirms the accuracy of the obtained models. The exceptions are Mixtures A and B, corresponding to the highest distances to the

TABLE 3.7: Optimisation criteria and optimum solutions (design variables in coded values).

	Scenario A	Scenario B	Scenario C	Scenario D
Optimisation constraints:				
X1: Vw/Vp	In range*	In range [-1.50; 1.50]	In range*	In range *
X2: Sp/p	In range *	In range [-1.50; 1.50]	In range*	In range*
X3: VECat/Vs	In range *	In range [-1.63;1.51]	In range*	In range [-1.60;1.25]
X4: sf/c	In range*	In range*	In range *	In range *
Y1: Dflow (mm)	In range [300;350]	Maximise	In range [300;350]	In range [300;350]
Y2: tf (h)	None	None	None	None
Y3: Aut_Shr ($\mu m\, m^{-1}$)	Minimise	Minimise	None	Minimise
Y4: ρ_28d ($\Omega\, m$)	None	None	Maximise	Maximise
Optimum solution:	Mixture A	Mixture B	Mixture C	Mixture D
X1: Vw/Vp	1.80	1.50	-0.65	-0.05
X2: Sp/p	-1.70	-1.50	-0.16	-2.00
X3: VECat/Vs	1.76	1.51	-2.00	0.00
X4: sf/c	-1.40	0.00	1.40	0.20
$d = \sqrt{\sum_{i=1}^{4}[X_i^2]}$	3.35	2.60	2.52	2.00

Notes: (*) range of variables was set at $[-2.0; 2.0]$, in terms of coded values; importance was set equal for all constraints plan.

centre of the CCD plan, which confirms the adequacy of the limit of 2.5 for d, in these type of CCD experimental plans. The experimental compressive strength results of UHPC optimised mixtures, assessed at 90 days, are presented in Table 3.8. In this case, no comparison with the predicted values can be established since it was not possible to model the Rc_28d response variable (as discussed in Section 3.3.2).

Considering the main goal of the current work of mitigating UHPC autogenous shrinkage, it is worth pointing that mixture D exhibited an autogenous shrinkage about 32% lower than the highest result found in the experimental plan of 1011 $\mu m\,m^{-1}$ (corresponding to mixture F10, see Table 3.4), due to the significant amount of water absorbed by ECat. VECat/Vs in mixture D is zero, expressed in coded values, i.e., 0.15 in actual values, corresponding to about 155 $kg\,m^{-3}$ of ECat and theoretically to about 46.6 $l\,m^{-3}$ of total absorbed water by the ECat (Section 3.2.1). This is within the range of extra water absorbed for internal curing of UHPC by other materials such as, SAP (33–56 $l\,m^{-3}$) [17] and LWS (11–63 $l\,m^{-3}$) [15] and is higher than the total water absorbed by 220 $kg\,m^{-3}$ of RHA (about 18.9 $l\,m^{-3}$) [9].

TABLE 3.8: Experimental and predicted engineering properties of optimum mixtures.

		Mixture A	Mixture B	Mixture C	Mixture D	C7
Dflow (mm)	measured	270	312	312	312	300
	predicted	**303**	**335**	**306**	**300**	**291**
	prediction interval	[283; 323]	[317; 353]	[290; 322]	[284; 314]	[277;305]
	predicted/measured	1.12	1.07	0.98	0.96	0.97
tf (h)	measured	1.48	1.87	3.19	2.33	2.33
	predicted	**1.50**	**1.81**	**3.18**	**1.86**	**2.4**
	prediction interval	[0.99; 2.06]	[1.31; 2.31]	[2.69; 3.69]	[1.37; 2.34]	[1.95; 2.85]
	predicted/measured	1.01	0.97	1.00	0.80	1.03
a_shr ($\mu m\,m^{-1}$)	Measured	649	753	953	689	699
	predicted value	**488**	**642**	**938**	**739**	**727**
	Prediction interval	[370; 606]	[532; 753]	[820; 1052]	[637; 841]	[625; 829]
	Predicted/measured	0.75	0.85	0.98	1.07	1.04
ρ_28d ($\Omega\,m$)	Measured	241.6	214	642	221	251
	Predicted	**141**	**144**	**710**	**199**	**225**
	Prediction interval	[128; 157]	[139; 158]	[480; 1363]	[177; 227]	[201; 254]
	Predicted/measured	0.58	0.67	1.11	0.90	0.90
Rc_90d	Measured	108.24 ± 5.28	132.36 ± 0.35	130.80 ± 2.82	135.80 ± 2.17	

3.4 Performance of fibre reinforced composite

UHPC exhibits a distinctly brittle failure under tension but provided it is reinforced with sufficiently high fibre content, using short high-strength steel fibres, the tensile strength of UHPC can be improved and ensured [14]. That UHPFRC can be applied in thin layers to protect/strengthen existing structures, without any further reinforcement [36]. The fibre orientation has a large influence on the tensile response of UHPFRC, most notably in the development of the hardening stage, and fibre content as high as 3% is often necessary to achieve a strain hardening behaviour in tension with a random fibre distribution [14].

The optimised UHPC mixture D was selected for further investigation of its performance as UHPFRC. For this purpose, 3% of micro steel fibres were incorporated in the UHPC mixture by replacing an equivalent volume of aggregates (fine sand plus ECat, maintaining ratio) (see Table 3.9) and tested regarding its flowability, autogenous shrinkage evolution, mechanical performance, cost and environmental impact/eco-efficiency.

3.4.1 Flowability

UHPFRC mixture presented in Table 3.9 exhibited a slump flow diameter of 282.5 mm, without application of compaction energy and revealed no fibre agglomeration (Figure 3.10). As such, the Dflow of the UHPFRC mixture prepared from the optimised UHPC mixture D with the incorporation of 3% fibres showed a Dflow of 9.4% smaller than that of mixture D (Table 3.7). This is in agreement with the findings of Marchão et al. [53], which concluded that the addition of fibres with a fibre factor, $\chi = \frac{Vf \times lf}{df}$, in between 1 and 2, like in the current study with $\chi = 1.95$ ($Vf = 3\%$ and $lf/df = 65$), results only in a slight and linear decrease of Dflow with increase of χ, without fibre agglomeration.

3.4.2 Autogenous shrinkage evolution

Figure 3.11 shows the effect of adding 3% steel micro fibres on autogenous shrinkage development of the UPHC mixture D. Since, steel microfibers partially replaced 3% of aggregates (85% sand and 15% ECat) there was no significant reduction in hydration activity (except for the reactions involving ECat), which is responsible for autogenous shrinkage. Thus, the observed reduction in autogenous shrinkage deformations is probably mainly due to the locally shrinkage-restraining effect of fibres [54]. As

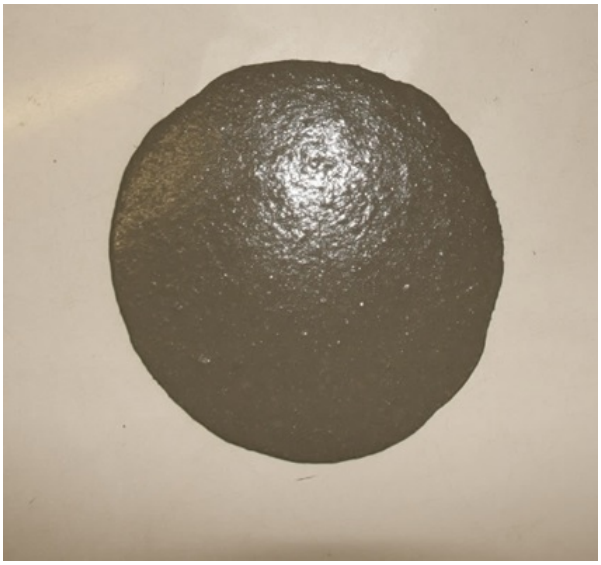

FIGURE 3.10: Final spread area of UHPFRC without fibre agglomeration.

the matrix shrinks, shear stresses develop along steel fibres, leading to compressive stresses in the microfibers and tensile stresses in the cementitious matrix [54]. The shrinkage-restraining effect of fibres is dependent on the elastic modulus of the fibres and matrix, and the fibres content and its aspect ratio [54].

3.4.3 Mechanical performance

Figure 3.12-a shows the compression results of the UHPFRC mixture undertaken on cubic specimens (50 mm), at the ages of 2, 7, 28 and 90 days. The experimental results are plotted against the theoretical values computed as proposed by Graybeal using the following equation [55] for untreated UHPFRC.

$$fc(t) = fc'\Big[1 - exp\Big(-\Big(\frac{t-0.9}{3}\Big)\Big)\Big] \tag{3.3}$$

where fc' is the 28 days compressive strength of untreated UHPFRC (147 MPa in the current study) and t is the age (days). In general, a satisfactory level of consistency is observed between the theoretical values and the experimental results. The biggest difference is observed at the initial stage of the curve, namely at 2 days when the compressive strength is 34% higher than the predicted value using Equation 3.3. UHPFRC specimens reached after 2 days casting 53% of the compressive strength at 90 days. This was followed by a less pronounced rate of compressive strength development in the subsequent days namely, being respectively at 7 days and 28 days after casting, 76% and 94% of the ultimate compressive strength.

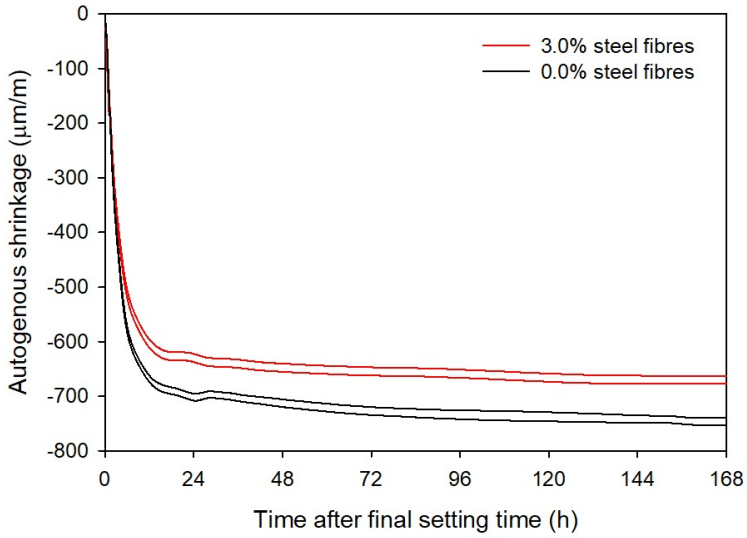

FIGURE 3.11: Autogenous shrinkage evolution of mixture D with and without steel fibres.

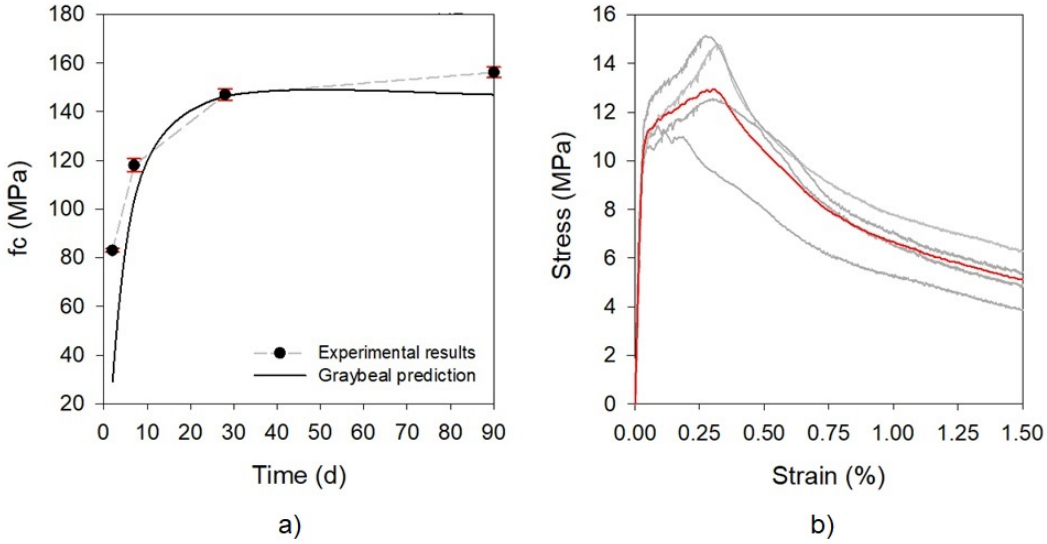

FIGURE 3.12: Mechanical properties of UHPFRC (mixture D + 3.0% steel fibres incorporation in volume): a) Compressive strength evolution up to 90 days; b) Uni-axial tensile stress-strain curves at 28 days (grey individual results and red average result).

3.4.4 Economic and environmental costs

Table 3.9 (3rd column) shows the cost influence of each material on the final product using reference prices for the Portuguese market. While limestone filler, ECat and aggregate insignificantly influence the total costs, the costs of fibre reinforcement represent about 3/4 the cost of UHPFRC. After the steel fibres, cement and silica fume represent the major proportion of the total cost. It is worth pointing that the total cost of the proposed UHPFRC mixture, of 572 €m^{-3}, is significantly lower than the price of commercial premixes currently marketed in Europe, higher than 1000 €m^{-3}, not including the cost of fibres, aggregates, superplasticizer and water. Thus, the use of non-proprietary UHPC mixtures, like the one shown here, can represent an important competitive advantage for the construction sector.

The embedded CO_2 emission of UHPFRC mixture was evaluated focusing on the amount of materials required for 1 m^3 to demonstrate its eco-efficiency. Reference values of levels of embodied carbon dioxide in the concrete raw materials provided in Refs. [56], [57], [58] were used, as indicated in Table 3.9. Embodied CO_2 of ECat was considered null since according to the standard ISO 14044 the allocation of environmental impacts of a recycling material is avoided when there is no changes of its inherent properties and it is used as a surrogate of a primary material. This is the case in the present study because ECat is being directly used in the UHPFRC composition with no additional processing step and representing a reduced demand of a natural resource, the sand. The results for the estimation of the embedded CO_2 emission of 1 m^3 UHPFRC are presented in Table 3.9, along with the contribution of each material to the total value. CO_2 emission of proposed UHPFRC is mainly due to the manufacture of micro steel fibres (50.1%) and cement production (45.9%). Yu et al. [59], using data points from several different UHPCs from literature, found a trend line between the compressive strength and the embodied CO_2 emissions (computed from the embodied CO_2 values for each component of concrete). The straight line that represents this trend as well as the corresponding equation are illustrated in Figure 3.13. Mixture D developed in the current study is below the trend line, which means that the designed UHPC has a lower environmental impact than other typical UHPC mixtures, being close to the eco-friendly UHPCs proposed by Yu et al. [59]. EUHPC-LP, EUHPC-FA and EUHPC–GGBS refer to different UHPC eco-mixes incorporating limestone powder, fly ash and ground granulated blast-furnace slag as cement replacement, respectively [59].

TABLE 3.9: Mixture design of fibre reinforced UHPC using selected mixture D, estimated cost and Global Warming Potential (GWP).

Raw Materials	Quantity kg m^{-3}	Cost €/m^3	GWP kg CO_2-eq/kg	GWP kg CO_2-eq/m^3
Cement	690.2	62.1 (11%)	0.8330 [56]	574.93 (45.9%)
Silica fume	33.6	38.6 (7%)	0.7900 [57]	26.51 (2.1%)
Limestone filler	250.6	7.5 (1%)	0.0712 [58]	4.31 (0.3%)
ECat	155.5	4.7* (1%)	0 [60]	0
Sand	775.0	11.6 (2%)	0.0011 [58]	0.82 (0.1%)
Superplasticizer	19.5	24.4 (4%)	0.9440 [58]	18.40 (1.5%)
Steel fibres	235.0	423 (74%)	2.6700 [56]	627.45 (50.1%)
Water	160.9	–	–	–
	Total:	572		1252

Notes: *Estimated cost (assumed equal to fly ash cost); between parentheses is presented the weight (percentage) of each component in the total value .

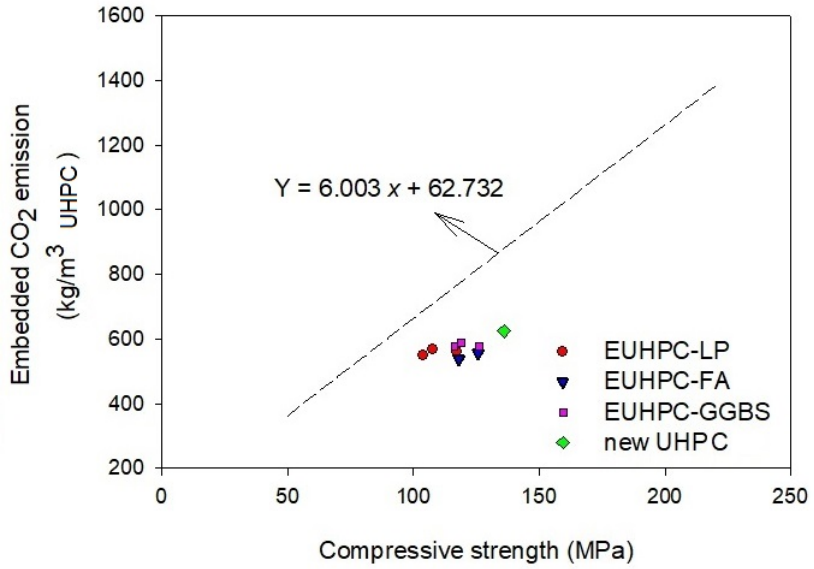

FIGURE 3.13: Comparison of embedded CO_2 emission of the new UHPC developed (Mixture D) and other eco-friendly UHPCs (adapted from [61]).

3.5 Conclusions

The current study revealed that spent equilibrium catalyst, a waste generated from oil refinery industry, can be turned into a value-added by–product when used as an internal curing agent to produce UHPFRC. Its use is not expected to affect the robustness of UHPFRC production since ECat is very well consistent regarding particle size distribution as well as physical and chemical composition among successive refinery deliveries.

Based on the mathematical empirical models derived from the DOE implementation, the following relationships between mix design variables and UHPC properties were established:

- UHPC flowability
  - Both sf/c and Vw/Vp have a significant positive influence on UHPC flowability.
  - The incorporation of ECat, as sand partial surrogate, besides extra water for ECat absorption, had only a slight negative effect on UHPC flowability.
- UHPC final setting time
  - As expected, an increase of Vw/Vp or sp/p, particularly for relatively high superplasticizer dosages as is the case in this study, retards the final setting time.
  - Replacement of sand with the ECat with huge specific surface area with water absorption ability led to a significant decrease in the final setting time.
- UHPC autogenous shrinkage
  - An increase of sf/c was found to significantly increase autogenous shrinkage. An opposing significant effect was found for VECat/Vs, which proves its beneficial effect to mitigate autogenous shrinkage of UHPC attributed to the absorbed water in the porous ECat particles.
- UHPC resistivity and compressive strength
  - A negative effect of ECat incorporation was found on both UHPC resistivity and compressive strength at 28 days while sf/c exhibited a significant positive effect on both these properties.

- An interaction effect ($\frac{VECat}{Vs} \times \frac{sf}{c}$) was also found to be significant to explain the resistivity at 28 days. The decrease in resistivity with an increase of VECat/Vs is stronger for higher values of sf/c.
- As expected, the resistivity at 28 days decreases with an increase of Vw/Vp.

The optimal UHPC mixture that represents the best compromise between low autogenous shrinkage, at early ages, and high resistivity at 28 days, while guaranteeing sufficient deformability and compressive strength was found for: $Vw/Vp = 0.394$; $Sp/p = 2.0\%$; $VECat/Vs = 0.15$; $sf/c = 0.049$ (and $w/c = 0.25$, $Vs/Vm = 0.39$). This optimal UHPC mixture contains 155 $\mathrm{kg\,m^{-3}}$ of ECat that corresponds to 46.6 $\mathrm{l\,m^{-3}}$ of extra water required to saturate the ECat. This value is within the range of extra water absorbed for internal curing of UHPC by other materials which use as internal curing agents is already consolidate such as, SAP (33–56 $\mathrm{l\,m^{-3}}$) [17] and LWS (11–63 $\mathrm{l\,m^{-3}}$) [15] and is higher than the total water absorbed by 220 $\mathrm{kg\,m^{-3}}$ of RHA (about 18.9 $\mathrm{l\,m^{-3}}$) [9].

The optimal UHPC mixture resulted in a reduction of about 32% in autogenous shrinkage measured 20 h after final setting, compared to the mixture with the highest result of autogenous shrinkage in the experimental plan (1011 $\mathrm{\mu m\,m^{-1}}$). The reduction of autogenous shrinkage is expected to result in proportionally lower self-induced stresses in the presence of external restraint, which might avoid cracking and/or allow for a reduction of fibre content in UHPFRC. Other properties influencing the development of self-induced stresses are the Young's modulus evolution and the tensile creep at early age, which however has not been investigated in the present study.

The UHPFRC mixture prepared combining the optimal UHPC mixture with 3% high-strength steel fibres ($lf/df = 65$):

- exhibited a compressive strength of 147 and 156 MPa after 28 and 90 days of water curing, respectively.
- exhibited a uni-axial tensile peak stress and peak strain ranging from 11 to 15 MPa and 0.27–0.47%, respectively, at 28 days.
- proved to be more eco-efficient and more cost efficient than typical UHPCs reported in the literature.

References

[1] Zachary B Haber, Igor De la Varga, and Benjamin A Graybeal. Properties and Behavior of UHPC-Class Materials (FHWA-HRT-18-036). Technical Report February, Federal Highway Administration, McLean, VA, 2018.

[2] Caijun Shi, Zemei Wu, Jianfan Xiao, Dehui Wang, Zhengyu Huang, and Zhi Fang. A review on ultra high performance concrete: Part I. Raw materials and mixture design. *Construction and Building Materials*, 101:741–751, 2015.

[3] Ekkehard Fehling, Michael Schmidt, Joost Walraven, Torsten Leutbecher, and Susanne Frohlich. *Ultra-High Performance Concrete UHPC: Fundamentals, Design, Examples*. Ernst & Sohn, Wiley, Berlin, Germany, 2014.

[4] Sabbie A. Miller. Supplementary cementitious materials to mitigate greenhouse gas emissions from concrete: can there be too much of a good thing? *Journal of Cleaner Production*, 178:587–598, 2018.

[5] R Yu, P Spiesz, and H J H Brouwers. Mix design and properties assessment of Ultra-High Performance Fibre Reinforced Concrete (UHPFRC). *Cement and Concrete Research*, 56:29–39, 2014.

[6] Sabbie A. Miller, Vanderley M. John, Sergio A. Pacca, and Arpad Horvath. Carbon dioxide reduction potential in the global cement industry by 2050. *Cement and Concrete Research*, (August):1–10, 2017.

[7] Tomasz Wierzbicki. Assessment and rehabilitation of central European highway structures - ARCHES Executive Summary Report iv. Technical report, FEHRL, Brussels, Belgium, 2010.

[8] Wei Huang, Hadi Kazemi-Kamyab, Wei Sun, and Karen Scrivener. Effect of cement substitution by limestone on the hydration and microstructural development of ultra-high performance concrete (UHPC). *Cement and Concrete Composites*, 77:86–101, 3 2017.

[9] Nguyen Van Tuan. *Rice husk ash as a mineral admixture for ultra high performance concrete*. PhD thesis, Technische Universiteit Delft, 2011.

[10] Ahmed Tafraoui, Gilles Escadeillas, and Thierry Vidal. Durability of the Ultra High Performances Concrete containing metakaolin. *Construction and Building Materials*, 112:980–987, 2016.

[11] N.A. Soliman and A. Tagnit-Hamou. Partial substitution of silica fume with fine glass powder in UHPC: Filling the micro gap. *Construction and Building Materials*, 139:374–383, 5 2017.

[12] Ana Mafalda Matos, Sandra Nunes, and Carla Costa. Mitigation of early age shrinkage of UHPFRC by using spent equilibrium catalyst. In *International RILEM Conference Materials, Systems and Structures in Civil Engineering 2016 Segment on Service Life of Cement-Based Materials and Structures*, Lyngby, Denmark, 2016.

[13] O. Mejlhede Jensen and P. Freiesleben Hansen. Autogenous deformation and change of the relative humidity in silica fume-modified cement paste. *ACI Materials Journal*, 93(6):539–543, 1996.

[14] Amin Abrishambaf, Mário Pimentel, and Sandra Nunes. Influence of fibre orientation on the tensile behaviour of ultra-high performance fibre reinforced cementitious composites. *Cement and Concrete Research*, 97:28–40, 7 2017.

[15] Weina Meng and Kamal Khayat. Effects of saturated lightweight sand content on key characteristics of ultra-high-performance concrete. *Cement and Concrete Research*, 101(February):46–54, 2017.

[16] Viktor Mechtcherine and Hans-Wolf Reinhardt, editors. *Application of Superabsorbent Polymers (SAP) in Concrete Construction. State of the Art Report Prepared by Technical Committee 225-SAP*. Springer, 2012.

[17] L. Dudziak and V. Mechtcherine. Reducing the cracking potential of ultra-high performance concrete by using Super Absorbent Polymers (SAP), 2010.

[18] J. Justs, M. Wyrzykowski, D. Bajare, and P. Lura. Internal curing by superabsorbent polymers in ultra-high performance concrete. *Cement and Concrete Research*, 76:82–90, 2015.

[19] Xinpeng Wang, Rui Yu, Zhonghe Shui, Qiulei Song, and Zhihao Zhang. Mix design and characteristics evaluation of an eco-friendly Ultra-High Performance Concrete incorporating recycled coral based materials. *Journal of Cleaner Production*, 165:70–80, 2017.

[20] M.A.A. Aldahdooh, N. Muhamad Bunnori, and M.A. Megat Johari. Influence of palm oil fuel ash on ultimate flexural and uniaxial tensile strength of green ultra-high performance fiber reinforced cementitious composites. *Materials & Design (1980-2015)*, 54:694–701, 2 2014.

[21] Viet Thien An Van, Christiane Rößler, Danh Dai Bui, and Horst Michael Ludwig. Rice husk ash as both pozzolanic admixture and internal curing agent in ultra-high performance concrete. *Cement and Concrete Composites*, 53:270–278, 2014.

[22] Eelco T.C. Vogt and Bert M. Weckhuysen. Fluid catalytic cracking: recent developments on the grand old lady of zeolite catalysis. *Chemical Society Reviews*, 44(20):7342–7370, 2015.

[23] Reza Sadeghbeigi. *Fluid Catalytic Cracking Handbook - An Expert Guide to the Practical Operation, Design, and Optimization of FCC Units*. Butterworth-Heinemann, United States, third edit edition, 2012.

[24] N T Castellanos and J T Agredo. Using spent fluid catalytic cracking (FCC) catalyst as pozzolanic addition - a review. *Ingenieria E Investigacion*, 30(2):35–42, 2010.

[25] Francesco Ferella, Valentina Innocenzi, and Fabio Maggiore. Oil refining spent catalysts: A review of possible recycling technologies. *Resources, Conservation and Recycling*, 108:10–20, 3 2016.

[26] J Payá, J Monzó, M V Borrachero, and S Velázquez. Cement equivalence factor evaluations for fluid catalytic cracking catalyst residue. *Cement & Concrete Composites*, 39:12–17, 2013.

[27] J. Payá, J. Monzó, M. V. Borrachero, and S. Velázquez. Evaluation of the pozzolanic activity of fluid catalytic cracking catalyst residue (FC3R). Thermogravimetric analysis studies on FC3R-Portland cement pastes. *Cement and Concrete Research*, 33(4):603–609, 2003.

[28] Ali Allahverdi, Shokoufeh Vakilinia, and Pooneh Gharabeglu. Effects of RFCC spent catalyst on some physicomechanical properties of portland cement paste. *Ceramics – Silikáty*, 55(2):161–168, 2011.

[29] Sandra Nunes and Carla Costa. Numerical optimization of self-compacting mortar mixture containing spent equilibrium catalyst from oil refinery. *Journal of Cleaner Production*, 158:109–121, 8 2017.

[30] Khalifa Al-Jabri, Mahad Baawain, Ramzi Taha, Zahran Saif Al-Kamyani, Khalid Al-Shamsi, and Aysser Ishtieh. Potential use of FCC spent catalyst as partial replacement of cement or sand in cement mortars. *Construction and Building Materials*, 39:77–81, 2013.

[31] Nan Su, Zong-Huei Chen, and Hung-Yuan Fang. Reuse of spent catalyst as fine aggregate in cement mortar. *Cement and Concrete Composites*, 23:111–118, 2001.

[32] R. Neves, C. Vicente, A. Castela, and M.F. Montemor. Durability performance of concrete incorporating spent fluid cracking catalyst. *Cement and Concrete Composites*, 55:308–314, 1 2015.

[33] Carla Costa, M Sofia Ribeiro, and Nuno Brito. Effect of Waste Oil-Cracking Catalyst Incorporation on Durability of Mortars. *Materials Sciences and Applications*, 5(November):905–914, 2014.

[34] Carla Costa and Paulo Marques. Low-Carbon Cement with Waste Oil-Cracking Catalyst Incorporation, 2012.

[35] Esteban Camacho Torregrosa. *Dosage optimization and bolted connections for UHPFRC ties*. PhD thesis, Universitat Politècnica de València, 2013.

[36] Eugen Brühwiler and Emmanuel Denarié. Rehabilitation of concrete structures using Ultra-High Performance Fibre Reinforced Concrete. In *UHPC-2008: The Second International Symposium on Ultra High Performance Concrete*, number 1, pages 1–8, Kassel, Germany, 2008.

[37] LNEC. E-64. Cements. Determination of density [In Portuguese]., 1979.

[38] Douglas C Montgomery. *Design and Analysis of Experiments*, volume 2. John Wiley & Sons, Inc., Hoboken, 8 edition, 2012.

[39] K. H. Khayat, A. Ghezal, and M. S. Hadriche. Utility of statistical models in proportioning self-consolidating concrete. *Materials and Structures*, 33(5):338–344, 2000.

[40] Ana Mafalda Matos, Lino Maia, Sandra Nunes, and Paula Milheiro-Oliveira. Design of self-compacting high-performance concrete: Study of mortar phase. *Construction and Building Materials*, 167:617–630, 4 2018.

[41] F Bayramov, C Taşdemir, and M.A Taşdemir. Optimisation of steel fibre reinforced concretes by means of statistical response surface method. *Cement and Concrete Composites*, 26(6):665–675, 2004.

[42] M.A.A. Aldahdooh, N. Muhamad Bunnori, and M.A. Megat Johari. Evaluation of ultra-high-performance-fiber reinforced concrete binder content using the response surface method. *Materials & Design*, 52:957–965, 2013.

[43] Iman Ferdosian and Aires Camões. Eco-efficient ultra-high performance concrete development by means of response surface methodology. *Cement and Concrete Composites*, 84:146–156, 11 2017.

[44] Mohammad Ali Mosaberpanah and Ozgur Eren. CO2 full factorial optimization of an ultra-high performance concrete mix design. *European Journal of Environmental and Civil Engineering*, 22(2):450–463, 2018.

[45] State-Ease Corporation. Design-expert software.

[46] Vagelis G. Papadakis. Experimental investigation and theoretical modeling of silica fume activity in concrete. *Cement and Concrete Research*, 29(1):79–86, 1999.

[47] Rob B Polder. Test methods for on site measurement of resistivity of concrete — a RILEM TC-154 technical recommendation. *Construction and Building Materials*, 15(2-3):125–131, 3 2001.

[48] D. Snoeck, O.M. Jensen, and N. De Belie. The influence of superabsorbent polymers on the autogenous shrinkage properties of cement pastes with supplementary cementitious materials. *Cement and Concrete Research*, 74:59–67, 8 2015.

[49] Carlos G. Berrocal, Karla Hornbostel, Mette R. Geiker, Ingemar Löfgren, Karin Lundgren, and Dimitrios G. Bekas. Electrical resistivity measurements in steel fibre reinforced cementitious materials. *Cement and Concrete Composites*, 89:216–229, 2018.

[50] Hao Huang and Guang Ye. Examining the "time-zero" of autogenous shrinkage in high/ultra-high performance cement pastes. *Cement and Concrete Research*, 97:107–114, 2017.

[51] Rui Zhong, Kay Wille, and Roberto Viegas. Material efficiency in the design of UHPC paste from a life cycle point of view. *Construction and Building Materials*, 160:505–513, 1 2018.

[52] A. Allahverdi, S. Vakilinia, and P. Gharabeglu. Effects of RFCC spent catalyst on some physiomechanical properties of Portland cement. *Ceramics-Silikáty*, 55(2):161–168, 2011.

[53] Carla A Marchão, Sandra B Nunes, Válter G Lúcio, Ana A Bras, and Joaquim A Figueiras. Development and application of a high performance fiber reinforced self-compacting concrete in post-tensioning anchorage zones. In *8th RILEM*

International Symposium on Fibre Reinforced Concrete: challenges and opportunities (BEFIB 2012), pages 457 – 469, 2012.

[54] V.Y. Garas. *Multi-scale investigation of tensile creep of ultra-high performance concrete for bridge applications*. PhD thesis, Georgia Institute of Technology, 2009.

[55] Doo-Yeol Yoo and Nemkumar Banthia. Mechanical properties of ultra-high-performance fiber-reinforced concrete: A review. *Cement and Concrete Composites*, 73:267–280, 2016.

[56] T. Stengel and P. Schießl. Life cycle assessment (LCA) of ultra high performance concrete (UHPC) structures. In *Eco-efficient Construction and Building Materials*, pages 528–564. Elsevier, 2014.

[57] Md. Uzzal Hossain, Chi Sun Poon, Ya Hong Dong, and Dongxing Xuan. Evaluation of environmental impact distribution methods for supplementary cementitious materials. *Renewable and Sustainable Energy Reviews*, 82:597–608, 2 2018.

[58] Harald S Müller, Michael Haist, and Michael Vogel. Assessment of the sustainability potential of concrete and concrete structures considering their environmental impact, performance and lifetime. 2014.

[59] R. Yu, P. Spiesz, and H.J.H. Brouwers. Development of an eco-friendly Ultra-High Performance Concrete (UHPC) with efficient cement and mineral admixtures uses. *Cement and Concrete Composites*, 55:383–394, 2015.

[60] ISO 14044:2006. Environmental management. Life cycle assessment. Requirements and guidelines., 2006.

[61] R. Yu. *Development of sustainable protective ultra-high performance fibre reinforced concrete (UHPFRC) : design, assessment and modeling*. PhD thesis, Eindhoven University of Technology, 2015.

4 Durability of new UHPC

The main goal of the current Chapter is to investigate several critical durability aspects of a non-proprietary UHPC incorporating a waste generated by the oil refinery industry (ECat), as an internal curing agent. To better support the analysis of the experimental results, this Chapter also reports on a comprehensive state of the art review on the durability of UHPC/UHPFRC's (published between 1996 and 2019) including both commercial and non-proprietary mixtures. Both direct and indirect transport properties measurements – MIP, water-permeable porosity, capillary water absorption, electrical resistivity and chloride migration – as well as the carbonation assessment and the dimensional resilience to potential deleterious reactions between alkali/silica and sulphates, revealed that the new UHPC possesses an excellent durability performance, typical of these materials. These results combined with its self-compatibility, low autogenous shrinkage and high compressive strength confirm the belief of the role of this new UHPC towards a high-tech-low-cost and eco-friendly construction.

4.1 Introduction

The key principles for designing Ultra-High Performance Fibre Reinforced Composites (UHPFRC) are the reduction in porosity, improvement in micro-structure, enhancement of the homogeneity and increase in toughness. The raw materials (nature and content), including the fibres content as well as the curing regimes, are the main factors that determine both the outstanding mechanical and durability performances of UHPFRC [1]. The binder materials of UHPFRC include a high proportion of cement (mean content is roughly 750 $\mathrm{kg\,m^{-3}}$ [1]) and reactive powder materials, like silica fume (SF), granulated blast furnace slag (GGBFS), fly ash (FA), metakaolin (MTCK), rice husk ash (RHA) (average amount of 200 $\mathrm{kg\,m^{-3}}$ [1]). If all reactive components are included, the binder content is about 800-1000 $\mathrm{kg\,m^{-3}}$ [2]. Non-reactive powder, as limestone filler (LF) or quartz flour (QF) are usually included in an average content around 169 $\mathrm{kg\,m^{-3}}$ [1]. The water/binder ratio (w/b) is often below 0.20. Consequently, a high content of superplasticizer on polycarboxylate

ether basis is necessary which is, on average, 30 $kg\,m^{-3}$ [1]. Fibres used in UHPFRC are typically short high-strength steel fibres, which allow incorporating a significant volume of fibres (Vf) (fibre contents ranging from 2 to 4% in volume). Besides, the use of special curing treatments, such as heat treatment, autoclave or steam curing and pressure, accelerates the UHPFRCs' hydration process and increases their density also contributing to the ultra-high compressive strengths. Considering the high cost of some constituent materials and the complexity of curing processes, the use of conventional materials (including, agricultural and other industrial residues), as well as, common technology, such as conventional casting and room temperature curing has been preferred by several authors in order to facilitate the production and applications of UHPFRC [3], [4], [5], [6], [7].

Most current applications of UHPFRC in new structures are factory prefabricated and on-site assembled, usually slender and lightweight elements for pedestrian footbridges and highway bridges, as well as architecturally appealing structures [8]. On-site fabrication of UHPFRC is mainly limited to rehabilitation and strengthening purposes. The main advantage of UHPFRC in this context is that it can play a double function (water tightness and strengthening) while enabling short-time interventions [9]. Although some applications around the world of UHPFRC already exists [8–13], it still faces some challenges for broader implementation. Within this context, a research programme initiated by the author (Chapter 3 and [14]) aiming to address some of those challenges, namely:

- To develop a rational and accurate method for the mixture design of the UHPC and its optimisation targeting engineering properties (based on Design of Experiments Approach)
- To use locally available supplementary cementitious materials (SCM), including industrial residues, to reduce the cement and SF dosages, and consequently the cost of UHPC, without impairing its strength (ensuring a minimum compressive strength of 150 MPa after regular curing regime)
- To mitigate autogenous shrinkage of UHPC, in order to minimise early ages cracking risk (which might impair its durability), particularly for the case of rehabilitation/strengthening applications where the deformations are restrained.

Following these purposes, the author optimised a new non-proprietary UHPC mixture incorporating the spent equilibrium catalyst (ECat) which is a by-product generated by the Portuguese oil refinery industry. New UHPC corresponded to the best compromise between low autogenous shrinkage at early ages and high electrical resistivity, without impairing self-compatibility and compressive strength [14] (Chapter 3). The

current Chapter focuses on the durability performance of this new non-proprietary UHPC developed [14] (Chapter 3). As such, a series of durability tests experimental results (Section 4.4) were compared with results reported in the literature for both other non-proprietary and commercially available UHPC materials. To achieve this objective, Section 4.2 presents a literature review, focusing on the critical properties for the long-term performance of UHPC and the influence of various material/curing parameters on the durability performance of UHPC. Section 4.3 reports the procedures used on the durability tests performed on the new UHPC to assess its porosity, water absorption by capillarity, electrical resistivity, chloride ions penetrability and expansive reactions susceptibility.

4.2 Literature review on durability of UHPC

4.2.1 Initial considerations

During the last two decades, the academics and industry around the world have conducted a considerable number of research projects for developing UHPFRC. The great majority of these projects were carried out in Japan, France, Switzerland, Germany, Denmark and USA. Some of these projects gave rise to commercial UHPC mixtures, available as premixes. More recently, non-proprietary mixtures emerged in order to achieve more eco-friendly and cost-effective solutions. The utilisation of by-products such as FA [15], [16], bottom ash [3], sugarcane bagasse ash [4], glass powder [5], [6], RHA [7], [17], GGBFS [18], [19], as partial surrogates of cement, SF or fine aggregate leads to a significant reduction in carbon dioxide (CO_2) emissions per ton of UHPC [20]. In addition, the introduction of coarse aggregate it was also set as a strategy to produce an environmental friendly UHPC [21].

A number of laboratory tests including the assessment of porosity, water absorption by capillarity, electrical resistivity, chloride penetration resistance, carbonation resistance and expansive reactions (alkali-aggregate reaction and external sulphate attack) generally estimates the UHPCs' durability performance. To understand the influence of various material parameters and curing regimes on the durability performance of UHPC, a review of key studies found in literature is presented in the next sections. The selected case studies for analysis, in the current work, describe results of researches in which UHPC/UHPFRC mixtures were produced in the laboratory, published between 1996 and 2019, including both proprietary and non-proprietary mixes.

4.2.2 Porosity

The aggressive agents in the cement matrices can undergo various transport mechanisms, namely, permeability, diffusion, migration and convection. In all cases, it is the pore size distribution (PSD) and its degree of continuity that most significantly affect the transport properties of the cement matrix. A typical PSD for hydrated cement matrices encompasses a broad range of pore sizes, from about nanometres to centimetres in diameter. Since a standard classification of the pores size for cement-based materials has not been established yet, some differences are found in literature concerning the nomenclature and the corresponding range of pores size [22]. Zhang et al. [23] proposed the following classification into four levels based on pore diameter (d): gel pores ($d < 0.01$µm), medium capillary pores (0.01µm $< d < 0.1$µm), large capillary pores (0.1µm $< d < 1$µm) and air voids ($d > 1$µm), which is adopted in the current work.

4.2.2.1 Mercury intrusion porosimetry

Mercury intrusion porosimetry (MIP) is one of the most widely used methods to characterise the pore structure of hydrated UHPC/UHPFRC [22]. Non-wetting mercury is forced into the porous material at incremental pressures, and at each step, the intruded volume is measured. It allows the pore size analysis to be undertaken over a wide range of pores sizes, from about 0.003 to 400 µm [22]. The data obtained from MIP can be converted into a pore size distribution curve [24] that may present several peaks. These peaks represent the pore diameters corresponding to the higher rate of mercury intrusion per change in pressure called “critical pore diameters”. In cement pastes, the first peak that arises for higher diameters is generally considered as corresponding to the capillary porosity (ranging from 0.01 µm to 10 µm) whereas the second peak corresponds to the gel pores (ranging from 0.001 µm to 0.01 µm) [24].

Owing to the very low w/b ratio (about 0.20) as well as to the large range of fine constituent materials that leads to a high packing density, the UHPC has almost no capillary pores, comprising typically gel pores, i.e., located within the CSH (Calcium silicates hydrate) layers smaller than 0.004 µm, [25]. Figure 4.1 presents examples of typical pore size distributions of an ordinary concrete (OC) (C35), a high-performance concrete (HPC) (C105) and UHPCs (C200 and C500).

The porosity is dependent on several factors, such as w/b ratio; binder composition namely, cement type and SCM including nano-materials; curing regime and age.

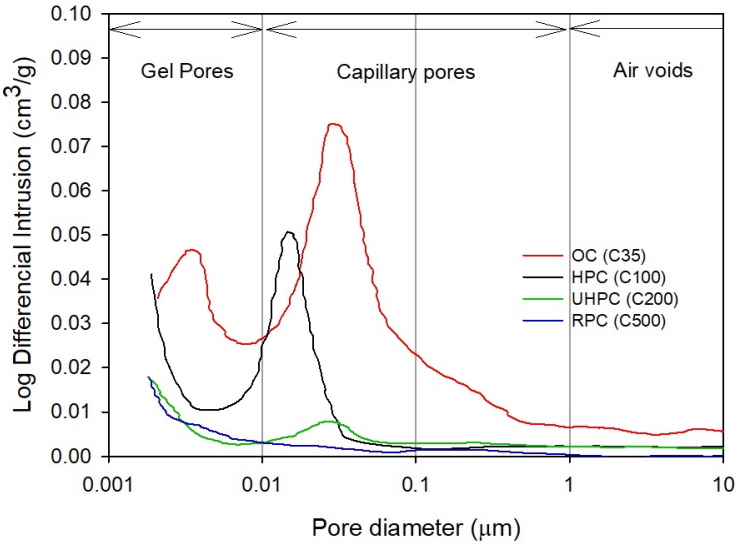

FIGURE 4.1: Pore size distribution differential curve of UHPCs (C200 and C500), HPC (C105) and OC (C35), adapted from [26] and classification of pores from [24].

Table 4.1 to Table 4.4 summarise some MIP results on UHPCs found in literature considering the factors mentioned above. Main conclusions are presented below.

w/b and binder composition The high compressive strength of UHPCs reported in Table 4.1 to Table 4.4 (100-279 MPa) are mainly due to its very low w/b ratio (0.13-0.24). Another factor contributing to the high strength is grading optimisation and combination of various ultra-fine particles (< 125 µm) in order to improve the packing density. In the initial studies on UHPCs, their binder composition often consisted of cement and SF. More recently, many researchers started to use other SCM as partial surrogates of either cement or SF (Table 4.1 to Table 4.4) in order to achieve certain technical, economic and ecological goals, which also has an impact on the UHPC micro-structure.

Pyoa and Kim [3] (line 7, Table 4.2) assessed the applicability of various industrial by-products such as coal bottom ash, FA, normal blast furnace slag (BFS) and fine BFS in UHPC by partially replacing cement, SF ($d_{50} = 0.3$µm) and silica powder ($d_{50} = 3.92$µm). They concluded that only a slight difference in total porosity (tending to be larger) was observed by adopting these various types of industrial by-products [3]. However, Chen et al. [16] (line 15, Table 4.4) showed that the total porosity decreases with the increase of FA content as a cement partial surrogate for UHPCs after exposure to 8 h of autoclave curing with pressure of 1.0 MPa. Abdulkareem et al. [27] (line 13, Table 4.4) showed that in UHPCs with 30% of

BFS as a partial cement surrogate, the BFS particles acted as heterogeneous nucleation sites accelerating the cement hydration reactions thus increasing the amount of CSH formed, and consequently decreasing the total porosity of UHPC. For higher BFS contents, the cement dilution effect prevailed over the heterogeneous nucleation decreasing the amount of hydrated products including portlandite, and thus the pozzolanic ability, making the UHPC microstructure more porous and decreasing the compressive strength. The use of both chemical activation (adding KOH) and thermal activation (at 90°C for two days) was found effective to boost the hydration reaction of blended UHPC with a high BFS content [27].

Huang et al. [28] (line 9, Table 4.3) studied two grades of MTCK (calcined kaolinite) to replace SF completely: a commercial MTCK with 95% kaolinite (from Burgess) produced by flash calcination; and a MTCK (from India) with 79% kaolinite obtained by calcination at 800°C for 60 minutes. Up to 3 days, the UHPC mixtures with MTCK tend to have higher porosities than the reference mixture with SF. However, as the hydration progressed, both the porosities and critical pore radius decreased faster for the mixtures with the MTCK than the reference mixture with SF, indicating that the refinement of pore structure by the calcined clays was more efficient than that of SF.

Tuan [29] (line 4, Table 4.1) assessed the effect of an agricultural waste, namely, RHA, on the hydration process and the microstructure formation of UHPC. It was found that the partial weight replacement of 20% of cement by both SF and RHA leads to the pore structure refinement and reduces total porosity of cement paste. The effect of RHA on the pore refinement of cement paste did not increase significantly with the mean particle size of RHA less than 5.6 µm. Furthermore, RHA can act as an internal curing agent, being able to mitigate autogenous shrinkage of UHPC, and further promoting the progress of cement hydration [29].

Huang et al. [30] (line 12, Table 4.3) showed LF, despite not presenting pozzolanic activity, can be another partial substitute for cement and SF in UHPC. As expected, as the hydration takes place, the mixture with LF undergoes significantly different pore structure development compared to the standard matrix including cement and SF as the binder. In fact, since the demand for superplasticizer was lower in the mixture with LF, the hydration started earlier, and at one day there were more hydration products formed, filling the space, and leading to fewer pores volume. Another difference is that the magnitude of the critical pore radius continues to decrease up to 28 days reaching around 0.004-0.005 µm. At long term, the values of the critical pore radius and total porosity were reasonably similar to the reference mixture [30].

Results in Table 4.1 to Table 4.4 also show that the incorporation of nano-particles to UHPC composition can also lead to significant reductions of the total porosity. Ghafari et al. [31] (line 6, Table 4.2) showed that the incorporation of nano-silica (NS) particles as partial cement replacement into UHPC led to a decrease in total porosity compared to the control mixture without NS (from 6.4% to 4.3%, respectively). The content of capillary pores reduced from 2.65% to 1.72%, which attributed to the increased formation of CSH. Wu et al. [32] (line 11, Table 4.3) investigated the effect of nano-$CaCO_3$ as a partial cement replacement on the microstructure development of UHPC. Test results indicated that the incorporation up to 3.2% nano-$CaCO_3$ reduced the total porosity of UHPC from 15.2% to 12%, attributed to both its filler effect in the pores and its chemical reaction with tricalcium aluminate (C_3A) to form hemi-and/or mono-carboaluminate. However, for nano-$CaCO_3$ content beyond 3.2% the porosity increased due to the nano-$CaCO_3$ particles agglomeration [32]. Meng and Khayat [15] (line 10, Table 4.3) found that the inclusion of carbon nanofibers (CNF) to the binder phase in UHPC originated refinement of the pore structure. As the CNF content was increased from 0 to 0.3% by mass of binder, the total porosity was reduced by 35% (from 13% to 8%); the gel pores increased by 68% while the pores between 0.01 µm-5 µm reduced by 76% [15].

In brief, the effect of the use of SCM material (either by-products or agricultural wastes) and LF as both cement and SF surrogates on the porosity of UHPC depend on different factors namely, the SCM chemical-mineralogical composition, particles size distribution and content as well as on hydration time of the UHPC. The research studies revealed that the proper UHPC mixture design allows the incorporation of other additions besides SF without impairing its MIP porosity.

Curing regime and age Results in Table 4.1 to Table 4.4 clearly show that the curing temperature also plays a significant role in the pore structure of UHPC. Heinz and Ludwig [33] (line 1, Table 4.1) measured the total, and capillary porosity for UHPC treated at various temperatures and concluded that heat-treatment leads to a reduction of the total and capillary porosity. A heat-treatment above 90°C enables the reduction of porosity to values around 4.2% and 2.9% , which is significantly lower compared to the porosity of specimens cured at 20°C (8.2%) [33]. This effect was corroborated by Scheydt and Muller [34] (line 5, Table 4.1) that found that heat treatment (90°C) significantly densifies the matrices just after three days.

Besides the curing temperature (T), the duration of heat treatment (Δt) and the delay time between casting of samples and the initiation of heat treatment (ti) are important factors in thermal curing (Figure 4.2). Cwirzen [35] (line 3, Table 4.1)

investigated the influence of the heat treatment regime on the micro-structure of UHPC subjected to various curing regimes at 90°C (Δt equal to 24, 48 and 96 h and ti equal to 24, 48 and 168 h were tested). The lowest porosity values, independently of the duration of heat treatment, were obtained for the specimens cured for 48 h with a delay between the casting and the initiation of heat treatment of 2 days. Furthermore, in this case increasing Δt resulted in a considerably lower porosity [35].

Chen et al [16] (line 15, Table 4.4) investigated the influence of different autoclave curing conditions on the microstructure of UHPC containing SF and different dosages of FA. The porosity decreases from 6.28% to 4.03% with the increase of FA content from 10% to 30%, for UHPCs after exposure to 8 h of autoclave curing with pressure of 1.0 MPa. Under the same autoclave pressure of 1.0 MPa, as the curing duration increased from 6 h to 10 h the porosity decreased from 4.95% to 3.38% [16].

Another important factor contributing to the porosity refinement is the curing time. Under normal curing conditions (fog room, at 20°C), Tuan [29] (line 4, Table 4.1) found the total porosity at 90 days was 43% to 62% lower than the total porosity at one day, depending on the binder composition. Studies of Huang et al. [30] (lines 9 and 12, Table 4.3) also show a significant reduction of total porosity with increasing curing time, under normal curing conditions.

The MIP total porosity results reported in Table 4.1 to Table 4.4 range from 2.0% to 18.0%. It should also be stressed that part of the variation found in MIP results reported in literature is probably due to differences in the procedures used for samples preparation, measurement conditions and/or data analysis.

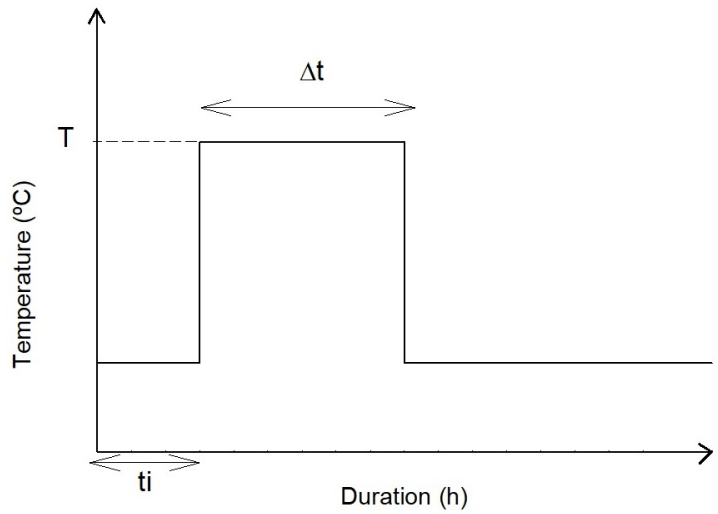

FIGURE 4.2: Main parameters to define the thermal curing procedure of UHPCs, adapted from [35].

Table 4.1: Systematisation of MIP results of UHPC/UHPFRCs obtained in different studies - Part 1.

	Ref.	Binder	w/b	Curing	fc,28d (MPa)	Total porosity (%)
1	[33]	CEM I	0.22	20°C and RH 93%	189	8.2
				65°C and RH 93%	198	5.3
				90°C and RH 93%	215	4.2
				105°C and RH 93%	231	4.0
				120°C and RH 93%	234	3.5
				180°C and RH 93%	279	2.9
2	[36]	CEM I 52.5R +SF +QF	0.24	Water cured	162/213	6.0
			0.17	50 N/mm^2 compression stress 4 hours+20°C and RH=65% 2 days+250°C 7 days	487	2.0
3	[35]	CEM I 42.5N +SF +QF	0.17	20°C for 28 days		5.8
				until 28 days ti=24 h/48 h/168 h sealed curing + T=90 °C for Δt=24 h + 20 °C and RH=95%		1.3/0.45/1.35
				ti=24 h/48 h/168 h sealed curing + T=90 °C for Δt=48 h + 20 °C and RH 95% until 28 days		1.13/1.09/0.95
				ti=24 h/48h/168h sealed curing + T=90 °C for Δt=96 h + 20°C and RH=95% until 28 days		0.92/0.54/0.85
4	[29]	CEM I 52.5N	0.18	1/7/28/90 days Fog room and RH>95%	165	11.15/8.13/ 7.5/6.95
		CEM I 52.5N+SF			165	9.18/6.49/ 4.55/3.98
		CEM I 52.5N+RHA			170	10.32/7.63/ 5.76/4.92
5	[34]	CEM I 52.5R +SF+QF	0.21	Water curing 20°C 28 days		8.9
				90 °C 3 days		5.4

Table 4.2: Systematisation of MIP results of UHPC/UHPFRCs obtained in different studies - Part 2.

	Ref.	Binder	w/b	Curing	fc,28d (MPa)	Total porosity (%)
6	[31]	CEM I 52.5 R+SF	0.16	Water immersion 20 °C	132	6.5
		CEM I 52.5 R+SF+1% NS			137	4.74
		CEM I 52.5 R+SF+2% NS			137	4.66
		CEM I 52.5 R+SF+3% NS			144	4.30
		CEM I 52.5 R+SF+4% NS			140	4.80
7	[3]	CEM I+SF+silica powder	0.22 (w/c)	28/90 days wet chamber 24 °C and RH=100%	154	3.0/2.0
		CEM IV+SF+silica powder			158	1.1/1.8
		CEM I+SF+bottom ash			145	3.6/2.2
		CEM I+SF+fine BFS+bottom ash			151	4.8/3.2
		CEM I+SF+BSF+ bottom ash			145	4.0/2.4
		CEM I+ SF+FA			152	4.0/2.6
8	[37]	CEM I 52.5N+SF+QF	0.19	20°C and HR>95% 56 days	150	7
		CEM I 52.5N+SF+QF+5% granulated copper slag			120	6.5
		CEM I 52.5N+SF+QF+10% granulated copper slag			130	6.8
		CEM I 52.5N+SF+QF+15% granulated copper slag			105	6.2
		CEM I 52.5N+SF+QF+20% granulated copper slag			125	6.3

Table 4.3: Systematisation of MIP results of UHPC/UHPFRCs obtained in different studies - Part 3.

	Ref.	Binder	w/b	Curing	fc,28d (MPa)	Total porosity (%)
9	[28]	CEM I 52.5 N+ SF	0.14	1/3/7/28 days sealed curing at 20 °C	140	16.0/14.0/ 12.5/11.0
		CEM I 52.5 N+MTCK (Burgess)			150	18.0/14.0/ 11.5/6.0
		CEM I 52.5 N+MTCK (India)			150	20.0/18/ 12.5/10.0
10	[15]	CEM III+Class C FA+SF	0.2	1 day heat curing 90 °C and RH=98% +lime-saturated water curing 23°C 7 days+ air-curing 23°C until 28 days	175	13
		CEM III+Class C FA+ SF+0.15% CNF			177	9.0
		CEM III+Class C FA+SF+0.30% CNF			181	8.0
11	[32]	CEM I 42.5+SF	0.18	Lime-saturated water curing 28 days	142.2	15.2
		CEM I 42.5+SF+1.6% nano-$CaCO_3$			145	12.5
		CEM I 42.5+SF+3.2% nano-$CaCO_3$			155	12.0
		CEM I 42.5+SF+4.8% nano-$CaCO_3$			135	17.5
		CEM I 42.5+SF+6.4% nano-$CaCO_3$			120	18.0
12	[30]	CEM I 52.5N+ micro-silica	0.13	1/7/14/21 /28/56 days Sealed curing	150	23.5/10.7/ 9.0/7.7/6.6
		CEM I 52.5N+micro-silica+LF			110	15.9/12.6/ 11.6/11.0/7.0

TABLE 4.4: Systematisation of MIP results of UHPC/UHPFRCs obtained in different studies - Part 4.

	Ref.	Binder	w/b	Curing	fc,28d (MPa)	Total porosity (%)
13	[27]	CEM I 52.5+ SF	0.13	3/90 days fog room at 20 °C	140	5.45/4.81
		CEM I 52.5+SF+30% BFS			140	4.47/3.85
		CEM I 52.5+SF+50% BFS			120	10.51/2.51
		CEM I 52.5+SF+80% BFS			100	12.57/4.04
14	[38]	PC+micro silica I+ silica powder	0.22	20 °C and at RH > 99% 24 h	158	8.5
				20 °C and RH > 99% sealed 24 h+water bath at 90 °C 72 h		9.32
				20 °C and RH>99% 24 h+water bath at 90 °C 72 h+20 °C in a water bath up to 28 days		5.02
		PC+micro silica II+ silica powder	0.2	20 °C and RH > 99% 24 h	166	5.8
				20 °C and RH>99% 24 h+water bath at 90 °C 72 h		5.37
				20 °C and RH>99% 24 h+water bath 90 °C 72 h + 20 °C water bath up to 28 days		3.73
15	[16]	PC+SF +10% FA	0.2	Autoclave 8h; 1 MPa	155	6.28
		PC+SF +20% FA		Autoclave 8h; 1 MPa	150	4.73
		PC+SF +30% FA		Autoclave 10h; 1 MPa	135	3.38
				Autoclave 8h; 1 MPa	140	4.03
				Autoclave 6h; 1 MPa	155	4.95

4.2.2.2 Water–permeable porosity

Some studies also reported on the water-permeable porosity of UHPC, as listed in Table 4.5. It should be emphasised that water-permeable porosity cannot be directly compared to MIP total porosity; the water-permeable porosity is usually significantly higher than total porosity given by MIP [25]. The water-permeable porosity results change with the efficiency of the saturation technique used [39]. The vacuum-saturation technique is considered the most efficient saturation method, compared to cold-water or boiling-water saturation [40].

Hannawi et al [41] (line 1, Table 4.5) investigated the effect of adding different types of fibres on the porosity of UHPFRC. Seven composite mixtures were prepared, a reference mixture without fibres and six mixtures with different types of fibres (Vf = 1.0%), steel (S), Wollastonite (W), Basalt (B), PVA, PP, and Barchip (B). Adding either steel, mineral or synthetic fibres had no significant influence on the porosity of mixtures in comparison with the UHPC without fibres (line 1, Table 4.5).

Chen et al. [42] (line 2, Table 4.5) measured the water-permeable porosity of a reference UHPC containing cement, SF and FA as binder and two other similar mixtures including 1% and 2% calcined Layered Double Hydroxides (C-LDH). Table 4.5 shows that the optimal amount of C-LDHs is around 1% since the water porosity decreases from 10.5 to 9.1% comparing with reference UHPC. With 2% C-LDHs it increases to 13.1% [42].

Yu et al. [20] (line 3, Table 4.6) tested several UHPC mixtures using FA, GGBS or LF to replace about 30% of cement. Besides, the authors accessed the effect of three different w/b (0.165, 0.18 and 0.20). They found that there is an optimal w/b ratio at which the water-permeable porosity of UHPC was minimum. Moreover, the water-permeable porosity of mixtures with FA or LF is similar but higher than that with GGBS and the reference mixture.

As expected, Wang et al. [43] (line 4, Table 4.6) found very low water–permeable porosity for specimens heat-treated at 90 °C during 72 hours compared to previous studies where the specimens were water cured.

In brief, Water–permeable porosity results of common cured UHPC/UHPFRC remained between 8.5% and 13.0%.

Table 4.5: Water-permeable porosity of UHPC/UHPFRCs obtained in different studies - Part 1.

	Ref.	Binder	Vf (%)	w/b	Curing	Saturation technique	fc,28d (MPa)	Permeable porosity (%)
1	[41]	CEM 52.5 +LF+ silicious filler	0	0.27 (w/c)	-	Cold water RILEM 49TER	141	9.9
			1 (S)				173	9.6
			1 (W)				145	9.8
			1 (B)				139	9.4
			1 (PVA)				138	10.6
			1 (PP)				125	10.5
			1 (B)				123	10.2
2	[42]	CEM 52.5 +FA+SF	0	0.18	Water curing	Vacuum NT Build 492	145 (56 days)	10.5
		CEM 52.5+ FA+SF+ 1% C-LDH					158 (56 days)	9.2
		CEM 52.5+ FA+SF+ 2% C-LDH					135 (56 days)	13

Table 4.6: Water-permeable porosity of UHPC/UHPFRCs obtained in different studies - Part 2.

	Ref.	Binder	Vf (%)	w/b	Curing	Saturation technique	fc,28d (MPa)	Permeable porosity (%)
3	[20]	CEM I 52.5R +NS	0	0.165	28/90 days water curing at 21 °C	Vacuum NT Build 492	120	9.0/7.0
				0.18			120	8.5/7.0
				0.20			115	10/8.0
		CEM I 52.5R+NS +FA		0.165			110	12.0/11.0
				0.18			110	12.5/11.0
				0.20			100	13.0/11.5
		CEM I 52.5R+NS +GGBS		0.165			115	11.5/9.5
				0.18			115	10.0/8.0
				0.20			110	11.5/10.0
		CEM I 52.5R+NS +LF		0.165			100	12.5/11.0
				0.18			100	12.0/11.0
				0.20			100	13.0/12.0
4	[43]	CEM 42.5 +SF	0	0.22	90°C 72 h +standard curing room 22°C and RH 90% until testing	Vacuum ASTM C 830	130	1.6
			1				150	1.5
			2				175	1.5
			3				200	1.4

4.2.3 Water absorption by capillarity

Table 4.7 to Table 4.9 summarise research studies on water absorption by capillarity of UHPC/UHPFRC. As discussed before for the porosity (section 4.2.2), the binder composition, namely the cement type and the incorporation of SF and/or alternative SCM in UHPC as partial surrogates of cement can also impact the water absorption capacity, as shown by results in lines 7, 8, 10 and 11 of Table 4.8 and 4.9, ranging from 0.0014 to 0.066 mg/(mm$^2\sqrt{\text{min}}$).

Roux et al. [44] (line 1, Table 4.7) observed that after 15 days of testing, the total water absorbed by reactive powder concrete (RPC) remained less than 0.02 mg/(mm^2) after 15 days of testing, which evidences existence of almost no capillary porosity, also confirmed by MIP results [44]. With specialized treatment, namely, applying pressure before and during setting of UHPFRC, a considerable decrease of sorption coefficient (around 50%) was obtained. High curing temperatures also accelerated the hydration process, leading to a denser matrix in a shorter time compared with standard curing room and thus, gave rise to lower sorption coefficient.

Reichmann and Schmidt [36] (line 2, Table 4.7) measured capillary water-absorption coefficients of UHPCs cured in water and heat treated, and obtained values of 0.0026 and 0.0013 mg/(mm$^2\sqrt{\text{min}}$), respectively, while obtained water-sorption coefficients of 0.015 and 0.077 mg/(mm$^2\sqrt{\text{min}}$), respectively, with HPC (C100) and OC (C35). This corroborated with Franke et al. research [45] (line 3, Table 4.7) which also found UHPC exhibited a capillary water-absorption 40 to 55 times lower than ordinary reference mortar ($w/c = 0.45$).

Pyo and Kim study [3] (line 7, Table 4.8) showed that extending the curing time from 28 to 90 days under normal curing conditions (wet chamber at 24 °C) was effective to reduce the sorption coefficient. The reduction amount in the sorption coefficient depends on the binder composition.

Several studies (lines 5, 7 and 9 of Table 4.7, Table 4.8 and Table 4.9, respectively) reported the addition of steel fibres decrease the sorptivity to some extent [3], [43], [46]. This is partly due to fibres bridging across the micro flaws formed due to early ages shrinkage and the induced less connected pores [46].

In brief, sorption coefficient results of UHPCs at 28 days, listed in Table 4.7, Table 4.8 and Table 4.9, range from 0.0006 to 0.066 mg/(mm$^2\sqrt{\text{min}}$).These values are relatively lower when compared to a good quality OC, with $w/c = 0.40$, which typically exhibits values higher than 0.09 mg/(mm$^2\sqrt{\text{min}}$) [47]. Binary and ternary blended

binders concretes made of fly-ash and ECat (generated by the Portuguese oil refinery) presented sorption coefficients ranging from 0.04 to 0.05 mg/(mm$^2\sqrt{\text{min}}$) [48].

4.2.4 Resistance to chloride ion penetration

The resistance to chloride-ion penetration is highly dependent on UHPC constituents (namely, SCM used) and proportions, w/b ratio, curing age as well as exposure concentration and time to chloride ions. Different methods have been used to assess the resistance to chloride penetration of UHPC, namely chloride diffusion, chloride migration and indirect tests based on electrical resistivity or diffusivity [52]. The rapid non-steady-state tests are more popular, in contrast to the steady-state tests mainly because steady-state tests are very time-consuming. The Rapid Chloride Permeability Test (RCPT) or "Coulomb test" is more widespread in EUA and Canada. Thus results found in the literature regarding RCPT test are described in Appendix A. More common chloride penetration tests in Europe are presented as follows.

4.2.4.1 Electrical Resistivity

An indirect, non-destructive and faster method of assessing the resistance to chloride ions penetration in cement-based materials is the electrical resistivity measuring. Resistivity measures how strongly a material opposes to a flow of electrical current, and it depends mainly on the nature and topography of pore structure, changes in the chemical composition of the pore solution, moisture and temperature conditions. Polder [53] recommends measuring concrete resistance using an alternating current (AC) with a frequency between 50 and 1000 Hz. Either two-electrode or four-electrode methods (Wenner) can be employed to measure the electrical current intensity, which is then transformed into resistivity by multiplying it with an appropriate geometrical factor [53].

Table 4.10 presents results of electrical resistivity of UHPC/UHPFRC found in several studies. Meng et al (2017) [54] (line 2 , Table 4.10) evaluated the surface electrical resistivity of UHPC mixtures including high volume of different combinations of SCM (FA and GGBFS) as cement and SF surrogates. Resistivity results range from 280 to 450 Ω m. The reference mixture, with 25% (by mass) of SF content in the binder composition, had the highest electrical resistivity. On the other hand, the mixture with cement and GGBS (50% of each) as binder had the lowest electrical resistivity.

Pyo et al. [3] (line 3 , Table 4.10) measured the resistivity on UHPC incorporating 25% of SF and 2% steel fibres and obtained 1250 Ω m at 56 days. Zachary et al. [55]

TABLE 4.7: UHPC/UHPFRC capillary water sorptivity analysed in different studies - Part 1.

	Ref.	Binder	Vf (%)	w/b	Curing	fc,28d (MPa)	Sorptivity (mg/(mm$^2\sqrt{\text{min}}$)
1	[44]	PC-V+SF	2	0.14	20 °C water cuing 28 days	170	0.0013
					Pressurised before and during setting+20 °C water curing 28 days	230	0.0006
2	[37]	CEM I 52.5R+ SF+QF	0	0.24 (w/c)	Water cured/heat cured 90°C 2 days	162/213	0.0026/0.0013
3	[45]	CEM I 52.5 R+QF+ micro-silica	0	0.17	90 °C 2 days	167	0.0043
		CEM I 42.5R+QF+ micro-silica		0.19		192	0.0057
4	[49]	CEM I 52.5R+ SF+QF	0	0.27 (w/c)	20 °C Water curing 28 days	135	0.044
5	[46]	PC+SF +QF	0	0.23 (w/c)	20 °C and RH>95% 5 days+ ambient laboratory conditions 20°C until testing	151	0.0081
		PC+SF +QF (lf=8 mm)	1			156	0.0075
			3			164	0.0069
			6			171	0.0061
		PC+SF +QF (lf=12 mm)	1			158	0.0076
			3			166	0.007
			6			173	0.0062
		PC+SF +QF (lf=16 mm)	1			159	0.0076
			3			165	0.007
			6			170	0.0062

Table 4.8: UHPC/UHPFRC capillary water sorptivity analysed in different studies - Part 2.

	Ref.	Binder	Vf (%)	w/b	Curing	fc,28d (MPa)	Sorptivity (mg/(mm$^2\sqrt{\text{min}}$))
6	[39]	CEM I 52.5N+SF	1.7	0.22	Water cured 20°C 28 days	155	0.0049
		CEM I 52.5N+SF +MTCK				146	0.007
7	[3]	CEM I+SF+ silica powder	0	0.22 (w/c)	28/90 days wet chamber 24°C and RH 100%	-	0.030/0.010
		CEM IV+SF+ silica powder				-	0.027/0.013
		CEM I+SF+bottom ash				-	0.037/0.013
		CEM I+SF+fine BSF+bottom ash				-	0.046/0.026
		CEM I+SF+BSF+bottom ash				-	0.037/0.016
		CEM I+SF+FA				-	0.039/0.019
		CEM I+SF+silica powder	1	0.22 (w/c)	28/90 days wet chamber 24°C and RH 100%	154	0.052/0.026
		CEM IV+SF+silica powder				158	0.052/0.019
		CEM I+SF+bottom ash				145	0.066/0.019
		CEM I+SF+fine BFS+bottom ash				151	0.066/0.037
		CEM I+SF+fine BFS+bottom ash				145	0.065/0.017
		CEM I+SF+FA				152	0.066/0.027

TABLE 4.9: UHPC/UHPFRC capillary water sorptivity analysed in different studies - Part 3.

	Ref.	Binder	Vf (%)	w/b	Curing	fc,28d (MPa)	Sorptivity (mg/(mm$^2\sqrt{\text{min}}$))
8	[50]	PC 52.5+SF	0	0.22	20°C and RH>95% 28 days	120	0.012
		PC 52.5+SF+1/6 RHA				120	0.012
		PC 52.5+SF+1/3 RHA				120	0.005
		PC 52.5+SF+1/2 RHA				130	0.009
		PC 52.5+SF+2/3 RHA				140	0.01
		PC 52.5+SF+5/6 RHA				130	0.008
9	[43]	Cement 42.5+ SF	0	0.18	90°C 72 h+ 22°C RH=90% 28 days	-	0.01250
			1			-	0.01175
			2			-	0.01125
			3			-	0.01075
10	[4]	PC+SF+QF	2.5	0.18	28/56 days water curing 27°C	180	0.0025/0.0021
		PC+SF +QF+5% TBA				180	0.0021/0.0015
		PC+SF +QF+10% TBA				180	0.0019/0.0015
		PC+SF +QF+15% TBA				190	0.0014/0.0012
		PC+SF +QF+20% TBA				180	0.0014/0.0012
11	[51]	PC+SF+LF	0	0.17	Moist curing 28 days	130	0.009
		PC+FA+LF		0.18		155	0.0064

(line 4 , Table 4.10) tested the surface resistivity of several proprietary UHPFRCs, incorporating 2% of steel fibres by volume. All the proprietary mixtures, except one, exhibited resistivity results of about 1000 Ω m and 3000 Ω m at 28 days. A non-proprietary UHPFRC mixture, incorporating longer fibres(lf = 30 mm), exhibited higher resistivity of about 3000 Ω m and close to 8000 Ω m at 28 and 56 days, respectively. Zachary et al. [55] raised attention to the fact that when testing UHPFRC fibres contact might occur creating an electrically conductive path within the specimen, thus making the test not valid for chloride penetration resistance assessment [55].

Roux et al. [44] (line 1, Table 4.10) evaluated the resistivity of a reactive RPC using the two electrodes methodology. Measurements were performed on specimens cured under water for 28 days, then after maintained at 92% Relative humidity (RH) during 30 days, and finally, maintained at 100% RH for 30 additional days. The resistivity of RPC was extremely high (11300 Ω m) in comparison to the resistivity of the HPC (960 Ω m) and that of normal concrete (160 Ω m) [44]. Besides, an extra curing of 5 days at 50 °C increased the resistivity to 12000 Ω m.

As a reference, binary and ternary blended binders ready-mixed concretes made of fly-ash and ECat (generated by the Portuguese oil refinery) presented, at 28 days, electrical resistivity ranging from 77 to 134 Ω m, and at 56 days, from 90 to 207 Ω m [48].

4.2.4.2 Rapid chloride migration test (based on NT BUILD 492)

The rapid migration test method (RCM), based on NT BUILD 492, is a non-steady state migration test that uses an external electrical field for accelerating chloride penetration. The test provides values of non-steady state migration coefficients (D_{nssm}) (test procedure more detailed in section 4.3.3.5). Lower D_{nssm} values indicate better chloride ion penetration resistance under electrically accelerated conditions. Table 4.11 shows results found in few studies that adopted this test method.

Chen et al. [42] (line 1, Table 4.11) the effect of 1 and 2% of C-LDHs incorporation on a reference UHPFRC including cement, SF and FA as binder. The calculated D_{nssm} of UHPFRC and UHPFRC incorporating 1% and 2% C-LDHs were 1.99×10^{-12}, 1.48×10^{-12} and 2.55×10^{-12} $m^2\,s^{-1}$, respectively. The chloride penetration depths ranged from 3.8 to 6.8 mm and the 1% C-LDHs presented the smallest penetration. These experimental results are in line with those of water-permeable porosity (section 4.2.2.2) that had already indicated that the incorporation of 1% C-LDHs improved

TABLE 4.10: Electrical resistivity of UHPC/UHPFRCs obtained in different studies.

	Ref.	Binder	Vf (%)	w/b	Curing	fc,28d (MPa)	Technique	Resistivity (Ω m)
1	[44]	PC-V+SF	2	0.14	28 days Water cured 20 °C+30 days at RH=92%+30 days at RH=100%	170	Two electrodes	11300 (88 days)
2	[54]	PC+SF	2	0.17	Water curing 23 °C	135	Wenner method	450 (28 days)
		PC+SF+ GGBBS		0.15		125		300 (28 days)
		PC+GGBS		0.16		124		280 (28 days)
		PC+SF+FA		0.16		124		380 (28 days)
		PC+FA		0.18		120		340 (28 days)
3	[3]	PC+SF	2	0.22 (w/c)	Water curing 23 °C	140	Two electrodes	1250 (56 days)
4	[55]	Cement+SF	2	0.11	Lime-saturated water 23 °C	131 (14 days)	Wenner method	2857 (28 days) 7979 (56 days)
		Pre-Blended				130 (14 days)		269 (28 days) 415 (56 days)
		Pre-Blended				139 (14 days)		1088 (28 days) 1300 (56 days)
		Pre-Blended				147 (14 days)		1161 (28 days) 1972 (56 days)
		Pre-Blended				120 (14 days)		989 (28 days) 1655 (56 days)

the durability. Arora et al. [51] (line 2, Table 4.11) obtained similar values of D_{nssm} for UHPC incorporating different combination of SCM.

Results presented in Table 4.11 ranged from 1.48×10^{-12} to 2.55×10^{-12} $m^2\,s^{-1}$. Thus, non-steady state migration chloride coefficients are definitely lower in UHPC compared to those of OC, which are usually above 5×10^{-12} $m^2\,s^{-1}$ [56], [57]. In addition, are also inferior than those of the binary and ternary blended binders concretes made of fly-ash and ECat (generated by the Portuguese oil refinery) that presented, at 28d, D_{nssm} ranging from 17.7×10^{-12} to 19.1×10^{-12} $m^2\,s^{-1}$ [48].

TABLE 4.11: Results of non-steady state migration chloride coefficients from RCM of UHPC/UHPFRCs obtained in different studies.

	Ref.	Binder	Vf (%)	w/b	Curing	fc,28d (MPa)	D_{nssm} (10^{-12} $m^2\,s^{-1}$)
1	[42]	Cement 52.5+FA+SF	2	0.18	-	145 (56 days)	1.99
		Cement 52.5+ FA+SF+ 1%C-LDH				158 (56 days)	1.48
		Cement 52.5+ FA+SF+ 2%C-LDH				135 (56 days)	2.55
2	[51]	PC+FA+ MTCK+LF	0	0.17	Moist curing 28 days	130	2.2
		PC+SF+LF		0.18		155	2.01

4.2.5 Resistance to carbonation

Carbonation consists in the formation of calcium carbonate ($CaCO_3$) through the reaction of CO_2 with the hydration cement products, CH or CSH. Thus, this process reduces the pH of the cementitious matrices promoting the steel depassivation that can trigger reinforcement corrosion. Carbonation is a complex process that depends on several factors, namely binder composition (the type of cement and SCM), water to cement ratio, as well as, environmental conditions such as CO_2 concentration, temperature and humidity. Independent of the environmental conditions, material's porosity and the binding capacity of the cement phases towards CO_2 determine the resistance to carbonation. In UHPC, as discussed before in section 4.2.2, the porosity is reduced, which diminishes the gas permeability significantly. Besides, due to the use of the high proportion of SF, a reduction or total consumption of portlandite can be expected. Both these two characteristics contribute to improving the resistance to carbonation significantly. The resistance of the concretes to the CO_2 penetration is

often evaluated by accelerated carbonation test in an enclosure enriched in CO_2 and with a favourable humidity (as shown in 8th column of Table 4.12 and Table 4.13). Table 4.12 and Table 4.13 presents carbonation depth results of UHPC/UHPFRC found in several studies. All studies corroborate that UHPC carbonation depth is shallow.

4.2.6 Expansive reactions

4.2.6.1 Alkalis-silica reaction

Alkalis-silica reaction (ASR) refers to the chemical reaction in concrete between alkali cations, namely Na^+ and K^+ (present in one of the concrete constituents such as the cement, SCM or admixtures), and a reactive siliceous aggregate. This reaction forms a deleterious expansive product leading to the mortar or concrete cracking.

For conventional concrete, it is generally accepted that no deleterious ASR occurs when equivalent alkali content (Na_2Oeq) of the concrete is lower than 3 $kg\,m^{-3}$ [60], [62]. Since in UHPC the cement, pozzolans and admixtures content is very high (as discussed in Section 4.1), the total alkali content can exceed this threshold. Thus, it makes sense evaluate the risk of damage due to ASR in UHPC, even if a cement with low alkali content is used. On the other hand, given the elimination of coarse aggregate and the characteristic very low permeability of UHPC, some authors argue that it is unlikely that ASR would be an issue under any curing regime [63].

Few studies concerning ASR in UHPCs were found in the literature. Piérard et al. [60] followed the "Oberholster test" methodology, which is based on the modified ASTM C 1260 procedure to verify ASR susceptibility of an UHPC presenting $w/c = 0.23$. Three cylinders (50 mm diameter, 160 mm long) were hot-cured at 80 °C for 24 hours and then the initial length was determined. Subsequent length measurements were taken daily for 20 days while the prisms were immersed in hot (80 °C) 1 N NaOH solution. The results indicate no expansion or deterioration after this severe test (expansion above the limit 0.1%) [60].

Graybeal [63] performed ASR testing on UHPFRC prisms (2% steel fibres in volume, $w/b = 0.12$) $25 \times 25 \times 280$ mm^3 following the ASTM C 1260 [64] procedure. This procedure involves hot curing (80 °Cinwater during one day, before initiate the length change measurements. Thus, two additional sets of specimens were tested in an untreated curing regime: a set in which the ASR length change measurements initiated after the specimens underwent 28 days of curing at ambient laboratory conditions; and an untreated set where the ASR testing was initiated immediately after

TABLE 4.12: Carbonation depth results of UHPC/UHPFRCs obtained in different studies - Part 1.

	Ref.	Binder	Vf (%)	w/b	Curing	fc,28d (MPa)	Exposure conditions	Carbonation depth (mm)
2	[39]	PC+SF	2	0.14	20°C water cured 28 days	170	18 months ambient conditions	No carbonation
							(2) accelerated test at RH=60% + 42 days 5% CO_2	No carbonation
							accelerated test as (2) + 90 days 100% CO_2	No carbonation
3	[58]	Cement 42.5+SF	2.5	0.15	90 °C steam 24 h	165	28 days 20% CO_2 20 °C and HR=70%	No carbonation
		Cement 42.5+SF +FA				125		No carbonation
4	[34]	CEM I 52.5R+ SF+QF	2.5	0.21	water cured 28 days/heat treated at 90°C 3 days	-	3 years at 20 °C and HR=65%	0.18
5	[59]	Cement+ micro -silica (CRC)	6	0.15	–	150-400	16 years at the atmosphere in-doors/outdoors, exposed climatic events	1.0
6	[60]	CEM I 42.5R+SF +QF	0	0.32 (w/c)	20 °C HR>95% 90 days	135	1 year 1% CO_2	1.5-2.0
				0.23 (w/c)		150		

TABLE 4.13: Carbonation depth results of UHPC/UHPFRCs obtained in different studies - Part 2.

	Ref.	Binder	Vf (%)	w/b	Curing	fc,28d (MPa)	Exposure conditions	Carbonation depth (mm)
7	[61]	Cement+SF +FA	1	0.17	14 days water curing+14 days 20°C and HR=55%	152	190 days in 4% CO_2 , 20 °C and RH=55%	0.04
8	[39]	CEM I 52.5 N+SF	1.5	0.22	20 °C water curing 28 days	155	19 months on CO_2 (50% CO_2, 50% of air) HR=65%	No carbonation
		CEM I 52.5N +SF +MTCK				46		No carbonation
9	[37]	CEM I 52.5N +SF +QF	0		20 °C and HR>95% 90 days		4, 8, 16 weeks in 10% CO_2, 20 °C and HR>60%	No carbonation
		CEM I 52.5N +SF +QF+ 5% granulated copper slag						No carbonation
		CEM I 52.5N+SF+QF+10% granulated copper slag						No carbonation
		CEM I 52.5N+SF+QF+15% granulated copper slag						No carbonation
		CEM I 52.5N+SF+QF+20% granulated copper slag						No carbonation

demoulding of the specimens (no curing). All the UHPC expansion results were one order of magnitude below the lower limit threshold of 0.1% after 14 days and even after 28 days of testing. Given the low permeability of UHPC, this study indicates that there should be no concern of ASR problems under any curing regime [63].

4.2.6.2 External sulphates

Due to the very low permeability of UHPFRC, the external sulphate attack would not be expected as it was already confirmed experimentally by some studies.

Reju and Jacob [65] tested the resistance to sulphate attack of an UHPFRC including 0.9% steel fibres and $w/b = 0.25$. After 28 days of curing, cubes specimens were weighed and immersed in 3 different sulphate solutions concentrations, namely with 3%, 4% and 5% sodium sulphate, for 60 days. Change in the mass of the specimens was assessed after 7, 14, 21, 30, 45 and 60 days of immersion, whereas the compressive strength of specimens were only determined after the 60 days of immersion. The results revealed no surface deterioration, nor reduction in mass up to 60 days of the specimen's exposure to the sulphate solutions. It was drawn that when the concentration of sulphate solution increases the compressive strength of UHPFRCs slightly decreases. On the other hand, the presence of SCM (namely, SF) in UHPFRC improves the sulphate resistance [65].

Ahmad et al. [66] prepared an UHPFRC with 2.0% steel fibres and $w/b = 0.15$. The authors tested the resistance to sulphate attack on 50 mm^3 specimens after 28 days of water curing followed by their immersion in a sulphate solution (2.5% $MgSO_4$ and 2.5% Na_2SO_4) during six months. Afterwards, loss of compressive strength was the indicator of sulphate attack occurrence. The very low decrease in the compressive strength (7%) verified in the UHPFRC when subjected to severe sulphate exposure confirmed its high resistance against sulphate attack [66].

The resistance to sulphate attack of several RPC was tested according to ASTM C 1012 by Chuang and Huang [67]. After 28 days of water curing, the initial length of the $75 \times 75 \times 280$ mm^3 specimens was determined and, then, the specimens were immersed in the Na_2SO_4 solution for 12 months. The evaluation of the length of the specimens revealed that the UHPCs expansion ($< 0.01\%$) was much lower when compared with ordinary concrete with $w/b = 0.48$ (0.05%). Moreover, UHPFRC with higher water to binder ratio (from $w/b = 0.25$ to $w/b = 0.30$) and without fibres exhibited higher expansion, as it would be expected [67].

Piérard et al. [68] evaluated the sulphate resistance of three different mixtures of UHPC (M1, M2 and M3), including different type of binder, aggregate and w/c (0.30 and 0.23). The test followed CUR Recommendation 48 [69] procedure. The UHPC prisms ($40 \times 40 \times 160$ mm^3) were immersed in a sodium sulphate solution, and the length variation was regularly measured. The results indicate no expansion or deterioration for all mixtures, even after 500 days of immersion [68].

4.3 Materials and methods

4.3.1 UHPC mix design

The author developed the non-proprietary UHPC mixture in the previous Chapter [14]. Raw materials consisted of ordinary Portland cement (Type I and class 42.5 R), silica fume ($SiO_2 > 90\%$), limestone filler (98% $CaCO_3$), siliceous natural sand, ECat (a waste generated in the fluid catalytic cracking unit of the Sines Refinery in Portugal), potable water and a polycarboxylate-based superplasticizer (Sp).

Table 4.14 shows the main physical characteristics of all solid materials (detailed in [14] or Chapter 3). Table 4.15 presents the proportions of UHPC mixture understudy, corresponding to a $w/b = 0.17$ and a $w/c = 0.23$. In this mixture, the aggregate fraction is composed of 85% siliceous natural sand and 15% ECat, by volume. ECat is used as an internal curing agent in UHPC since it can absorb a significant amount of water (30%, by mass) due to its high specific surface (see Table 4.14), and has already proved to have a beneficial effect mitigating autogenous shrinkage of UHPC [14] (Chapter 3).

The UHPC mixture presented in Table 4.15 combined with 3% high-strength steel fibres ($lf = 13$ mm and $df = 0.2$ mm) exhibits good deformability in the fresh state; a compressive strength of 147 and 156 MPa after 28 and 90 days of water curing (20°C). A tensile strain-hardening behaviour with multiple micro-cracking formation (uniaxial tensile peak stress and peak strain ranging from 11 to 15 MPa and 0.27–0.47%, respectively, at 28 days were accessed. Further details concerning the origin and characteristics of ECat, the mix design approach, as well as the properties of the UHPC mixture (both in the fresh and hardened state), can be found in Chapter 3 [14] .

Table 4.14: Main physical properties of constituent materials.

	Cement	*LF*	*SF*	*ECat*	*Sand*
Specific gravity ($kg\,m^{-3}$)	3110	2668	2200	2660	2570
Specific surface area ($m^2\,kg^{-1}$)	438 (Blaine)	540 (Blaine)	19632 (BET)	150070 (BET)	-
Size distribution	(Laser diffraction)	(Laser diffraction)	(TEM)	(Laser diffraction)	(Sieving)
d_{10} (µm)	1.4	0.7	0.11	59	100
d_{50} (µm)	20	3.2	0.13	79	320
d_{90} (µm)	25	10	0.8	140	520
24h water absorption (%) (EN 1097-6)	-	-	-	30	0.5

Table 4.15: UHPC mixture proportions.

	Raw Materials	$kg\,m^{-3}$
Binder	Cement	690.2
	Silica fume	33.6
	Limestone filler	250.6
Aggregates	ECat	155.5
	Siliceous sand	852.1
Admixture	Superplasticizer	19.5
Water	Mixing water	160.9
	ECat's absorption water	46.6

4.3.2 Mixing procedure and specimens preparation

The UHPC was prepared using a mortar mixer with a vertical axis (following EN 196-1). The mixing sequence is as follows:

- Mixing ECat (dry state) with 80% mixing water plus the water needed for ECat absorption for 5 minutes;
- Adding sand and remaining powder materials and mixing for 2.5 minutes;
- Stopping to scrape material adhering to the mixing bowl and mixing for another 2.5 minutes;
- Introducing the rest of the water plus 75% of Sp and mixing for 2.5 minutes.

Mixing was carried out at a low speed of 140 rotmin^{-1}. The incorporation of ECat leads to an increase in the duration of mixing, in the first part, to allow the ECat saturation with water. After mixing, all specimens were cast in one lift without any mechanical vibration due to the self-compacting ability of the mixture. Then, specimens were covered with a plastic sheet and demoulded after one day.

Depending on the durability property to be evaluated, different moulds (shape and size) were used to prepare the test specimens, as shown in Table 4.16. Specimens were cured in a controlled environment chamber at 20 ± 2 °C and $HR > 95\%$, until the age of testing, excluding the specimens for carbonation and expansive reactions tests which followed specific curing regimes.

4.3.3 Test methods

A series of durability tests were performed on the hardened state of the newly developed UHPC mixture with ECat incorporation to allow for a direct comparison with results from other non-proprietary and commercially-available UHPC mixtures (summarised in Section 4.2), as well as, to evaluate how far this class of material is superior to that of normal- and high-strength concretes. Table 4.16 lists the selected durability tests, and further procedure details are in the following sections. The tests procedures were based on International standards and specific Portuguese recommendations.

TABLE 4.16: Durability testing plan carried out the on UHPC mixture with ECat incorporation.

Durability indicator	*Test standard/technique*	*Age at testing*	*Number of specimens*	*Specimens geometry and size*
Total porosity and pore size distribution	MIP	28, 90 days	2 (1 for each age)	Cylindrical $h = 30$ mm, $\varnothing = 9$ mm
Water permeable porosity	Vacuum saturation technique (NT Build 492)	28 days	6	Cylindrical $h = 30$ mm, $\varnothing = 50$ mm
Water absorption by capillarity	RILEM TC 116-PCD	28 days (+7 days at 40°C, until constant mass)	5	Prismatic $40 \times 40 \times 45$ mm^3
Electrical Resistivity	Two electrode method	2, 7, 14, 21, 28, 35, 42 days	3	Cubic $50 \times 50 \times 50$ mm^3
Resistance to chlorides migration	NT Build 492	28 and 90 days	6	Cylindrical $h = 50$ mm, $\varnothing = 100$ mm
Carbonation resistance	RILEM CPC-18	3, 6, 9 and 12 months	3	Prismatic $40 \times 40 \times 160$ mm^3
Risk of ASR	ASTM C 1260 (Figure 4.3)	up to 184 days	3	Prismatic $25 \times 25 \times 250$ mm^3
	ASTM C 1260 adapted (Figure 4.3)	up to 184 days	3	
Resistance to sulphate attack	Portuguese specification LNEC E-462	up to 26 weeks	6	Prismatic $20 \times 20 \times 160$ mm^3

4.3.3.1 Mercury intrusion porosimetry

The total porosity and pore size distribution were determined at 28 and 90 days by MIP, using Poremaster-60 equipment, which can measure pore sizes from 200 µm to 0.0035 µm. In the MIP testing, the applied low and high pressures were 0.14 and 412 MPa, respectively, the contact angle was 140°, and the surface tension was 480 $mN\,m^{-1}$. For each investigated age, 28 and 90 days, a cylindrical specimen measuring approximately 9 mm of diameter and 30 mm of height was tested.

4.3.3.2 Water permeable porosity

The water-permeable porosity was determined, at 28 days of curing age, on six replicates of UHPC cylindrical samples (50 mm diameter and 30 mm height), at 28 days of curing age. The conditioning of the UHPC cylindrical specimens following the vacuum saturation method prescribed in NT Build 492 [70]. After conditioning, the mass of the saturated sample weighed in air (ms) and its hydrostatic mass (mw) were determined. Next, specimens were allowed to dry in a ventilated heater at 105 ± 1°C. The samples were maintained at that temperature until the mass stabilized (md), which occurred when two consecutive weight measures, separated by 24 h, did not differ by more than 0.05%. The water-permeable porosity (POR) of each replicate sample was determined using Equation 4.1, and the corresponding average was taken as the test result for the UHPC with ECat incorporation under study.

$$POR = \frac{ms - md}{ms - mw} \quad (\%) \tag{4.1}$$

4.3.3.3 Water absorption by capillarity

The water absorption by capillarity was determined on five replicates of UHPC prismatic samples ($40 \times 40 \times 45$ mm^3) following the recommendation RILEM TC 116-PCD [71]. In brief, the procedure consisted of drying the specimens in a ventilated heater at 40°C until constant mass achieved. Then, the test specimens were placed in a shallow water bath which level was adjusted automatically so that the surface of the sample was kept immersed to a constant depth of approximately 3 mm. The mass of each specimen was monitored at time intervals after contact with water (5, 10, 20, 30, 60, 90, 120, 180 and 240 minutes) up to four hours from its first contact with water. The water uptake per unit area (i) was calculated, for each time increment, from the mass of water absorbed (mg) divided by the cross-sectional area of the test face

exposed to water (mm^2). The sorptivity, S $mg/(mm^2\sqrt{min})$, was obtained from the slope of the plot of the water uptake per unit area ($mg\,mm^{-2}$) against the square root of time of immersion ($\sqrt{min}$). The corresponding average corresponds to sorptivity for the UHPC under study.

4.3.3.4 Electrical resistivity

The electrical resistivity was measured at different ages from 2 until 42 days of curing age, on three replicates cubic samples (50 mm^3) using the two electrodes technique. The electrodes constituted by stainless steel plates and moist sponges (to ensure a proper electrical connection) fixed at two opposite surfaces of each sample. A digital multimeter (Keithley) was used to monitor the electrical current intensity of AC arising from a sinusoidal wave with a peak voltage of ±10 V and frequency of 100 Hz created by a signal generator. Recommendations suggest measuring using an AC with a frequency between 50 and 1000 Hz [53]. The electric resistivity (ρ), is calculated using the Ohm's Law (see Equation 4.2). The average resistivity of three specimens is the electrical resistivity for the UHPC under study.

$$\rho = \frac{V \times A}{I \times L} \quad (\Omega\,m) \tag{4.2}$$

4.3.3.5 Rapid chloride migration test

The resistance to chloride migration was evaluated, at both 28 and 90 days, on six replicates of UHPC cylindrical specimens (100 mm diameter and 50 mm height), following the procedure described in the standard NT Build 492. In brief, the procedure consisted in vacuum soak the samples with a $Ca(OH)_2$ saturated solution and, after, apply an electrical potential during 6 to 96 h to force chloride ions to migrate (from a 10% NaCl catholyte solution) through the samples. Each sample was subsequently axially split into two pieces, and then the freshly broken surfaces were sprayed with 0.1 M silver nitrate solution. The chloride migration depth was measured as the depth of visible white silver chloride precipitated (see Figure 4.7). The non-steady-state migration coefficient, D_{nssm}, were determined using (Equation 4.3) for each specimen replicate, and the average is considered the D_{nssm} for UHPC under study.

$$D_{nssm} = \frac{0.0239(273+T)L}{(U-2)t} \times \left(x_d - 0.0238\sqrt{\frac{(273+T)Lx_d}{U-2}} \right) \times 10^{-12} \quad (\mathrm{m^2\,s^{-1}}) \tag{4.3}$$

where U is the absolute value of the applied voltage (V); T is the average value of the initial and final temperatures in the 0.3 M NaOH anolyte solution (K); L is the measured values of specimen thickness (mm); x_d is the average value of the chloride penetration depths (mm); and t is the test duration (h).

The chlorides content at different depths was determined in one half of B-2.1 specimen. The "dry drilling method" sampling procedure, according to RILEM Recommendation TC 178-TMC [72], was employed to obtain powdered samples corresponding to depth steps of approximately 5 mm. Three samples were analysed collected at to 0-5 mm, 5-10 mm and 10-15 mm depths. Determination of chloride content was performed by chemical analysis following the procedure described in EN 196-2.

4.3.3.6 Accelerated carbonation test

The resistance to carbonation was evaluated, at 3, 6, 9 and 12 months, on three replicates of UHPC prismatic samples ($40 \times 40 \times 160$ mm^3) following the procedure described in the RILEM CPC-18 [73]. The samples were wet cured for 14 days, and then stored in a room with controlled temperature and RH (20 ± 2 °C and $50 \pm 3\%$, respectively) for 14 days. Next, the samples were kept in chamber exposed to an accelerated carbonation environment of $5 \pm 0.1\%$ CO_2, $RH = 60 \pm 5\%$, and temperature of 20 ± 2 °C. At the predefined testing ages, a slice with approximately 1 cm thickness was cut from each sample, and the freshly broken surfaces were sprayed with 1% solution of phenolphthalein. Since the phenolphthalein turns pink on non-carbonated areas, the carbonation area was assessed by the depth of the sample area in which the phenolphthalein remains colourless. It should be noted that the threshold pH value of the phenolphthalein indicator is 9.5 [47]; thus, the total absence of carbonation cannot be guaranteed.

4.3.3.7 Expansion due to ASR

The potential risk of alkali-silica reaction in UHPC was monitored following the test procedure prescribed in the American standard ASTM C 1260 [64] with two modifications. The first modification relates to the materials and mix-proportions used. Instead of using the mortars proportioning specified in the standard, the samples were

produced using the materials and mix-proportions indicated, previously, in sections 4.3.1 and 4.3.2.

Another modification is concerned with the curing method. The procedure described in the standard ASTM C 1260 [64] specifies the samples demoulding after 24 h, subsequent placement in an 80°C water bath for the following 24 h, and then their placement in an 80°C sodium hydroxide solution bath until test completion. However, since submerging the UHPC in a water bath at 80°C is somewhat similar to the steam-based curing regimes wherein the UHPC is placed in a high-heat, high-humidity environment, it was anticipated that the test method described in standard ASTM C 1260 may inadvertently lead to accelerated hydration of the UHPC. Thus, two sample sets were prepared for testing. Samples of Set 1 were cured following the ASTM C 1260 procedure whereas the samples of Set 2, undergone 28 days curing at 20°C and $HR \geq 95\%$ before immersing in an 80°C sodium hydroxide solution bath. A scheme of two curing sets is presented in Figure 4.3. Three specimens ($25 \times 25 \times 250$ mm^3) were cast for each set, and the average is considered the expansion due to ASR. The initial reading (L_0) for the samples of Set 2 was measured at 28 days instead of their length after 24 h immersion in hot water as it is prescribed in the standard and followed for samples of Set 1 (see Figure 4.3). After the initial reading, the length changes were monitored periodically (about 3 times per week, during the first 2 weeks, and then once a week) up to 28 days of immersion in NaOH solution. Afterwards, assessments of length change were performed every two weeks and the test was concluded when specimens achieved an ASR expansion approximately of 0.1% (after half a year in NaOH solution, as it will be presented in section 4.3.4.6).

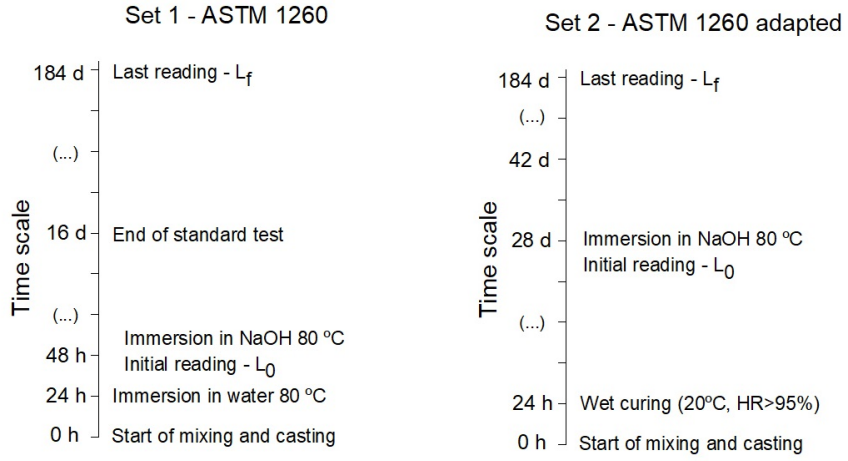

FIGURE 4.3: ASR tested sets: Set 1 - Standard test and Set 2 - Adapted test.

4.3.3.8 Expansion due to external sulphates

The resistance to external sulphate attack of the UHPC was evaluated on six replicates of UHPC prismatic specimens ($20 \times 20 \times 160$ mm^3) following the procedure described in the Portuguese LNEC specification E-462 [74]. The samples remained in the mould 24 h after casting and then were demoulded and immersed in saturated calcium hydroxide (CH) solution at 20°C, during 28 days. At that time, the length of the samples was measured for reference as the initial reading (L_0). Then, two curing conditions were adopted, i.e., half of the samples were immersed in a sodium sulphate solution (16 g l^{-1} SO_4^{2-}) (that was renewed every two weeks) and the remaining samples were maintained in the CH saturated solution. The samples length were monitored throughout 168 days every two weeks. The expansion due to external sulphates is the difference between the average expansion of sulphate cured samples, and the CH cured samples.

4.3.4 Results and Discussion

4.3.4.1 Porosity and Water-permeable porosity

Figure 4.4 shows the MIP pore size distribution of the UHPC at 28 and 90 days. From 0.0035 µm (lower limit of the equipment used), at 28 days, the UHPC presents a bimodal pore size distribution. The first peak, i.e., the first "critical pore diameter", that represents the capillary porosity [24] (section 4.2.2.1), was 0.07 µm, and the second peak that represents the gel pores was 0.008 µm. There were not found more pores with a diameter larger than 0.1 µm. The total porosity was 4.8%, which is in good agreement with previous studies performed in other UHPCs (Table 4.1 to Table 4.4 and discussed in Section 4.2.2.1). As perceived in Figure 4.4, the porosities of specimens further reduced with the age since the two main families pores found at 28 days closed, see Figure 4.4-b. This means that the pore structure became increasingly finer, which might be due to the delayed pozzolanic reactions that continue promoting cement matrix densification. The total porosity was 4.1% at 90 days.

The water-permeable porosity of UHPC, at 28 days, was found to be $14.27 \pm 0.07\%$. This value is significantly larger than that obtained by MIP, as expected. As already mentioned (section 4.2.2.2), the water-permeable porosity is usually significantly higher than the total porosity obtained by MIP [25]. Besides, the result obtained in this work is of the same order of magnitude of the values obtained with others UHPC (see Table 4.5).

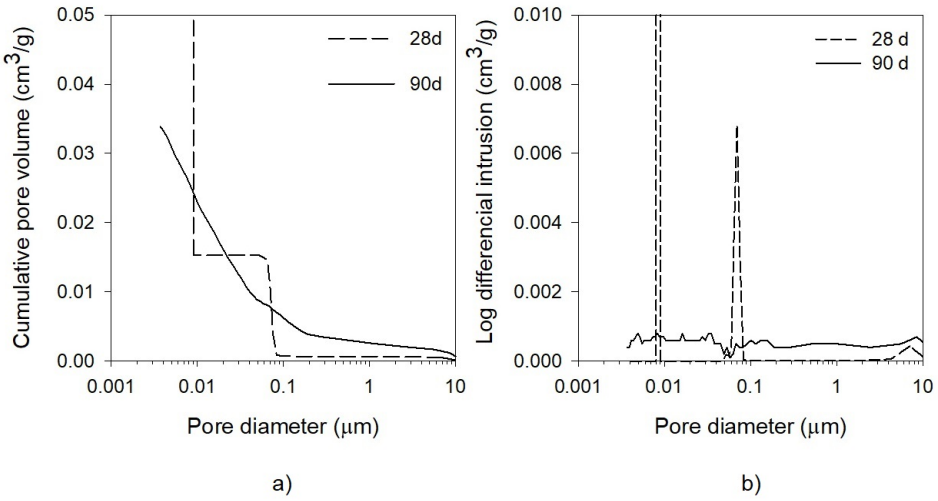

FIGURE 4.4: Pore size distribution of the UHPC samples after 28 and 90 days: a) cumulative pore volume and b) differential intrusions.

4.3.4.2 Water absorption by capillarity

Figure 4.5 plots the cumulative capillary water absorbed (mass per unit of inflow area) by the UHPC, at 28 days of age, against square-root of elapsed time (t) of immersion in water during the first four h of measurement. The average sorptivity is 0.014±0.001 mg/(mm$^2\sqrt{\text{min}}$). The result obtained in this work is the range of the values obtained with others UHPC cured in similar conditions (see Table 4.7, Table 4.8 and Table 4.9 in section 4.2.3). As already mentioned (section 4.2.3), good OC (w/c=0.40), exhibits sorptivity above 0.09 mg/(mm$^2\sqrt{\text{min}}$) [47] and ready-mixed concretes with the same ECat than that used in this study has sorptivity above 0.04 mg/(mm$^2\sqrt{\text{min}}$) [48]. Thus, the UHPC understudy presented a much lower sorptivity. This fact may be attributed to its extremely low water content, the presence of pozzolanic materials (SF and ECat) and the absence of coarse aggregates that contribute to cementitious matrix densification and significantly lower and discontinuous capillary porosity that lowers the capillary sorption capacity. Moreover, these results are in accordance with low porosity revealed by MIP (section 4.3.4.1).

4.3.4.3 Electric resistivity

As expected, the electrical resistivity of the UHPC with ECat incorporation, presented in Figure 4.6, increases with the hydration progress. In fact, UHPC exhibits a significant increase on the resistivity results over time, namely, from 67.4 Ω m at 2 days to 339.6 Ω m at 42 days. At a reference age of 28 days resistivity was 221 ± 16

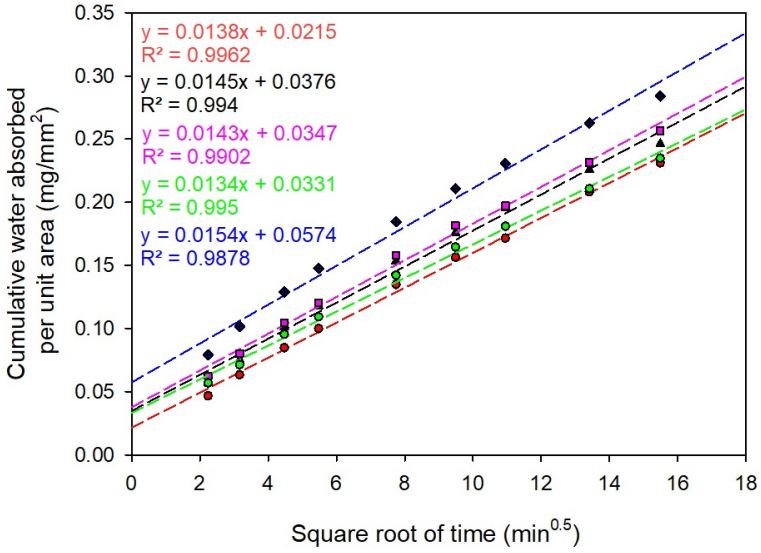

FIGURE 4.5: Experimental results and linear regression of water absorption by capillarity during 4 hours on test specimens.

Ω m. The intense growth in the electrical resistivity (presented in Figure 4.6) also suggests that very likely electrical resistivity continue to increase beyond the 42 days.

Higher electrical resistivity of the cement-based materials corresponds to higher densification of the matrix microstructure that promotes increased durability. As such, the resistivity values obtained in this study (Figure 4.6) are higher than that of the ready-mixed concretes incorporating the same ECat (that is used in this study presented) which electrical resistivity, at 28 days, ranging from 77 to 134 Ω m [48] which is indicative of an increased potential durability of the new UHPC. Table 4.10 (section 4.2.4.1) summarises results obtained on other UHPC/UHPFRCs reveals that for these materials, the electrical resistivity can assume a broad range of values including of the same order of magnitude of that obtained in this study e.g. Meng et al. [54].

4.3.4.4 Chloride ion penetration

Table 4.17 and Figure 4.7 present chloride penetration depths (x_d), obtained for replicates samples the new UHPC after 28 and 90 days of curing, as well as, the correspondent non-steady state chloride migration coefficients, D_{nssm}. As can be observed, the value of D_{nssm} is $2.0 \pm 0.1 \times 10^{-12}$ $m^2\,s^{-1}$. This result is of the same order of magnitude of those presented in Table 4.11 for other UHPC/UHPFRC. However, for ready-mixed concretes incorporating the same ECat as that used in this study the D_{nssm}m, at 28 days of age, was 17 ± 0.1310^{-12} $m^2\,s^{-1}$ [48]. Thus, the UHPC is expected to be more resistant in terms of chloride attack. In fact, the ingress

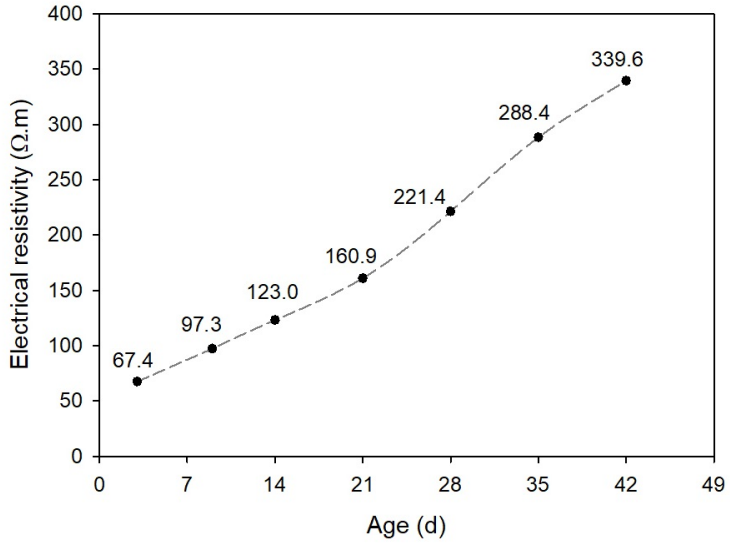

FIGURE 4.6: Evolution of the experimental results of electrical resistivity of UHPC over curing age.

behaviour of chloride ions in the cement-based composite matrix is affected by several factors which are partly related both to the characteristics of the cement composite material and to the composition of the external salt solution [75]. It appears that the ions can only enter capillaries pores above a certain size [75]. If the capillaries or the pore sizes become small enough, it is less likely for the ions to be able to diffuse into the matrix, even at a high concentration [75]. As stated by MIP results, the volume of capillaries pores in UHPC is low and the capillary network is hardly connected (in accordance with sorptivity results) which significantly increases the resistance to the chlorides entrance. In addition, the small penetration depth identified by the colourimetric analysis, Figure 4.7, seems to be in accordance with chloride content determination by the chemical analysis presented in Table 4.18. Significantly higher content of chloride was found between 0-5 mm, but it drastically reduces as it is further from the penetration front.

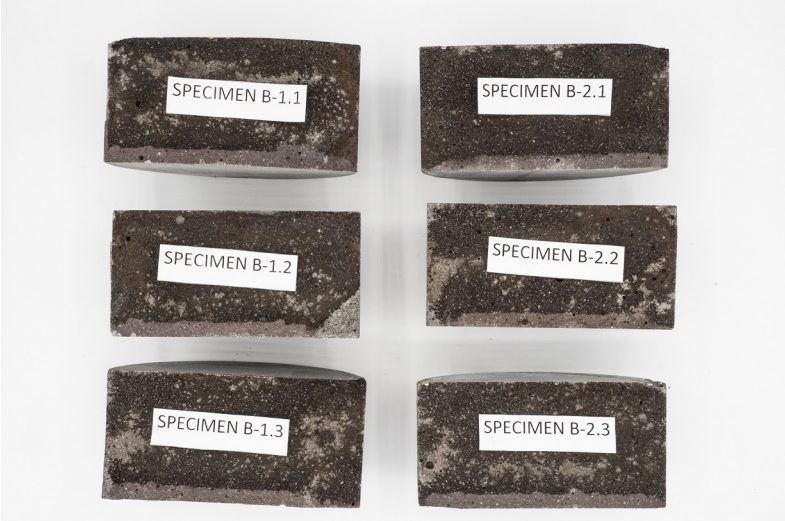

FIGURE 4.7: Split surfaces of cylinder specimens after the rapid chloride permeability test at 28 days; chlorides ingress from the side of the bottom surface (penetration depth of chloride ions in the lighter part).

TABLE 4.17: Rapid chloride migration test results obtained in replicates samples of the UHPC.

Curing time	Specimen reference	t (h)	U (V)	Average temperature during test (°C)	x_d (mm)	D_{nssm} (10^{-12} $m^2\,s^{-1}$)
28 days	B-1.1	24	40	22.07	5.68	1.77
	B-1.2			21.51	6.43	2.03
	B-1.3			21.79	6.07	1.91
	B-2.1			22.00	6.39	1.99
	B-2.2			21.72	6.78	2.12
	B-2.3			21.86	6.60	2.09
90 days	A-1.1	96	60	22.58	6.58	0.36
	A-1.2			22.26	7.28	0.39
	A-1.3			21.93	7.60	0.41
	A-2.1			22.70	7.23	0.39
	A-2.2			22.24	6.44	0.34
	A-2.3			22.15	5.52	0.29

TABLE 4.18: Chloride content on B-2.1 UHPC specimen.

Penetration depth from chloride front (mm)	*Chloride content by mass of sample (%)*
0-5	0.470%
5-10	0.240%
10-15	0.056%

4.3.4.5 Accelerated carbonation test

Although the accelerated carbonation test was extended up to 12 months, which constitutes a very significant duration (generally they last less than 3 months), no carbonation could be detected on the tested UHPC. The literature review presented in Section 4.2.5 corroborated the findings of the present study.

4.3.4.6 Expansion due to alkali-silica reaction

Figure 4.8 presents the results for ASR series tests. The standard method ASTM C 1260 [64] specifies that expansion values less than 0.10% after 14 days of testing. In this case, the expansion was of 0.018 ± 0.002 % for samples of Set 1, i.e., one order of magnitude below this lower threshold, which is indicative that the UHPC behaviour against ASR shall be innocuous in most cases. Although after 28 days water cured samples (Set 2), the expansion was higher, namely 0.072 ± 0.002 % it was still lower than the reference threshold valued of 0.1%. Apparently, there should be no concern of ASR as suggested by previous findings reported ins section 4.2.6.1. After 184 days of immersion in NaOH solution at 80 °C specimens did not show any damage as observed in Figure 4.9 and Figure 4.10.

Figure 4.8 presents the expansion results of ASR tests. The standard ASTM C 1260 specifies that mortar expansion values less than 0.10% after 14 days of testing are indicative of innocuous behaviour. Since in this case, the expansion after 14 days of testing for samples of Set 1 (according to standard curing method) was of 0.018 ± 0.002% i.e., one order of magnitude below the threshold referred in the standard it is indicative that no deleterious expansion due to ASR is anticipated in the UHPC in most cases. Although after 28 days water cured samples (Set 2), the expansion was higher, namely 0.072 ± 0.002%, it was still lower than the reference threshold value of 0.1%. Even after long exposure to NaOH solution, during 184 days, specimens showed no evidence of significant deterioration (see Figure 4.9 and Figure 4.10). These results indicating that there should be no concern regarding ASR expansion are in accordance with previous findings obtained in other UHPC/UHPFRC, as reported in section 4.2.6.1. Moreover, the occurrence of alkali-silica reaction requires the presence of water, and since the UHPC under study exhibited low open porosity including to water (Section 4.3.4.1) this deleterious reaction is disfavoured. In addition, the ECat possesses a three-dimensional network microstructure with a very high specific surface area (150070 $m^2\,kg^{-1}$, Table 4.14) with cation absorption affinity. As such, the ECat has alkali-ions trapping ability that leads to a reduction of these ions availability to participate in the reaction with the aggregates. In fact, a previous study [76]

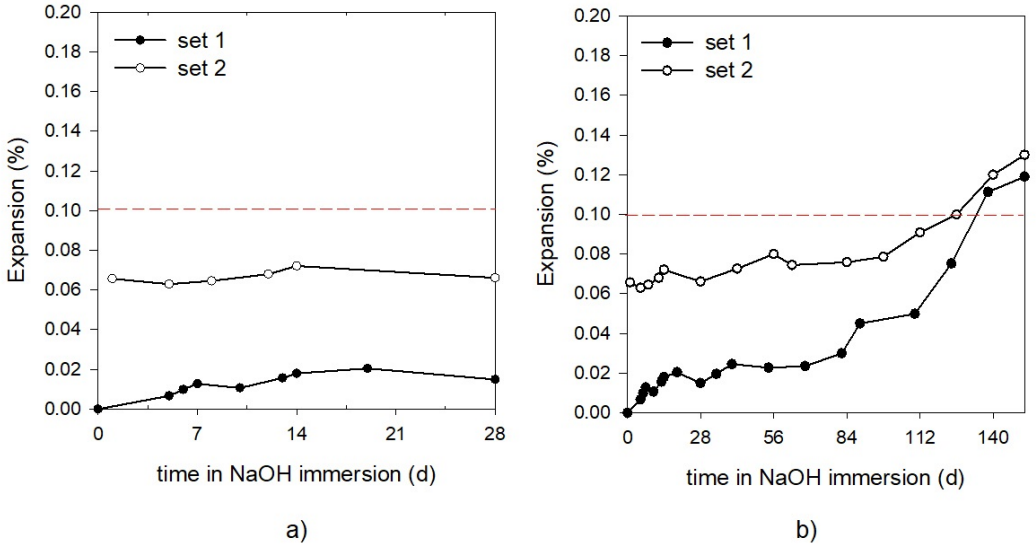

FIGURE 4.8: Change in length of UHPC bar specimens due to ASR.

on mortars using the same ECat in the binder composition as well as reactive sand showed that the increased content of ECat up to 15% (w/w) significantly mitigates the ASR expansion up to 46% concerning the mortar without ECat incorporation.

4.3.4.7 Expansion due to external sulphates

In terms of expansion due to external sulphates, UHPC showed superior performance, without expansion after 26 weeks of exposure to rich sulphate solution. These results showed good agreement with the visual examination, indicating no deterioration of UHPC specimens, see Figure 4.11. This corroborates previous studies found in literature and discussed in section 4.2.6.2.

4.4 Conclusions

The current work investigated the durability performance of a new non-proprietary UHPC mixture incorporating the ECat (which is a by-product generated by the Portuguese oil refinery industry) as an internal curing agent. The experimental results - MIP, water-permeable porosity, capillary water absorption, electrical resistivity, chloride migration, carbonation, alkali-silica reactivity and sulphates attacks (Table 4.19) extrapolated the evidence of ultra-high performance of the new UHPC to include its durability beyond its low early age shrinkage, self compactability and mechanical strength (showed in Chapter 3). Moreover, the extensive review on other commercial

FIGURE 4.9: UHPC specimens set 1 after long term ASR test.

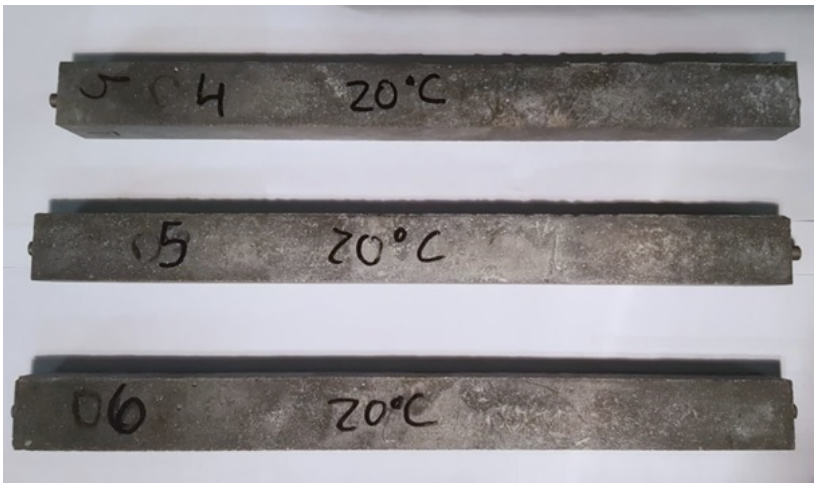

FIGURE 4.10: UHPC specimens set 2 after long term ASR test.

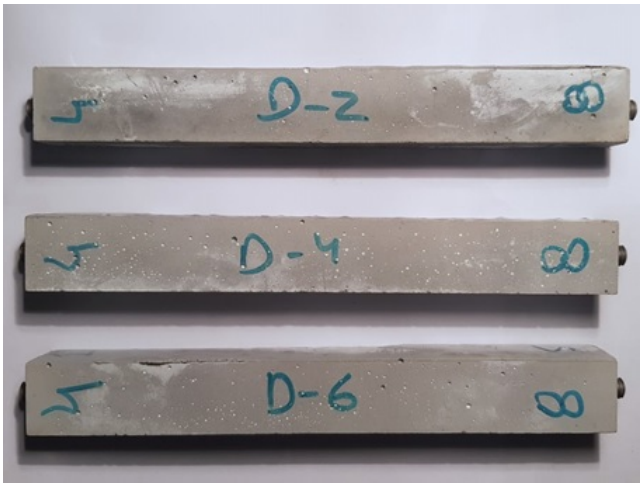

FIGURE 4.11: UHPC specimens after 168 days sulphate solution exposure.

and non-proprietaries UHPC/UHPFRC investigations (Section 4.2) also showed that, in general, the results obtained in the current study compare well with the results found in literature obtained under similar curing conditions. Major finding in this investigation is the belief reinforcement that the use of ECat as an internal curing agent in UHPC is feasible, particularly in mixtures for rehabilitation/strengthening purposes that require low early-ages cracking risk and on-site fabrication under normal casting and curing conditions.

TABLE 4.19: Summary of the durability test results for UHPC.

Durability property indicator	Result ± standard deviation or error	Range of results from literature (Section 4.2)
MIP (%)	4.8 (28d)	2.0-18.0
	4.1 (90d)	
Porosity accessible to water (%)	14.27 ± 0.07	1.5-13.0
Sorptivity ($mg/(mm^2\sqrt{min})$)	0.014 ± 0.001	0.0006-0.066
Electrical resistivity ($\Omega\,m$)	221 ± 16	269-2857
D_{nssm} (10^{-12} $m^2\,s^{-1}$)	2.01 ± 0.10 (28d)	1.48-2.55
	0.36 ± 0.04 (90d)	
Carbonation depth (mm)	0 (after 1 year of exposure)	0-2
ASR expansion (%)		
- ASTM C 1260 (set 1)	0.018 ± 0.002	Mitigation of ASR
- ASTM C 1260 adapted (set 2)	0.072 ± 0.002	
Sulphate expansion (%)	0	Mitigation of sulphate expansion

References

[1] T. Stengel and P. Schießl. Life cycle assessment (LCA) of ultra high performance concrete (UHPC) structures. In *Eco-efficient Construction and Building Materials*, pages 528–564. Elsevier, 2014.

[2] Dehui Wang, Caijun Shi, Zemei Wu, Jianfan Xiao, Zhengyu Huang, and Zhi Fang. A review on ultra high performance concrete: Part II. Hydration, microstructure and properties. *Construction and Building Materials*, 96:368–377, 10 2015.

[3] Sukhoon Pyo, Million Tafesse, Heeae Kim, and Hyeong-Ki Kim. Effect of chloride content on mechanical properties of ultra high performance concrete. *Cement and Concrete Composites*, 84:175–187, 11 2017.

[4] A. Rajasekar, K. Arunachalam, M. Kottaisamy, and V. Saraswathy. Durability characteristics of Ultra High Strength Concrete with treated sugarcane bagasse ash. *Construction and Building Materials*, 171:350–356, 5 2018.

[5] Vitoldas Vaitkevičius, Evaldas Šerelis, and Harald Hilbig. The effect of glass powder on the microstructure of ultra high performance concrete. *Construction and Building Materials*, 68:102–109, 10 2014.

[6] N.A. Soliman and A. Tagnit-Hamou. Partial substitution of silica fume with fine glass powder in UHPC: Filling the micro gap. *Construction and Building Materials*, 139:374–383, 5 2017.

[7] François Toutlemonde and Jacques Resplendino. *Designing and Building with UHPFRC - State of the Art and Development.* wiley, 2013.

[8] Eugen Brühwiler and Emmanuel Denarié. Rehabilitation and Strengthening of Concrete Structures Using Ultra-High Performance Fibre Reinforced Concrete. *Structural Engineering International*, 4:450–457, 2013.

[9] Emmanuel Denarie and Eugen Bruhwiler. Cast-on site UHPFRC for improvement of existing structures – achievements over the last 10 years in practice and research. In *7th workshop on High Performance Fiber Reinforced Cement Composites*, Stuttgart, Germany, 2015.

[10] Sina Nabaei and Sébastien Nendaz. Rehabilitation of transportation infrastructures: the potential of new materials. In *IABSE Conference – Structural Engineering: Providing Solutions to Global Challenges*, Geneva, Switzerland, 2015.

[11] Eugen Brühwiler, Malena Bastien-Masse, Hartmut Mühlberg, Bernard Houriet, Blaise Fleury, Stéphane Cuennet, Philippe Schär, Frédéric Boudry, and Marco Maurer. Strengthening the Chillon viaducts deck slabs with reinforced UHPFRC. In *IABSE Conference – Structural Engineering: Providing Solutions to Global Challenges*, Geneva, Switzerland, 2015.

[12] Sohaib Awan and Mohammed Ahmed Ismaeil. Possibility to Improve Strength and Structural Stability of Bridge Deck Slabs by Using Ultra High Performance Fiber Reinforced Concrete. *Archives of Civil and Mechanical Engineering*, 11(3):320–334, 2014.

[13] Ekkehard Fehling, Michael Schmidt, Joost Walraven, Torsten Leutbecher, and Susanne Frohlich. *Ultra-High Performance Concrete UHPC: Fundamentals, Design, Examples*. Ernst & Sohn, Wiley, Berlin, Germany, 2014.

[14] Ana Mafalda Matos, Sandra Nunes, Carla Costa, and José L. Barroso-Aguiar. Spent equilibrium catalyst as internal curing agent in UHPFRC. *Cement and Concrete Composites*, 104:103362, 11 2019.

[15] Weina Meng and Kamal H. Khayat. Effect of graphite nanoplatelets and carbon nanofibers on rheology, hydration, shrinkage, mechanical properties, and microstructure of UHPC. *Cement and Concrete Research*, 105:64–71, 3 2018.

[16] Tiefeng Chen, Xiaojian Gao, and Miao Ren. Effects of autoclave curing and fly ash on mechanical properties of ultra-high performance concrete. *Construction and Building Materials*, 158:864–872, 1 2018.

[17] Viet Thien An Van, Christiane Rößler, Danh Dai Bui, and Horst Michael Ludwig. Rice husk ash as both pozzolanic admixture and internal curing agent in ultra-high performance concrete. *Cement and Concrete Composites*, 53:270–278, 2014.

[18] Halit Yazici, Huseyin Yigiter, A. S. Karabulut, and Bulent Baradan. Utilization of fly ash and ground granulated blast furnace slag as an alternative silica source in reactive powder concrete. *Fuel*, 87(12):2401–2407, 2008.

[19] Halit Yazıcı, Mert Y. Yardımcı, Hüseyin Yigiter, Serdar Aydın, and Selcuk Turkel. Mechanical properties of reactive powder concrete containing high volumes of ground granulated blast furnace slag. *Cement and Concrete Composites*, 32(8):639–648, 2010.

[20] R. Yu, P. Spiesz, and H.J.H. Brouwers. Development of an eco-friendly Ultra-High Performance Concrete (UHPC) with efficient cement and mineral admixtures uses. *Cement and Concrete Composites*, 55:383–394, 2015.

[21] Kay Wille and Christopher Boisvert-Cotulio. Material efficiency in the design of ultra-high performance concrete. *Construction and Building Materials*, 86:33–43, 2015.

[22] Mariana Moreira C Canut. *Pore structure in blended cement pastes*. PhD thesis, Technical University of Denmark, 2011.

[23] Junzhi Zhang, Fan Bian, Yurong Zhang, Zhaofeng Fang, Chuanqing Fu, and Jie Guo. Effect of pore structures on gas permeability and chloride diffusivity of concrete. *Construction and Building Materials*, 163:402–413, 2 2018.

[24] Guang Ye. *Experimental Study and Numerical Simulation of the Development of the Microstructure and Permeability of Cementitious Materials*. PhD thesis, Technische Universiteit Delft, 2003.

[25] Wei Wang, Jian Liu, Franck Agostini, Catherine A. Davy, Frédéric Skoczylas, and Dominique Corvez. Durability of an Ultra High Performance Fiber Reinforced Concrete (UHPFRC) under progressive aging. *Cement and Concrete Research*, 55:1–13, 1 2014.

[26] Michael Schmidt, Ekkehard Fehling, and Michael Schmidt. Ultra-High-Performance Concrete : Research , Development and Application in Europe. *ACI Special publication*, 2005.

[27] Omar M. Abdulkareem, Amor Ben Fraj, Marwen Bouasker, and Abdelhafid Khelidj. Effect of chemical and thermal activation on the microstructural and mechanical properties of more sustainable UHPC. *Construction and Building Materials*, 169:567–577, 4 2018.

[28] Wei Huang, Hadi Kazemi-Kamyab, Wei Sun, and Karen Scrivener. Effect of replacement of silica fume with calcined clay on the hydration and microstructural development of eco-UHPFRC. *Materials and Design*, 121:36–46, 2017.

[29] Nguyen Van Tuan. *Rice husk ash as a mineral admixture for ultra high performance concrete*. PhD thesis, Technische Universiteit Delft, 2011.

[30] Wei Huang, Hadi Kazemi-Kamyab, Wei Sun, and Karen Scrivener. Effect of cement substitution by limestone on the hydration and microstructural development of ultra-high performance concrete (UHPC). *Cement and Concrete Composites*, 77:86–101, 3 2017.

[31] Ehsan Ghafari, Hugo Costa, Eduardo Júlio, António Portugal, and Luisa Durães. The effect of nanosilica addition on flowability, strength and transport properties of ultra high performance concrete. *Materials and Design*, 59:1–9, 2014.

[32] Zemei Wu, Caijun Shi, and Kamal Henri Khayat. Multi-scale investigation of microstructure, fiber pullout behavior, and mechanical properties of ultra-high performance concrete with nano-CaCO3 particles. *Cement and Concrete Composites*, 86:255–265, 2 2018.

[33] Detlef Heinz and Horst-Michael Ludwig. Heat Treatment and the Risk of DEF Delayed Ettringite Formation in UHPC. In M. Schmidt, E. Fehling, and C. Geisenhanslüke, editors, *International Symposium on Ultra High Performance Concrete*, pages 717–730, Kassel, Germany, 2004.

[34] JC Scheydt and HS Müller. Microstructure of ultra high performance concrete (UHPC) and its impact on durability. In *3rd International Symposium on on Ultra High Performance Concrete*, pages 349–356, Kassel, Germany, 2012.

[35] A. Cwirzen. The effect of the heat-treatment regime on the properties of reactive powder concrete. *Advances in Cement Research*, 19(1):25–33, 2007.

[36] Thomas Teichmann and Michael Schmidt. Influence of the packing density of fine particles on structure, strength and durability of UHPC. In M. Schmidt, E. Fehling, and C. Geisenhanslüke, editors, *International Symposium on Ultra High Performance Concrete*, pages 313–323, Kassel, Germany, 2004.

[37] Romy Suryaningrat Edwin, Elke Gruyaert, Jeroen Dils, and Nele De Belie. Influence of Vacuum Mixing on the Carbonation Resistance and Microstructure of Reactive Powder Concrete Containing Secondary Copper Slag as Supplementary Cementitious Material (SCM). *Procedia Engineering*, 171:534–542, 1 2017.

[38] Nam Kon Lee, K.T. Koh, Min Ook Kim, and G.S. Ryu. Uncovering the role of micro silica in hydration of ultra-high performance concrete (UHPC). *Cement and Concrete Research*, 104:68–79, 2 2018.

[39] Ahmed Tafraoui, Gilles Escadeillas, and Thierry Vidal. Durability of the Ultra High Performances Concrete containing metakaolin. *Construction and Building Materials*, 112:980–987, 2016.

[40] Md. Safiuddin and Nataliya Hearn. Comparison of ASTM saturation techniques for measuring the permeable porosity of concrete. *Cement and Concrete Research*, 35(5):1008–1013, 5 2005.

[41] Kinda Hannawi, Hui Bian, William Prince-Agbodjan, and Balaji Raghavan. Effect of different types of fibers on the microstructure and the mechanical behavior of Ultra-High Performance Fiber-Reinforced Concretes. *Composites Part B: Engineering*, 86:214–220, 2 2016.

[42] Yuxuan Chen, Rui Yu, Xinpeng Wang, Jie Chen, and Zhonghe Shui. Evaluation and optimization of Ultra-High Performance Concrete (UHPC) subjected to harsh ocean environment: Towards an application of Layered Double Hydroxides (LDHs). *Construction and Building Materials*, 177:51–62, 7 2018.

[43] Rui Wang, Xiaojian Gao, Qiyan Li, and Yingzi Yang. Influence of splitting load on transport properties of ultra-high performance concrete. *Construction and Building Materials*, 171:708–718, 5 2018.

[44] N. Roux, C. Andrade, and M. A. Sanjuan. Experimental study of durability of reactive powder concretes. *Journal of Materials in Civil Engineering*, 8:1–6, 1996.

[45] Lutz Franke, Gernod Deckelmann, and Holger Schmidt. Behaviour of ultra-high-performance concrete with respect to chemical attack. In *2nd International Symposium on Ultra High Performance Concrete*, pages 453–460, Kassel, Germany„ 2008. Kassel University Press.

[46] Safeer Abbas, Ahmed M. Soliman, and Moncef L. Nehdi. Exploring mechanical and durability properties of ultra-high performance concrete incorporating various steel fiber lengths and dosages. *Construction and Building Materials*, 75:429–441, 1 2015.

[47] A M Neville. *Properties of concrete*. Longman Group Limited, fifth edition, 2011.

[48] Carla Costa and José Marques. Feasibility of Eco-Friendly Binary and Ternary Blended Binders Made of Fly-Ash and Oil-Refinery Spent Catalyst in Ready-Mixed Concrete Production. *Sustainability 2018, Vol. 10, Page 3136*, 10(9):3136, 2018.

[49] E Ghafari, H Costa, E Júlio, A Portugal, and L Durães. Optimization of UHPC by adding nanomaterials. In *3rd International Symposium on UHPC and Nanotechnology for High Performance Construction Materials*, pages 71–78, Kassel, Germany, 2012.

[50] Huanghuang Huang, Xiaojian Gao, Hui Wang, and Huan Ye. Influence of rice husk ash on strength and permeability of ultra-high performance concrete. *Construction and Building Materials*, 149:621–628, 9 2017.

[51] Aashay Arora, Asim Almujaddidi, Farrokh Kianmofrad, Barzin Mobasher, and Narayanan Neithalath. Material design of economical ultra-high performance concrete (UHPC) and evaluation of their properties. *Cement and Concrete Composites*, 104:103346, 11 2019.

[52] Luping Tang, Lars-Olof Nilsson, and P.A. Muhammed Basheer. *Resistance of Concrete to Chloride Ingress*. CRC Press, Taylor and Francis, 2017.

[53] R Polder, C. Andrade, B. Elsener, O. Venesland, J. Gulikers, R. Weidart, and M. Raupach. Test methods on site measurement of resistivity of concrete – A RILEM TC-154 technical recommendation. *Materials and Structures*, 33:603–611, 2000.

[54] Weina Meng, Mahdi Valipour, and Kamal Henri Khayat. Optimization and performance of cost-effective ultra-high performance concrete. *Materials and Structures*, 50(1):1–29, 2 2017.

[55] Zachary B. Haber, Igor De la Varga, Benjamin A. Graybeal, Brian Nakashoji, and Rafic El-Helou. Properties and Behavior of UHPC-Class Materials. Report No FHWA-HRT-18-036. Technical Report March, U.S. Department of Transportation, 2018.

[56] Karla Hornbostel, Claus K. Larsen, and Mette R. Geiker. Relationship between concrete resistivity and corrosion rate – A literature review. *Cement and Concrete Composites*, 39:60–72, 5 2013.

[57] V. Baroghel-Bouny. Conception des bétons pour une durée de vie donnée des ouvrages - Association Francaise de Genie Civil | AFGC | Paris, 2004.

[58] Liu Juanhong, Song Shaomin, and Wang Lin. Durability and Micro-structure of Reactive Powder Concrete. *Journal of Wuhan University of Technology - Materials and Science*, 24(3):506–509, 2009.

[59] Carmen Andrade and Julio Torres. Long term carbonation of UHPC. In *RILEM-fib-AFGC Int. Symposium on Ultra-High Performance Fibre-Reinforced Concrete - UHPFRC 2013*, volume 4, pages 249–256, Marseille, France, 2013.

[60] Julie Piérard, Bram Dooms, and Niki Cauberg. Durability evaluation of different types of UHPC. In *RILEM-fib-AFGC Int. Symposium on Ultra-High Performance Fibre-Reinforced Concrete, UHPFRC 2013* –, Marseille, France, 2013.

[61] Iman Ferdosian. *Material Development and Self-healing Capacity of Eco-Efficient Ultra-High Performance Concrete (EEUHPC)*. PhD thesis, University of Minho, 2016.

[62] Zhengqi Li, Kaveh Afshinnia, and Prasada Rao Rangaraju. Effect of alkali content of cement on properties of high performance cementitious mortar. *Construction and Building Materials*, 102:631–639, 1 2016.

[63] Benjamin Graybeal and Jussara Tanesi. Durability of an Ultrahigh-Performance Concrete. *Journal of Materials in Civil Engineering*, 19(10):848–854, 2007.

[64] ASTM C 1260-07. Standard Test Method for Potential Alkali Reactivity of Cement-Aggregate Combinations (Mortar-Bar Method), 2007.

[65] R. Reju and G. Jiji Jacob. Investigations on the chemical durability properties of Ultra High Performance Fibre Reinforced Concrete. In *International Conference*

on Green Technologies, ICGT 2012, pages 181–185, Trivandrum, Kerala, India, 2012.

[66] Shamsad Ahmad, Ibrahim Hakeem, and Mohammed Maslehuddin. Development of an optimum mixture of ultra-high performance concrete. *European Journal of Environmental and Civil Engineering*, 20(9):1106–1126, 10 2016.

[67] Mei Ling Chuang and Wei Hsing Huang. Durability Analysis Testing on Reactive Powder Concrete. *Advanced Materials Research*, 811:244–248, 9 2013.

[68] Julie Piérard, Bram Dooms, and Niki Cauberg. Evaluation of Durability Parameters of UHPC Using Accelerated Lab Tests. In *3rd International Symposium on UHPC and Nanotechnology for High Performance Construction Materials*, pages 371–376, Kassel, Germany, 2012.

[69] CUR-Recommendation 89. Measures to prevent damage to concrete by alkali-silica reaction (ASR), 1999.

[70] NT Build 492. Concrete, mortar and cement-based repair materials: Chloride migration coefficient from non-steady-state migration experiments, 1999.

[71] RILEM. RILEM TC 116-PCD: Permeability of concrete as a criteria of its durability. *Materials and Structures*, 32(April):174–179, 1999.

[72] Vennesland, M. A. Climent, and Carmen Andrade. Recommendation of RILEM TC 178-TM.Testing and modelling chloride penetration in concret.Methods for obtaining dust samples by means of grinding concrete in order to determine the chloride concentration profile. *Materials and Structures/Materiaux et Constructions*, 46(3):337–344, 2013.

[73] RILEM Recomendation CPC-18 Measurement of hardened concrete carbonation depth, 1988.

[74] LNEC. E 462. Cimentos. Resistência dos cimentos ao ataque por sulfatos., 2004.

[75] Tiewei Zhang and Odd E Gjerv. Diffusion behavior of chloride ions in concrete. *Cement and Concrete Research*, 26(6):907–917, 1996.

[76] Carla Costa, M Sofia Ribeiro, and Nuno Brito. Effect of Waste Oil-Cracking Catalyst Incorporation on Durability of Mortars. *Materials Sciences and Applications*, 5(November):905–914, 2014.

5 Water capillary transport in cracked UHPFRC

The primary goal of the present Chapter was to investigate the influence of cracking on water transport by capillary suction of UHPFRC. Prismatic specimens were firstly loaded under four-point bending up to specific crack open displacement (COD). Target COD, under loading, was varied between 200 and 400 µm*, in steps of 50* µm*. After unloading, a COD recovery was observed with residual COD ranging between 116-334* µm *and 75-248* µm *for UHPFRC-1.5% and UHPFRC-3.0% specimens, respectively. The crack pattern created was characterized (number of cracks and crack width) before capillarity testing. Sorptivity results of cracked UHPFRC-1.5% and -3.0% specimens remained in the range of 0.024 to 0.044* $\mathrm{mg/(mm^2\sqrt{min})}$*, which are about 2 to 4 times higher than the sorptivity results of non-cracked UHPFRC specimens. However, the maximum sorptivity observed on cracked UHPFRC is relatively low as compared to typical sorptivity results found in good quality conventional concrete or engineered cementitious composites (ECC).*

This Chapter corresponds to the published journal paper: Matos, A.M., Nunes, S., Barroso Aguiar, J.L., Capillary transport of water in cracked and non-cracked UHPFRC specimens, Journal of Advanced Concrete Technology, Volume 17, Issue 5, May 2019, Pages 244-259.

5.1 Introduction

Ultra-High-Performance Fibre Reinforced Cement-based Composites (UHPFRC) emerged from the development of three different families of composites, namely, self-compacting concrete (SCC), fibre reinforced concrete (FRC) and high-performance concrete (HPC) [1]. The design of UHPFRC aims a densely compacted cementitious matrix (herein referred to as UHPC). So that, it is generally employed a high content of reactive powders, the minimal amount of water, a high-range water reducer and adequate fine aggregate gradation, to produce high flowability and improved mechanical and durability properties [2]. The binder phase of UHPC is commonly composed of Portland

cement and silica fume. Due to the very low water/binder mass ratio (w/b) only part of the total cement hydrates, thus cement and silica fume can be partially or entirely replaced by fly ash, blast furnace slag, metakaolin, rice husk ash, in order to reduce the cost or even improve some properties of UHPC. Depending on compositions, production process and special curing conditions, the compressive, tensile and flexural strengths of UHPFRC can reach values as high as 200 to 800 MPa, 25 to 150 MPa and 30 to 141 MPa, respectively [3]. Nevertheless, the number of non-proprietary UHPFRC mixtures found in literature produced with ordinary materials (minimising the use of natural resources) and room temperature curing conditions has been increasing, in an attempt to increase the general acceptance and number of applications of UHPFRC.

Most elements in concrete structures are subjected to drying and wetting cycles and are rarely saturated, under service conditions. Under dry or partially saturated conditions, the rate of ingress of water, which may carry aggressive agents, is mostly controlled by capillary absorption rather than diffusion or pressure-induced flow. Therefore, flow driven by capillary suction is a significant transport process that should be considered as a criterion for long term durability of UHPFRC. The most widely used laboratory test method to assess capillary transport is the method proposed by Hall [4], which provides a procedure to determine the rate of water absorption (also called sorptivity).

Sorptivity results of sound UHPC/UHPFRC specimens found in literature, showing that it is sensitive to changes in mix composition, the degree of hydration and curing conditions. Roux et al. observed that after 15 days of testing, total water absorbed by reactive powder concrete (RPC) remained less than 0.2 $\mathrm{mg\,mm^{-2}}$, which evidences the existence of almost no capillary porosity [5]. However, with a special curing treatment, namely, applying pressure before and during setting of UHPFRC a considerable decrease of the sorptivity coefficient (around 50%) occurred [5]. High curing temperatures also accelerate the hydration process, and therefore a denser matrix can be obtained in a shorter time compared with standard curing room, giving rise to lower sorptivity. Teichmann and Schmidt [6] measured sorptivity of 0.03 and 0.013 $\mathrm{mg/(mm^2\sqrt{min})}$ for water cured and heat-treated UHPCs, respectively; while high-performance (C100) and normal concretes (C35) exhibited sorptivity of 0.015 and 0.08 $\mathrm{mg/(mm^2\sqrt{min})}$, respectively [6]. Franke et al. [7] also found that UHPC exhibits a capillary water absorption 40 to 55 times lower than ordinary reference mortar (w/c=0.45) [7]. The binder composition, particularly the cement type and the incorporation of alternative supplementary cementing materials (SCM) in UHPC, can also impact the water absorption capacity. For example, the addition

of rice husk ash [8] or treated bagasse ash [9] was found to reduce the sorptivity of UHPC. Ternary blended mixtures of cement, silica fume and metakaolin might increase the water capillary absorption compared to conventional UHPFRC including cement and silica fume, according to [10]. However, the differences observed in these sorptivity results are not significant to cause a significant difference in durability. Several studies reported that the addition of steel fibres decrease the sorptivity to some extent [11], [2], [12]. This is partly due to fibres bridging across the micro-flaws formed due to early ages shrinkage and the induced less connected pores [12].

The superior mechanical and durability performance of UHPFRC makes it particularly suitable for use in new construction and thin layers/jackets for strengthening and waterproofing existing reinforced concrete structures, particularly when exposed to aggressive environments. In those cases, the durability requirements can be even more demanding than the mechanical ones [13]. Indeed, a promising field of application is the rehabilitation and strengthening of reinforced concrete structures, in which a new layer of UHPFRC replaces the deteriorated concrete (cracked, carbonated, chloride attacked). The combination of existing concrete with the UHPFRC as a protective layer, which can be reinforced, provides an efficient way of increasing the durability (prolonging the service life), the stiffness and structural resistance capacity while keeping compact cross-sections. Besides contributing to structural capacity, the tensile performance of UHPFRC is essential for coping with the autogenous deformations and for ensuring water-tightness even when subjected to critical tensile deformations. While the limit of elasticity in tension of 7-9MPa ensures that the UHPFRC layers remain uncracked under restrained autogenous deformations, the hardening branch up to the tensile strength of 8-16MPa and strains of 0.2%-0.4% is crucial for ensuring the low permeability even when the UHPFRC suffers significant mechanical actions [14], [15]. This tensile response mostly depends on the fibre-to-matrix bond mechanics [16], [17] and the fibre distribution/orientation [18]. If the former is tailored during mix design, the latter is influenced by the rheology, casting methods, geometry and dimensions of the specimen. Therefore, the "in-structure" tensile response can differ from that characterised in laboratory tests and cracking might occur in the UHPFRC layer. Further research is needed to study the influence of cracking on UHPFRC durability.

Only a few studies on the water transport properties of UHPFRC under applied loads (cracked state) were found in the literature. Charron et al. [15] studied the permeability, and the capillary absorption of UHPFRC submitted to high tensile deformations. Direct tensile tests were performed on UHPFRC prisms of $50 \times 200 \times 500$ mm^3 notched at mid-length. Upon reaching a predefined level of deformation, during

the tensile test, the specimen was unloaded, and a core of 100 mm in diameter was extracted for absorption tests. Absorption measurements on undamaged UHPFRC specimens showed a very low value of sorptivity, namely 0.0027 mg/(mm$^2\sqrt{\text{min}}$), which is related to the limited amount of capillary pores in UHPFRC. Also, relatively low values were measured for specimens with a residual strain of 0.05% and 0.13% which presented sorptivity values of 0.0034 and 0.0050 mg/(mm$^2\sqrt{\text{min}}$), respectively. However, for the highest level of deformation (total displacement of 0.33 mm, in the softening domain), water capillary absorption presented an abrupt increase, with a sorptivity of 0.01 mg/(mm$^2\sqrt{\text{min}}$). In that case, the localised macro-crack within the specimens acts as a large artificial capillary pore, which increases the absorption capacity of the material considerably.

Ma et al. used dumbbell-shaped UHPFRC specimens in which uniaxial tensile stress of 0%, 30%, 50% and 80% of ultimate tensile stress were applied [19]. After unloading, the specimens, the capillary absorption test was carried out. The sorptivity values obtained at 0%, 30%, 50% and 80% of ultimate tensile stress were 0.0012, 0.0019, 0.0026 and 0.01 mg/(mm$^2\sqrt{\text{min}}$), respectively. The number of micro-cracks and new pores increase with the increase of applied tensile loading, and they provide passageways for water penetration into UHPC. The increase of the maximum amount of absorbed water is not very significant when the applied tensile stress is below 50% of ultimate tensile stress; however, it becomes noticeable when the applied tensile stress reaches 80% of ultimate tensile stress [19].

Recently, Wang et al. investigated the influence of splitting tensile loading damage effect on transport properties of UHPFRC incorporating different contents of steel fibres (0%, 1%, 2% and 3%) [2]. Cylindrical specimens with 100 mm diameter and 50 mm height were subjected to different splitting loads with stress levels varying from 50% to 80% of the ultimate splitting tensile strength. Then, in the unloaded state (considering residual crack open displacement - COD_{res}), sorptivity and penetrable porosity were measured, and the crack pattern was characterised. The COD_{res} varied between 15 to 43 µm, 25 to 65 µm and 30 to 84 µm, for 1%, 2% and 3% fibre dosages incorporation, respectively. As expected, sorptivity increased with a higher level of splitting load and higher crack open displacement after unloading (COD_{res}). The measured sorptivity values for different steel fibre contents are similar for the COD_{res} up to about 20-30 µm, which corresponds to a stress level of 30% of the ultimate splitting tensile strength. Then, for higher COD_{res} and, consequently, higher stress level, sorptivities values for different steel fibre dosage incorporation vary in a more significant level, generally increasing with decrease of fibre dosage. For example, the sorptivity value were 0.023 mg/(mm$^2\sqrt{\text{min}}$), 0.018 mg/(mm$^2\sqrt{\text{min}}$) and

0.016 mg/(mm$^2\sqrt{\text{min}}$) for the UHPC samples containing 1%, 2% and 3% steel fibres, respectively, when the COD_{res} is around 40 µm. A higher steel fibres content was found to play a positive effect on improving the transport properties of UHPFRC with the same COD_{res} value [2].

As mentioned above, cracking in thin UHPFRC layers might occur under service conditions, which can harm its durability. This concern is addressed in the current Chapter by evaluating the water absorption by capillarity in both non-cracked and cracked UHPFRC specimens, with two different fibre contents (1.5% and 3.0%). Then, different damage levels were introduced on prismatic specimens, through four-point bending test (target COD ranging between 200 and 400 µm, in steps of 50 µm). The crack pattern observed on the tensile face of the specimen was characterised. Then the sorptivity tests were carried out to understand how micro- and macro-cracking formation in UHPFRC can degrade its resistance to water penetration.

5.2 Materials and Methods

5.2.1 Raw materials and mixture proportions

The cement used in this study is ordinary Portland cement, Type I with a strength grade of 42.5 R, under requirements of EN 197-1. As SCM, silica fume (SF) with a specific surface area of 19632 $m^2\,kg^{-1}$, SiO_2> 90%, complying the requirements of EN 13263-1, was used, and limestone filler ($CaCO_3$ = 98%) having a specific surface of 550 $m^2\,kg^{-1}$, and complying with the requirements of EN 12620. The aggregate fraction is composed of 85% siliceous natural sand (d_{max} = 1 mm) and 15% ECat (a spent equilibrium catalyst, generated by Sines Refinery, Portugal), by volume. Table 5.1 presents the main chemical properties and the specific surface area of ECat. ECat, particularly due to its zeolite constituent, it is a highly micro-porous material in which most of the surface area is internal. The high specific surface of the ECat (150 070 $m^2\,kg^{-1}$) with water affinity explains its significant water absorption. The 24 h water absorption of ECat is 30%, by mass according to the standard EN 1097-6. So that, additional water was added to UHPFRC mixtures considering the water absorption provided by ECat (30% by mass of ECat dosage). More details concerning the origin of ECat can be found in Chapter 3 or [20], [21]. The reduced water content of typical UHPFRC mixtures, make necessary using a high range water reducer is needed. So that, it was added a polycarboxylate-based superplasticizer, with main properties, a solid powder content of 40% and density of 1080 $kg\,m^{-3}$, complying with EN 934-2. High strength short steel fibres with diameter of 0.2 mm

and 13 mm in length ($lf/df = 65$) were used as reinforcement. The tensile strength and modulus of elasticity of the fibres are 2750 MPa and 200 GPa, respectively.

Table 5.2 presents the mixture composition of the non-proprietary UHPC developed by the author (see Chapter 3). The optimisation constraints were low autogenous shrinkage, high resistivity, self-compatibility and compressive strength close to 150 MPa, in standard water curing room. Steel fibres were added to UHPC in two different volume fractions, 1.5% and 3.0%, by replacing an equivalent volume of siliceous natural sand, to manufacture two UHPFRC mixtures, UHPFRC-1.5% and UHPFRC-3.0%, respectively.

Table 5.1: Chemical composition and specific surface area of ECat.

Chemical composition (% by mass)									Specific surface area $m^2\,kg^{-1}$
SiO_2	Al_2O_3	Fe_2O_3	CaO	MgO	SO_3	Na_2O	K_2O	LOI	
40.30	54.45	0.45	0.06	0.15	0.00	0.43	0.02	1.05	150 070 (BET)

Table 5.2: UHPC mixture proportions.

	Raw Materials	$kg\,m^{-3}$
Binder	Cement	690.2
	Silica fume	33.6
	Limestone filler	250.6
Aggregates	ECat	155.5
	Siliceous sand	852.1
Admixture	Superplasticizer	19.5
Water	Mixing water	160.9
	ECat's absorption water	46.6

5.2.2 Mixing procedure, fresh state characterisation and specimens preparation

UHPFRC mixtures were produced using a mixer under requirements of EN 196-1. The mixing procedure had the following steps: (1) mixing ECat (dry state) with 80% mixing water plus ECat's water absorption (30% by mass) for 5 minutes; (2) adding sand and remaining powder materials and mixing for 2.5 minutes; (3) stopping to scrape material adhering to the mixing bowl and mixing for another 2.5 minutes; (4) introducing the rest of the water plus 75% of Sp and mixing for 2.5 minutes; (5) adding the rest of Sp and mixing for 1.5 minutes; (6) fibres incorporation and mix for 2 minutes.

Immediately after mixing, the mixtures self-compactability was assessed using the mini-slump flow test according to EFNARC recommendations [22]. Several prismatic specimens ($40 \times 40 \times 160$ mm^3) were moulded in one lift without any mechanical vibration due to the self-compacting ability of the mixtures. The experimental plan is presented in Table 5.3. Besides, three cubic specimens (50 mm^3) were moulded for each UHPFRC mixture to evaluate the compressive strength at 7 and 28 days. The specimens were then covered with a plastic sheet and demoulded after one day and then water cured in a controlled environment chamber at 20 ± 2 °C and $HR \geq 95\%$, until the testing age. No special curing treatment was applied to UHPFRC specimens.

TABLE 5.3: Number of prismatic specimens ($40 \times 40 \times 160$ mm^3) prepared for each test condition.

Series	Flexural behaviour	Crack pattern and water capillary absorption					
		Non-cracked	Target COD_{load} (µm)				
		(COD_{load}=0 µm)	200	250	300	350	400
UHPFRC-1.5%	5	3	3	3	3	3	3
UHPFRC-3.0%	5	3	3	3	3	3	3

5.2.3 Mechanical testing

The compressive strength of both UHPFRC mixtures was assessed at 7 and 28 days, following ASTM C109/C109M procedure. Three specimens were tested for each age.

Flexural strength of specimens of UHPFRCs was assessed at 28 days, through a four-point bending test. The device for applying loads (see Figure 5.1) consists of 1) two supporting rollers; 2) two upper rollers (loading), which divide the load applied by the machine equally between the two rollers. Rollers were manufactured from steel and had a circular cross-section with a diameter of 10 mm. They are at least 10 mm longer than the width of the test specimen. The distance, I, between the outer rollers (i.e. the span) is equal to 3d, where $d = 40$ mm is the width of the specimen. The distance between the loading rollers is equal to d. The loading rollers are equally spaced between the support rollers, as shown in Figure 5.1. All dimensions were adjusted from the test set-up suggested in EN 12390-5. The flexural strength (f_{cf}) can be computed from the maximum load sustained (F_{max}) as follows:

$$f_{\mathrm{cf}} = \frac{F_{\mathrm{max}} \times I}{d_1 \times {d_2}^2} \tag{5.1}$$

where $I = 120$ mm is the distance between the supporting rollers (mm), $d_1 = 40$ mm is the width of the test beam (mm) and $d_2 = 40$ mm corresponds to depth of tested beam (mm).

FIGURE 5.1: Four-point bending test configuration and positioning of the LVDTs on the lateral surface of the prism.

5.2.4 Cracking procedure

UHPFRC specimens cracking was produced through the four-point bending test, using the test configuration described in the previous section. Two LVDTs, with a range of 5 mm and a precision of 1.6 µm, were installed at the front and back surfaces of each specimen, perpendicular to the loading direction, to monitor the COD evolution, see Figure 5.1. At 28 days, prismatic specimens were cracked by imposing different cracks open displacements (COD) between 200 and 400 µm, in steps of 50 µm, to obtain different crack patterns (see Table 5.3). Three specimens were used for each COD condition, as indicated in Table 5.3. When the target COD was achieved (COD_{load}), the specimen was unloaded, and the residual COD was recorded (COD_{res}). The tests were carried out in a 300 kN Instron testing machine, under displacement control with a displacement rate of 0.003 mm s^{-1}, which was kept constant during the experiment. After removing the specimen from the test set-up, its central part was dry cut, and a smaller prism was obtained with dimensions of $40 \times 40 \times (46 - 52)$ mm^3 as shown in Figure 5.2, which was then used for crack pattern characterisation and later in the water absorption by capillarity test.

The specimens reference considered the fibre content, the target COD_{load} and the specimen replicate number. For example, "1.5%-200-1", corresponds to specimen number one, incorporating 1.5% steel fibres with a target COD_{load} of 200 µm. Besides,

non-cracked specimens were considered for reference purposes and named as 1.5%-0 and 3.0%-0.

5.2.5 Characterisation of the crack pattern

Before cracking the specimens, a coloured grid was marked on the tensile face of the specimen (in between the two loading points) as shown in Figure 5.2, to facilitate the crack pattern characterisation. Since UHPFRC develops multiple micro-cracking before reaching the peak load, often crack path branching occurs, which makes it very difficult to distinguish every single crack and to count the total number of cracks. Therefore, in this study, only the cracks found over three horizontal lines, A, B and C, shown in Figure 5.3-a were characterised, within the central 40 mm length zone, corresponding to maximum bending moment zone. Besides, the 40 mm length was subdivided into four equal segments of 10 mm length each (Figure5.3-a) to allow easier localisation of each crack. This allowed organising the data of crack pattern characterisation in the form of a matrix (3×4), corresponding to 3 lines (A, B and C) by four columns (segments 1, 2, 3 and 4). The cracks found over each line were observed, in the unloaded state, and photographed using a Multizoom Nikon AZ100 microscope together with a PC and a DS-U2 digital camera. A Nikon-AZ Plan Fluor 5× objective was used, and the magnification range was adjusted to crack dimension. Figure5.3-b presents a typical photo of a crack obtained by microscope. Later, using image analysis software (ImageJ), six measurements along each crack were done, as shown in Figure 5.3-b. The median of the six measurements along each crack (Figure 5.3-b) was considered in this study as the representative value of the crack width.

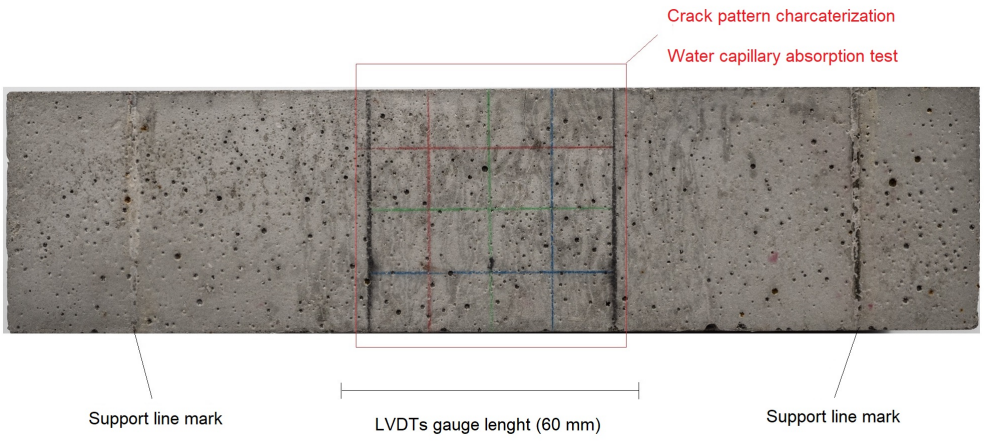

FIGURE 5.2: Segment of the prismatic specimen used for crack pattern characterisation and sorptivity testing.

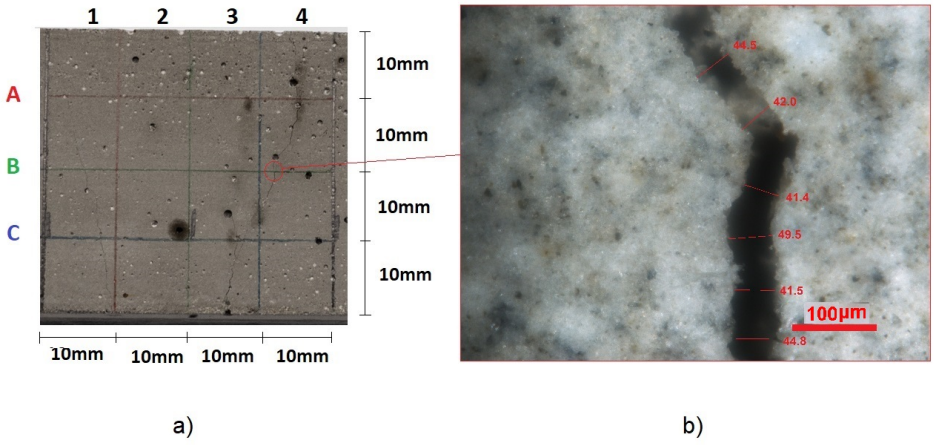

FIGURE 5.3: a) Grid used for measuring the number of cracks and crack widths; b) Example of a crack observed in 1.5%-350- 3 specimen, and corresponding 6 measurements of the crack width.

5.2.6 Capillary water absorption test

After characterising the crack pattern, the specimens were allowed to dry in a ventilated heater at 40 ± 1 °C until constant mass. Specimens were weighed periodically, and equilibrium was assumed when the mass loss was less than 0.05% in two 24 h consecutive measurements. Samples dried at 40°C cooled at ambient temperature (21 ± 2 °C), during 24 h before initiating the test. The mass before and after cooling was recorded and the difference was always $< 0.05\%$, meaning constant moisture content. The time required for the conditioning regime to complete was about seven days.

Water absorption was determined using conventional gravimetric measurement in a simple vertical capillary rise setup by monitoring the increase in sample mass overtime at ambient room temperature (21 ± 2 °C) and following the recommendation RILEM TC 116-PCD. The testing surface of each specimen was placed on plastic rods in a tray containing shallow water to a depth of about 2-3 mm from the bottom of the prism. The measured cumulative water absorbed was plotted against the square root of elapsed time. For one-dimensional absorption into an unsaturated semi-infinite homogeneous medium, cumulative absorption (i) is given by the following expression [4]:

$$i = S_0 + S \times t^{0.5} \tag{5.2}$$

where S is the sorptivity of the material mg/(mm$^2\sqrt{\text{min}}$)), t is the elapsed time

(minutes) and S_0 (mg/(mm^2) is the fitting constant. The sorptivity coefficient (S) was determined from the slope of the best fitting line, using linear regression analysis, drawn across at least nine readings taken from the start of the test up to 4 hours. Three replicate specimens for each test condition were tested, including non-cracked prisms for control purposes for both fibre contents (see Table 5.3).

5.3 Results and discussion

5.3.1 Workability and mechanical properties of UHPFRCs series

UHPFRC were self compactable, attested by spread flow diameters of 302 and 283 mm for 1.5% and 3.0% fibre contents, respectively. It is well established that the spread flow diameter decreases with an increase of the fibre factor (χ), which takes into account the combined effect of fibres aspect ratio and fibre content [23]. Small values of the fibre factor ($\chi < 1.0$) has little impact on the final spread diameter. On the other hand, $\chi > 2$ can promote fibre agglomeration during the mixing process and, consequently, an abrupt reduction of workability [24]. The first line of Table 5.4 presents the fibre factor for UHPFRC series under study. By doubling the fibre content, no sudden loss of workability was observed, as could be anticipated from χ values lower than 2 (see Table 5.4).

As expected, very high compressive strengths were obtained, higher than 100 MPa at seven days and reaching 121 MPa and 147 MPa for fibre contents of 1.5% and 3.0%, respectively, at 28 days. Incorporation of higher fibre dosage slight improves the compressive strength. This corroborates with other authors and is due to the fibre ability to delay the micro-crack formation and to arrest crack propagation [25], [3].

Figure 5.4 shows the flexural behaviour of UHPFRC specimens, including the individual stress/load - strain curves for all the valid specimens. For each series, 1.5% and 3.0%, five specimens were tested, and at least four results were considered valid (the crack localised within the measuring length covered by the LVDTs). Table 5.5 presents the flexural strength (f_{cf}) as well as the first-cracking stress (f_{cr}) for each single specimen tested. As can be observed in Figure 5.4 both mixtures exhibited flexure hardening behaviour. The f_{cf} achieved with 1.5% and 3.0% fibre contents were 23.3 ± 2.5 and 36.2 ± 1.6 MPa, respectively. The first crack occurred at stresses of 10.8 ± 0.9 and 14.7 ± 1.0 MPa for 1.5% and 3.0% fibre contents, respectively. In

TABLE 5.4: Slump flow diameter and compressive strength of tested mixtures.

	UHPFRC-1.5% ($\chi = 0.90$)	UHPFRC-3.0% ($\chi = 1.95$)
Dflow	302 mm	283 mm
Rc		
7 days	104 ± 5.1 MPa	118 ± 2.6 MPa
28 days	121 ± 2.5 MPa	147 ± 2.3 MPa

$\chi = \frac{Vf \times lf}{df}$ where Vf is the volume of fibres per m^3, lf and df are length and diameter of fibres

general, f_{cf} is approximately twice the f_{cr} (see Table 5.5). The first-cracking and the peak flexural stresses increased with the fibre content. However, the maximum load showed more substantial difference according to the fibre content, which is in agreement with other authors' findings [3], [25], [26], [27]. Also, the specimens exhibiting higher peak stresses provided more brittle behaviour in the softening region (lower post-peak ductility), as also found by [25].

The strain-hardening stage (before the peak load) is characterised by multiple cracking formations, without localisation of any significant crack. Figure 5.5 illustrates the multiple cracking stages, characterised by tiny crack openings that naked eyes cannot observe, and the surface needs to be sprayed with alcohol to reveal them. After the peak load, a softening behaviour is found, which is characterised by a macro-crack formation, as exemplified in Figure 5.6.

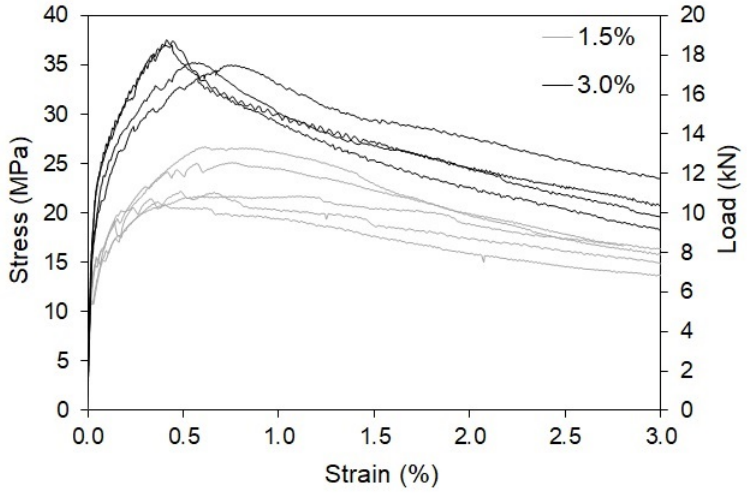

FIGURE 5.4: Four point bending stress/load–strain relationships for all valid specimens.

TABLE 5.5: Main four-point bending test parameters for each individual specimen.

Series	Specimen	f_{cr} (MPa)	f_{cf} (MPa)	$COD_{f_{cf}}$ (µm)
1.5%	1	11.2	21.7	464.6
	2	11.3	20.8	244.0
	3	10.6	22.2	292.3
	4	10.2	26.6	372.0
	5	10.7	25.1	455.9
3.0%	1	15.0	34.9	454.2
	2	14.7	35.2	331.1
	3	15.0	37.5	249.4
	4	13.9	37.0	265.2

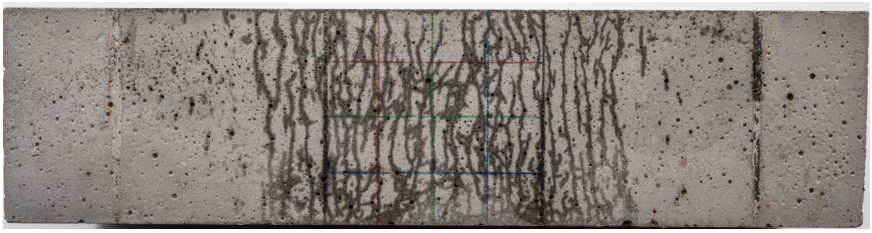

FIGURE 5.5: Multiple cracking observed in specimen 3.0%-250-3, after spraying the surface with alcohol.

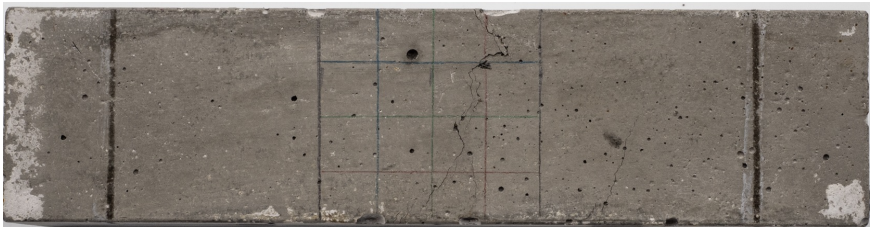

FIGURE 5.6: Localised macro-crack observed in specimen 3.0%-400-2.

5.3.2 Crack pattern characterisation

5.3.2.1 COD recovery after unloading (COD_{load} and COD_{res})

Figure 5.7 and Figure 5.8 presents the load-displacement curves obtained in cracking procedure for UHPFRC-1.5% and UHPFRC-3.0% specimens, respectively. Besides, detailed data concerning the cracking procedure can be found in Tables C.1 and C.2 of Appendix C for UHPFRC-1.5% and UHPFRC-3.0% series, respectively. It can be drawn that target values of COD_{load} were achieved with a reasonable approximation ($\pm 15\%$), for all tested specimens. Measured values of COD_{res} as a function of COD_{load}

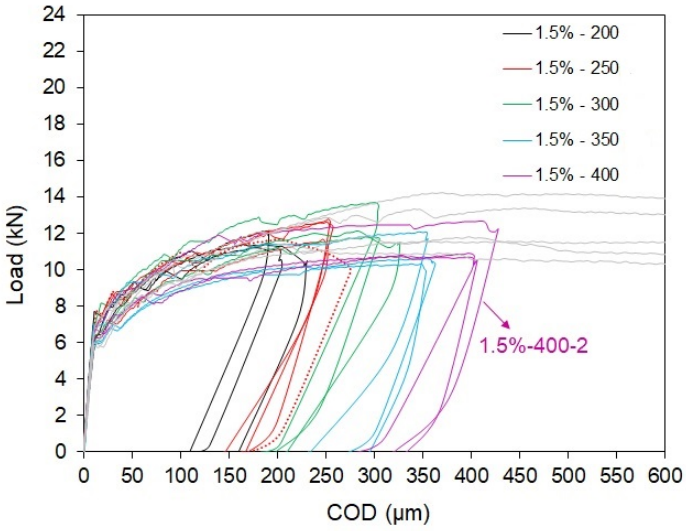

FIGURE 5.7: Load-displacement curves obtained while establishing target COD_{load} for UHPFRC-1.5% series specimens.

are represented in Figure 5.9, showing a good linear relation between COD_{res} and COD_{load} for each fibre content. A similar trend was already observed by Ma et al. [19]. Furthermore, lower COD_{res} values were found with the increase of fibre content, for equivalent COD_{load}.

5.3.2.2 Crack pattern characterisation

Appendix B presents the matrices with data of measured crack widths (in µm) for all specimens. In these matrices, a colour scale (from green to red) was adopted to allow easy visualisation of crack open dimension. Tables C.1 and C.2 of Appendix C, detail the summary of crack pattern parameters, the average number of cracks counted over lines A, B and C (N); the minimum (Min), maximum (Max) and the median crack width (Med); for UHPFRC-1.5% and UHPFRC-3.0% series, respectively.

Concerning the number of cracks, no clear tendency arisen for UHPFRC-3.0% specimens, but it seems they slightly increase with the damage level as perceived in Figure 5.10-b. On the other hand, the average number of cracks is roughly constant for UHPFRC-1.5% specimens, except for 1.5%-400-3 specimen as depicted in Figure 5.10-a. The average number of cracks observed over a length of 40 mm remained below 6 and 8 for UHPFRC-1.5% and UHPFRC-3.0% specimens, respectively, as illustrated in Figure 5.10. The median of crack width results is under 53 µm and 34 µm for UHPFRC-1.5% and UHPFRC-3.0% specimens, respectively, as shown in Figure 5.11-a. This confirms that an increase of fibre content is effective to suppress the development of cracks, resulting in smaller micro-cracks. Figure 5.11-b

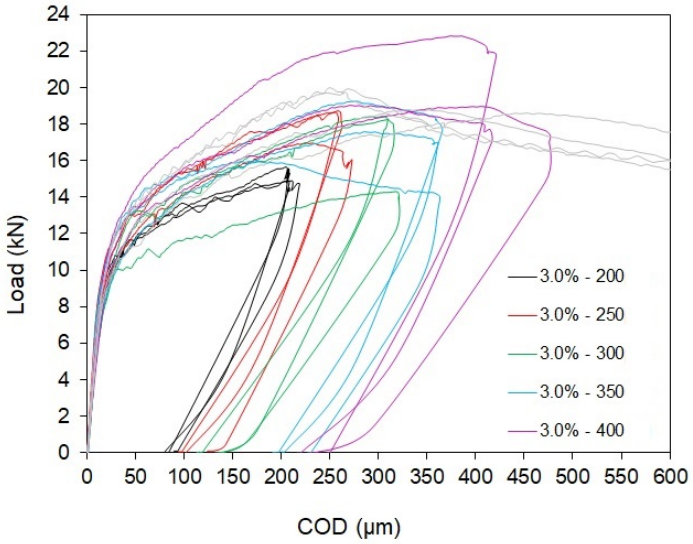

FIGURE 5.8: Load-displacement curves obtained while establishing target COD_{load} for UHPFRC-3.0% series specimens.

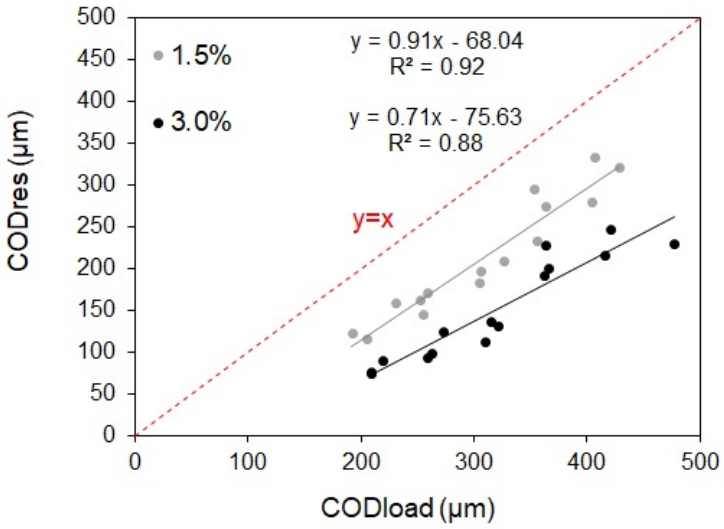

FIGURE 5.9: Relation between COD_{load} and COD_{res}.

shows the maximum crack width results. Up to a COD_{res} of about 125 µm maximum crack width remained below 100 µm. A more significant increase of maximum crack width (> 200 µm) was observed with $COD_{res} > 275$ µm and $COD_{res} > 200$ µm for UHPFRC-1.5% and UHPFRC-3.0%, respectively.

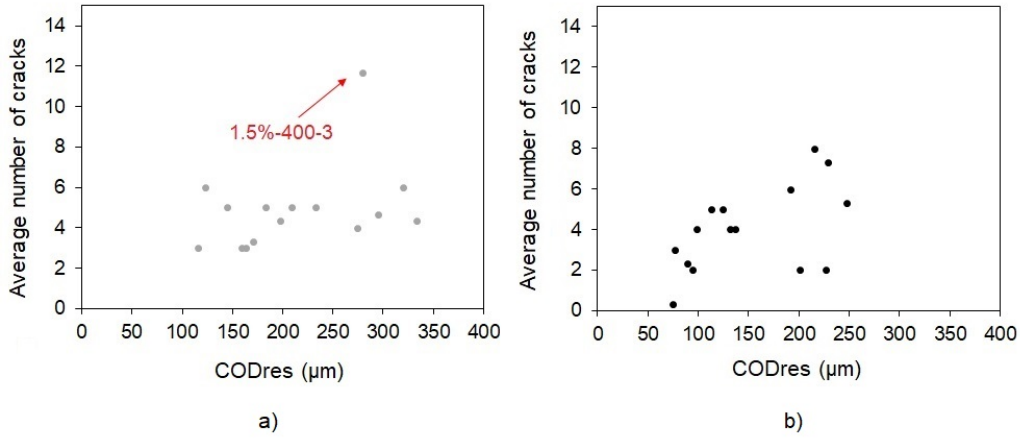

FIGURE 5.10: Average number of cracks over the length of 40 mm for: a) 1.5% and b) 3.0%.

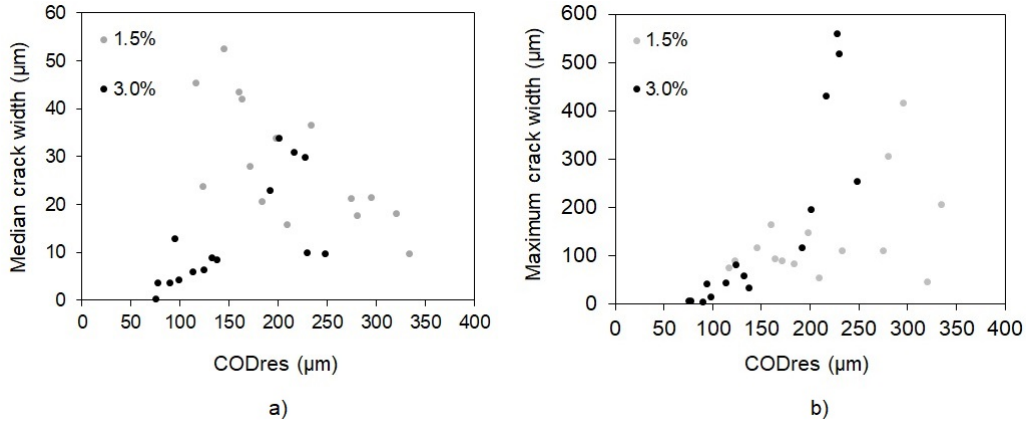

FIGURE 5.11: a) Median crack width and b) Maximum crack width results.

5.3.3 Water capillary absorption

Figure 5.12 and Figure 5.13 show cumulative water absorbed (mass per unit of inflow area) against square-root of elapsed time (t) for UHPFRC with 1.5% and 3.0% fibre contents, respectively. Note that the plots show data from the first 4 hours of measurement. Besides cracked specimens, cumulative water absorbed by reference specimens (non-cracked, 0 µm) is included in the graphs. Appendix C provides more detailed information on these test results.

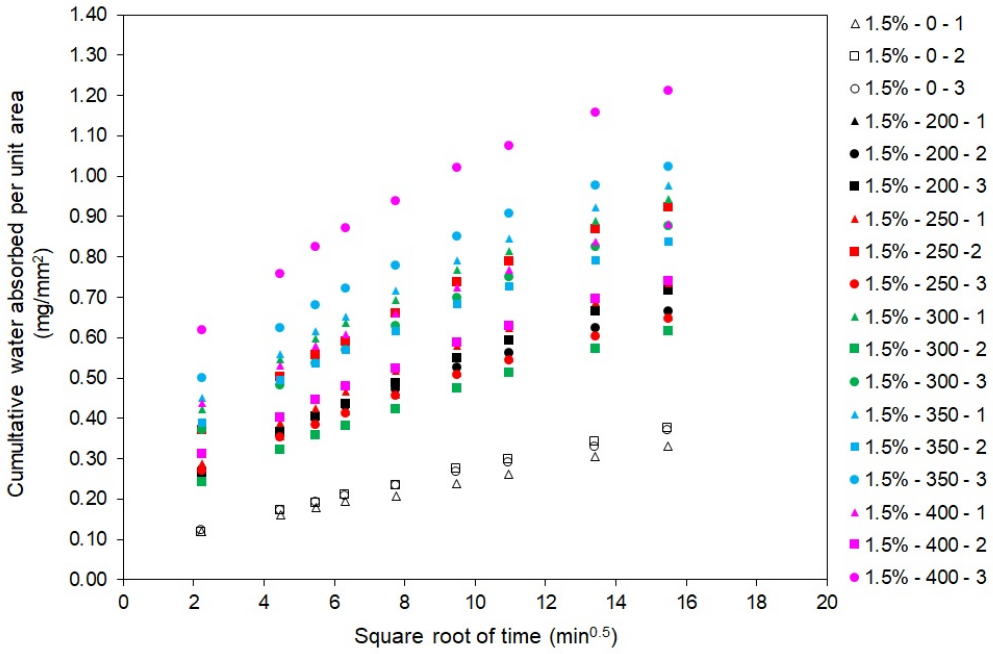

FIGURE 5.12: Cumulative capillary water absorption of UHPFRC-1.5% specimens.

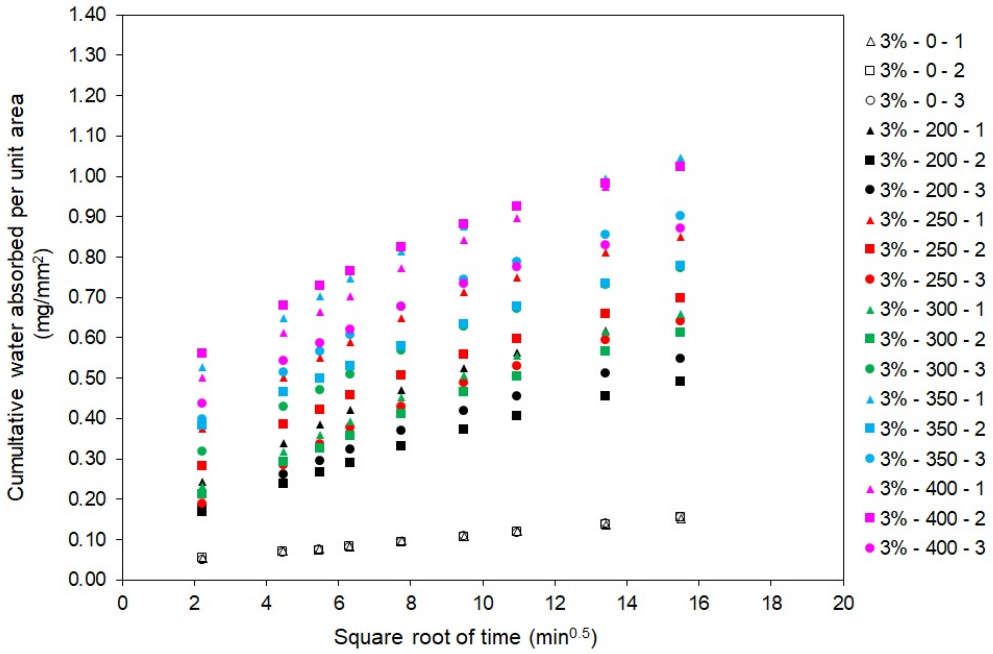

FIGURE 5.13: Cumulative capillary water absorption of UHPFRC-3.0% specimens.

Typical pictures from specimens after 4 h water exposure are presented in Figure 5.14 and Figure 5.15 for 1.5% and 3.0% specimens, respectively. In these figures, a natural boundary between the wet and dry zones can be observed in control specimens (non-cracked), whereas cracked specimens presented an irregular demarcation boundary. With micro-cracks formation, a wet front occurs, since the micro-cracks get fulfilled

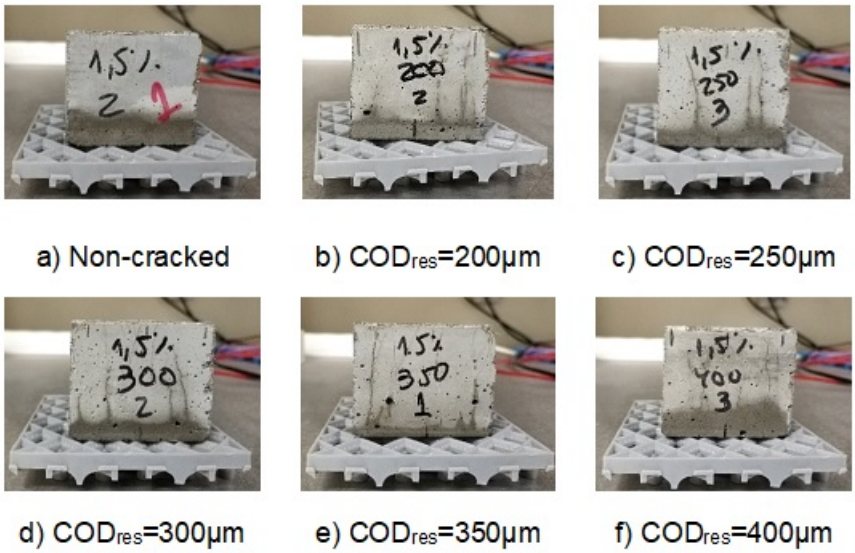

FIGURE 5.14: Depth of water penetration after 4 h of test duration, corresponding to UHPFRC-1.5% specimens.

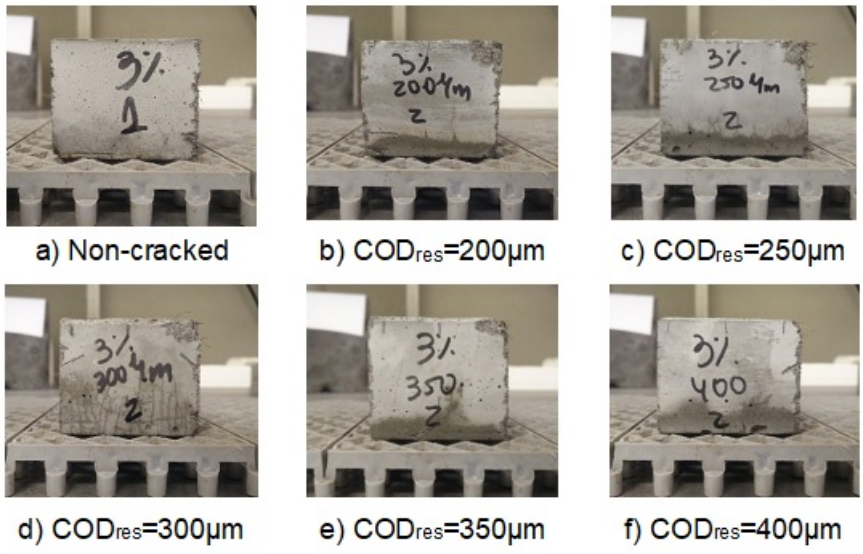

FIGURE 5.15: Depth of water penetration after 4 h of test duration, corresponding to UHPFRC-3.0% specimens

with water due to their suction capacity. When a macro-crack localises in one of the previously formed micro-cracks, the remaining of the specimen unloads and cracks in those zones can close, thus resulting in a lower suction effect. Figure 5.14 and Figure 5.15 show that in addition to crack width, crack length and tortuosity may also influence the sorptivity values of UHPFRC.

Figure 5.12 and Figure 5.13 clearly show that undamaged UHPFRC specimens have a constant and very low rate of water absorption, compared to cracked specimens. The sorptivity of undamaged UHPFRC specimens was 0.0178 and 0.0076 mg/(mm$^2\sqrt{\text{min}}$) for 1.5% and 3.0% fibre content, respectively. These results are in agreement with results from previous research works also depicted in Figure 5.17 [5], [6], [8], [9], [10], [11], [28]. When compared to good quality conventional concrete ($w/c = 0.40$), exhibiting sorptivity above 0.09 mg/(mm$^2\sqrt{\text{min}}$) [29] or even with engineered cementitious composite (ECC) with indicative values of sorptivity around 0.028 mg/(mm$^2\sqrt{\text{min}}$) [30], the UHPFRCs under study presented very low sorptivities in the undamaged state (see Figure 5.17). This may be attributed to the very low water content, the absence of coarse aggregates and the dense cementitious matrix that provide a significantly lower capillary porosity and thus very low capillary sorption capacity of UHPFRC.

Figure 5.16 and Figure 5.17 also represent the results cumulative water absorbed during the four h test duration and the sorptivity concerning the cracked specimens. respectively, as a function of COD_{res}. In general, the total water absorbed increased with the imposed deformation, as shown in Figure 5.16. The sorptivity results of cracked specimens exhibited less variation (15% and 13%, for 1.5% and 3.0% fibre contents, respectively) compared to the cumulative water absorbed results (20% and 23% for 1.5% and 3.0% fibre contents, respectively). Besides, results of total water absorbed on cracked specimens, for a given target COD_{load}, exhibited a much larger scatter when compared to non-cracked specimens (see also Tables C.1 and C.2 in Appendix C), which can be explained by the variable crack patterns and the relatively small size of the specimens. The use of larger specimens, with a potentially higher number of cracks, might improve the accuracy of results. Nevertheless, it would make the crack analysis process even more time-consuming.

Despite some differences in terms of crack patterns, sorptivity results of cracked UHPFRC-1.5% and UHPFRC-3.0% specimens remained below 0.044 mg/(mm$^2\sqrt{\text{min}}$). In addition, the maximum measured sorptivity for the cracked UHPFRC specimens, 0.044 mg/(mm$^2\sqrt{\text{min}}$), remains relatively low when compared to that of ordinary concrete (OC) with $w/c = 0.40$, as depicted in Figure 5.17. The sorptivity values

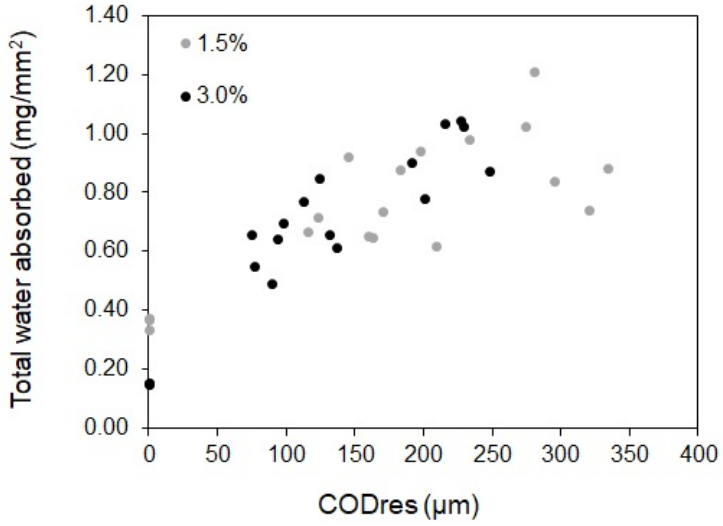

FIGURE 5.16: Total of water absorbed during test.

of cracked UHPFRC specimens possibly represent an upper limit of sorptivity in actual structures because the effect of self-healing was not considered, due to the short experiment duration (4 h). These features provide UHPFRC with distinct barrier qualities, proving that even when cracked, it can act as a protective layer increasing the durability (and service life) in the rehabilitation of structures or elements.

5.4 Conclusions

From the test results and analysis, the following conclusions were established:

- Workability and mechanical properties:
  - UHPFRC non-proprietary mixtures, UHPFRC-1.5% and UHPFRC-3.0%, exhibited self-compacting ability in the fresh state.
  - UHPFRC-1.5% and UHPFRC-3.0% mixtures exhibited a compressive strength of 121 and 147 MPa after 28 days of wet curing, respectively.
  - The four-point bending flexural strength of UHPFRC almost doubled by changing the fibre content from 1.5% to 3.0%; an average flexural strength of 23.3 and 36.2MPa was reached, respectively. This increment of fibre content had less impact on the first cracking stress.
  - Specimens exhibiting higher peak stresses provided more brittle behaviour in the softening region (lower post-peak ductility).
- COD recovery and crack pattern:

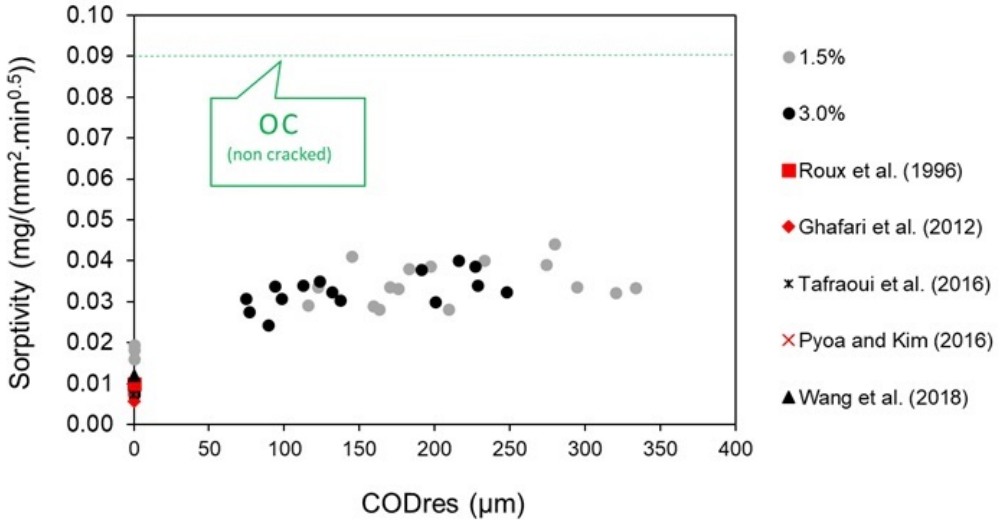

FIGURE 5.17: Sorptivity of UHPFRCs specimens and OC.

- After unloading COD recovery occurred. Residual COD ranged between 116-334 µm and 75-248 µm for UHPFRC-1.5% and UHPFRC-3.0% specimens, respectively.
- A good linear relation was found between COD_{res} and COD_{load} for each fibre content. The COD_{res} values were lower when the fibre content increased to 3.0% for equivalent COD_{load}.
- The average number of cracks observed over a length of 40 mm remained below 6 and 8 for UHPFRC-1.5% and UHPFRC-3.0% specimens, respectively.
- The median of crack width results remained under 53 µm and 34 µm for UHPFRC-1.5% and UHPFRC-3.0% specimens, respectively.
- A significant increase on maximum crack width (> 200µm) was observed with $COD_{res} > 275$µm and $COD_{res} > 200$µm for UHPFRC-1.5% and UHPFRC-3.0%, respectively.

- Capillary water absorption:
  - Average sorptivity results of undamaged UHPFRC specimens were 0.0178 and 0.0076 mg/(mm$^2\sqrt{\text{min}}$) for 1.5% and 3.0% fibre contents, respectively. These results are in agreement with results from previous research works.
  - Despite the observed differences in terms of crack pattern, sorptivity results of cracked UHPFRC specimens remained in the range of 0.024 to 0.044 mg/(mm$^2\sqrt{\text{min}}$).

– The maximum measured sorptivity for the cracked UHPFRC specimens, 0.044 mg/(mm$^2\sqrt{\text{min}}$), remains relatively low when compared to that of conventional concrete ($w/c = 0.4$).

References

[1] Esteban Camacho Torregrosa. *Dosage optimization and bolted connections for UHPFRC ties*. PhD thesis, Universitat Politècnica de València, 2013.

[2] Rui Wang, Xiaojian Gao, Qiyan Li, and Yingzi Yang. Influence of splitting load on transport properties of ultra-high performance concrete. *Construction and Building Materials*, 171:708–718, 5 2018.

[3] Doo-Yeol Yoo and Nemkumar Banthia. Mechanical properties of ultra-high-performance fiber-reinforced concrete: A review. *Cement and Concrete Composites*, 73:267–280, 2016.

[4] Christopher Hall. Water movement in porous building materials—I. Unsaturated flow theory and its applications. *Building and Environment*, 12(2):117–125, 1 1977.

[5] N. Roux, C. Andrade, and M. A. Sanjuan. Experimental study of durability of reactive powder concretes. *Journal of Materials in Civil Engineering*, 8:1–6, 1996.

[6] Thomas Teichmann and Michael Schmidt. Influence of the packing density of fine particles on structure, strength and durability of UHPC. In M. Schmidt, E. Fehling, and C. Geisenhanslüke, editors, *International Symposium on Ultra High Performance Concrete*, pages 313–323, Kassel, Germany, 2004.

[7] Lutz Franke, Gernod Deckelmann, and Holger Schmidt. Behaviour of ultra-high-performance concrete with respect to chemical attack. In *2nd International Symposium on Ultra High Performance Concrete*, pages 453–460, Kassel, Germany„ 2008. Kassel University Press.

[8] Huanghuang Huang, Xiaojian Gao, Hui Wang, and Huan Ye. Influence of rice husk ash on strength and permeability of ultra-high performance concrete. *Construction and Building Materials*, 149:621–628, 9 2017.

[9] A. Rajasekar, K. Arunachalam, M. Kottaisamy, and V. Saraswathy. Durability characteristics of Ultra High Strength Concrete with treated sugarcane bagasse ash. *Construction and Building Materials*, 171:350–356, 5 2018.

[10] Ahmed Tafraoui, Gilles Escadeillas, and Thierry Vidal. Durability of the Ultra High Performances Concrete containing metakaolin. *Construction and Building Materials*, 112:980–987, 2016.

[11] Sukhoon Pyo, Million Tafesse, Heeae Kim, and Hyeong-Ki Kim. Effect of chloride content on mechanical properties of ultra high performance concrete. *Cement and Concrete Composites*, 84:175–187, 11 2017.

[12] S. Abbas, M. L. Nehdi, and M. A. Saleem. Ultra-High Performance Concrete: Mechanical Performance, Durability, Sustainability and Implementation Challenges. *International Journal of Concrete Structures and Materials*, 10(3):271–295, 9 2016.

[13] N.M. Azmee and N. Shafiq. Ultra-high performance concrete: From fundamental to applications. *Case Studies in Construction Materials*, 9:e00197, 12 2018.

[14] J.-P. Charron, E. Denarié, and E. Brühwiler. Permeability of ultra high performance fiber reinforced concretes (UHPFRC) under high stresses. *Materials and Structures*, 40(3):269–277, 4 2007.

[15] Jean-Philippe Charron, Emmanuel Denarié, and Eugen Brühwiler. Transport properties of water and glycol in an ultra high performance fiber reinforced concrete (UHPFRC) under high tensile deformation. *Cement and Concrete Research*, 38(5):689–698, 2008.

[16] Kay Wille and Antoine E. Naaman. Pullout Behavior of High-Strength Steel Fibers Embedded in Ultra-High-Performance Concrete. *ACI Materials Journal*, 109(4):479–488, 7 2012.

[17] Kay Wille and Antoine E. Naaman. Effect of Ultra-High-Performance Concrete on Pullout Behavior of High-Strength Brass-Coated Straight Steel Fibers. *ACI Materials Journal*, 110(4):451–462, 7 2013.

[18] Amin Abrishambaf, Mário Pimentel, and Sandra Nunes. Influence of fibre orientation on the tensile behaviour of ultra-high performance fibre reinforced cementitious composites. *Cement and Concrete Research*, 97:28–40, 7 2017.

[19] Zhiming Ma, Tiejun Zhao, and Xiaochuan Yao. Influence of applied loads on the permeability behavior of ultra high performance concrete with steel fibers. *Journal of Advanced Concrete Technology*, 14(14):770–781, 2016.

[20] Sandra Nunes and Carla Costa. Numerical optimization of self-compacting mortar mixture containing spent equilibrium catalyst from oil refinery. *Journal of Cleaner Production*, 158:109–121, 8 2017.

[21] Ana Mafalda Matos, Sandra Nunes, Carla Costa, and José L. Barroso-Aguiar. Spent equilibrium catalyst as internal curing agent in UHPFRC. *Cement and Concrete Composites*, 104:103362, 11 2019.

[22] EFNARC. The European Guidelines for Self-Compacting Concrete - Specification, Production and Use, 2005.

[23] Ivan Markovic. *High-Performance Hybrid-Fibre Concrete: Development and Utilisation*. PhD thesis, Technische Universiteit Delft, 2006.

[24] Carla A Marchão, Sandra B Nunes, Válter G Lúcio, Ana A Bras, and Joaquim A Figueiras. Development and application of a high performance fiber reinforced self-compacting concrete in post-tensioning anchorage zones. In *8th RILEM International Symposium on Fibre Reinforced Concrete: challenges and opportunities (BEFIB 2012)*, pages 457 – 469, 2012.

[25] Doo-Yeol Yoo, Joo-Ha Lee, and Young-Soo Yoon. Effect of fiber content on mechanical and fracture properties of ultra high performance fiber reinforced cementitious composites. *Composite Structures*, 106:742–753, 12 2013.

[26] Zhang Yunsheng, Sun Wei, Liu Sifeng, Jiao Chujie, and Lai Jianzhong. Preparation of C200 green reactive powder concrete and its static–dynamic behaviors. *Cement and Concrete Composites*, 30(9):831–838, 2008.

[27] Su-Tae Kang, Yun Lee, Yon-Dong Park, and Jin-Keun Kim. Tensile fracture properties of an Ultra High Performance Fiber Reinforced Concrete (UHPFRC) with steel fiber. *Composite Structures*, 92(1):61–71, 1 2010.

[28] Yuxuan Chen, Rui Yu, Xinpeng Wang, Jie Chen, and Zhonghe Shui. Evaluation and optimization of Ultra-High Performance Concrete (UHPC) subjected to harsh ocean environment: Towards an application of Layered Double Hydroxides (LDHs). *Construction and Building Materials*, 177:51–62, 7 2018.

[29] A M Neville. *Properties of concrete*. Longman Group Limited, fifth edition, 2011.

[30] Hezhi Liu, Qian Zhang, Chongshi Gu, Huaizhi Su, and Victor C. Li. Influence of micro-cracking on the permeability of engineered cementitious composites. *Cement and Concrete Composites*, 72:104–113, 2016.

6 Chloride ingress in cracked UHPFRC

One of the most significant causes of deterioration of reinforced concrete elements is the chloride ingress. Most of the studies on chloride penetration in UHPFRC have focused on determining the transport properties of sound, non-cracked specimens. Since the UHPFRC layers might crack under service conditions, changing its local transport properties, a faster ingress of chloride ions and onset of corrosion might occur. Considering this concern, an experimental campaign for assessing chloride ingress in loaded and/or cracked UHPFRC was developed. UHPFRC specimens were firstly preloaded under four-point bending up to a pre-defined crack open displacement. Then, specimens were exposed to wetting-drying cycles in a chloride solution (3.5%), for 1 year. It is argued that the chloride penetration is definitively influenced by the load and cracking conditions, which promoted a higher penetration depth and significant chloride content, above the chloride threshold suggested by European standard, up to a depth of 20 mm. In terms of mechanical performance, flexural strength was not affected; but stiffness might be reduced, particularly when a macro-crack forms.

6.1 Introduction

6.1.1 Scope

Ultra-high performance fibre reinforced composites (UHPFRC) have been successfully employed for structural applications thanks to their outstanding compressive strength and tensile toughness along with its remarkable durability [1], [2], [3]. The exceptional UHPFRC durability is due to its extremely low permeability and diffusivity, achieved by maximising the microstructure packing density, using a high amount of binder and very fine additions, low water to binder ratio (w/b) and absence of coarse aggregates. UHPC is significantly more durable than ordinary concrete (OC) and even high-performance concrete (HPC) [4], [5]. Standard laboratory tests have demonstrated this on undamaged UHPC specimens, employing porosity, chloride ion penetration,

air penetration and water absorption tests [4], [6–9]. Another distinguishing feature of UHPFRC is its behaviour under tension. The tensile response of UHPFRC with sufficient fibre content and/or preferential fibre orientation presents a first elastic branch followed by strain-hardening accompanied by the formation of a stable micro-crack pattern up to the peak stress. After the peak-stress, strain-localisation occurs, and a macro-crack forms with large energy dissipation capacity before complete stress release [10]. Under bending, even with lower fibre contents, an apparent strain-hardening behaviour can occur, with multiple micro-cracks formation [11].

An exciting field of application for UHPFRC is the rehabilitation and strengthening of reinforced concrete structures, particularly when exposed to aggressive environments, in which a new layer of UHPFRC replaces the deteriorated concrete (cracked, carbonated, chloride attacked). The combination of existing concrete with the UHPFRC as a protective layer, which can be reinforced, provides an efficient way of increasing the durability, the stiffness and structural resistance capacity while keeping compact cross-sections. Besides contributing to structural capacity, the tensile performance of UHPFRC is essential for coping with the autogenous deformations and for ensuring water-tightness even when subjected to critical tensile strains. While a first-cracking stress of 7-9 MPa, in uniaxial tension, ensures that the UHPFRC layers remain non-cracked under restrained autogenous deformations, the hardening branch up to the tensile strength of 8-16 MPa and peak strains of 0.2%-0.4% is crucial for ensuring the low permeability even when the UHPFRC suffers significant tensile stresses [12], [13]. This tensile response mostly depends on the fibre-to-matrix bond mechanics [14], [15] and the fibre distribution/orientation [10]. If the former can be tailored during mix-design, the latter is influenced by the rheology, casting methods, geometry and dimensions of the specimen. Therefore, the in-structure tensile response can differ from that characterised in laboratory tests and cracking might occur in the UHPFRC layer.

In terms of UHPFRC durability, one of the most significant causes of deterioration to be considered is chloride ingress, which can cause corrosion of steel fibres or steel reinforcement, in the case of reinforced UHPFRC layers. Most of the studies on chlorides penetration in UHPFRC have focused on determining the transport properties of sound specimens [8]. However, as discussed above, the UHPFRC layers might crack under service conditions, which might change the local transport properties of the new cover, allowing rapid ingress of chloride ions and the onset of corrosion. Thus, further research is needed to study the influence of cracking on UHPFRC resistance to chlorides ingress.

6.1.2 Previous studies on the influence of cracking on the chloride ingress in UHPFRC

So far, few results on the impact of combined mechanical loading or cracking on the chloride ingress in UHPFRC are available in the literature. Main conclusions of publications dealing with this subject are described in the following paragraphs.

Thomas et al. [16] reported an on-site research on the durability of UPHFRC. Three series of UHPFRC beams produced by two different institutions, the U.S. Army Corps of Engineers' (USACE) and the University of New Brunswick (UNB), were placed at the mid-tide level of the marine exposure site at Treat Island. USAGE series consisted of very-high strength fibre-reinforced concrete (VHSC) beams with w/b=0.20 and 3.0% fibres in volume. On the other hand, UNB series consisted of UHPFRC beams either with steel (2.0% in volume – UNB-FM series) or plastic fibres (4.0% fibres in volume – UNB-FO series) using a premixed commercially available UHPC (Ductal). The beams remained from 5 to 15 years in the marine environment, which is approximately equivalent to 100 freeze-thaw cycles per year. Then, some samples from each series were retrieved for mechanical testing, chloride profiling, among other tests. Visual analysis revealed that specimens were in excellent condition with no evidence of surface scaling, mass loss or cracking. Flexural and compressive strength of UNB series, FM and FO, remained intact after marine exposure. In terms of chloride attack, the maximum chlorides penetration depth for all specimens ranged approximately from 7 to 12 mm. Figure 6.1 depicted the chloride profiles for the UHPFRC specimens and compares with the profiles obtained for a high-performance concrete (HPC) (with 8.5% silica fume and $w/c = 0.33$), after 12 years at the mid-tide level at Treat Island. Figure 1 clearly show chloride penetration depth of UHPCs is shallower compared to HPC. The chloride content becomes null at a depth of about 10 mm and 25 mm for UHPC and HPC specimens, respectively. Besides, the chloride content close to specimens' surface is significantly lower on UHPC specimens (roughly 0.2%) while in HPC was above 1.0%. Thus, it can be expected UHPC to provide considerably more protection to embedded steel reinforcement [16].

Ma et al. [17] investigated the influence of applied loads, both of compression and tension, on the chloride permeability of a UHPFRC ($w/b = 0.20$ and 2% volume of steel fibres). Different tensile and compressive load levels applied to UHPFRC specimens, namely, 0%, 30%, 50% and 80% of peak tensile and compressive load, respectively. A dumbbell-shaped specimen was used in the uniaxial tensile test and prismatic specimens of $100 \times 100 \times 300$ mm^3 size in the compressive test. After applying the target load and unloading, the chloride penetration test was conducted,

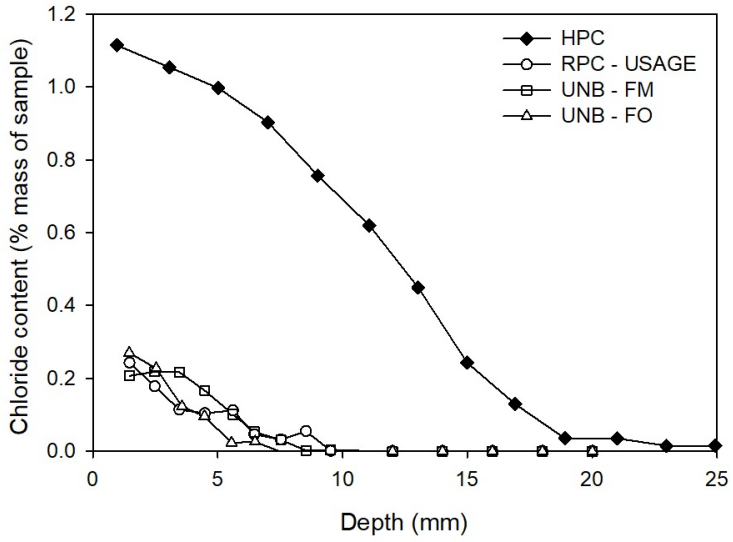

FIGURE 6.1: Chloride Profiles for UHPC and comparison with HPC [16].

which consisted of exposing specimens to a 5% NaCl solution during 7 and 28 days for tensile loaded specimens, and during 28 days for UHPFRC compressive loaded specimens. Besides, the authors evaluated the influence of self-healing on the permeability to chlorides of UHPFRC after suffering the loading damage. For that purpose, the specimens were moved into a saturated $Ca(OH)_2$ solution after unloading, during 28 days regarding tensile loaded specimens, and 7 and 28 days in the case of compressive loaded specimens. Afterwards, these specimens were exposed to chlorides following the procedure previously described. At the end of testing, the chloride content was evaluated, at several depths up to 12 mm, as presented in Table 6.1 and Table 6.2, for tensile and compressive loaded specimens, respectively.

Concerning tensile loaded specimens, the maximum chloride content decreases with the increase of penetration depth, and it increases with the increase of applied load and chloride penetration time (see Table 6.1). The increments of chloride content were not obvious when the applied tensile loading was 30% of ultimate tensile stress (see lines 2 and 9 in Table 6.1); however, they significantly increased when the applied tensile stress was above 50% of ultimate tensile stress (see lines 3-4 and 10-11 in Table 6.1), since more cracks passageways are provided for chloride water solution penetrate UHPFRC, see Table 6.1. Such as, the maximum chloride content at 0%, 30%, 50% and 80% of ultimate tensile stress was 0.143%, 0.165%, 0.383% and 0.502% after 28 days chloride exposure, respectively (see Table 6.1, lines 9 to 12). The chloride content of UHPFRC after self-healing was significantly lower (namely close to surface), as shown in Table 6.1 by comparing lines 2-4 with lines 5-7, and lines 9-11

Table 6.1: Chloride content of UHPFRC after suffering different tensile loadings [17].

Line nº	Conditioning of specimens	Percentage of ultimate tensile stress	Chloride content (%) at different penetration depths			
			1 mm	5 mm	10 mm	12 mm
1	Loading + 7 days chloride exposure	0%	0.103	0.037	0.036	0.037
2		30%	0.115	0.037	0.036	0.036
3		50%	0.213	0.057	0.041	0.037
4		80%	0.328	0.066	0.038	0.037
5	Loading + 28 days self-healing + 7 days chloride exposure	30%	0.102	0.038	0.036	0.037
6		50%	0.162	0.051	0.037	0.038
7		80%	0.296	0.059	0.039	0.036
8	Loading + 28 days chloride exposure	0%	0.143	0.054	0.037	0.036
9		30%	0.165	0.057	0.038	0.036
10		50%	0.383	0.127	0.041	0.036
11		80%	0.502	0.286	0.064	0.037
12	Loading + 28 days self-healing + 28 days chloride exposure	30%	0.143	0.049	0.038	0.036
13		50%	0.343	0.084	0.039	0.036
14		80%	0.482	0.217	0.112	0.037

with lines 12-14, for 7 and 28 days chloride exposure, respectively. This phenomena demonstrated that the self-healing treatment could improve the resistance to chloride penetration [17]. The chloride content also increased with the increase of applied compressive loading. The maximum chloride content of UHPFRC loaded with 0%, 30%, 50% and 80% of ultimate compressive strength was 0.156%, 0.351%, 0.430% and 0.466%, respectively, see lines 1-4 of Table 6.2. Also, the maximum chloride content of UHPFRC after exposure to the self-healing treatment decreased as shown in lines 5-10 of Table 6.2, especially when treatment lasted 28 days (lines 8-10, Table 6.2). The authors concluded that processing the UHPFRC through a self-healing treatment is an effective method to repair the UHPC after suffering loading damage [17].

Wittmann et al [18] studied the influence of several levels of tensile loading on chloride penetration in UHPFRC (w/b=0.20 and 1.5% volume of steel fibres). Dumbbell specimens were exposed to sustained tensile stress in a stiff steel rig with the following stress levels: 30%, 50%, and 80% of the tensile strength. Besides, specimens suffering the same damage (30%, 50%, and 80% of the tensile strength) but in the unloaded

Table 6.2: Chloride content of UHPFRC after suffering different compressive loadings [17].

Line nº	Conditioning of specimens	Percentage of ultimate tensile stress	Chloride content (%) at different penetration depths			
			1 mm	5 mm	10 mm	12 mm
1	Loading + 28 days chloride exposure	0%	0.156	0.049	0.035	0.037
2		30%	0.351	0.088	0.032	0.041
3		50%	0.43	0.12	0.043	0.038
4		80%	0.466	0.18	0.045	0.043
5	Loading + 7 days self-healing + 28 days chloride exposure	30%	0.325	0.101	0.038	0.037
6		50%	0.417	0.129	0.045	0.038
7		80%	0.456	0.174	0.046	0.044
8	Loading + 28 days self-healing + 28 days chloride exposure	30%	0.253	0.057	0.036	0.036
9		50%	0.312	0.104	0.040	0.039
10		80%	0.347	0.125	0.046	0.039

state, as well as, non-damage specimens (0%) were also tested. Chloride capillary absorption under imposed constant strain was performed using a box 40×100 mm^2 fixed to the surface of the specimen. The capillary penetration of 5% NaCl solution was performed during 28 days. Besides, to study the potential of self-healing, identical pre-damaged and unloaded specimens were placed in a saturated $Ca(OH)_2$ solution for 28 days immediately after application of the tensile stress. After self-healing treatment, chloride capillary absorption was evaluated by applying the procedure described above. At the end of chloride exposure, the chloride content was determined as can be seen in Table 6.3.

Non-cracked specimens (line 1 in Table 6.3) absorbed a fewer chlorides (0.139% at specimen's surface) and the content became very low after 2.5 mm depth. Under tensile load, the chloride ingress slightly increased for tensile stresses corresponding to 30% of the tensile strength (line 2 in Table 6.3). In case the higher stress, 50% and 80% of the tensile strength, considerable amounts of chloride were transported into the specimens, 0.514% and 0.723% at specimen's surface, respectively, presenting still significant amount of chlorides up to 9.5 mm depth, see lines 3 and 4 in Table 6.3. For the same load levels, but tested in an unloaded state, lower amount of chlorides penetrated in UHPFRC specimens compared with the previous ones as can be seen comparing lines 2-4 and lines 5-7 of Table 6.3. As expected, less chlorides penetrated after self-healing storage, see lines 8-10 in Table 6.3. The authors concluded that if actors in the design and construction process did not consider the influence of applied

Table 6.3: Chloride content of UHPFRC after suffering different compressive loadings [18].

Line nº	Conditioning of specimens	Percentage of ultimate tensile stress	Chloride content (%) at different penetration depths				
			0.5 mm	2.5 mm	5.0 mm	9.5 mm	15 mm
1	28 days chloride exposure (uncracked)	0%	0.139	0.058	0.048	0.031	0.034
2	Under load + 28 days chloride exposure	30%	0.233	0.092	0.056	0.034	0.034
3		50%	0.514	0.264	0.189	0.064	0.036
4		80%	0.723	0.464	0.391	0.139	0.036
5	Unloaded + 28 days chloride exposure	30%	0.167	0.078	0.056	0.033	0.036
6		50%	0.384	0.176	0.131	0.039	0.037
7		80%	0.511	0.308	0.285	0.067	0.04
8	Unloaded + 28 days self-healing + 28 days chloride exposure	30%	0.145	0.070	0.045	0.036	0.033
9		50%	0.344	0.176	0.084	0.036	0.033
10		80%	0.479	0.227	0.216	0.104	0.040

tensile stress, the prediction of service life might be unrealistic [18].

Parant et al. [19] studied the effect of cracking, loading and chlorides on mechanical performance of an UHPFRC developed by the authors, with $w/b = 0.16$ and 11% volume of steel fibres composed of 3 fibre sizes: a micro-fibre or steel wool, a straight meso-fibre with 5 mm length, and a twisted macro-fibre of about 30 mm length. Two different curing types were applied: heat-treated during four days at 90 °C and standard air-cured at 20 °C ambience. In brief, slabs specimens were damaged through 4 points bending method up to specific service load (30 MPa and 42 MPa to air-cured and heat-treated samples, respectively). Then, specimens suffered 2500 fatigue cycles. Finally, the specimens, for each of the two curing, were kept in four different environmental ambiences:

- Virgin specimens (V): neither damaged by fatigue, neither charged nor corroded. They stayed at laboratory ambience (20 ± 2 °C and $RH = 50\% \pm 10$).
- Damaged and corroded specimens (DC): after fatigue cycles, they were left in an aggressive environment, unloaded.
- Damaged and loaded under flexure specimens (DF): after fatigue cycles, they were kept in the creep frame.

- Damaged, corroded and loaded under flexure (DCF): after fatigue cycles, they were kept in the creep frame in an aggressive environment.

The aggressive environment, in which DC and DCF specimens were kept, consisted of a weekly cycle with one wetting day and six drying days during 30 weeks in a chloride solution (5% NaCl, 20 °C). At the end of exposure to fatigue cycles and/or aggressive media, the flexural behaviour was assessed.

In general, results showed no degradation of the UHPFRC mechanical properties due to the aggressive environment and/or loading. Control specimens (V) presented the lower bending strength, and their Young's modulus was respectively 53 GPa and of 58 GPa for the untreated specimens and those heat-treated. DCF specimens displayed the highest strength and a quasi-total recovery of their initial stiffness. DC and DF specimens exhibited similar mechanical behaviours, and their strength was higher than the virgin specimens. The DC stiffness was initially the same one as the virgin specimens, but it decreased when the tensile bending stress reached 5 MPa. After 5 MPa, the curve got closer to one of the DF specimens. For specimens subjected to the wetting–drying cycles (DC), it seemed that self-healing took place. However, as the cracks were partially or even fully closed, fault of maintained loading and the initial fineness of the cracks, the water flow until the fracture tip was limited in-depth. Still, that was insufficient to lead to a total recovery of initial stiffness. The results obtained on the specimens pre-damaged by fatigue and maintained loaded in the aggressive environment (DCF) can be explained either by a self-healing of the matrix between the lips of the micro-cracks and by partially healing of fibres–matrix interface. The authors concluded that results obtained might be attributed to the mix design of the UHPC matrix and the high-volume fraction of the reinforcement; that produced a diffuse micro-cracking pattern and a hardening behaviour. The very fine crack widths created, allowed a fast-self-healing of micro-cracks, limiting the influence of the external environment consequently.

Chunping et al. [20] investigated the durability of flexural loaded UHPFRC specimens (w/b=0.16 and 2% volume of steel fibres) with nano-TiO_2 incorporation, namely, 0 and 1%, and so-called, UHPC-T0, and UHPC-T1, respectively. The applied load was 50% of the ultimate flexural capacity and both the compressive and tensile surfaces of the specimens were exposed to chlorides solution (10% NaCl) for 90 days. Then, the specimens were dried, and powder samples collected from the exposed surface at different depths. After 90 days of immersion, the chloride diffusion depth in all UHPC specimens were less than 5 mm. When the UHPC specimens were non-loaded, the chloride concentrations of UHPC-T0 and UHPC-T1 specimens at a thickness of 0-5 mm were almost the same, 0.15%. Under a flexural load, the chloride concentration

in the tensile region of the specimens increased, while the chloride concentration in the compressive area decreased. Thus, the tensile stress negatively influenced the chloride ingress resistance of the UHPC due to the micro-cracks, accelerating the chloride penetration process. Compared with the control UHPC, the addition of nano-TiO_2 particles reduced the chloride concentration in the tensile region. This could be because nano-TiO_2 could improve the toughness of UHPC [20].

6.1.3 Research objectives

The author developed a new UHPFRC mixture using locally available raw materials (Europe). This mixture aimed to be functional to rehabilitation applications (without special curing treatments) and able to be cast on-site (self-compacting). Besides, it was optimised in terms of early-age autogenous shrinkage, durability, cost and eco-efficiency (lower cement + silica fume contents and incorporating a waste material from Portuguese oil refinery) (see Chapter 3).

An evaluation of several durability indicators of new developed UHPC (without steel fibres) to determine the resistance against various aggressive agents was conducted in a previous study [21] and results of durability indicators show that new UHPC presents very high durability compared to OC and even HPC. Besides, it corroborates with the range of durability parameters found in literature for other UHPFRC [21]. The experimental characterisation of the capillary transport properties on cracked and non-cracked UHPFRC, with different fibre dosages, was also presented in a previous work [22], and it showed its excellent tightness to water. However, it is needed to determine whether this UHPFRC retains its long-term durability when exposed to chlorides, in the case of cracking, under service conditions.

This concern is addressed in the current Chapter by evaluating the chlorides ingress in non-cracked, cracked-unloaded and cracked-loaded UHPFRC specimens, with a typical fibre content of 3.0%. After different damage levels were introduced on prismatic specimens, by means of four-point bending test (target CODs of 300, 350 and 400 µm), the crack pattern observed on the tensile face of the unloaded specimens was characterised; and then the specimens were then subjected to wetting–drying cycles, using a concentrated chloride solution (3.5% NaCl), during a period of 1 year. The main goal of this research was to develop an understanding of how micro- and macro-cracks formation in UHPFRC facilitates the chlorides ion penetration.

6.2 Materials and methods

6.2.1 Raw materials and mixture proportions

UHPFRC under study consists of a ternary binder mixture. The main constituent is CEM I 42.5R Portland cement complying with EN 197-1. The selected SCM were, silica fume (specific surface area of 19632 $m^2\,kg^{-1}$ and a SiO_2 content > 90%) fulfilling the requirements of EN 13263-1 and limestone filler (specific surface of 550 $m^2\,kg^{-1}$ and $CaCO_3$> 98%), complying with the requirements of EN 12620. The aggregate fraction is constituted by 85% siliceous natural sand (0-1 mm) and 15% ECat (a spent equilibrium catalyst, generated by Sines Refinery, Portugal), by volume. ECat presents high specific surface (150 070 $m^2\,kg^{-1}$) with high water absorption of 30%, by mass. Thus, it was necessary to add extra water for ECat's absorption during mixing. More details concerning the origin and properties of ECat can be found elsewhere [8]. A polycarboxylate type superplasticiser with a specific gravity of 1080 $kg\,m^{-3}$ and 40% solid content and potable water were included. As reinforcement, 3.0% by volume of smooth short steel fibres, with 13 mm length and 0.21 mm diameter, and 2750 MPa of tensile strength, were used. Table 6.4 presents the mixture proportions of the new UHPFRC.

Table 6.4: UHPFRC mixture proportions.

	Raw Materials	$kg\,m^{-3}$
Binder	Cement	690.2
	Silica fume	33.6
	Limestone filler	250.6
Aggregates	ECat	155.5
	Siliceous sand	775.0
Reinforcement	Steel Fibres	235.0
Admixture	Superplasticizer	19.5
Water	Mixing water	160.9
	ECat's absorption water	46.6

6.2.2 Specimens manufacture and curing

UHPFRC mixtures were produced using a mixer as specified in with EN 196-1. The mixing procedure followed the steps described in Table 6.5. Several prismatic specimens ($40 \times 40 \times 160$ mm^3) were moulded in one lift without any mechanical vibration

due to the self-compacting ability of the mixtures. The number of specimens produced for each condition is detailed in Table 6.6. The specimens were then covered with a plastic sheet and demoulded after one day and then water cured in a controlled environment chamber at 20 ± 2 °C until the testing age.

The referencing of specimens considered the fibre content, the target COD and the specimen replicate number. For example, 3.0%-350-1, corresponds to a specimen (replica) number one, incorporating 3.0% steel fibres and a target COD_{load} of 350 µm. Specimens for assessment of flexural strength were named as 3.0%-W28-i and 3.0%-W379-i corresponding to a water curing time of 28 and 379 days, respectively.

Table 6.5: Mixing sequence.

Steps	*Duration*	*Speed*
Add ECat (dry state) + 80% mixing water + ECat water absorption	5.0 min	140 ± 5 rot min^{-1}
Add cement + limestone filler + silica fume + sand and mix	2.5 min	
Stop to scrape material adhering to the mixing bowl and mix	2.5 min	
Add the rest of the water + 75% of Sp and mix	2.5 min	
Add the rest of Sp and mix	1.5 min	
Add fibres and mix	2.0 min	

6.2.3 Mechanical testing

Flexural strength through a four-point bending test of UHPFRCs specimens assessed at 28 and 379 days for water cured specimens and at 138 and 379 days for samples exposed to chlorides (see Table 6.6).

The device for applying loads (see Figure 6.2) consists of 1) two supporting rollers; 2) two upper rollers (loading), which divides the load applied by the machine equally between the two rollers. Rollers were manufactured from steel and have a circular cross-section with a diameter of 10 mm. They are at least 10 mm longer than the width of the test specimen. The distance, I, between the outer rollers (i.e. the span) is equal to 3d, where $d = 40$ mm is the width of the specimen. The distance between the loading rollers is equal to d. The loading rollers are equally spaced between the support rollers as shown in Figure 6.2. All dimensions were adjusted from the test

TABLE 6.6: Experimental plan: number of prismatic specimens ($40 \times 40 \times 160$ mm^3) prepared for each test condition and outcomes (Notes: L-d = Load-displacement).

Specimens reference	N.º of specimens	Curing	Cracking age	Target COD_{load}	Testing age	Outcomes
Four-point bending tests						
3.0%-W28d-i	5	Water at 20ºC up to 28 d	-	-	28 d	L-d curves
3.0%-W379d-i	5	Water at 20 °C up to 379 d	-	-	379 d	L-d curves, Initial chloride content (C_0)
Exposure to wetting-drying cycles (3.5% NaCl water solution, 20 °C) after cracking at 28 d						
3.0%-0-i (uncracked and exposed to chlorides)	5	Water at 20ºC up to 28 d	28 d	0 µm	379 d	L-d curves after chlorides cycles, Chlorides profile and Chloride penetration depth
3.0%-300-i (exposed to chlorides in loaded state)	2	Water at 20ºC up to 28 d	28 d	300 µm	138 d	L-d curves after chlorides cycles
	2					Chlorides profile
	3				379 d	L-d curves after chlorides cycles
	2					Chlorides profile and Chloride penetration depth
3.0%-350-i (exposed to chlorides in unloaded state)	5	Water at 20ºC up to 28 d	28 d	350 µm	379 d	L-d curves after chlorides cycles
	3					Crack pattern, Chlorides profile and Chloride penetration depth
3.0%-400-i (exposed to chlorides in unloaded state)	5	Water at 20ºC up to 28 d	28 d	400 µm	379 d	L-d curves after chlorides cycles
	3					Crack pattern, Chlorides profile and Chloride penetration depth

FIGURE 6.2: Four point bending test.

set-up suggested in EN 12390-5. The flexural strength (f_{cf}) can be computed from the maximum load sustained (F_{max}) as follows:

$$f_{\mathrm{cf}} = \frac{F_{\mathrm{max}} \times I}{d_1 \times {d_2}^2} \tag{6.1}$$

where $I = 120$ mm is the distance between the supporting rollers (mm), $d_1 = 40$ mm is the width of the test beam (mm) and $d_2 = 40$ mm corresponds to depth of tested beam (mm).

6.2.4 Cracking procedure

UHPFRC specimens cracking was produced through the four-point bending test, using the test configuration described in the previous section. After 28 days of water curing, prismatic specimens were cracked by imposing different crack open displacements (COD), 300, 350 and 400 µm, considering possible service conditions and obtaining different crack patterns. The number of specimens used for each test condition is in Table 6.6. Two LVDTs, with a range of 5 mm and a precision of 1.6 µm, were installed at the front and back surfaces of each specimen, perpendicular to the loading direction, to monitor the COD evolution, see Figure 6.2. The tests were carried out in a 300 kN Instron testing machine, under displacement control with a displacement rate of 0.003 $\mathrm{mm\,s^{-1}}$, which was kept constant during the experiment. When the target COD was achieved ($\mathrm{COD_{load}}$), the specimens 3.0%-350-i and 3.0%-400-i were unloaded, and the residual COD was recorded ($\mathrm{COD_{res}}$). Then, the pattern of the crack observed in the tensile face of these specimens characterised

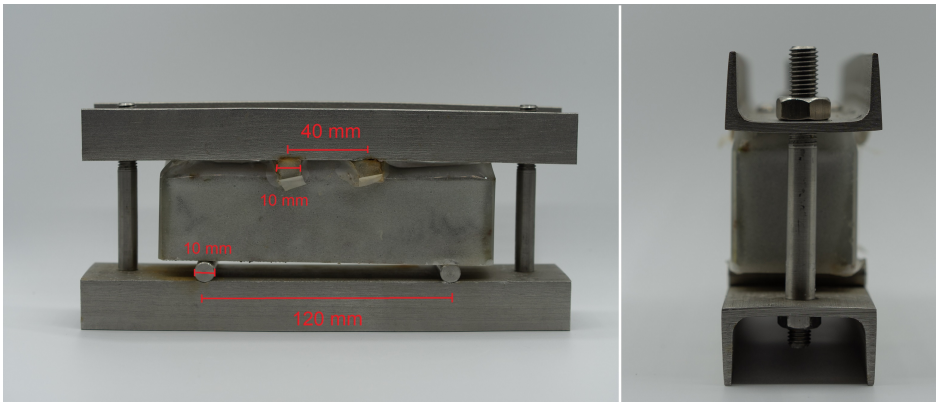

FIGURE 6.3: Illustration of the loading device.

according to the procedure described in section 6.2.5. Meanwhile, specimens were allocated in the testing room test (at 20 ± 2 and $RH = 50 \pm 5\%$) during seven days before starting the chloride cycles described in section 6.2.6.

In the particular case of 3.0%-300-i specimens, when the predefined $COD_{\text{load}} = 300\mu m$, the specimens were unloaded and taken out from the Instron machine. Then, they were immediately allocated on a stainless-steel frame, as shown in Figure 6.3, while keeping the LVDTs on the specimens. Subsequently, the specimens were re-loaded up to the predefined COD_{load} of 300 µm using threaded rods tightened by a torque wrench. Preserving the LVDTs on the specimen allowed achieving the target COD again. Afterwards, LVDTs were removed carefully, and the frame sustained the target COD. Thus, 3.0%-300-i specimens were subject to wetting-drying chlorides cycles in a loaded state.

Before initiating the wetting-drying cycles, the side and compression surfaces of all prisms were sealed using a waterproof tape to ensure the chloride penetration only through the cracked surface, as can be seen in Figure 6.3 and Figure 6.4. Is must be noted that it was not possible to protect the loaded surfaces of specimens kept in the stainless-steel frame (3.0%-300-i).

6.2.5 Characterisation of the crack pattern

Before cracking the specimens, a coloured grid was marked on the tensile face of the specimen (in between the two loading points) as shown in Figure 6.4 and detailed in Figure 6.5, to facilitate the crack pattern characterisation. Since UHPFRC develops multiple micro-cracking before reaching the peak load, often crack path branching occurs which makes it very difficult to distinguish every single crack and to count the total number of cracks. Therefore, in this study only the cracks found over

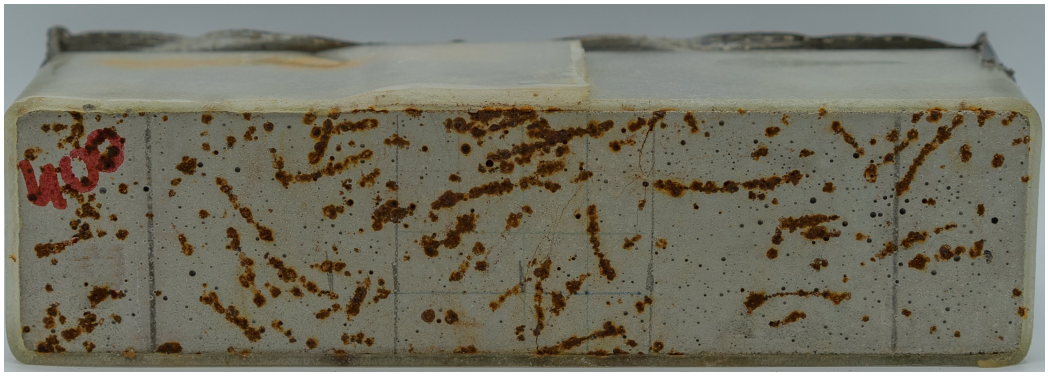

FIGURE 6.4: Tensile surface of specimen 3.0%-400-5 after cracking.

three horizontal lines (A, B and C shown in Figure 6.5) were characterised, within the central 40 mm length zone, corresponding to maximum bending moment zone. Besides, the 40 mm length was subdivided into four equal segments of 10 mm length each (Figure 6.5) to allow easier localisation of each crack. This allowed organising the data of crack pattern characterisation in the form of a matrix (3×4), corresponding to 3 lines (A, B and C) by four columns (segments 1, 2, 3 and 4). The cracks found over each line were observed, in the unloaded state, and photographed using a Microscope Multizoom Nikon AZ100 with the help of a PC and a DS-U2 digital camera. The objective was a Nikon-AZ Plan Fluor 5x, and the magnification range was adjusted to crack dimension. A typical photo obtained is presented in Figure 6.6. Later, using image analysis software (ImageJ), the crack width was evaluated taking six measurements along each crack, as shown in Figure 6.6. The median of the six measures taken along each crack (see Figure 6.6) was, in this study, the representative value of the crack width. On loaded specimens, kept inside the frame, it was not possible to perform the crack pattern characterisation.

6.2.6 Exposure to chloride rich environment

For the long term chloride experiment the 3.0%-0-i (non-cracked), 3.0%-300-i (loaded, kept in stainless steel frame), 3.0%-350-i and 3.0%-400-i (unloaded, with residual cracks) specimens were tested, as described in Table 6.6. As mentioned before, the side surfaces of all prisms were sealed to ensure the chloride penetration only through the cracked surface. The tensile surfaces of the specimens were exposed to chlorides, by partially immersing the specimens in a chloride solution simulating seawater (3.5% NaCl). The specimens were subjected to a weekly based wetting-drying cycle consisting of two days of partial immersion and five days of drying at 20 °C and $RH = 50\%$. Most specimens were subjected to chloride cycles during 379 days. In the case of 3.0%-300-1, 3.0%-300-2, 3.0%-300-3 and 3.0%-300-4 specimens, the wetting-drying

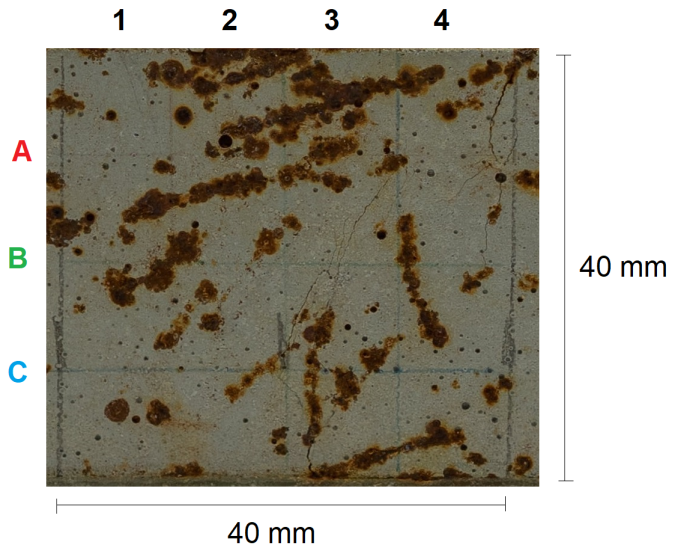

FIGURE 6.5: Schematic matrix for crack opening measurement on maximum bending moment zone for a specimen 3.0%-400-5.

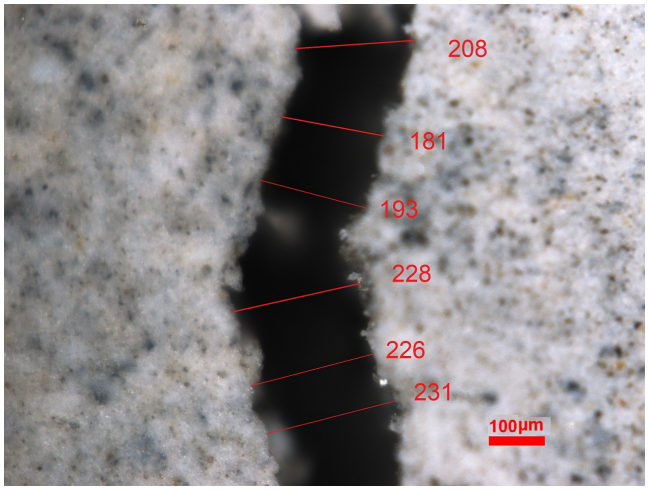

FIGURE 6.6: Typical photo made from measurement of one crack (specimen 3.0%-400-5, localisation in the matrice: A-4).

cycles were stopped after 138 days (see Table E.2 in Appendix E) for an earlier assessment of the chlorides penetration in UHPFRC, as well as, the four-point flexural behaviour. The chlorides bath was kept covered to avoid as much as possible the water evaporation. The level of the solution in the box was measured once a week and refilled when necessary.

6.2.7 Chloride penetration depth and chloride content

After the chloride exposure described in section 6.2.6, some specimens were used to assess chloride penetration depth and the chloride content (see details in Table 6.6). These specimens were dry cut longitudinally in two parts with a diamond saw. A 0.1 molar silver nitrate solution was sprayed on one of the parts. The chloride penetration depth was then measured from the visible white silver chloride precipitation. An example of that is illustrated in Figure 6.7.

The other half of the cut specimens was used for chemical analysis to determine the chloride content. The samples were taken from the central part of the specimen (in between the two load points) in the direction of chloride penetration on a cracked and non-cracked area. The dry drilling method sampling procedure, according to RILEM Recommendation TC 178-TMC [23] was employed to obtain powdered samples corresponding to depth steps of approximately 5 mm. The steel fibres were removed from the powder sample using a magnet. As reference, the initial chloride content (C_0) was determined on a specimen not exposed to chlorides, following the same procedure and at the same depths. The determination of chlorides content followed the procedure described in EN 196-2, which gives the total chloride content expressed as chloride ion (Cl^-) by mass of sample without fibres (UHPC).

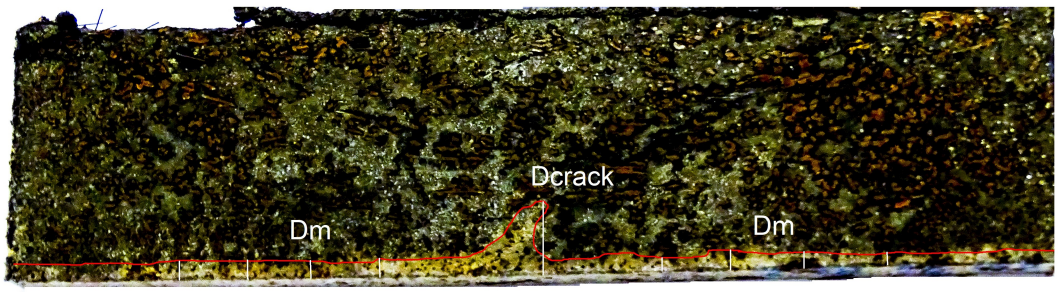

FIGURE 6.7: Chloride penetration profiles on a cracked specimen.

6.3 Results and Discussion

6.3.1 Crack pattern characterisation

6.3.1.1 COD recovery after unloading (COD_{load} and COD_{res})

Figures 6.8-b, -c and -d show the load-displacement curves obtained while establishing target COD_{load}, as well as, the curves of specimens tested under four-point bending up to the beginning of softening region, at 28 days (grey lines). These curves are also depicted in Figure 6.8-a up to the end of test. Figures 6.8-b, -c and -d show that the target values of COD_{load} were achieved with a reasonable approximation ($\pm 15\%$), for all tested specimens. Table E.2 in Appendix E presents data regarding the main cracking parameters for each specimen, i.e., maximum load achieved during the cracking procedure (Fcr,max) and the values of COD_{load} and COD_{res}. COD_{res} obtained after unloading as a function of COD_{load} are represented in Figure 6.9, showing a good linear relation between COD_{res} and COD_{load}. This trend corroborates with previous studies of by Ma et al. [17] and also with previous studies carried out by the author in Chapter 5 (presented in Figure 6.9 in red colour).

6.3.1.2 Crack pattern characterisation

The matrices with data on measured crack widths (in µm) are presented in Appendix D. A colour scale was adopted to allow easy visualisation of crack open dimension. A summary of crack pattern parameters, namely, the average number of cracks counted over lines A, B and C (N); the minimum (Min), maximum (Max) and median crack width (Med) can be consulted in Appendix E.

Concerning the number of cracks, no clear tendency was found, but it seems they slightly increase with the damage level. The average number of cracks observed over a length of 40 mm remained below 9 (see Figure 6.10-a) while the median of crack width results is under 32 µm (see Figure 6.10-b) and it seems they slightly increase with the damage level. These results agree with previous findings of the author (Chapter 5) depicted in Figure 6.10 (red marks). Figure 6.10-c shows the maximum crack width results in which can be drawn that: up to a COD_{res} of about 200 µm, the maximum crack width remained below 75 µm; and a more significant increase of maximum crack width (> 200 µm), indicative of macro-crack formation, occurs for higher COD_{res}.

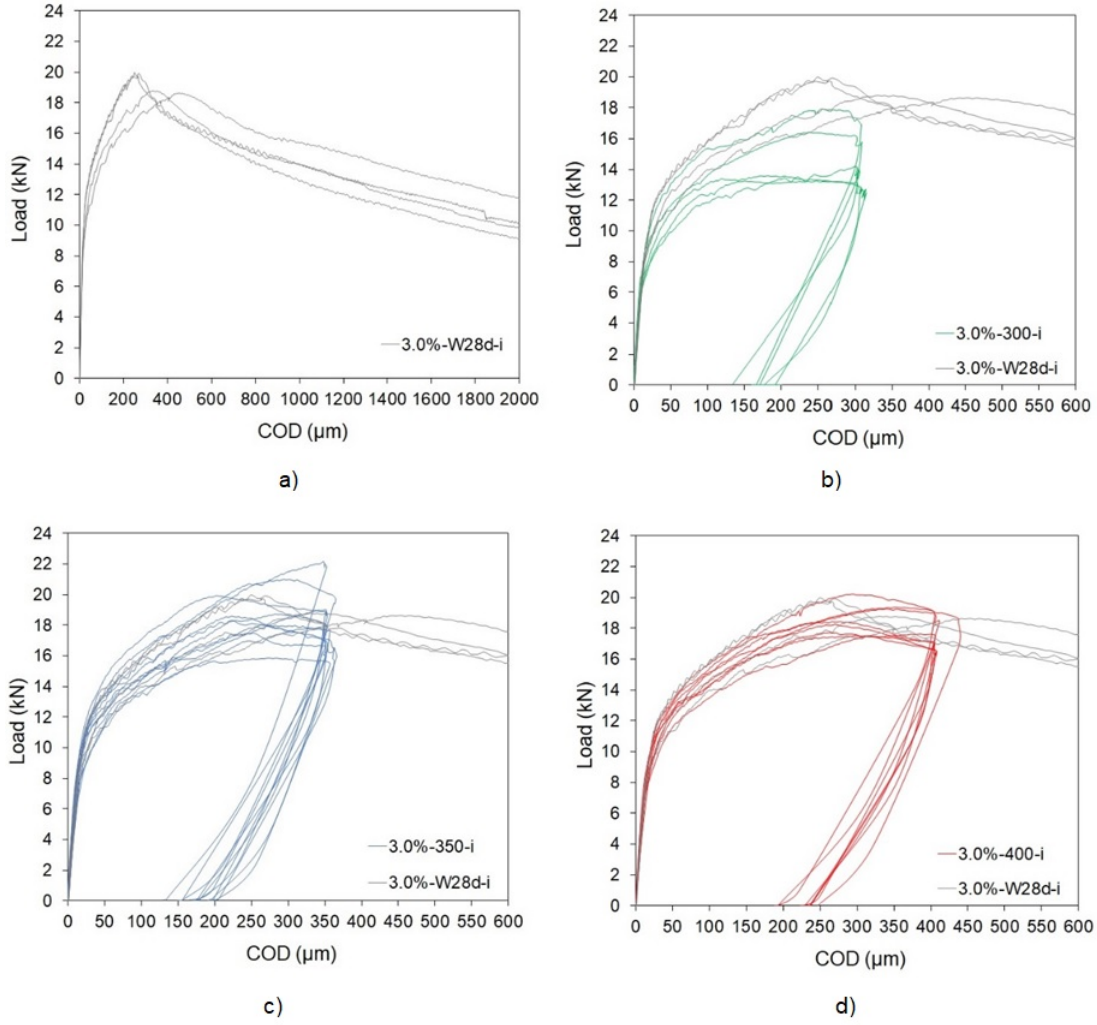

FIGURE 6.8: a) Four-point bending load-displacement relationship after 28 days of water curing and Load-displacement curves obtained at 28 days while establishing target: b) $COD_{\text{load}} = 300$ µm, c) $COD_{\text{load}} = 350$ µm and d) $COD_{\text{load}} = 400$ µm.

6.3.2 Mechanical properties

6.3.2.1 Water cured specimens

Figure 6.11 shows the flexural behaviour of UHPFRC specimens, including the individual load-displacement curves for all the valid specimens. For each testing age, 28 and 379 days, five specimens were tested, and at least four results were considered valid (the crack localised within the measuring length covered by the LVDTs). Average results, i.e., average peak load (Fmax) and COD at F_{max} ($COD_{F_{max}}$) are summarised in Table 6.7 (2^{nd} and 3^{rd} lines for 3.0%-W28-i and 3.0%-W379-i specimens, respectively) and Table E.1 of Appendix E contains the detailed results. As can be observed in Figure 6.11, mixtures exhibited flexural hardening behaviour. The

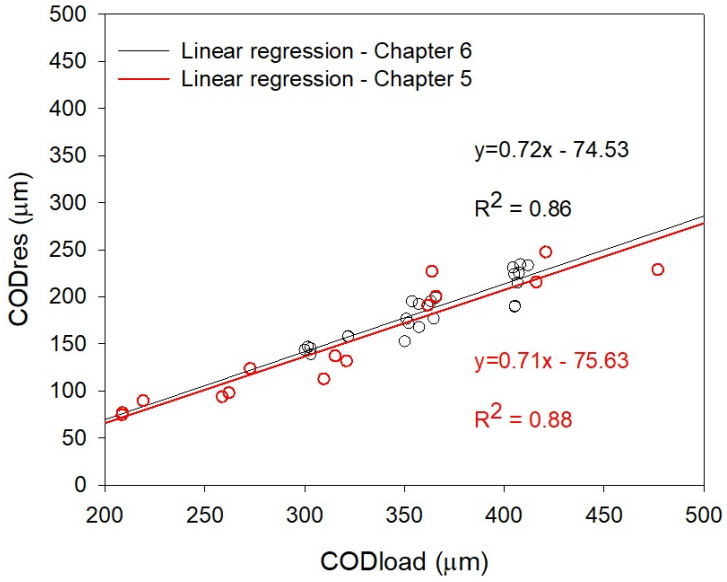

FIGURE 6.9: Relation between COD_{load} and COD_{res}.

flexural hardening stage (before the peak load) is characterised by multiple cracking formation, without localisation of any significant crack. After the peak load, a softening behaviour is observed, which is characterised by a macro-crack formation. The average peak forces, F_{max}, achieved after 28 and 379 days of water curing were 19.3 ± 0.6 and 19.1 ± 1.7 kN, respectively. Specimens exhibiting higher peak stresses provided more brittle behaviour in the softening region (lower post-peak ductility) [24]. From Figure 6.11-b, it can be observed that some of the 3.0%-W379-i specimens exhibit higher initial stiffness, which might be due to further microstructure development with increasing curing time.

6.3.2.2 Specimens exposed to chlorides

After wetting-drying cycles, the specimen's 3.0%-300-i were removed from the frame and then left at rest for one week before being reloaded to failure under four-point bending test. The remaining specimens, 3.0%-0-i, 3.0%-350-i, 3.0%-400-i, were also kept in rest one week before mechanical tests.

Figure 6.12 presents curves of reloading to failure for the different tested series. Table 6.7 summarises the average results for each set of specimens ($F_{max}$and $COD_{F_{max}}$) and Table E.2 of Appendix E reports the individual results. The comparison of the specimen's flexural behaviours shows the following points:

- Non-cracked specimens (3.0%-0-i) showed similar average peak loads to the cracked specimens; however, their initial stiffness is, in general, higher.

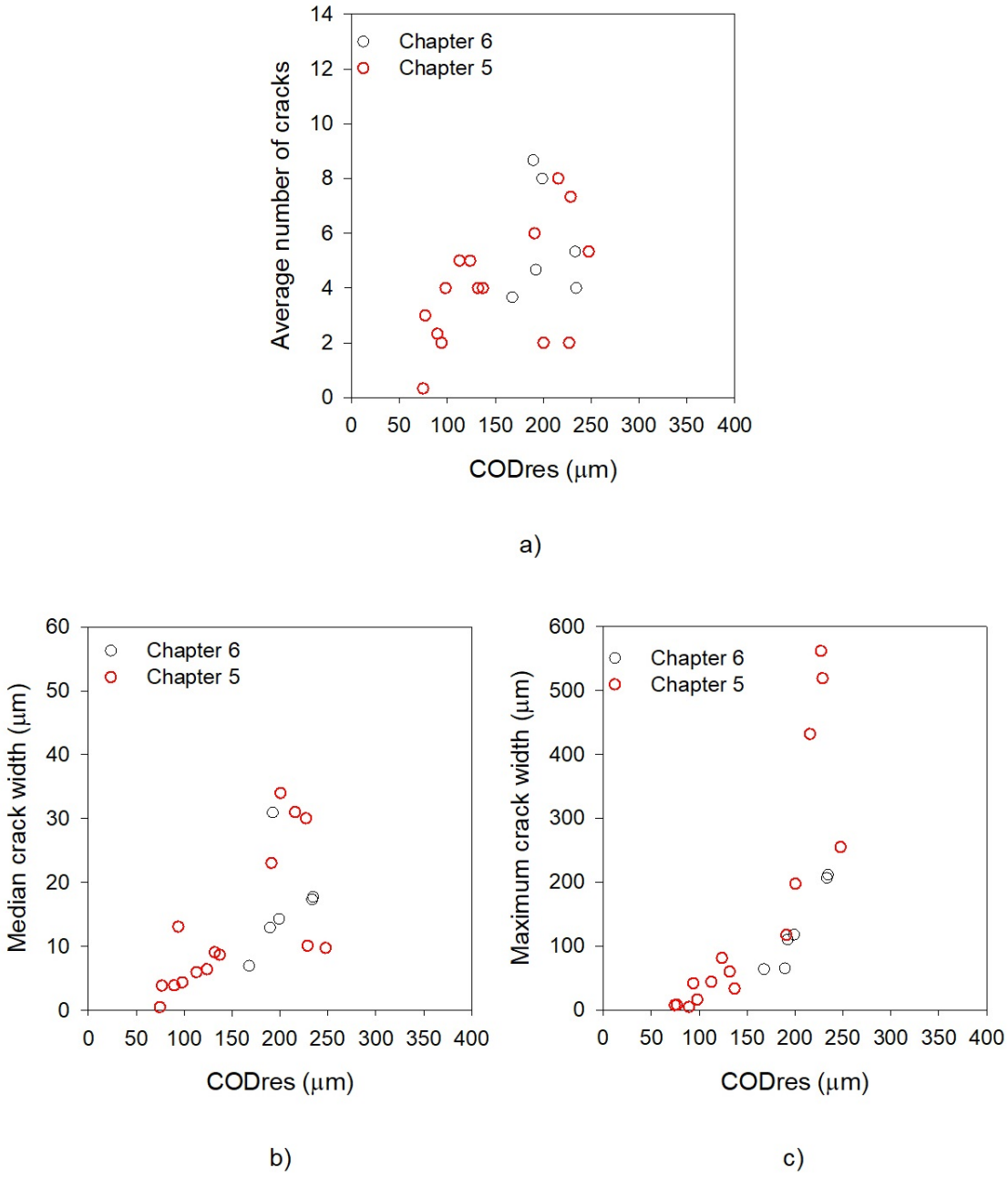

FIGURE 6.10: Relation between COD_{res} and a) Average number of cracks over the length of 40 mm; b) Median crack width; c) Maximum crack width.

- Cracked-loaded specimens (3.0%-300-i) presented similar or improved bending behaviour compared to 3.0%-0-i specimens, both in terms of peak load and initial stiffness (see Figure 6.12-b).
- Cracked-unloaded specimens 3.0%-350-i and 3.0%-400-i showed similar average peak loads but lower stiffness compared to 3.0%-0-i specimens (see Figure 6.12-b).

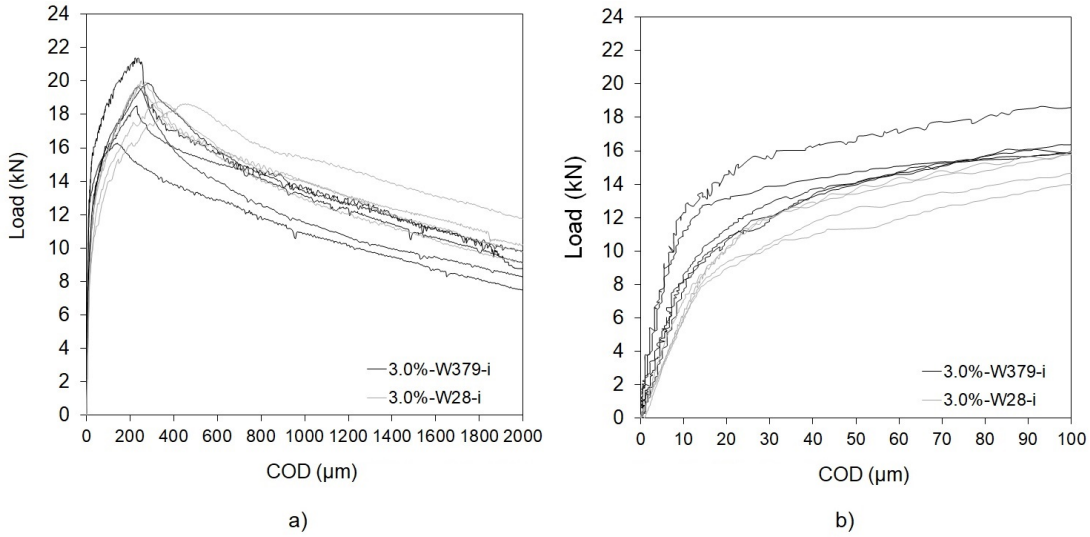

FIGURE 6.11: Four point bending load–displacement relationships for 28 and 379 old days.

In cracked UHPFRC specimens, the phenomenon of autogenous healing of cracks could be anticipated due to the very fine crack widths, the large amount of anhydrous clinkers and the presence of wetting–drying cycles [19]. Results presented in Figure 6.12 clearly show the autogenous healing of cracks was more pronounced in 3.0%-300-i specimens compared to other cracked specimens (3.0%-350-i and 3.0%-400-i); and this self-healing occurred under tensile loading. Similar findings were reported by Parant et al. [19]. This improved behaviour of the 3.0%-300-i specimens cracked up to $COD_{\text{load}} = 300$ µm, and maintained loaded in aggressive environment, can be explained by the lower damage imposed to these specimens, leading to the formation of only fine microcracks (as reported by the author in Chapter 5). On the contrary, in the case of 3.0%-350-i and 3.0%-400-i specimens a macro-crack has formed (as evidenced by maximum crack width results reported in Figure D.1 of Appendix D and photos shown in Appendix F), which could not be completely sealed by the autogenous healing, thus causing an irreversible decrease in the initial stiffness. [19].

6.3.3 Chloride penetration

6.3.3.1 Visual and microscopic analysis

All specimens remained in excellent condition after the chlorides cycles with no evidence of surface scaling, material loss or additional cracking, which corroborates with previous findings [16]. However, corrosion on fibres close to the exposed surface it was generally observed, as exemplified shown in Figure 6.13. Previous research confirmed

Table 6.7: Four-point bending test results summary.

Specimens	Nº of specimens	Testing age (days)	Fmax (kN)	COD_{Fmax} (µm)
3.0% - W28 - i	4	28	19.3 ± 0.6	325 ± 93
3.0% - W379 - i	4	379	19.1 ± 1.7	225 ± 51
3.0% - 0 - i (uncracked exposed to chlorides)	5	379	21.3 ± 1.7	275 ± 47
3.0% - 300 - i (exposed to chlorides in loaded state 138 d)*	2	138	23.5 ± 2.1	174*
3.0% - 300 - i (exposed to chlorides in loaded state)	3	379	18.2 ± 2.2	213 ± 91
3.0% - 350 - i (exposed to chlorides in unloaded state)	5	379	19.8 ± 0.5	255 ± 41
3.0% - 400 - i (exposed to chlorides in unloaded state)	5	379	19.0 ± 0.9	277 ± 47

*One specimen presented the crack localised out the measuring length covered by the LVDTs

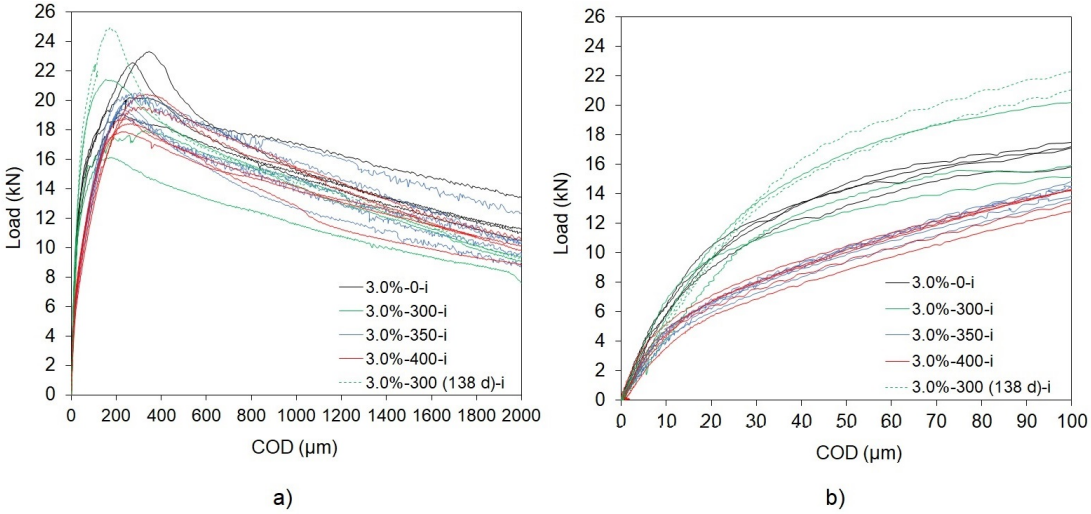

FIGURE 6.12: a) Four point load-displacement relationships for all valid specimens tested at end of chlorides cycles and b) Load-displacement curves up to $COD = 100$ µm.

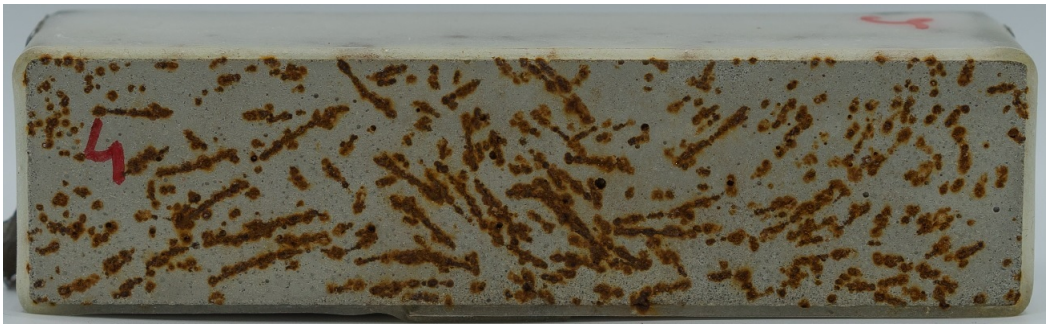

FIGURE 6.13: Exposed specimen surface after wetting-drying cycles (3.0%-0-4).

that fibres located at depths up to 3 mm suffered severe corrosion whereas the rest of the fibres, i.e., those fully embedded inside of the concrete, remained free from corrosion [25], [26], [27]. Moreover, specimens were also observed using the Microscope Multizoom Nikon AZ100 (referred in section 6.2.5) to detect micro-cracks. An example is shown in Figure 6.14, which presents some evidences of self-healing, with formation of new hydration products in the crack mouth. The presence of self-healing products seems to corroborate with mechanical performance after long term chloride exposure presented in section 6.3.2.2.

6.3.3.2 Chloride penetration depth and chlorides profile analysis

After cutting and removing powder on the specimen surface, a 0.1 molar silver nitrate solution was sprayed on one of the cut sections. Visible white silver chloride precipitation indicates the chloride penetration depth, which can be seen in Appendix F,

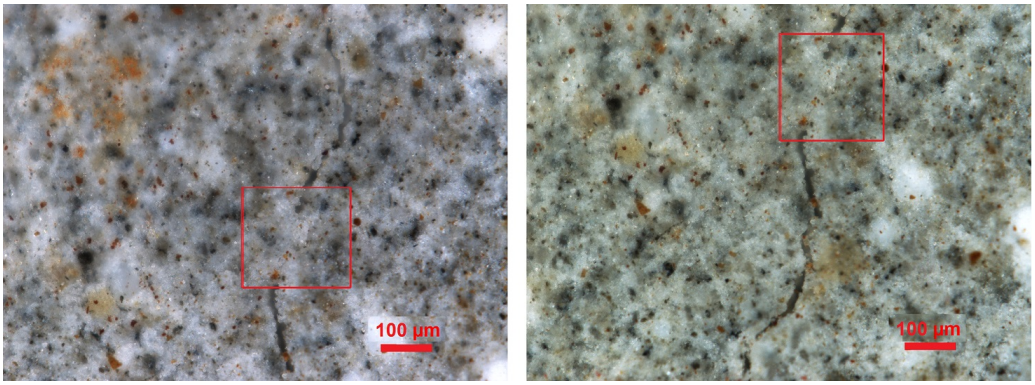

FIGURE 6.14: Possible evidence of self-healing products (3.0%-300-1).

namely, Figure F.1 and Figure F.2, Figure F.3 to Figure F.6, and Figure F.7 to Figure F.9, for 3.0%-300-i, 3.0%-350-i and 3.0%-400-i specimens, respectively. It must be noted that some reaction occurred between the fibres and the silver nitrate solution, which is perceived in Figures of Appendix F. Besides, detailed values of penetration depth concerning each specimen is presented in Table E.2 of Appendix E.

For cracked specimens, 3.0%-350-i and 3.0%-400-i, two regions of chloride penetration depth could be distinguished, the penetration in the non-cracked zone (D_m) and the penetration in the main crack zone (D_{crack}), as indicated in Figure 6.7 on section 6.2.7. D_{crack} was located where a macro-crack was found in between the two loading points. In the cracked specimens (3.0%-350-i and 3.0%-400-i), a localised and significant chloride penetration (between 10-17 mm) was observed close to the macro-crack. On the other hand, in reference specimens or healthy areas of cracked specimens, more uniform penetration occurred (roughly 2-3 mm). Concerning loaded-cracked specimens, 3.0%-300-i, a different chloride penetration pattern was observed, since these specimens present mainly micro-cracking, instated of a evident macro-crack as observed in series 3.0%-350-i and 3.0%-400-i. This micro-cracks promoted suction of aqueous chloride solution, giving rise to small penetration through them, as can be seen in Figure F.1 and Figure F.2 of Appendix F. The maximum chloride penetration depth was 18-19 mm, while in non-cracked zone was 2 mm. It must be noted that, in 3.0%-300-i specimens, some chloride precipitation occurred in the loaded surface of the specimens (see Figure F.1 and Figure F.2 of Appendix F), since it was not possible to protect this surface with the waterproof tape.

Figure 6.15 presents the chloride profiles for each series specimen and it also depicts the C_0 (blue line in Figure 6.15-a, b, c and d). The chloride content values, at different depths for each specimen, are listed in Table E.2 of Appendix E. The chloride content is expressed as the percentage of chloride ions by mass of the sample (without steel fibres - UHPC).

The non-cracked specimens (3.0%-0-i) showed a high chloride concentration close to the specimen's surface with a decreasing level towards the inner of the specimen. These results are in agreement with the colourimetric analysis with silver nitrate. The maximum chloride content varied between 0.47-0.79% at a depth ranging from 0 to 5 mm, then, between 5-10 mm depth, the chloride content drastically decreased (around 50%) for values between 0.26%-0.41%, see Figure 6.15-a. Afterwards chloride profiles kept decreasing with an asymptotic shape converging to 0.20% as depicted in Figure 6.15-a.

On cracked specimens, samples taken near a macro-crack and non-cracked areas were analysed and depicted in Figure 6.15-b, -c and -d, using full and dashed lines, respectively, (chloride profiles data is also compiled in Table E.2 of Appendix E). Generally, chlorides profiles appear to be similar despite the different COD_{load} applied. In fact, on cracked-unloaded specimens, 3.0%-350-i and 3.0%-400-i, the chlorides could penetrate inwards more rapidly due to the induced macro-crack. Maximum chloride content takes place close to the surface and then decreases as the penetration depth increases. The maximum chloride content, near the surface, varied between 0.61-0.98% and 0.62-0.90% for 3.0%-350-i and 3.0%-400-i specimens, respectively. Regarding the non-cracked area, maximum chloride content, near the surface, was 0.84% and 0.80% for 3.0%-350-i and 3.0%-400-i specimens, respectively. The main difference between crack and the non-cracked area is that the chloride content drastically reduced after 5 mm from the surface of specimens and it keeps nearly constant up to 20 mm depth. These findings corroborate with colourimetric analysis with silver nitrate, in which penetration front is different in non-cracked and cracked areas (Figure F.3 to Figure F.6, and Figure F.7 to Figure F.9, for 3.0%-350-i and 3.0%-400-i specimens, respectively, in Appendix F). Besides, as can be observed in Figure 6.16-b, it seems higher median crack width gave rise to higher chloride content. On the other hand, chloride content did not show any tendency regarding maximum crack width, as can be seen in Figure 6.16-a. This seems to make sense, since up to a certain value of crack width the suction capacity should be dominant. It should be noted that is common practice to discard the first mm of a chloride profile sample and take the next increment, around the 10 mm depth, as a constant initial, pseudo surface concentration [28], thus Figure 6.16 illustrates results of chloride content concerning only 5-10 mm depth.

On cracked-loaded specimens, 3.0%-300-i, the maximum chloride content in the cracked area was 0.61-0.65% as can be seen in Figure 6.15-b. After 138 days of chloride cycles, the chloride concentration on cracked zone was similar and varied between 0.43-0.62%. The 3.0%-300-i specimens presented also improved behaviour

in terms of resistance to ingress of chlorides, compared to the remaining cracked specimens, which might be explained by the occurrence of self-healing. After the first wetting-drying cycles the fine micro cracks sealed, which slowed the chlorides ingress. These results are in agreement with the bending test results previously discussed section 6.3.3.2.

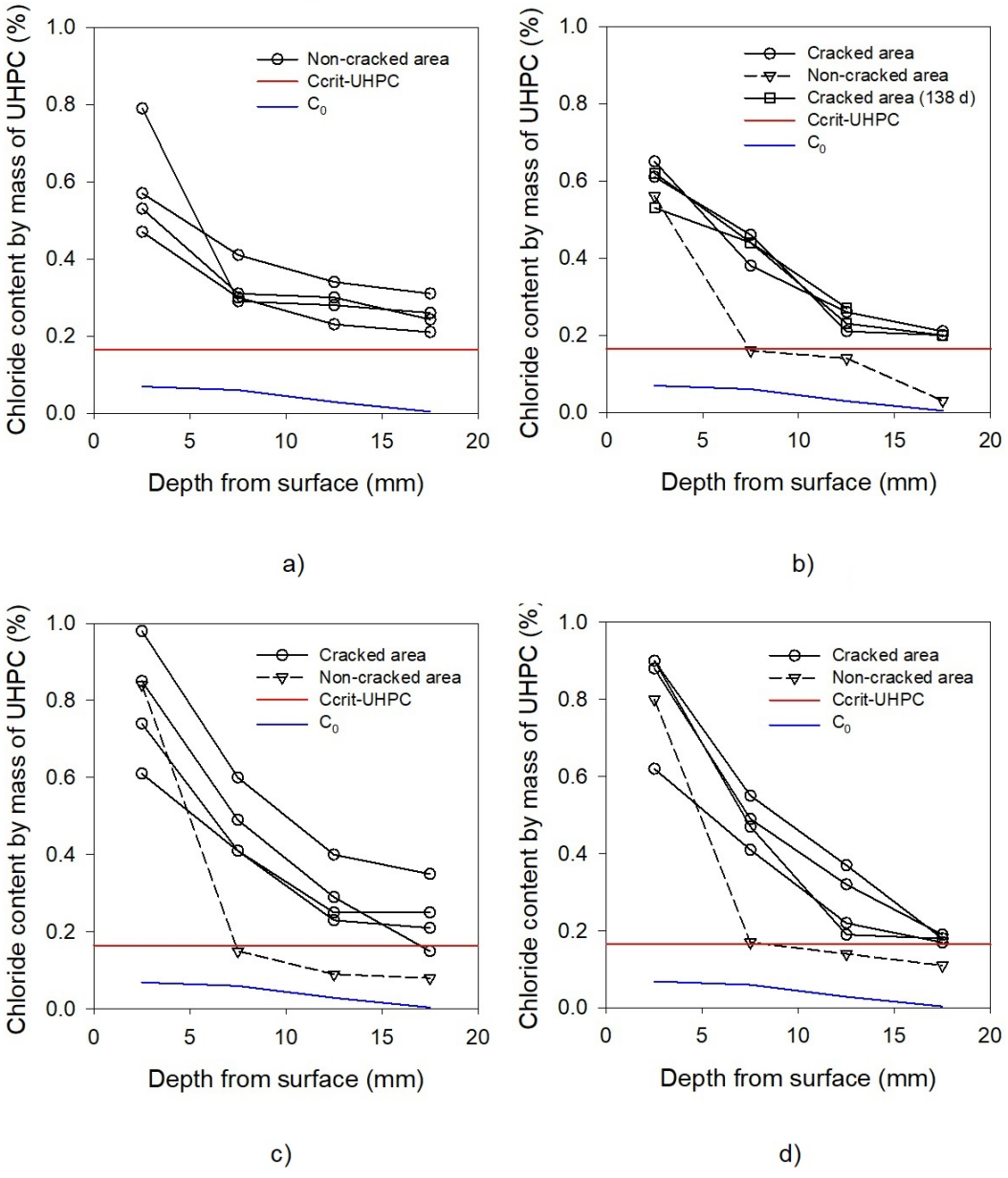

FIGURE 6.15: Chloride profiles for: a) 3.0%-0-i; b) 3.0%-300-i; c) 3.0%-350-i and d) 3.0%-400-i specimens.

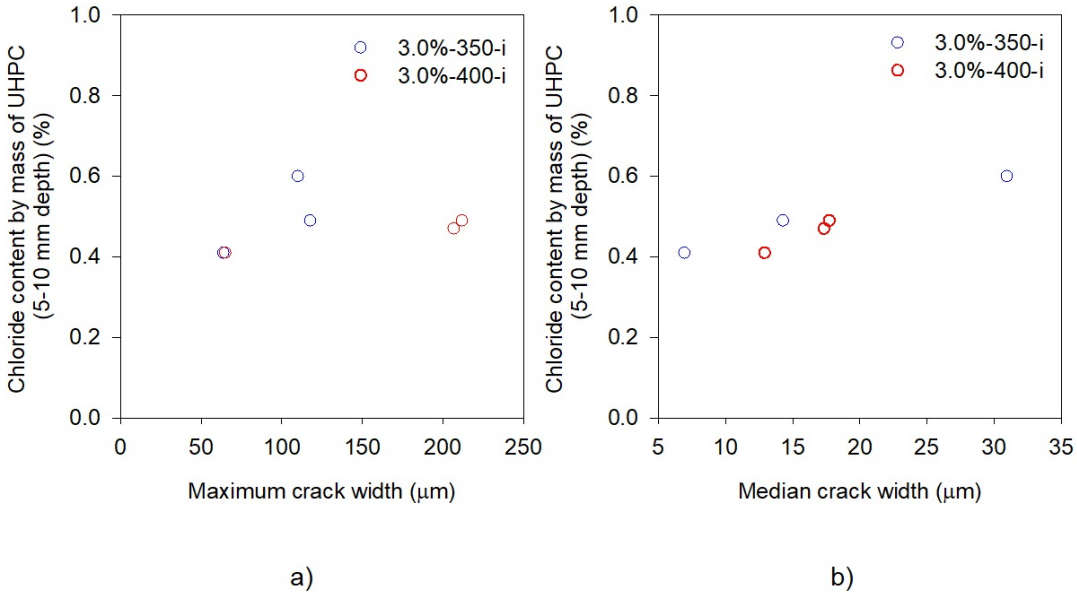

FIGURE 6.16: Relationship between chloride content (5-10 mm depth) on: a) maximum crack width and b) median crack width.

6.3.3.3 Critical chloride content and UHPFRC cover

The critical chloride content (Ccrit) can be defined as the content of chloride at the steel depth that is necessary to sustain local passive film breakdown and hence initiate the corrosion process [29]. The critical chloride content is often referred as a percentage of the of cement content. Different authors have reported different chloride thresholds to depassivate the reinforcing steel [30], [31]. International standards present limits on the tolerable chloride content in cement-based composites. For example, the European standard EN 206-1 restricts the chloride content to 0.40% by mass of binder for reinforced concrete structures. The Ccrit suggested in EN 206-1 is depicted in Figure 6.15, red lines. It should be noted that Ccrit=0.40% corresponds to the mass of cement plus type II additions, thus this limit needed to be converted in terms of mass of UHPC, the result being $Ccrit = 0.16\%$.

Non cracked specimens (Figure 6.15-a) presented significant content of chlorides, higher than $Ccrit = 0.16\%$ up to 20 mm depth. Regarding non-cracked areas of cracked series specimens, 3.0%-300-i, 3.0%-350-i and 3.0%-400-i, the surface chloride content (considering 5-10 mm [28]), was about 0.16% of UHPC mass (Figure 6.15-b, -c and -d). On the other hand, chloride content assessed on the main (and visible) crack revealed that up to a depth of 20 mm the chloride content was above 0.16%. Though, it shows a decreasing tendency for higher depths.

Based on the results from this experimental campaign only, one can conclude that

a minimum of 20 mm cover to reinforcement might be necessary to avoid rebar corrosion. This would be feasible considering the typical thickness of new reinforced UHPFRC layers, of 40-80 mm, as suggested in Figure 6.17 [32].

Nevertheless, it should be pointed that : i) these Ccrit value suggested in EN 206-1 is not a proper chloride threshold value, but rather a practical limit value for the production of fresh concrete [31]; ii) wetting and drying cycles in laboratory environment can be more severe than in-situ exposure due to ambience (temperature, humidity, carbonation, seawater composition) and scale factors. These can also be concluded from comparing the results of in situ campaign performed by Thomas et al. [16] and the remaining works reported in section 6.1.2. The chloride content after 5-15 years on field [16] were similar to those obtained in (faster) laboratory experiments. Field experiments are preferred when studying this topic, but these are very time-consuming and most times unfeasible, taking into account a PhD project duration. However, they can play an essential role in checking or calibrating laboratory results.

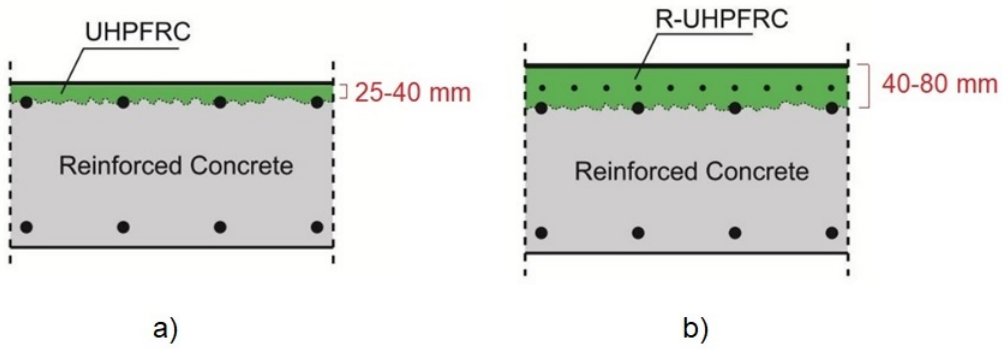

FIGURE 6.17: Basic configuration of composite structural elements combining R-UHPFRC and conventional RC: a) UHPFRC layer (thickness 25 to 40 mm) has a protective function only; b) R-UHPFRC layer (thickness of 40 to 80 mm or more) has both structural resistance and protective features [32].

6.4 Conclusions

The existence of cracks is one of the leading causes of the rapid deterioration of structural concrete members. In this study, an experimental program was conducted to evaluate the effect of cracking, and loading condition on the chloride penetration in a UHPFRC recently developed. The results presented in this Chapter contribute with a step forward on the durability design coupling mechanical and environmental loads. The following conclusions were drawn:

- COD recovery and crack pattern:

  - After unloading, COD recovery occurred. Residual COD ranged between 132-243 µm.
  - COD_{res} and COD_{load} presented a linear relationship.
  - The average number of cracks observed over a length of 40 mm remained below 9.
  - The median of crack width was under 32 µm, and it seems they slightly increase with the damage level.
  - Up to a COD_{res} of about 200 µm maximum crack width remained below 75 µm. A more significant increase of maximum crack width (> 200 µm) was observed for higher COD_{res}.

- Four-point bending behaviour:
  - Control specimens, i.e., water cured, exhibited flexure hardening behaviour. The peak loads reached 19.3 ± 0.6 and 19.1 ± 1.7 kN,at 28 and 379 days, respectively.
  - Loaded and micro-cracked specimens, 3.0%-300-i, exposed to chloride cycles, presents a quasi-total recovery of their initial stiffness, as well as, no loss of flexural strength.
  - Cracked-unloaded specimens, 3.0%-350-i and 3.0%-400-i, had a considerable loss of their initial stiffness, while, flexure strength was not significantly affected.
  - The improved behaviour of the 3.0%-300-i specimens can be explained by the lower damage imposed to these specimens, leading to the formation of only fine micro-cracks. Contrarily, in the case of 3.0%-350-i and 3.0%-400-i specimens, a macro-crack has formed, which could not be completely sealed by the autogenous healing, thus causing an irreversible decrease in the initial stiffness.

- Exposure to chloride environment:
  - All specimens were in excellent condition with no evidence of surface scaling or additional cracking, after long term chloride exposure.
  - Corrosion of fibres closer to surface was observed, as expected.
  - Observation of specimens using an optical microscope seems to indicate the presence of self-healing, with formation of new hydration products.

- A penetration depth of approximately 10-18 mm was found on the crack's surrounding area. However, in non-cracked regions, the penetration depth was of about 2-3 mm, which was similar to the penetration over non-cracked specimens (3.0%-0-i).
- The maximum chloride content, considering 5-10 mm depth, on cracked area, varied between 0.41-0.60% and 0.49-0.55% for 3.0%-350-i and 3.0%-400-i specimens, respectively
- On cracked-loaded specimens, 3.0%-300-i, considering 5-10 mm depth, the maximum chloride content on the cracked area was 0.38-0.46%.
- The foremost difference between crack and the non-cracked area is that the chloride content drastically reduced after 5 mm from the surface of specimens and it keeps nearly constant up to 20 mm depth.
- There is still no agreement about the value of Ccrit. European standards suggested a Ccrit=0.40% by mass of binder (cement plus type II additions), which is equivalent to 0.16% by mass of the UHPC under study.
- Chloride contents observed in these experimental campaigns, up to 20 mm depth, were superior to Ccrit=0.16% by mass of UHPC, particularly, near the macro-crack of specimens 3.0%-350-i and 3.0%-400-i.
- Based on this campaign results only, a UHPFRC cover of at least 20 mm would be recommended. However, it should be considered that accelerated test in the laboratory can be more severe than the exposure of real structures to natural ambient conditions. Thus, real field tests would be important to calibrate laboratory results.

References

[1] Juliano Provete Vincler, Thomas Sanchez, Vicky Turgeon, David Conciatori, and Luca Sorelli. A modified accelerated chloride migration tests for UHPC and UHPFRC with PVA and steel fibers. *Cement and Concrete Research*, 117:38–44, 3 2019.

[2] Emmanuel Denarie and Eugen Bruhwiler. Cast-on site UHPFRC for improvement of existing structures – achievements over the last 10 years in practice and research. In *7th workshop on High Performance Fiber Reinforced Cement Composites*, Stuttgart, Germany, 2015.

[3] E Brühwiler. Rehabilitation and strengthening of concrete structures using Ultra-High Performance Fibre Reinforced Concrete. In Alexander et al., editor, *Concrete Repair, Rehabilitation and Retrofi tting III*, pages 72–79. Taylor & Francis Group, 2012.

[4] Zhidong Zhou and Pizhong Qiao. Durability of ultra-high performance concrete in tension under cold weather conditions. *Cement and Concrete Composites*, 94:94–106, 11 2018.

[5] Wei Wang, Jian Liu, Franck Agostini, Catherine A. Davy, Frédéric Skoczylas, and Dominique Corvez. Durability of an Ultra High Performance Fiber Reinforced Concrete (UHPFRC) under progressive aging. *Cement and Concrete Research*, 55:1–13, 1 2014.

[6] S. Abbas, M. L. Nehdi, and M. A. Saleem. Ultra-High Performance Concrete: Mechanical Performance, Durability, Sustainability and Implementation Challenges. *International Journal of Concrete Structures and Materials*, 10(3):271–295, 9 2016.

[7] Dehui Wang, Caijun Shi, Zemei Wu, Jianfan Xiao, Zhengyu Huang, and Zhi Fang. A review on ultra high performance concrete: Part II. Hydration, microstructure and properties. *Construction and Building Materials*, 96:368–377, 10 2015.

[8] Ana Mafalda Matos, Sandra Nunes, Carla Costa, and José L. Barroso-Aguiar. Spent equilibrium catalyst as internal curing agent in UHPFRC. *Cement and Concrete Composites*, 104:103362, 11 2019.

[9] Rui Wang, Xiaojian Gao, Qiyan Li, and Yingzi Yang. Influence of splitting load on transport properties of ultra-high performance concrete. *Construction and Building Materials*, 171:708–718, 5 2018.

[10] Amin Abrishambaf, Mário Pimentel, and Sandra Nunes. Influence of fibre orientation on the tensile behaviour of ultra-high performance fibre reinforced cementitious composites. *Cement and Concrete Research*, 97:28–40, 7 2017.

[11] Antoine E. Naaman. High Performance Fiber Reinforced Cement Composites. In Caijun Shi and Y L Mo, editors, *Engineering Materials for Technological Needs: Volume 1. High-Performance Construction Materials Science and Applications*, chapter 3, page 448. World scientific, 2008.

[12] J.-P. Charron, E. Denarié, and E. Brühwiler. Permeability of ultra high performance fiber reinforced concretes (UHPFRC) under high stresses. *Materials and Structures*, 40(3):269–277, 4 2007.

[13] Jean-Philippe Charron, Emmanuel Denarié, and Eugen Brühwiler. Transport properties of water and glycol in an ultra high performance fiber reinforced concrete (UHPFRC) under high tensile deformation. *Cement and Concrete Research*, 38:689–698, 2008.

[14] Kay Wille and Antoine E. Naaman. Pullout Behavior of High-Strength Steel Fibers Embedded in Ultra-High-Performance Concrete. *ACI Materials Journal*, 109(4):479–488, 7 2012.

[15] Kay Wille and Antoine E. Naaman. Effect of Ultra-High-Performance Concrete on Pullout Behavior of High-Strength Brass-Coated Straight Steel Fibers. *ACI Materials Journal*, 110(4):451–462, 7 2013.

[16] Michael Thomas, Brian Green, Ed ONeal, Vic Perry, Sean Hayman, and Ashlee Hossack. Marine Performance of UHPC at Treat Island. In *3rd International Symposium on UHPC and Nanotechnology for High Performance Construction Materials*, Kassel, Germany, 2012. Kassel Univ. Press.

[17] Zhiming Ma, Tiejun Zhao, and Xiaochuan Yao. Influence of applied loads on the permeability behavior of ultra high performance concrete with steel fibers. *Journal of Advanced Concrete Technology*, 14(14):770–781, 2016.

[18] Folker H. Wittmann, X. Yao, P. Wang, P. Zhang, and T. Zhao. Influence of an Imposed Tensile Stress and Subsequent Self-healing on Capillary Absorption and Chloride Penetration into HPFRCC. In *High Performance Fiber Reinforced Cement Composites (HPFRCC7)*, number July, pages 243–250. RILEM, 2015.

[19] Edouard Parant, Rossi Pierre, and Fabrice Le Maou. Durability of a multiscale fibre reinforced cement composite in aggressive environment under service load. *Cement and Concrete Research*, 37(7):1106–1114, 2007.

[20] G U Chunping, Wang Qiannan, Liu Jintao, and Sun Wei. The effect of nano-TiO2 on the durability of ultra-high performance concrete with and without a flexural load. *Ceramics-Silikáty*, 62(4):374–381, 2018.

[21] Ana Mafalda Matos, Sandra Nunes, Carla Costa, and José L. Barroso Aguiar. Durability of an UHPC containing spent equilibrium catalyst. *under review*, 2019.

[22] Ana Mafalda Matos, Sandra Nunes, and José L. Barroso Aguiar. Capillary Transport of Water in Cracked and Non-cracked UHPFRC Specimens. *Journal of Advanced Concrete Technology*, 17(5):244–259, 5 2019.

[23] Vennesland, M. A. Climent, and Carmen Andrade. Recommendation of RILEM TC 178-TM.Testing and modelling chloride penetration in concret.Methods for obtaining dust samples by means of grinding concrete in order to determine the chloride concentration profile. *Materials and Structures/Materiaux et Constructions*, 46(3):337–344, 2013.

[24] Doo-Yeol Yoo, Joo-Ha Lee, and Young-Soo Yoon. Effect of fiber content on mechanical and fracture properties of ultra high performance fiber reinforced cementitious composites. *Composite Structures*, 106:742–753, 12 2013.

[25] Carlos G Berrocal, Lundgren Karin, and Löfgren Ingemar. Influence of steel fibres on corrosion of reinforcement in concrete in chloride environments: A review. In *FIBRE CONCRETE 2013*, Prague, Czech Republic, 2013.

[26] Jean-Louis Granju and Sana Ullah Balouch. Corrosion of steel fibre reinforced concrete from the cracks. *Cement and Concrete Research*, 35(3):572–577, 3 2005.

[27] Ana Mafalda Matos, Stefan Chaves Figueiredo, Sandra Nunes, and Erik Schlangen. Durability of fibre reinforced cementitious composites: coupling mechanical and chloride environment loads. In *RILEM-week 2018, 4th International Conference on Service Life Design for Infrastructures*, Delft, The Netherlands, 2018. RILEM.

[28] John P. Broomfield. *Corrosion of steel in concrete. Understanding, investigation and repair*. Taylor & Francis, 2 edition, 1997.

[29] Ki Yong Ann and Ha Won Song. Chloride threshold level for corrosion of steel in concrete. *Corrosion Science*, 49(11):4113–4133, 11 2007.

[30] C. Alonso, C. Andrade, M. Castellote, and P. Castro. Chloride threshold values to depassivate reinforcing bars embedded in a standardized OPC mortar. *Cement and Concrete Research*, 30(7):1047–1055, 2000.

[31] Ueli Angst, Bernhard Elsener, Claus K. Larsen, and Øystein Vennesland. Critical chloride content in reinforced concrete - A review. *Cement and Concrete Research*, 39(12):1122–1138, 12 2009.

[32] Kerstin Wassmann, Eugen Brühwiler, and Peter Lunk. Strengthening of RC Slabs using UHPFRC – Concepts and Applications. In *4th International Symposium on Ultra-High Performance Concrete and High Performance Materials*, Kassel, Germany, 2016.

7 Conclusions and Future developments

7.1 Conclusions

UHPFRC has become one of the most promising cement-based composites of the 21st century because of its remarkable mechanical properties and excellent durability characteristics. These engineering properties led to a new concept of hybrid structures in the field of rehabilitation/strengthening of the existing infrastructures, where thin layers of UHPFRC are applied in critical locations related to environmental exposure and mechanical demand [1].

However, regarding the material constituents, the use of a high amount of cement and SCM to produce UHPC, namely, Portland cement and silica fume, cause some apparent disadvantages in terms of cost and limited availability. This constrains the applications of UHPC, especially in developing countries. Besides, UHPC has a high carbon footprint and environmental impact due to its high cement content, leading to high energy consumption and CO_2 emissions. Since it is more commonly used in the prefabrication industry, it usually implies special production and curing methods, and therefore extra financial and environmental costs. These restrictions motivated designing and optimising mixtures with local available raw materials and lower amount of cement and SF, bringing advantages regarding cost and GWP. Considering that UHPFRC was developed for rehabilitation/strengthening requiring on-site fabrication, common technology, such as conventional curing, was used to ease and promote in-situ applications.

On the other hand, high autogenous shrinkage can be another of the disadvantages of UHPFRC, namely when applied on an old concrete substrate. Thus, the second core theme of this research was to obtain UHPFRC with lower early-age shrinkage and reduced cracking risk, along with reducing its environmental and economic impact.

From the experimental studies and result analyses the following conclusions can be drawn:

Chapter 2 Preliminary study using DOE approach showed that numerical optimisation allowed further improvement of cement-based composites properties in both the fresh and hardening states. DOE approach can contribute to better understand, optimise and design cement-based composites for applications with very demanding performance requirements.

Chapter 3 revealed that spent equilibrium catalyst, a waste generated from the oil refinery industry, can be turned into a value-added by-product when used as an internal curing agent to produce UHPFRC. Its use is not expected to affect the robustness of UHPFRC production since ECat is typically tailor-made for each oil-refinery based on the feed composition and desired products spectra. DOE approach determined the optimal UHPC mixture, which represents the best compromise between low autogenous shrinkage and high resistivity while guaranteeing sufficient deformability and compressive strength. This optimal UHPC mixture contains 155 $\mathrm{kg\,m^{-3}}$ of ECat that corresponds to 46.6 $\mathrm{l\,m^{-3}}$ of extra water required to saturate the ECat. The UHPFRC mixture prepared to combine the optimal UHPC mixture with 3% high-strength steel fibres ($lf/df = 65$):

- exhibited a compressive strength of 147 and 156 MPa after 28 and 90 days of wet curing, respectively
- exhibited uniaxial tensile peak stress and peak strain ranging from 11 to 15 MPa and 0.27 to 0.47%, respectively, at 28 days
- proved to be more eco-efficient and more cost-efficient than typical UHPCs reported in the literature.

Chapter 4 The results obtained in Chapter 4 indicated a promising durability performance of new UHPC compared to OC and even with HPC. Even though the new mixture contains lower amount of cement and silica fume, durability indicators obtained were in the range of indicators of other UHPFRC commercially available or non-proprietary. The resistance to carbonation of the UHPC mixes being very high, steel rebars and reinforcing fibres are much longer protected from carbonation induced corrosion than in ordinary concrete mixes. The UHPC also showed an excellent performance mitigating expansive reactions, namely, alkali-silica and external sulphates attack, and against ingress of aggressive substances such as chlorides. The highly dense hardened state of UHPC, caused by a very low w/b and high powder contents (cement+silica fume+Ecat+limestone) including very active pozzolans

(silica fume+ECat), gived rise to a very low porosity, confirmed through MIP and sorptivity, is the primary reason for this enhanced durability.

Chapter 5 addressed the influence of micro-cracking on UHPFRC with different fibre dosage. Concerning undamaged UHPFRC specimens, average sorptivity results were 0.0178 and 0.0076 mg/(mm$^2\sqrt{\text{min}}$) for 1.5% and 3.0% fibre contents, respectively. These results are in agreement with results from previous research work on other UHPFRCs. Sorptivity results of cracked UHPFRC-1.5% and UHPFRC-3.0% specimens remained in the range of 0.024 to 0.044 mg/(mm$^2\sqrt{\text{min}}$), which are relatively low values when compared to that of sound good quality conventional concrete ($w/c = 0.4$). Besides, the sorptivity values of cracked UHPFRC specimens possibly represent an upper limit of sorptivity in actual structures because the effect of self-healing was not considered, due to the short experiment duration (4 h). These features provide UHPFRC with distinct barrier qualities, inidicating that even when cracked, it can act as a protective layer increasing the durability (and service life) in the rehabilitation of structures or elements.

Chapter 6 aimed to provide additional insights about the long term durability of new UHPFRC, considering coupling mechanical and chloride loads, namely, chloride penetration through micro-cracks, simulating service conditions. After one year of wetting-drying chloride cycles, all UHPFRC specimens were in good condition with no evidence of surface scaling or additional cracking. In general, cracked specimens, had a slight loss of their initial stiffness, while, flexure strength was not significantly affected, which indicated that healing occurred. The presence of cracks influenced the chloride penetration. The chloride can penetrate inwards more rapidly due to the induced cracking promoting a more accessible entrance for the ions. Maximum chloride content took place close to the surface on crack area, and it was between 0.38%-0.59% for cracked specimens. Then it decreased as the penetration depth increased. The chloride content observed in these experimental campaigns, up to 20 mm depth, were superior to Ccrit (0.16% by mass of UHPC), particularly surrounding macro-crack area of specimens 3.0%-350-i and 3.0%-400-i. Thus, based on this campaign results only, a UHPFRC cover of at least 20 mm would be recommended. However, it should be considered that accelerated test in the laboratory can be more severe than the exposure of real structures to natural ambient conditions. Thus, real field tests would have an important role calibrating laboratory results.

7.2 Future developments

From this study, the following developments are recommended for further research:

- At the material scale
  - Further optimisation of new UHPC: the final goal is that the applied fibres can be homogeneously accommodated between the aggregate particles, and that at the same time (highly flowable) self-compacting mixtures can be produced. The flowability loss during the time needs to be further checked considering the element to cast, transport time, temperature, in order to predict the flowability at real casting time.
  - The addition of steel fibres to UHPC mixture results in significant environmental and financial costs, as stated in Chapter 3. Considering the specific case of application, more eco and cost-effective solutions might be found.
  - Assessing hydration kinetics of pastes containing cement and ECat, containing cement ECat and LF, and containing cement, ECat, LF and SF, in order to better understand the effect of each raw material on the hydration process.
  - Modelling of hydration and micro-structure development of cement paste containing ECat. The effects of internal water curing of ECat on the hydration and micro-structure development of cement paste should be evaluated.
  - Evaluating the autogenous shrinkage at different temperatures.
  - Studying the micro-structure of UHPFRC, in particular, characterising the ITZ between cementitious paste and steel fibre reinforcement or aggregates and evaluating its impact on durability.
  - Evaluating the self-healing products.
  - Studying other durability indicators as gas permeability.
- At structural scale
  - Performing tensile creep testing. From a structural point of view, it is of utmost importance to know the stresses that occur in cementitious materials since early ages, associated either to volumetric changes induced by heat of hydration release, to autogenous shrinkage deformations or to early

loading (like pre-stress application, and formwork or propping removal). To accomplish this goal, it is essential to assess the early evolution of several mechanical properties and phenomena of cementitious materials, like creep, elasticity modulus and shrinkage. It must be understood how changes in the evolving micro-structure translate into macro behaviour, namely, formation of micro-cracks.

- Testing conducted under drying-wetting cycles and submerged conditions introduced in the current thesis used a single curing temperature and a regular chloride water immersing solution. Following a similar integrated testing approach, further research is needed on UHPFRC using different curing temperatures and other aggressive immersing solutions.
- Composite "UHPFRC-concrete" elements are a new type of construction and their feasibility and structural response have to be investigated. Thus, studying of hybrid structural elements including new UHPFRC are needed, including the modelling, namely considering time dependent deformation (shrinkage and creep), using an appropriate software.
- Performing field experiments on UHPFRC, monitoring either mechanical and durability properties. This has an important role on checking or calibrating laboratory results or models.

References

[1] E Brühwiler. Rehabilitation and strengthening of concrete structures using Ultra-High Performance Fibre Reinforced Concrete. In Alexander et al., editor, *Concrete Repair, Rehabilitation and Retrofi tting III*, pages 72–79. Taylor & Francis Group, 2012.

A Results based on ASTM C 1202 - Chapter 4

While the Rapid Migration Test (RMT) is famous in Europe, the Rapid Chloride Permeability Test (RCPT) or "Coulomb test" is more widespread in EUA and Canada. In both methods, the penetration of chloride ions is exerted by an external electrical field, using cylinders specimens with the dimensions of 100 mm diameter and 50 mm thickness. The significant differences between the two methods are the concentration of NaCl solution (3% in the RMT versus 10% in the RCPT), the voltage used across the electrodes (usually 30 V in RMT versus 60 V in RCPT) and the test duration (usually 24 h in RMT versus 6h in RCPT). Both RMT and RCPT tests are non-steady state tests. Besides, ASTM C 1202 rates the chloride permeability as high if passed coulombs are above 4000; with 2000 to 4000 coulombs, as moderate; with 1000 to 2000 coulombs, as low; and with less than 1000 coulombs, as very low [1].

Graybeal [2] (line 1, Table A.1) reported that untreated UHPFRC specimens achieved values of 360 and 76 Coulombs at 28 days and 56 days, respectively. All steam-treated UHPFRC specimens were in the negligible range defined by ASTM C 1202.

Ahlborn [3] (line 2, Table A.1) testedtested UHPFRC specimens at 28 days following two different curing regimes: ambient air curing and thermal treatment (specimens were subjected to a 90°C and 100% relative humidity steam bath for a total curing time of 48-hours immediately after demoulding). The average charge passed was 75 and 15 Coulombs for air-cured and thermal-treated specimens, respectively. Besides, the ionic movement in the thermal-treated specimens was independent of the age at testing (7 days or 28 days) [4].

More recently, Haber et al. [5] (line 3, Table A.1) tested five different commercially-available UHPC-class materials incorporating 2% fibre volume. The specimens were air-cured during two curing periods of 28 and 56 days. It was observed that U-B exhibited much higher charge passed values than any other UHPC material tested, and far above from other results found in the literature. The high charge passed result would be typical in highly porous cementitious systems. The authors believed it was caused by the fibres included in U-B which might have created an electrically

conductive path between the two ends of the specimen, making the test not valid for chloride penetration assessment. The remaining UHPC materials show much lower charge passed values even at early ages (i.e., 28 days), within ranges of "very low" or "negligible" chloride penetrability, according to ASTM C1202 qualitative indications. In all of them, the 56-day charge passed is lower than that at 28 days, which is indicative of the continuous hydration taking place in the system, further decreasing the total porosity.

According Alkaysi et al.[6] (line 4, Table A.2), non-property UHPFRC made with the Portland Type I/GGBS cement showed very low chloride permeability, in average 168 Coulombs, while specimens made with white cement presented 340 Coulombs and Portland type V cement 495 Coulombs.

Faizal el al [7] (line 5, Table A.2) found that the incorporation of nano-metaclay in UHPC can decrease RCPT results. The Coulombs passed of the UHPC, and a series of nano metaclayed-UHPC decreased considerably up to 56 curing days after it kept almost constant up to one-year assessments. Among the UHPC concrete, the difference is insignificant, but the trend is still the same. It was expressed that incorporating 1, 3 and 5% nano-metal clay in UHPC can decrease RCPT results.

Arora et al. [8] (line 7, Table A.3) stated that economical UHPC, incorporing different dosages of metaclay, presented migration coefficients that are an order of magnitude lower than that of conventional OPC concrete. This has considerable implications in service-life of concrete structures designed using UHPCs.

Results from Table A.1, Table A.2 and Table A.3 show most of UHPC/UHPFRCs exhibited chloride ion penetrations in the negligible ($<$ 100 Coulombs passed) or very low ranges (100-1000 Coulombs), according to ASTM C 1202 classification.

TABLE A.1: Systematisation of results from RCPT test for a reference age of 28 days, between others - Part 1.

	Ref.	Binder	Vf (%)	w/b	Curing	fc,28d (MPa)	Charge Passed–28 days (coulombs)	Charge Passed–X days (coulombs)
1	[2]	PC+SF	2	0.12	steam treatment	181	18	
					untreated	112	360	76 (56 days)
					tempered steam	154	39 (56 days)	26
					delayed steam treatment	173	18	
2	[3]	PC+SF	1.5	0.2	Air curing	165	75	
					Thermal treatment	214	15	10 (7days)
3	[5]	U-A:cement+SF	3	0.11	Ambient laboratory conditions 23 ºC and RH=50 %	131	302	53 (56 days)
		U-B:Pre-Blended	2			130	5100	2501 (56 days)
		U-C:Pre-Blended	4.5			139	425	298 (56 days)
		U-D:Pre-Blended	2			147	789	495 (56 days)
		U-E:Pre-Blended	2			120	470	303 (56 days)

TABLE A.2: Systematisation of results from RCPT test for a reference age of 28 days, between others - Part 2.

	Ref.	Binder	Vf (%)	w/b	Curing	fc,28d (MPa)	Charge Passed–28 days (coulombs)	Charge Passed–X days (coulombs)
5	[6]	White cement+SF+0.25 silica powder	1.5	0.25	-	195	89	-
		White cement+SF+0.15 silica powder				189	295	
		White cement+SF				174	637	
		PC-V+SF+0.25 silica powder				174	940	
		PC-V+SF+0.15 silica powder				187	489	
		PC-V+SF				178	57	
		Type I/GGBS+SF+0.25 silica powder				173	138	
		Type I/GGBS+SF+0.15 silica powder				181	229	
		Type I/GGBS+SF				190	138	
6	[7]	PC-I	0	0.2	Water curing	-	1000	700 (90 days)
		PC-I+1% metaclay					800	500 (90 days)
		PC-I+3% metaclay					800	500 (90 days)
		PC-I+ 5% metaclay					1000	500 (90 days)

TABLE A.3: Systematisation of results from RCPT test for a reference age of 28 days, between others - Part 3.

	Ref.	Binder	Vf (%)	w/b	Curing	fc,28d (MPa)	Charge Passed–28 days (coulombs)	Charge Passed–X days (coulombs)
6	[9]	PC-I+SF	0	0.19	Water curing	137	290	205 (60 days)
					90 ºC 48 h+water curing	150	158	123
		PC+SF+ 10% RHA			Water curing	165	262	189
					90 ºC 48 h+water curing	190	135	117
		PC+SF+ 20% RHA			Water curing	169	248	168
					90 ºC 48 h+water curing	205	112	71
		PC+SF+ 30% RHA			Water curing	175	221	162
					90 ºC 48 h+water curing	230	100	65
		PC+SF+ 40% RHA			Water curing	152	207	134
					90 ºC 48 h+water curing	181	86	52
		PC+SF+ 50% RHA			Water curing	141	163	121
					90 ºC 48 h+water curing	166	65	40
7	[8]	PC+SF+LF	0	0.17	Moist curing 28 days	130	238	
		PC+SF+ FA+LF		0.18		155	365	

References

[1] P. Kumar Mehta and Paulo J. M. Monteiro. *Concrete: Microstructure, Properties, and Materials*. McGraw-Hill, third edition, 2006.

[2] Benjamin A. Graybeal. Material Property Characterization of Ultra-High Performance Concrete. Publication n.º FHWA-HRT-06-103. Technical report, 2006.

[3] Theresa M. Ahlborn, Erron J. Peuse, and Donald Li Misson. Ultra High Performance Concrete for Michigan Bridges Material Performance – Phase I Final Report. Technical report, Center for Structural Durability Michigan Tech Transportation Institute, Michigan, 2008.

[4] T. M. Ahlborn, D. L. Misson, E. J. Peuse, and C. G. Gilbertson. Durability and strength characterization of ultra-high performance concrete under variable curing regimes. In *Second International Symposium on Ultra High Performance Concrete*, pages 197–204, Kassel, Germany, 2008.

[5] Zachary B. Haber, Igor De la Varga, Benjamin A. Graybeal, Brian Nakashoji, and Rafic El-Helou. Properties and Behavior of UHPC-Class Materials. Report No FHWA-HRT-18-036. Technical Report March, U.S. Department of Transportation, 2018.

[6] Mo Alkaysi, Sherif El-Tawil, Zhichao Liu, and Will Hansen. Effects of silica powder and cement type on durability of ultra high performance concrete (UHPC). *Cement and Concrete Composites*, 66:47–56, 2 2016.

[7] Mohd Faizal, Md Jaafar, Hamidah Mohd Saman, Muhd Norhasri, Muhd Sidek, Noorli Ismail, and Nur Farhayu Ariffin. Chloride Resistance Behavior on Nano-Metaclayed Ultra-High Performance Concrete. *MATEC Web of Conferences*, 103(01023), 2017.

[8] Aashay Arora, Asim Almujaddidi, Farrokh Kianmofrad, Barzin Mobasher, and Narayanan Neithalath. Material design of economical ultra-high performance concrete (UHPC) and evaluation of their properties. *Cement and Concrete Composites*, 104:103346, 11 2019.

[9] M. Vigneshwari, K. Arunachalam, and A. Angayarkanni. Replacement of silica fume with thermally treated rice husk ash in Reactive Powder Concrete. *Journal of Cleaner Production*, 188:264–277, 7 2018.

B Crack matrix - Chapter 5

FIGURE B.1: Localisation of cracks observed in UHPFRC specimens and corresponding crack widths (in µm)

C Summary of test results - Chapter 5

TABLE C.1: Summary of test results for UHPFRC-1.5% series

Specimen	N	Crack width (µm)			Cracking procedure			Capillary water absorption test		
		Med	Min	Max	COD_{load} (µm)	COD_{res} (µm)	Maximum Load (kN)	Total water absorbed (mg/(mm^2))	S (mg/(mm$^2\sqrt{\text{min}}$))	R^2
1.5% - 0 - 1								0.332	0.016	0.997
1.5% - 0 - 2								0.375	0.019	0.996
1.5% - 0 - 3								0.370	0.018	0.997
1.5% - 200 - 1	3	44	6	166	231	159	11.38	0.653	0.029	0.986
1.5% - 200 - 2	3	46	10	76	205	116	11.20	0.666	0.029	0.987
1.5% - 200 - 3	6	24	3	89	192	122	12.12	0.716	0.034	0.991
1.5% - 250 - 1	3	28	5	91	258	170	12.66	0.734	0.034	0.985
1.5% - 250 - 2	5	53	17	117	255	145	12.76	0.922	0.041	0.982
1.5% - 250 - 3	3	42	7	95	252	163	11.69	0.647	0.028	0.991
1.5% - 300 - 1	4	34	12	149	306	197	11.79	0.943	0.039	0.982
1.5% - 300 - 2	5	16	2	54	327	209	12.09	0.617	0.028	0.992
1.5% - 300 - 3	5	21	3	85	304	183	13.70	0.878	0.038	0.985
1.5% - 350 - 1	5	37	6	112	356	233	12.11	0.979	0.040	0.987
1.5% - 350 - 2	5	22	2	417	354	295	10.35	0.839	0.034	0.985
1.5% - 350 - 3	4	21	1	110	364	274	10.59	1.024	0.039	0.977
1.5% - 400 - 1	4	10	1	206	407	334	10.73	0.882	0.033	0.988
1.5% - 400 - 2	6	18	1	46	429	320	12.63	0.740	0.032	0.988
1.5% - 400 - 3	12	18	2	306	404	280	10.89	1.212	0.044	0.976

TABLE C.2: Summary of test results for UHPFRC-3.0% series

Specimen	N	Crack width (µm)			Cracking procedure			Capillary water absorption test		
		Med	Min	Max	COD_{load} (µm)	COD_{res} (µm)	Maximum Load (kN)	Total water absorbed (mg/(mm^2))	S (mg/(mm$^2\sqrt{\text{min}}$))	R^2
3.0% - 0 - 1								0.151	0.007	0.998
3.0% - 0 - 2								0.154	0.008	0.997
3.0% - 0 - 3								0.154	0.008	0.999
3.0% - 200 - 1	0	1	0	7	208	75	15.65	0.656	0.031	0.973
3.0% - 200 - 2	2	4	2	5	219	90	14.89	0.491	0.024	0.989
3.0% - 200 - 3	3	4	2	8	209	77	14.89	0.549	0.028	0.987
3.0% - 250 - 1	5	6	2	81	273	124	16.96	0.849	0.035	0.962
3.0% - 250 - 2	4	4	2	16	262	98	18.71	0.697	0.031	0.979
3.0% - 250 - 3	2	13	2	41	259	94	18.65	0.641	0.034	0.980
3.0% - 300 - 1	4	9	3	60	321	132	14.28	0.659	0.032	0.986
3.0% - 300 - 2	4	9	3	33	315	137	18.27	0.613	0.030	0.991
3.0% - 300 - 3	5	6	4	44	310	113	18.41	0.772	0.034	0.975
3.0% - 350 - 1	2	30	18	561	364	227	15.96	1.045	0.039	0.975
3.0% - 350 - 2	2	34	2	197	366	200	19.27	0.778	0.030	0.990
3.0% - 350 - 3	6	23	3	117	362	191	17.60	0.903	0.038	0.975
3.0% - 400 - 1	8	31	2	432	416	216	19.00	1.032	0.040	0.987
3.0% - 400 - 2	7	10	2	519	477	229	18.99	1.023	0.034	0.967
3.0% - 400 - 3	5	10	2	255	421	248	22.81	0.871	0.032	0.972

D Crack matrix - Chapter 6

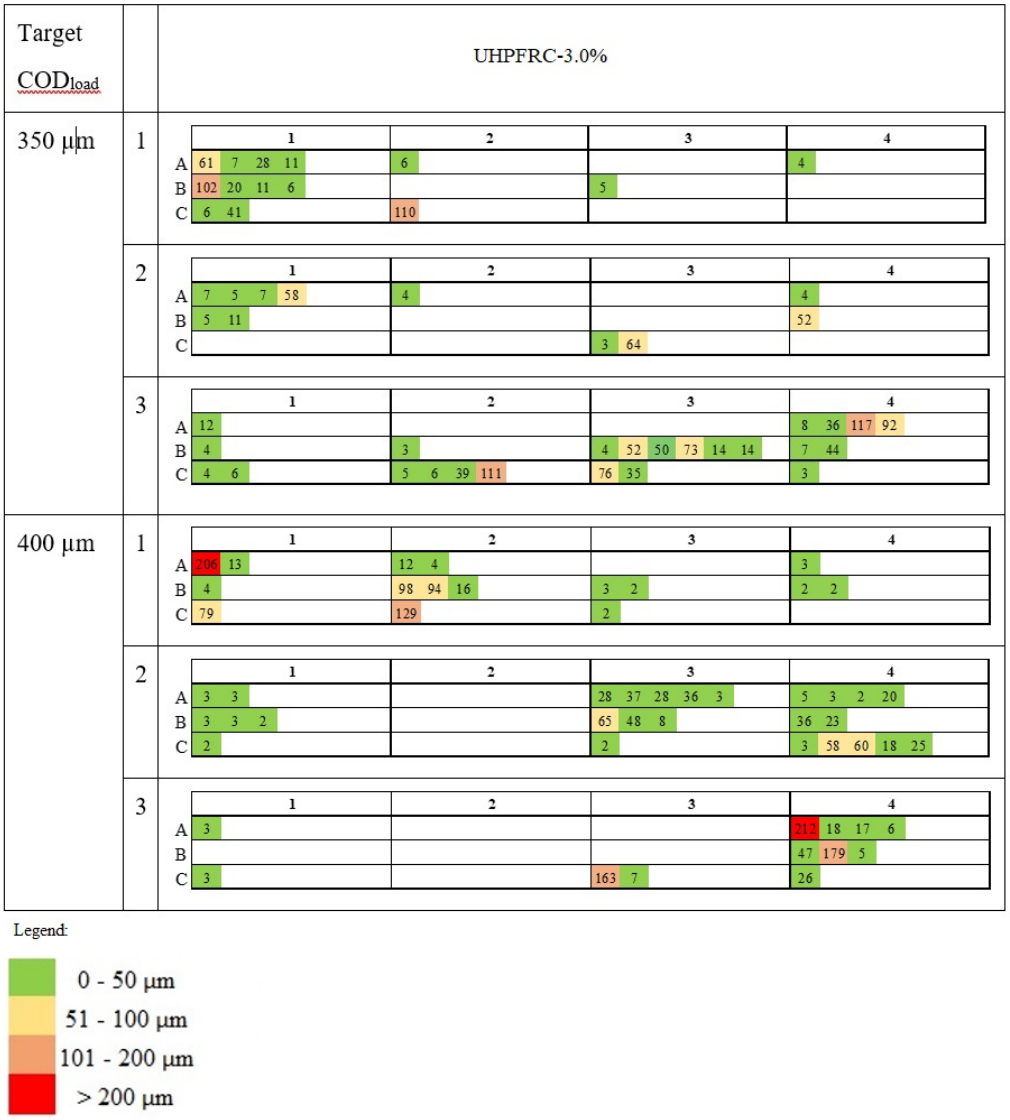

FIGURE D.1: Localisation of cracks observed in UHPFRC-3.0% specimens and corresponding crack widths (in µm)

E Summary of test results - Chapter 6

Table E.1: Summary of test results for water cured specimens.

Series	Specimen	Curing	Testing age (d)	Fmax (kN)	COD_{Fmax} (µm)
3.0%-W28	1	water, 28 days	28	18.62	454
	2			18.78	331
	3			20.00	249
	4			19.74	265
3.0%-W379	1	water, 379 days	379	16.28	139
	2			21.36	237
	3			19.68	238
	4			18.52	231
	5			19.88	278

TABLE E.2: Summary of test results for specimens exposed to chlorides cycles. (Notes: *Crack out of LVDTs range;**Tested after 138 days of chloride exposure)

Specimen	N	Crack widths (µm)			Cracking procedure				Mechanical properties after chlorides exposure		Chloride content (%)				Chloride penetration depth (mm)	
		Median	Min	Max	COD_{load} (µm)	COD_{res} (µm)	COD_{res} tested (µm)	Fcr,max (kN)	Fmax (kN)	COD_{Fmax} (kN)	0-5 (µm)	5-10 (mm)	10-15 (mm)	15-20 (mm)	D_{crack}	D_m
3.0% - 0 - 1**											0.45	0.08	0.02	-		1.80
3.0% - 0 - 2									23.33	341	0.79	0.26	0.28	0.29		2.65
3.0% - 0 - 3									20.21	257	0.53	0.31	0.30	0.24		2.17
3.0% - 0 - 4									22.57	271	0.57	0.41	0.34	0.31		1.95
3.0% - 0 - 5									19.05	232	0.47	0.30	0.23	0.21		2.57
3.0% - 300 - 1**					300	144	300	16.19			0.62	0.44	0.23	0.20		
3.0% - 300 - 2**					302	147	300	17.86			0.43	0.44	0.27	-		
3.0% - 300 - 3**					322	157	300	19.14	24.96	174						
3.0% - 300 - 4**					303	145	300	18.41	22.00	*						
3.0% - 300 - 5					300	144	300	16.19	17.97	317						
3.0% - 300 - 6					302	147	300	17.86	16.13	170						
3.0% - 300 - 7					322	158	300	19.14	21.43	152						
3.0% - 300 - 8					303	139	300	18.41			0.65	0.38	0.26	0.21	17.50	1.94
3.0% - 300 - 9					303	145	300	18.41			0.61	0.46	0.21	0.20	18.55	1.51
3.0% - 350 - 1					363	195	195	17.99	19.16	233						
3.0% - 350 - 2					351	177	177	18.58	20.53	304						
3.0% - 350 - 3					352	172	172	17.47	19.16	210						
3.0% - 350 - 4	5	31	4	110	357	192	192	15.86			0.98	0.60	0.40	0.35	13.46	2.78
3.0% - 350 - 5	4	7	3	64	357	168	168	18.71			0.61	0.41	0.25	0.25	11.34	3.03
3.0% - 350 - 6	8	14	3	117	366	199	199	18.31			0.85	0.49	0.29	0.15	13.59	3.42
3.0% - 350 - 7					354	195	195	19.92	20.18	291						
3.0% - 350 - 8					365	177	177	20.97			0.74	0.41	0.23	0.21	13.43	3.42
3.0% - 350 - 9					350	153	153	17.81	19.78	236						
3.0% - 400 - 1					405	190	190	17.60	20.42	334						
3.0% - 400 - 2					405	224	224	17.53	18.78	243						
3.0% - 400 - 3	5	17	2	206	412	233	233	19.26			0.90	0.47	0.19	0.18	10.71	2.18
3.0% - 400 - 4	9	13	2	65	405	190	190	19.36			0.62	0.41	0.22	0.17	8.50	3.04
3.0% - 400 - 5	4	18	3	212	408	234	234	17.71			0.88	0.49	0.32	0.19	12.16	2.50
3.0% - 400 - 6					407	226	226	18.26	17.88	227						
3.0% - 400 - 7					404	231	231	18.42	18.43	262						
3.0% - 400 - 8					407	215	215	17.63	19.55	320						

F Chloride penetration depth - Chapter 6

FIGURE F.1: Specimen 3.0%-300-8: chlorides ingress from the side of the bottom surface (penetration depth of chloride ions in lighter part).

FIGURE F.2: Specimen 3.0%-300-9: chlorides ingress from the side of the bottom surface (penetration depth of chloride ions in lighter part).

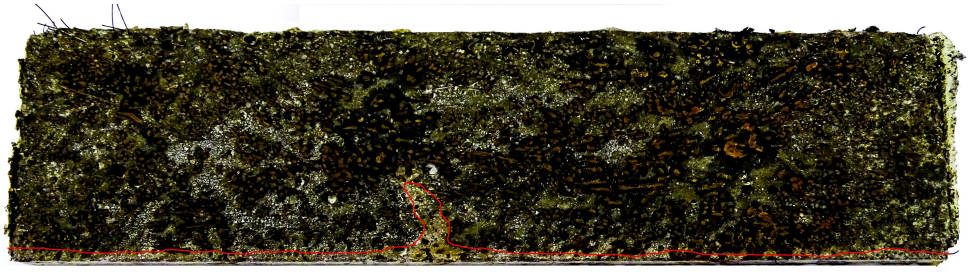

FIGURE F.3: Specimen 3.0%-350-4: chlorides ingress from the side of the bottom surface (penetration depth of chloride ions in lighter part).

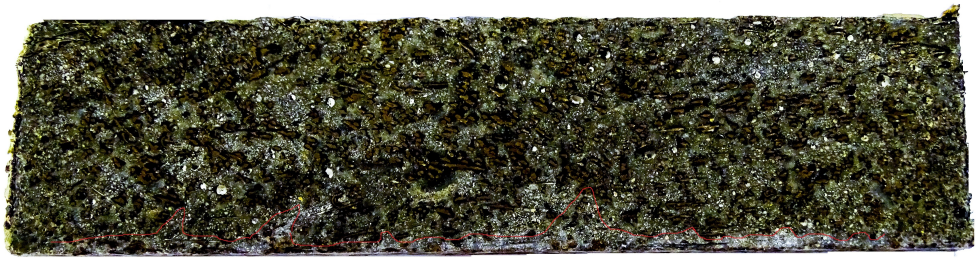

FIGURE F.4: Specimen 3.0%-350-5: chlorides ingress from the side of the bottom surface (penetration depth of chloride ions in lighter part).

FIGURE F.5: Specimen 3.0%-350-6: chlorides ingress from the side of the bottom surface (penetration depth of chloride ions in lighter part).

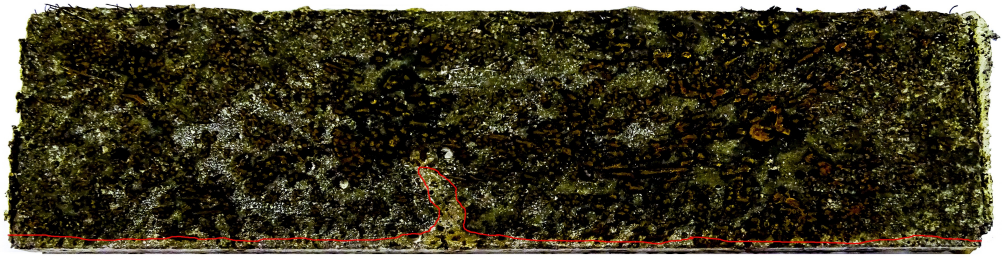

FIGURE F.6: Specimen 3.0%-350-8: chlorides ingress from the side of the bottom surface (penetration depth of chloride ions in lighter part).

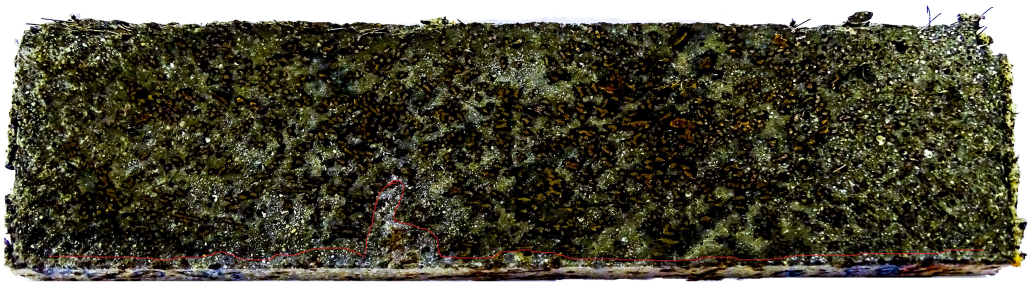

FIGURE F.7: Specimen 3.0%-400-3: chlorides ingress from the side of the bottom surface (penetration depth of chloride ions in lighter part).

FIGURE F.8: Specimen 3.0%-400-4: chlorides ingress from the side of the bottom surface (penetration depth of chloride ions in lighter part).

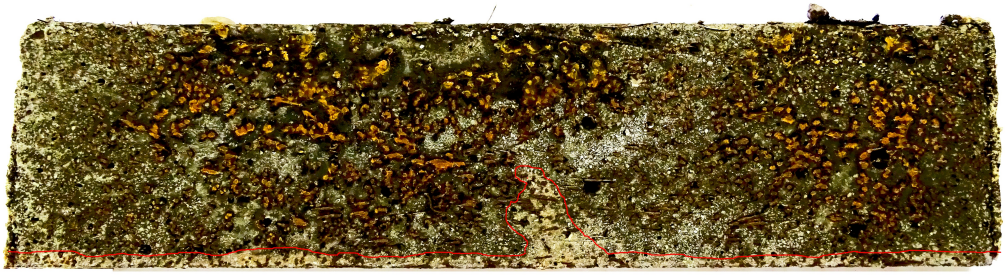

FIGURE F.9: Specimen 3.0%-400-5: chlorides ingress from the side of the bottom surface (penetration depth of chloride ions in lighter part).